

**AN EXPERIMENTAL AND COMPUTATIONAL STUDY ON DIFFUSION
DRIVEN STRUCTURAL CHANGES IN Fe-Ti BASED DISSIMILAR JOINTS
UNDER EQUILIBRIUM AND NON-EQUILIBRIUM CONDITIONS**

By

T.N. PRASANTHI

Enrollment No: ENGG02200904023

Indira Gandhi Centre for Atomic Research, Kalpakkam

*A thesis submitted to the
Board of Studies in Engineering Sciences
In partial fulfillment of requirements
for the Degree of*

DOCTOR OF PHILOSOPHY

of

HOMI BHABHA NATIONAL INSTITUTE

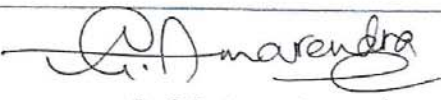
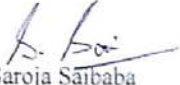


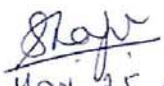
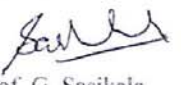


March, 2016

Homi Bhabha National Institute

Recommendations of the Viva Voce Committee

As members of the Viva Voce Committee, we certify that we have read the dissertation prepared by T.N. PRASANTHI entitled "An Experimental and Computational Study on Diffusion Driven Structural Changes in Fe-Ti Based Dissimilar Joints Under Equilibrium and Non-equilibrium Conditions" and recommend that it may be accepted as fulfilling the thesis requirement for the award of Degree of Doctor of Philosophy.

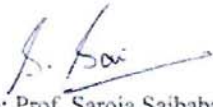
Chairman	 Prof. G. Amarendra	Date: May 25, 2017
Guide / Convener	 Prof. Saroja Saibaba	Date: 25/05/2017
External Examiner	 Prof. Sudarsanam Suresh Babu	Date: MAY 25, 2017 05/25/2017
Member 1	 Prof. Shaju K. Albert	Date:  May 25, 2017
Member 2	 Prof. G. Sasikala	Date: 25/05/2017

Final approval and acceptance of this thesis is contingent upon the candidate's submission of the final copies of the thesis to HBNL.

I hereby certify that I have read this thesis prepared under my direction and recommend that it may be accepted as fulfilling the thesis requirement.

Date: May 25, 2017

Place: Kalpakkam


Guide: Prof. Saroja Saibaba

STATEMENT BY AUTHOR

This dissertation has been submitted in partial fulfillment of requirements for an advanced degree at Homi Bhabha National Institute (HBNI) and is deposited in the Library to be made available to borrowers under rules of the HBNI.

Brief quotations from this dissertation are allowable without special permission, provided that accurate acknowledgement of source is made. Requests for permission for extended quotation from or reproduction of this manuscript in whole or in part may be granted by the Competent Authority of HBNI when in his or her judgment the proposed use of the material is in the interests of scholarship. In all other instances, however, permission must be obtained from the author.


T.N. PRASANTHI

DECLARATION

I, hereby declare that the investigation presented in the thesis has been carried out by me. The work is original and has not been submitted earlier as a whole or in part for a degree / diploma at this or any other Institution / University.

T.N. Prasanthi
T.N. PRASANTHI

List of Publications arising from the thesis

I. Published:

1. A study on the diffusion phenomena in Fe-C/Ti system under equilibrium and non-equilibrium conditions, **T.N. Prasanthi**, C. Sudha, S. Saroja, Metall. Mater. Trans A, 48 (2017) 1969-1980.
2. Formation and reversion of metastable fcc phase in Ti-5Ta-2Nb explosive clad, **T.N. Prasanthi**, C. Sudha, Ravikirana, S. Saroja, Mater. Chara., 116 (2016) 24-32
3. Effect of alloying elements on interdiffusion phenomena in explosive clads of SS/Ti-5Ta-2Nb alloy, **T.N. Prasanthi**, C. Sudha, S. Saroja, J. Mater. Sci., 51 (2016) 5290-5304.
4. Optimization of heat treatments for reversion of strain induced martensite in 304L SS explosive clad, **T.N. Prasanthi**, C. Sudha, P.K. Parida, Arup Dasgupta, S. Saroja, J. Mater. Engg. Perform., 25 (2016) 536-544.
5. Explosive cladding and post weld heat treatment of mild steel and titanium, **T.N. Prasanthi**, C. Sudha, Ravikirana, S. Saroja, Mater. Design, 93 (2016) 180-193.
6. Friction welding of mild steel and titanium: Optimization of process parameters and evolution of interface microstructure, **T. N. Prasanthi**, C. Sudha, Ravikirana, S. Saroja, N. Naveen Kumar, G.D. JanakiRam, Mater. Design, 88 (2015) 58-68.
7. Reverse transformation of deformation induced phases and associated changes in the microstructure of explosively clad Ti-5Ta-2Nb and 304L SS, **T.N. Prasanthi**, C. Sudha, S. Murugesan, V. Thomas Paul, S. Saroja, Metall. Mater. Trans. A, 46 (2015) 4429-4435.
8. Prediction and confirmation of phases formed in the diffusion zone of Ti-5Ta-2Nb/304L SS explosive clads, **T.N. Prasanthi**, C. Sudha, P.K. Parida, A. Dasgupta, S. Saroja, Metall. Mater. Trans. A, 46 (2015) 1519-1534.
9. Assessment of mechanical property of Ti-5Ta-2Nb and 304L SS explosive clad and correlation with microstructure, C. Sudha, **T.N. Prasanthi**, V. Thomas Paul, S. Saroja, M. Vijayalakshmi, Procedia Engg., 86 (2014) 42-50.

II. Communicated:

1. Molecular dynamics simulation of diffusion of Fe in hcp Ti lattice, **T.N. Prasanthi**, C. Sudha, S. Saroja, J. Exp. The. Phys., 2016.

III. Manuscript under preparation:

1. Defect aided diffusivity of Fe in hcp Ti lattice: Molecular Dynamics Study.

IV. Conference Proceedings:

1. Interdiffusion studies between Ti-5Ta-2Nb alloy and 304L austenitic stainless steel joined by explosive cladding process, *C.Sudha, T.N. Prasanthi, S. Saroja, M. Vijayalakshmi*, Proc. T.T.Chen Hon. Sym. Hydrometall. Electrometall. Mater. Charac. (Eds.) John Wiley & Sons, USA, 2012, pp.717-730.
2. Assessment of mechanical property of Ti-5Ta-2Nb and 304L SS explosive clad and correlation with microstructure, *C. Sudha, T.N. Prasanthi, V. Thomas Paul, S. Saroja, M. Vijayalakshmi*, ICONS-2014, 4-7th Feb., Kalpakkam, India, pp. 315-322.

V. Conference Presentations:

1. Joining of Ti-5Ta-1.8Nb and 304L stainless steel by explosive welding and characterization of the microstructure, *T.N. Prasanthi, C. Sudha, S. Saroja, M. Vijayalakshmi*, 63rd NMD-ATM IIM, 16-17th November 2009, Kolkata, India - **Best paper Award.**
2. Evolution of the bond strength and corrosion resistance of Ti-5Ta-1.8Nb/304L SS explosive clads, *T.N. Prasanthi, C. Sudha, H. Khalid Rafi, S. Saroja, M. Vijayalakshmi*, National Welding Seminar, 21-23rd December 2010, Vizag, India.
3. Reversion of deformation induced martensite in austenitic stainless steel, *T.N. Prasanthi, C. Sudha, P.K. Parida, Arup Dasgupta, S. Saroja*, 67th NMD-ATM, 12-15th Nov. 2013, IIT-BHU, Varanasi, India – **Best paper Award**


T.N. PRASANTHI

*Om ajnana timirandhasya jnananjana salakaya
chaksur unmilitam yena tasmai sri gurave namah*

*I offer my respectful obeisances unto my master, who has opened my eyes, with
the torch of knowledge.*

*Dedicated to
All my Teachers and Mentors*

Acknowledgements

I take this opportunity to express my sincere gratitude to the people who have supported me during the course of my Ph.D in various capacities.

*Words are not sufficient to express my deep sense of gratitude to **Dr. Saroja Saibaba** my research supervisor and Head, Microscopy and Thermo-physical Property Division, Physical Metallurgy Group (PMG) for her constant guidance, encouragement and advice. I acknowledge **Dr. C. Sudha**, for her immense support and encouragement throughout the period of my research work. Without their continuous motivation and patience, it would have been extremely difficult to realize the thesis.*

*I sincerely thank **Dr. T. Jayakumar**, former Director Metallurgy and Materials Group, and former Chairman of my doctoral committee (DC) for his motivation. I thank the DC members **Dr. G. Amarendra**, **Dr. Shaju K. Albert** and **Dr. G. Sasikala** for their useful suggestions and encouragement to improve the quality of the research work.*

*I thank **Dr. A.K. Bhaduri**, Director IGCAR, Kalpakkam and former Directors **Dr. Baldev Raj**, **Shri. S.C. Chetal**, **Dr. P.R. Vasudeva Rao** and **Dr. S.A.V. Satyamurty** for providing me an opportunity to pursue the research work.*

*I am grateful to **Dr. Manoj Warriar**, BARC (Vizag) for educating me in MD simulations and **Dr. G. JanakiRam** (IIT, Madras) for providing experimental support for fabrication of friction joints.*

*I thank **Dr. M. Vijayalakshmi**, former Associate Director, PMG for her support and encouragement. I am extremely thankful to my colleagues and fellow research scholars **Dr. R. Anand** for initiating me into computation methods, **Ravikirana** and **Thomas Paul** for the TEM analysis, **C. Jyothi** for XRD experiments, **T. Saravanan** for fabrication jobs and **Naveen** for friction welding,*

*I am deeply indebted to **Chanchal**, **Akash**, **Pragna**, and all colleagues in PMG for being very supportive.*

*On a personal note I acknowledge **Mr. Syam Subbarao**, my guru whose interesting lectures in Physics made me to choose research as my profession.*

*I am grateful to my husband **Kranti Kishore**, my parents **Pardha Saradhi & Mallika Prabhavathi** and my brother **Mohan Satyanarayana** for their unconditional affection and moral support without which I would not have enjoyed my research work.*


T.N. PRASANTHI

CONTENTS

SYNOPSIS	vii
LIST OF FIGURES	xx
LIST OF TABLES	xxix
LIST OF SYMBOLS AND ABBREVIATIONS	xxx

CHAPTER 1

INTRODUCTION

1.1	Dissimilar joints of 304LSS/Ti-5Ta-2Nb alloy for reprocessing applications	1
1.2	Review of the literature on solid state welding processes adopted to join various Fe/Ti based systems	2
1.3	Fabrication of Fe-C/Ti joints with optimized welding parameters	5
1.4	Heat treatment conditions for Fe/Ti dissimilar weld joints	7
1.4.1	<i>Selection of post weld heat treatments for Fe-C/Ti friction and explosive joints</i>	7
1.4.2	<i>Reversion annealing treatments for deformation induced phases in 304LSS and Ti-5Ta-2Nb alloy</i>	9
1.5	Growth kinetics of the diffusion zones and estimation of interdiffusion parameters	11
1.5.1	<i>Growth kinetics of the diffusion zones in Fe/Ti based systems</i>	11
1.5.2	<i>Estimation of interdiffusion parameters</i>	12
1.5.3	<i>Diffusion models available for multicomponent systems</i>	14
1.6	Molecular dynamics simulations of diffusion of Fe in hcp Ti lattice	15
1.7	Scope of the thesis	17

CHAPTER 2

EXPERIMENTAL AND COMPUTATIONAL METHODS

2.1	Introduction	21
-----	--------------	----

2.2	Specimen fabrication details	21
2.2.1	<i>Fabrication of diffusion couples of MS/Ti</i>	23
2.2.2	<i>Fabrication of MS/Ti friction welds</i>	23
2.2.3	<i>Fabrication of MS/Ti explosive clads</i>	24
2.2.4	<i>Fabrication of 304LSS/Ti-5Ta-2Nb explosive joints</i>	27
2.3	Mechanical property evaluation	27
2.4	Heat treatment schedules	29
2.5	Techniques for characterization of the dissimilar joints	30
2.5.1	<i>X-ray diffraction (XRD) analysis</i>	30
2.5.2	<i>Microstructural analysis and microhardness measurements</i>	31
2.5.3	<i>Microchemical characterization</i>	32
2.5.4	<i>Electron back scatter diffraction analysis</i>	33
2.5.5	<i>Transmission electron microscopy investigations</i>	34
2.6	Evaluation of growth kinetics of the diffusion zones and interdiffusion parameters	37
2.6.1	<i>Estimation of interdiffusion parameters</i>	37
2.7	Prediction of phases and computation of bond strength using JMatPro [®]	41
2.8	Diffusion of Fe in hcp Ti lattice - Molecular Dynamics simulations	42
2.9	Summary	44

CHAPTER 3

MICROSTRUCTURE AND PROPERTY EVALUATION IN Fe-C/Ti FRICTION AND EXPLOSIVE JOINTS IN ‘AS WELDED’ AND HEAT TREATED CONDITIONS

3.1	Introduction	45
-----	--------------	----

3.2	Characterization of ‘as received’ mild steel and Grade 2 Ti plates	47
3.3	Interface microstructure in diffusion couples of MS and Ti	48
3.4	Optimization of friction welding parameters and fabrication of joints	50
	3.4.1 <i>Variation of welding parameters in trial welds</i>	50
	3.4.2 <i>Evolution of interface microstructure in friction joints</i>	52
3.5	Optimization of post weld heat treatments for friction joints	56
	3.5.1 <i>Phase evolution – simulated at different temperatures</i>	56
	3.5.2 <i>Variation in the microstructure during thermal exposure</i>	58
3.6	Structural changes at the interface during diffusion annealing treatments	61
	3.6.1 <i>Microstructural and microchemical changes at the interface</i>	61
	3.6.2 <i>Prediction of phases at the friction joint interface</i>	64
	3.6.3 <i>Confirmation of the phases at the interface</i>	66
3.7	Fabrication and assessment of explosive clads of MS-Ti	70
	3.7.1 <i>Fabrication and optimization of load ratio</i>	70
	3.7.2 <i>Evolution of microstructure in base, flier plates and interface of explosive clad joints</i>	77
	3.7.3 <i>Confirmation of the deformation induced phases in explosive joints</i>	80
3.8	Optimization of post clad heat treatments	86
	3.8.1 <i>Prediction of evolution of phases at the explosive clad interface</i>	86
	3.8.2 <i>Evolution of microstructure during thermal exposure</i>	89
3.9	Structural changes at the interface of explosive clad joints during diffusion annealing treatments	90
	3.9.1 <i>Microstructural and microchemical changes at the interface</i>	90

3.9.2	<i>Prediction and confirmation of the phases at the explosive clad interface</i>	93
3.10	Summary	95

CHAPTER 4

STRUCTURAL CHANGES DURING DEFORMATION AND ANNEALING IN 304LSS/Ti-5Ta-2Nb EXPLOSIVE CLAD JOINTS

4.1	Introduction	97
4.2	Characterization of 'as received' SS and TiTaNb alloy	99
4.3	Assessment of SS/TiTaNb explosive clad joints	99
4.4	Optimization of post clad heat treatments	102
4.5	Deformation induced structural changes in parent metals	106
4.5.1	<i>Microstructural changes in base and flier plates of explosive joints</i>	106
4.5.2	<i>Confirmation of metastable phases by TEM investigations</i>	108
4.6	Stability of metastable phases during thermal exposure	112
4.6.1	<i>Study of reverse transformation of metastable phases by HTXRD</i>	112
4.6.2	<i>Reversion of α' martensite and associated structural changes in SS</i>	116
4.6.3	<i>Mechanism of $\alpha' \rightarrow \gamma$ transformation in SS</i>	119
4.6.4	<i>Reversion of fcc phase and associated structural changes in TiTaNb alloy</i>	126
4.6.5	<i>Mechanism of fcc \rightarrow hcp(α) transformation in TiTaNb alloy</i>	127
4.7	Structural changes due to interdiffusion on thermal exposure	136
4.7.1	<i>Microstructural and microchemical variations across the interface</i>	136

4.7.2	<i>Prediction of phases formed due to microchemical variations</i>	140
4.7.3	<i>Confirmation of secondary phases in the diffusion zone</i>	144
4.7.4	<i>Effect of secondary phases on bond strength of the explosive joints</i>	152
4.8	Summary	153

CHAPTER 5

INTERDIFFUSION IN Fe-Ti BASED SYSTEMS UNDER EQUILIBRIUM AND NON-EQUILIBRIUM CONDITIONS

5.1	Introduction	154
5.2	Growth kinetics of the diffusion zones under equilibrium conditions and estimation of interdiffusion parameters in MS/Ti joints	157
5.2.1	<i>Evolution of interface microstructure</i>	157
5.2.2	<i>Growth kinetics of the diffusion zones</i>	159
5.2.3	<i>Diffusion driven microchemical changes at the interface</i>	161
5.2.4	<i>Estimation of interdiffusion parameters</i>	162
5.3	Growth kinetics of the diffusion zones under non-equilibrium conditions and estimation of interdiffusion parameters in MS/Ti joints	164
5.3.1	<i>Evolution of interface microstructure</i>	164
5.3.2	<i>Growth kinetics of the diffusion zones</i>	167
5.3.3	<i>Diffusion driven microchemical changes at the interface</i>	169
5.3.4	<i>Estimation of interdiffusion parameters</i>	171
5.4	Role of defects on kinetics of interdiffusion	175
5.5	Effect of alloying elements on interdiffusion in SS/TiTaNb explosive joints	176

5.5.1	<i>Evolution of interface microstructure in SS/TiTaNb explosive joints</i>	176
5.5.2	<i>Growth kinetics of the diffusion zones</i>	179
5.5.3	<i>Microchemical variation due to interdiffusion</i>	181
5.5.4	<i>Determination of interdiffusion parameters</i>	184
5.4.5	<i>Estimation of effective interdiffusion coefficients</i>	190
5.6	Summary	195

CHAPTER 6

MOLECULAR DYNAMICS SIMULATION OF DIFFUSION OF Fe IN HCP Ti LATTICE

6.1	Introduction	197
6.2	Validation of modified embedded atom method potentials	198
6.3	Diffusion of Fe in HCP Ti lattice – MD simulations	201
6.3.1	<i>Diffusion of Fe in defect free HCP Ti lattice</i>	201
6.3.2	<i>Diffusion of Fe in HCP Ti lattice - Introducing point and line defects</i>	206
6.3.3	<i>Estimation of jump frequency in Ti lattice consisting of point and line defects</i>	210
6.4	Summary	211

CHAPTER 7

SUMMARY AND SCOPE OF THE FUTURE WORK

7.1	Summary of the work	212
7.2	Scope for future work	218
	REFERENCES	220

Abstract

The thesis entitled “**An Experimental and Computational Study on Diffusion Driven Structural Changes in Fe-Ti Based Dissimilar Joints Under Equilibrium and Non-equilibrium Conditions**” presents the results of an in-depth study on diffusion driven microstructural and microchemical changes in Fe/Ti based dissimilar joints due to interdiffusion under equilibrium and non-equilibrium conditions. The thesis addresses the following four themes:

- ⇒ Microstructure and property evaluation in Fe-C/Ti friction and explosive joints in ‘as welded’ and heat treated conditions.
- ⇒ Structural changes during deformation and annealing in 304LSS/Ti-5Ta-2Nb explosive clad joints.
- ⇒ Interdiffusion in Fe-Ti based systems under equilibrium and non-equilibrium conditions.
- ⇒ Molecular Dynamics simulations of diffusion of Fe in hcp Ti lattice.

The systematic and elaborate design of experiments in the thesis have provided very useful inputs for the optimization of process parameters for friction and explosive cladding, which aimed at obtaining a defect and intermetallic free interface between steel and Ti. The microstructural and microchemical variations across the interface provided the basis to design appropriate heat treatments for explosive clad joints of multicomponent 304L austenitic stainless steel (SS) and Ti-5Ta-2Nb alloy required for fabrication of the dissolver in a fast reactor reprocessing plant. Further, the temperature and time window for post weld heat treatment (PWHT) of the Fe-Ti dissimilar joints based on the detailed experimental investigations coupled with bond strength values computed using JMatPro[®] simulations has been established. The thesis also compares the interdiffusion characteristics at the interface with different extents of deformation between friction and explosive joints. Apart from the role of defects on the kinetics of interdiffusion, the influence of alloying elements in the multicomponent 304LSS / Ti-5Ta-2Nb system has been established. With a view to understand the defect aided diffusion at an atomistic level, Molecular Dynamics simulations of diffusion of Fe in HCP Ti lattice by introducing point and line defects in the lattice has been studied. By systematic transmission electron microscopy studies, the mechanism of reversion of the strain induced α' martensite and metastable fcc Ti that formed during explosive cladding in 304LSS and TiTaNb alloy respectively has been understood. On the whole the thesis is very comprehensive and addresses not only a technologically important problem in dissimilar joints but also provides a deep insight into the fundamental role of defects and alloying elements on interdiffusion in Fe-Ti based systems.

SYNOPSIS

1. INTRODUCTION:

Dissimilar joints of Fe-Ti based systems are encountered in chemical and nuclear industries due to the excellent mechanical and adequate corrosion properties of the metals [1]. Fabrication of the joints is a challenge due to formation of FeTi, Fe₂Ti intermetallic phases at the interface which degrade the properties as there is poor mutual solubility between Fe and Ti [2]. This difficulty is further enhanced with alloying additions due to the formation of secondary phases and ternary compounds such as σ (Cr rich phase), χ (Fe₂Cr₅Ti₁₇) and λ ((Fe,Cr)₂Ti) due to interdiffusion [3]. Over the years different joining techniques have been adopted to either prevent the formation of brittle phases or disperse them as isolated phases thereby preserving the integrity of the joint [4]. These solid state welding techniques include diffusion bonding, friction welding, explosive cladding and friction stir welding which have specific advantages over fusion joining methods like absence of heat affected zone, high energy density, no melting of base metals and formation of metallic bond by severe plastic deformation [5]. Further, performance of the joints under thermal exposure is crucial, which in turn depends on the temperature and time dependent stability of the parent materials as well as the interface.

The objective of the present research work is to achieve a fundamental understanding of the interdiffusion phenomena in Fe-Ti system and the consequent microstructural and microchemical variations across the interface, which controls the long term performance of the joints during service. This knowledge is required to understand the growth characteristics of the interface in a multicomponent system

namely the 304L austenitic stainless steel (SS) and Ti-5Ta-2Nb alloy explosive joint, fabricated for an important industrial application in spent fuel reprocessing plants of fast reactors [6]. The present research work includes an elaborate study on diffusion characteristics under equilibrium and non-equilibrium conditions, which bring about structural and chemical changes in the parent materials and interface that influence the properties.

2. SCOPE OF THE THESIS:

This thesis entitled “**An Experimental and Computational Study on Diffusion Driven Structural Changes in Fe-Ti Based Dissimilar Joints Under Equilibrium and Non-equilibrium Conditions**” presents the results of an in-depth study on diffusion driven microstructural and microchemical changes in Fe/Ti based dissimilar joints due to interdiffusion under equilibrium and non-equilibrium conditions. In addition to detailed experimental investigations, computational methods such as JMatPro[®] and Molecular Dynamics simulations are also employed. Main themes of the thesis are as follows:

- Microstructure and property evaluation in Fe-C/Ti friction and explosive joints in ‘as welded’ and heat treated conditions.
- Structural changes during deformation and annealing in 304LSS/Ti-5Ta-2Nb explosive clad joints.
- Interdiffusion in Fe-Ti based systems under equilibrium and non-equilibrium conditions.
- Molecular Dynamics simulations of diffusion of Fe in hcp Ti lattice.

A brief description of the above themes is presented in the following sections:

2.1 Microstructure and property evaluation in Fe-C/Ti friction and explosive joints in 'as welded' and heat treated conditions:

The mild steel/Ti joints are prepared by friction and explosive welding methods under optimised conditions to achieve a weld interface free from intermetallic phases and other weld defects. Systematic characterization of parent metals and interface with varying welding parameters enabled the selection of friction force=0.8 tonnes, upset force=1.6 tonnes, burn off length=3 mm and rotational speed=1000 rpm as optimum for friction welding; Similarly, explosive load ratio, flier plate velocity, detonation velocity and type of explosive used for explosive cladding process are 1.07, 300 m/s, 2000 m/s and homogeneous mixture of Ammonium nitrate + TNT respectively. Figure 1(a) shows the BSE image with superimposed composition profile of the MS/Ti friction joint interface. Although, interdiffusion up to a distance of $\sim 3 \mu\text{m}$ is seen at the interface, it has not resulted in observable change in microstructure. Electron microscopy investigations from few isolated regions at the interface revealed formation of fine (20-50 nm) FeTi particles (Fig. 1(b)). However, a high UTS value ($\sim 670 \text{ MPa}$) of the interface, computed by JMatPro[®], suggested that the presence of fine intermetallic phases has no detrimental effect on the bond strength of the welds.

Three explosive clads were fabricated by varying the load ratio as 1.07, 2.01 and 3.0. The explosive joint with a load ratio of 1.07 exhibited a sinusoidal wavy interface of uniform wavelength and amplitude of ~ 840 and $120 \mu\text{m}$ respectively (Fig. 1(c)). As the load ratio increases, formation of fine grain structure close to the interface followed by dendritic solidification structure typical of a cast structure is observed on MS side. Large dissipation of kinetic energy during explosive cladding is the reason for increase

in temperature at the interface which leads to the similar microstructures in explosive cladding as that in fusion welding technique at high energy conditions ($R \geq 2$). Based on the analysis of interface microstructure and microchemistry, a load ratio of 1.07 was selected as optimum. A closer examination revealed entrapment of the molten metal at the vortex of the wavy interface which was evident from X-ray elemental maps of Fe and Ti (inset in Fig. 1(c)).

Severe plastic deformation during explosive cladding resulted in the formation of acicular martensite (α') and metastable fcc Ti phases in base (MS) and flier (Ti) plates respectively. Electron probe micro analysis (EPMA) and JMatPro[®] simulations suggested coexistence of intermetallic Fe_2Ti and TiC phases at the vortex regions of the wavy interface. However, the high measured values of bond strength established that these phases were confined to only vortices at the wavy interface and do not degrade the mechanical property of the clad.

Variation in the interface microstructure and microchemistry due to interdiffusion during thermal exposure in the temperature range of 500-600 °C is studied to optimize the post weld heat treatments (PWHT) of the joints.

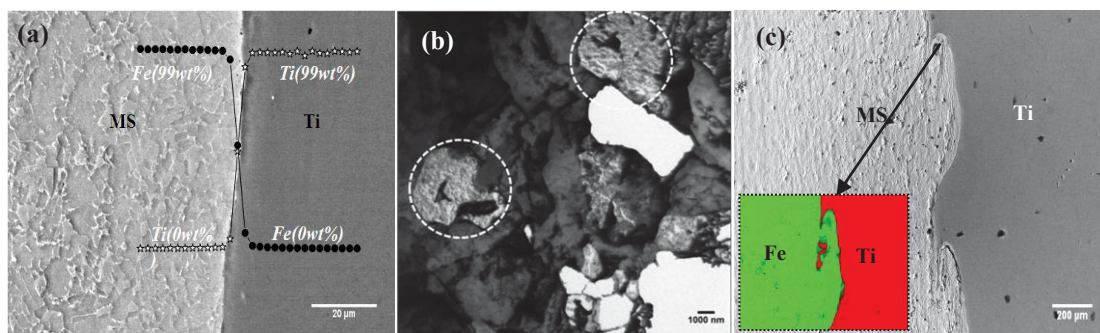


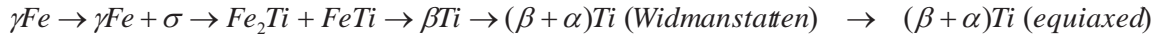
Fig. 1(a) BSE image of the MS/Ti friction joint with concentration profile superimposed, (b) TEM-BF image showing isolated regions (dotted circle) with different contrast consisting of FeTi phase and (c) BSE image of explosive clad showing wavy interface; entrapment of the molten metal is evident from the X-ray elemental maps in the inset

JMatPro[®] predicted mole fraction of the phases at the joint interface and consequent change in the bond strength further, helped in optimising the window for PWHT of the MS/Ti friction and explosive joints as 500-550 °C for ~10 h. Diffusion annealing for a duration of 100 h at an elevated temperature of 800° C, showed that the width of the reaction zone is limited to ~12 µm in friction joints while it is ~120 µm in explosive joints.

2.2 Structural changes during deformation and annealing in 304LSS/Ti-5Ta-2Nb explosive clad joints:

In 304LSS/Ti-5Ta-2Nb explosive clad joints, the parent metals showed signatures of deformation induced phase transformations under the influence of high pressure (~20-30 GPa) and large strain rate ($>10^5 \text{ s}^{-1}$). Based on detailed electron microscopy investigations, the presence of α' (bcc) martensite in SS and metastable fcc phase in Ti has been established. An elaborate study is carried out to understand the mechanism of reversion of metastable phases by X-ray and electron microscopy techniques. The austenite phase during reversion nucleates within the martensite laths while α (hcp) phase in Ti nucleates within the fcc as well as on the fcc/ α interfaces. The reversion process is significant at temperatures $\geq 600^\circ \text{C}$ for short durations (~2 h) and the mechanism of reversion in both the cases is established as diffusion controlled nucleation and growth process. Post Weld Heat Treatments for the SS/TiTaNb explosive joints are designed in the temperature range of 500-550 °C for durations not exceeding 10 h at which the interface is devoid of intermetallic phases and parent metal microstructure and microhardness values are restored.

Diffusion annealing at a temperature of 800 °C for 20 h showed formation of distinct diffusion zones. Width of the total reaction zone is (Fig. 2(a)) measured as ~175 µm. A correlation of the microchemistry with ternary isothermal section of Fe-Cr-Ti at 800 °C [7], suggested the formation of σ , FeTi + Fe₂Ti, and β Ti(Fe) phases in the diffusion zone. Based on the above analysis it was understood that the diffusion reactions between SS and TiTaNb did not show formation of all the compounds as depicted in the equilibrium phase diagram. The sequence of phase formation in the present study is as follows:



Using microchemistry obtained using EPMA as input, JMatPro[®] simulations predicted the formation of Cr rich σ phase on SS side very close to the interface, coexistence of FeTi and Fe₂Ti intermetallic phases at the interface and β Ti(Fe) phase in TiTaNb side. The site specific specimens from the diffusion zones were prepared by Focused ion beam (FIB) technique to unambiguously confirm these phases by TEM. Figure 2(b) shows Pt deposition in a region consisting of Widmanstätten α - β and equiaxed α Ti phase during the course of FIB specimen preparation.

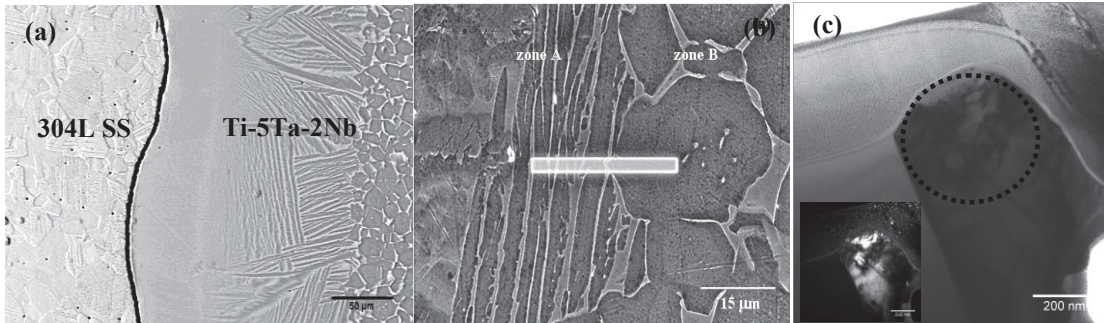


Fig. 2 BSE image of (a) SS/TiTaNb interface annealed at 800 °C for 20 h, (b) site selection by Pt deposition for FIB specimen preparation and (c) TEM-BF and DF (inset) images of the FIB extracted interface confirming FeTi intermetallic phase.

The TEM-BF image (Fig. 2(c)) of the ion milled specimen extracted from the interface showed the presence of fine phases (circled) which were confirmed by the DF image (in inset) to be FeTi intermetallic phase.

2.3 Interdiffusion in Fe-Ti based systems under equilibrium and non-equilibrium conditions:

Equilibrium and non-equilibrium diffusion driven growth characteristics of the reaction zones in a ternary Fe-C-Ti system and multicomponent SS-TiTa Nb have been studied in the temperature range of 500-800 °C for various durations. Effective interdiffusion coefficients in ternary Fe-C-Ti system were determined employing Dayananda's approach [8]. Interdiffusion under equilibrium conditions have been studied in diffusion annealed defect free friction joint. The non-equilibrium diffusion was evaluated in explosive clad joints where large number density of lattice defects influenced the kinetics of interdiffusion. Change in molar volume with concentration showed an agreement with ideal Vegard's law under equilibrium conditions, whereas a negative deviation was observed under non equilibrium conditions. The activation energy for interdiffusion under equilibrium was calculated as ~147 kJ/mol whereas it is far lower in the non-equilibrium case (~117 kJ/mol). This was in agreement with the ~12 µm wide diffusion zone in the diffusion annealed friction joints which was far lower than the ~112 µm wide diffusion zone in explosive joints (Fig. 3(a)). Correlation of microchemical data with ternary isothermal section of Fe-C-Ti [9], showed the diffusion zone to consist of FeTi+Fe₂Ti+TiC phases in friction welds and FeTi+TiC+βTi phases in explosive clads. Faster diffusion kinetics in explosive clads

can be understood based on (i) large number density of lattice defects and (ii) formation of disordered $\beta\text{Ti(Fe)}$ phase.

These studies further extended to understand the effect of alloying elements on interdiffusion in the multicomponent 304LSS/Ti-5Ta-2Nb explosive joints. EPMA elemental concentration profiles and electron microscopy imaging of the interface structure have clearly established the formation of distinct diffusion zones as a function of temperature and time. Concentration and temperature dependent interdiffusion coefficients and activation energies in Fe-Ti (neglecting the other diffusing elements) system were evaluated using the Den Broeder [10] and Wagner methods [11]. In multicomponent SS-TiTaNb system, although molar volume matched with ideal Vegard's law at low temperatures, a non linear negative deviation was observed at high temperatures ($\geq 700^\circ\text{C}$) (Fig. 3(b)). This was attributed to the formation of FeTi, Fe₂Ti and $\beta\text{Ti(Fe)}$ secondary phases. Interdiffusion parameters evaluated by Wagner's method showed sluggish diffusion of Fe and Ti at a concentration corresponding to the two phase mixture of FeTi+Fe₂Ti (Fig. 3(c)). Interstitial diffusion of Fe and diffusion in order intermetallic phases are responsible for the faster and slower diffusion kinetics in $\beta\text{Ti(Fe)}$ phase and FeTi+Fe₂Ti phases respectively.

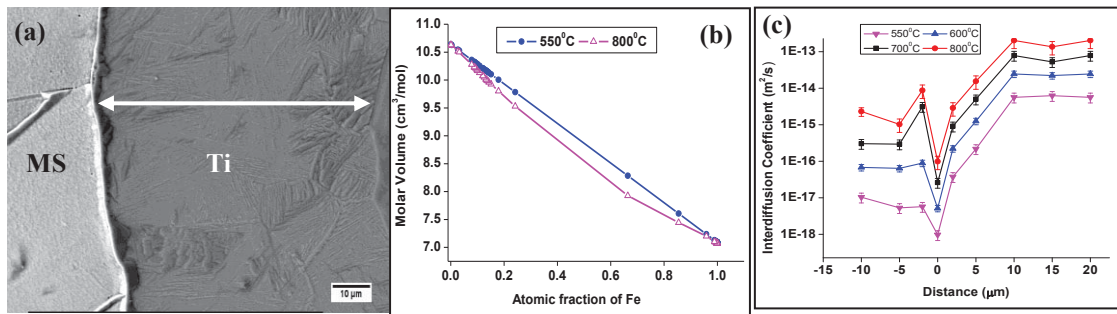


Fig. 3 BSE image of (a) MS/Ti explosive clad annealed at 800 °C for 100 h, (b) change in molar volume as a function of atomic fraction of Fe and (c) effective interdiffusion coefficients plotted as a function of distance across the interface.

Further, equating the total flux of diffusing species across the interface, $\sim 22 \mu\text{m}$ shift of the interface was observed at 800°C .

2.4 Molecular Dynamics(MD) simulations of diffusion of Fe in hcp Ti lattice:

Diffusion of Fe in hcp Ti lattice was studied by MD simulations in a defect free lattice and after introducing point and line defects to obtain an insight into defect aided diffusion. The interatomic potentials used in the simulations were validated by calculating the cohesive energy, bulk modulus and sublimation energy which showed good agreement with the reported values [12].

A single Fe atom was allowed to diffuse in a hcp Ti lattice containing 4000 Ti atoms. Simulations were carried out in the temperature range of $500\text{--}900^\circ\text{C}$ at an interval of 100°C for 10 ps in a super cell of size $10 \times 10 \times 10 \text{ \AA}^3$. Figure 4(a) shows a plot of Fe atom trajectory in Ti lattice and the mean square displacement was calculated as a function of time of simulation. From the plot of $\ln D$ vs $1/T$, D_0 and activation energy (Q) values were obtained as $\sim 1.257 \times 10^{-10} \text{ m}^2/\text{s}$ and 117 kJ/mol respectively.

In order to understand the role of defects, vacancies were created in Ti by random removal of atoms from their lattice positions (Fig. 4(b)) while dislocations were created by deleting half plane of atoms from the centre plane of hcp lattice. The diffusivity of Fe in hcp Ti lattice, in the presence of point defects was in the range of $9.9 \times 10^{-16} \text{ m}^2/\text{s}$ (500°C) to $4.2 \times 10^{-14} \text{ m}^2/\text{s}$ (900°C).

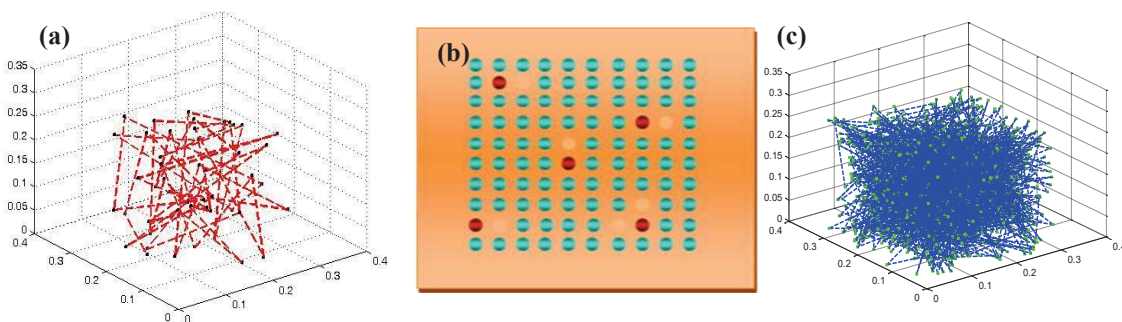


Fig. 4(a) Fe atom trajectory in a defect free hcp Ti lattice, (b) super cell with vacancies created at random and (c) Fe atom trajectory in hcp Ti lattice in the vicinity of vacancies

A faster relaxation of Fe atom in the vicinity of defects (Fig. 4(c)) was observed from the diffusion trajectories. Thus MD simulations reinforced the higher diffusivity of Fe in hcp Ti lattice in the presence of lattice defects.

3. ORGANISATION OF THE THESIS:

This thesis consists of seven chapters which are organised as follows:

Chapter 1 titled as “**Introduction**”, briefly presents a review of the existing literature on binary and multicomponent Fe-Ti systems, emphasising the various methods adopted to join the two metals. Further, different approaches developed over the years to study interdiffusion phenomena in dissimilar systems have been described. This chapter also highlights the relevance and scope of the present research work.

In **Chapter 2** titled “**Experimental and Computational methods**”, details of fabrication of Fe-Ti based joints, heat treatments and specimen preparation for various techniques is provided. A brief description of the experimental techniques, operating conditions, data analysis and sources of errors as well as computational methods namely Molecular Dynamics and JMatPro[®] simulations is also provided.

Chapter 3 titled “**Microstructure and property evaluation in Fe-C/Ti friction and explosive joints in ‘as welded’ and heat treated conditions**” presents the basis for selection of parameters to fabricate the MS-Ti joints by friction and explosive cladding methods. The in-depth characterization of microstructure, microchemistry and evaluation of bond strength together with the JMatPro[®] computations used to assess the quality of welds is elaborated in this chapter. This chapter also includes the results on evolution of structural changes during thermal exposure used for optimization of PWHT.

Chapter 4 titled as “**Structural changes during deformation and annealing in 304LSS/Ti-5Ta-2Nb explosive clad joints**” deals with the results on deformation induced phase transformations in 304L SS and Ti-5Ta-2Nb alloy during explosive cladding. A detailed discussion on the mechanism and kinetics of reversion of these metastable phases during annealing is included. The microstructural and microchemical changes at the interface during annealing are elaborated. Detailed TEM investigations to confirm the prediction of various secondary phases at the interface is also included in this chapter.

Chapter 5 titled as “**Interdiffusion in Fe-Ti based systems under equilibrium and non-equilibrium conditions**” provides a brief study on the structural changes in the diffusion annealed friction and explosive joints of Fe-C-Ti and SS304L-TiTa Nb. Concentration and temperature dependent interdiffusion parameters are evaluated by DB and Wagner methods using smoothly varying and step like concentration profiles respectively. Average effective interdiffusion coefficients in the diffusion zone of Fe-C-Ti and Fe-Cr-Ti systems have been estimated using Dayananda’s method. The higher

kinetics of growth of zones in explosive clads is understood in terms of the defect aided diffusion both in ternary and multicomponent systems.

Chapter 6 titled as “**Molecular Dynamics simulations of diffusion of Fe in hcp Ti lattice**” elaborates the results on MD simulation of Fe atom diffusion in hcp Ti lattice. Interatomic potentials for the simulations have been validated by estimating the physical properties of Fe-Ti system. Defect aided diffusion is studied by introducing point and line defects into Ti lattice, the results of which are described in this chapter.

Chapter 7 presents the summary of important findings of this research work and also identifies the scope for further studies.

The topics addressed in this thesis are summarised as a flowchart in Fig. 5.

References:

1. Baldev Raj, U. Kamachi Mudali, Prog. Nucl. Energy, 48 (2006) 283-313.
2. J.L. Murray, Phase diagrams of binary Ti alloys, ASM International, Metals park OH, (1987) 99-111.
3. M. Ghosh, S. Chatterjee, Mater. Sci. Engg. A, 358 (2003) 152-158.
4. S. Kundu, S. Chatterjee, D. Olson, B. Mishra, Metall. Mater. Trans. A, 38 (2007) 2053-2060.
5. R.A. Patterson, Fundamentals of solid state welding, ASM Handbook, ASM International, USA, 6 (1993) 528-533.
6. U. Kamachi Mudali, B.M. Ananda Rao, K. Shanmugam, R. Natarajan, Baldev Raj, J Nucl. Mater., 321 (2003) 40-48.
7. V. Raghavan, The Fe-Cr-Ti phase diagram, Phase Diagrams of Ternary Iron Alloys, Part 1, ASM International, 1987.
8. M.A. Dayananda, Def. and Diffus. Forum, 297-301 (2010) 1451-1460.
9. V. Raghavan, C-Fe-Ti- Phase diagram evaluations, J. Phase Equilibria, 24 (2003) 62-66.
10. F.J.A. Den Broeder, Scripta Metall., 3 (1969) 321-325.
11. C. Wagner, Acta Metall., 17 (1969) 99-107.
12. I. Sa, B. J. Lee, Scripta Mater., 59 (2008) 595.

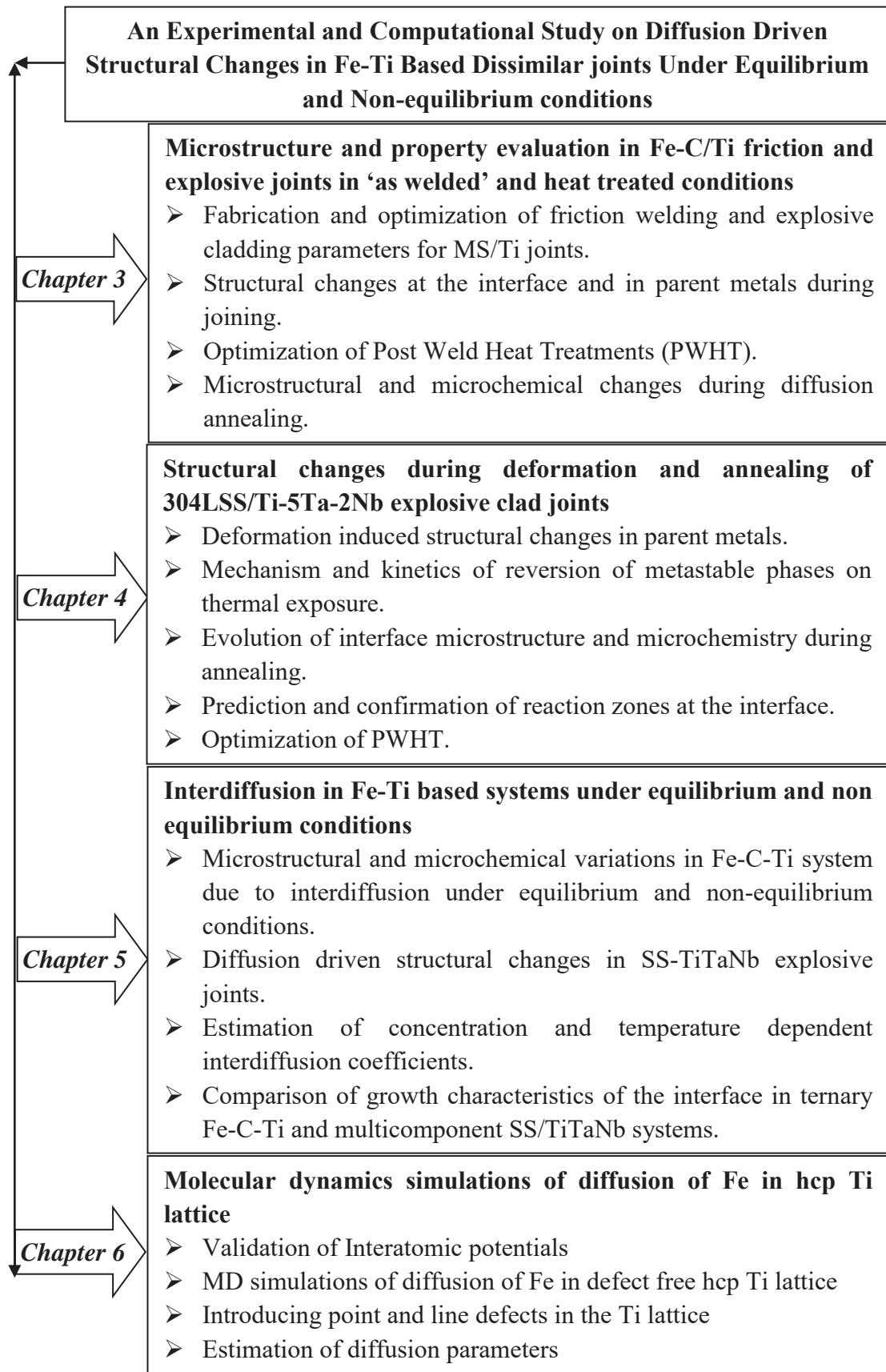


Fig. 5 Flow chart showing organization of the themes in Chapters 3 to 6

LIST OF FIGURES

Figure No.	Figure Caption	Page No.
1.1	Schematic showing objective of the thesis	5
2.1	Schematic of (a) friction welding process and (b) friction joint after machining	23
2.2	Schematic showing the (a) geometrical arrangement in explosive cladding process and (b) bonding during explosive cladding	25
2.3	Top view (Ti side) of the MS/Ti clads fabricated with a load ratio of (a) 1.07, (b) 2.01, (c) 3.0; de-bonding at an edge revealed by ultrasonic examination is represented by dotted lines; (all dimensions are in mm) and (d) transverse section of the clad fabricated with R value of 1.07	26
2.4	Schematic of (a) MS/Ti ‘as clad’s showing orientation of the specimens fabricated for tensile and shear tests, dimensions of (b) tensile and (c) shear test specimens (all dimensions are in mm)	28
2.5	Schematic showing transverse tensile test specimen of SS/TiTaNb explosive joint (all dimensions are in mm)	28
2.6	BSE images showing (a) site selection by Pt deposition for FIB-based specimen preparation, (b) trenches formed (arrow marked) due to Ga ion milling on either side of the lamella and (c) specimen lifted out using in-situ manipulator, to be further thinned for TEM analysis	36
2.7	Flow chart showing the procedure adopted for determining $D(C)$ values in the present research work	38
3.1	(a) Secondary electron (SE) image with superimposed hardness value and (b) XRD pattern of mild steel in ‘as received’ condition	47
3.2	(a) SE image with superimposed hardness and (b) XRD pattern of Ti Grade 2 in ‘as received’ condition	47
3.3	(a) Back scattered electron image of diffusion coupled MS-Ti joint and (b) XRD pattern obtained from the cross-section specimen showing evidences for the formation of secondary phases at the interface	49
3.4	(a) to (h) BSE images from cross section of the friction welds fabricated with different welding parameters (for the number at the right corner of each image refer Table 2.3)	51
3.5	BSE image of the MS/Ti friction joint fabricated with optimized welding parameters; corresponding composition profile is superimposed	52
3.6	XRD pattern obtained from cross section of the MS/Ti friction joint	54
3.7	TEM bright field (BF) images obtained from the MS/Ti friction joint interface showing (a) isolated regions (shown by dotted circle) with different contrast, (b) presence of fine particles of nm size (arrow marked) in a magnified view of the isolated region circled in panel ‘a’	55

	and (c) SAD pattern showing overlapping reflections from both bcc-Fe and FeTi phase along $[\bar{1}12]$ and $[\bar{1}11]$ zone axis respectively.	
3.8	JMatPro [®] predicted mole fraction of the phases across MS/Ti friction joint heat treated at (a) 500 °C - 1 h, (b) 500 °C - 20 h, (c) 600 °C - 1 h and (d) 600 °C - 20 h respectively	57
3.9	Predicted bond strength of the friction joints heat treated at (a) 500 °C, 600 °C and (b) 800 °C respectively	58
3.10	BSE images showing the interface of MS/Ti friction joints heat treated at 500 °C for duration of (a) 1, (b) 5, (c) 10 and (d) 20 h respectively; microhardness profiles are superimposed on the micrograph	59
3.11	BSE images showing the interface of MS/Ti friction joints heat treated at 600 °C for duration of (a) 1, (b) 5, (c) 10 and (d) 20 h respectively; microhardness profiles are superimposed	60
3.12	BSE images showing the interface microstructure of MS/Ti friction joints with superimposed hardness profile after heat treatment at (a) 500 °C, (b) 600 °C, (c) 700 °C and (d) 800 °C for 100 h respectively	61
3.13	Concentration profiles obtained across the MS/Ti friction joints after heat treatment at (a) 500 °C, (b) 600 °C, (c) 700 °C and (d) 800 °C for 100 h respectively	64
3.14	JMatPro [®] predicted mole fraction of phases plotted as a function of distance across the MS/Ti weld interface at (a) 500 °C, (b) 700 °C and (c) 800 °C for 100 h respectively	65
3.15	XRD patterns obtained from MS/Ti friction joint heat treated at temperatures of (a) 500 °C and (b) 800 °C for 100 h respectively	66
3.16	TEM (a) BF image of the friction joint heat treated at a temperature of 800 °C for 100 h showing fine secondary particles, (b) corresponding SAD pattern confirmed the presence of FeTi intermetallic phase along $[\bar{1}11]$ zone axis and (c) EDS spectrum obtained from the circled region in (a) further confirmed the Fe and Ti rich nature of the phase	67
3.17	TEM (a) BF image showing a large grain at the interface, (b) corresponding SAD pattern showed with overlapping reflections from bcc-Fe and TiC phase along $[\bar{1}12]$ and $[011]$ zone axis respectively and (c) DF image corresponding to $[220]_{TiC}$ reflection further confirming the formation of TiC phase	69
3.18	BSE images showing the interface microstructure of MS/Ti explosive clads fabricated with (a) R=1.07, (b) 2.01 and (c) 3.0 respectively; inset in panel (a), (b) (c) represents vortex region, dendritic structure and fine grain region at the interface respectively	71
3.19	BSE images showing interface of the MS/Ti clads fabricated with (a) R=1.07, (b) 2.01 and (c) 3.0 with superimposed hardness profiles respectively	72

3.20	Tensile specimens before and after testing, (b) SE image of fracture surface showing typical brittle fracture, (c) Fe rich EDX spectrum from the fracture surface confirmed failure on MS side and (d) microcracks on the fracture surface of the clads fabricated with a R value of 2.01	74
3.21	Shear tested specimen and the inset shows the flow pattern of the tested piece, (b) fractograph typical of a ductile + brittle mode of failure and (c) dominant Ti peaks in EDX spectrum indicated failure on Ti side	75
3.22	Electron image of the MS/Ti 'as clad' interface showing a vortex region (arrow marked) and the corresponding X-ray maps for (b) Fe and (c) Ti	78
3.23	Concentration profiles obtained across the clad interface from (a) straight interface region and (b) vortex region respectively	78
3.24	Prediction of the phases using JMatPro [®] in regions showing (a) straight interface and (b) vortex region respectively	79
3.25	XRD patterns of (a) MS, (b) Ti and (c) interface regions of the MS/Ti explosive clad	81
3.26	TEM-BF image obtained from deformed region on MS side showing grain triple point decorated with planar defects (arrow marked), (b) typical lath type structure and (c) corresponding SAD pattern confirmed twinning of ferrite grains along $[\bar{1}2\bar{3}]$ zone axis	83
3.27	TEM-BF image obtained from deformed Ti side show elongated grains, (b) overlapping reflections confirmed α phase along zone axis $[\bar{2}1\bar{1}0]$ and $[0001]$, (c) BF image showed lamellar shaped grains with different contrast, (d) corresponding SAD pattern confirmed formation of fcc phase along $[\bar{1}1\bar{2}]$ zone axis and (e) DF image of the $[\bar{2}\bar{2}0]$ reflection of fcc phase gave further confirmation	84
3.28	(a) TEM-BF image showing fine needle like features at the clad interface (b) overlapping reflections confirmed coexisting of intermetallic phase Fe_2Ti and parent α Fe along the zone axis $[0001]$ and $[\bar{1}11]$ respectively and (c) DF image of the $[\bar{1}100]_{\text{Fe}_2\text{Ti}}$ gives further confirmation	85
3.29	Concentration profiles across the MS/Ti explosive clad heat treated at (a) 500 °C, (b) 600 °C for 1 h and corresponding mole fraction of the phases predicted using JMatPro [®] as a function of distance at (c) 500 °C and (d) 600 °C respectively	87
3.30	Predicted UTS value plotted as a function of distance for MS/Ti explosive clads heat treated clads at (a) 500 °C, 600 °C and (b) 800 °C respectively	88
3.31	BSE images showing variation in the interface microstructure of MS/Ti explosive clads heat treated at 600 °C for (a) 1 and (b) 5 h and	90

	500 °C for (c) 10 and (d) 20 h respectively; corresponding hardness values are superimposed	
3.32	BSE images showing variation in the interface microstructure of MS/Ti explosive clads with thermal exposure at (a) 500 °C, (b) 600 °C, (c) 700 °C and (d) 800 °C for 100 h respectively; hardness profiles are superimposed	91
3.32	Concentration profiles obtained across the MS/Ti explosive clads heat treated at (a) 500 °C, (b) 600 °C, (c) 700 °C and (d) 800 °C for 100 h respectively	93
3.33	JMatPro [®] predicted mole fraction of phases across MS/Ti explosive clads heat treated at (a) 500 °C and (b) 800 °C for 100 h respectively	94
3.34	XRD patterns obtained from the cross-section specimens of the explosive clad heat treated at 500 and 800 °C (for 100 h duration)	95
4.1	SE images of (a) SS, (b) TiTaNb alloy in ‘as received’ condition with microhardness value superimposed and corresponding XRD patterns for (c) SS and (d) TiTaNb respectively	100
4.2	Ultrasonically tested SS/TiTaNb clad showing de-bonding at the edges	101
4.3	Stress vs strain curve for the clad and (b) fracture surface showed brittle mode of failure	101
4.4	BSE image showing interface microstructure of the clad	102
4.5	BSE images obtained from the cross-section of the clad heat treated at temperatures of 550 °C for 2 and 5 h (a and b) and 600 °C for 2 and 5 h (c and d) respectively; hardness profiles are superimposed on the micrographs, (e) Concentration profiles obtained across the clad interface at 550 °C for 5 h and (f) mole fraction of the phases predicted using JMatPro [®]	104
4.6	Predicted UTS across the clad interface at (a) 550 °C and (b) 600 °C respectively	106
4.7	SE images showing signatures of deformation in (a) base – SS and (b) flier - TiTaNb plates respectively	107
4.8	XRD patterns obtained from deformed (a) SS and (b) TiTaNb sides of the clad providing evidence for the formation of deformation induced phases during cladding	108
4.9	TEM (a) BF image showing deformed microstructure of S, (b) SAD pattern obtained from circled region in Fig. 4.9(a) showed deformation twins of γ along [011] zone axis and (c) overlapping reflections of arrow marked region showed coexistence of bcc and γ phases along $[\bar{1}11]$ and $[11\bar{1}]$ zone axis respectively	109
4.10	TEM (a) BF image showing elongated grains of TiTaNb clad, (b) overlapping reflections in the SAD pattern (obtained from circled region) confirmed α phase along $[\bar{1}213]$ and $[0001]$ zone axes, (c) BF image of a globular particle and (d) SAD pattern confirmed presence	111

	of β phase of Ti along $[012]$ zone axis, which is further confirmed by the DF image of the $[\bar{1}\bar{2}1]_{\beta}$ reflection (inset)	
4.11	TEM (a) BF image showing elongated grains within which fine needle like features were present and (b) corresponding SAD pattern confirmed the presence of metastable fcc phase of Ti along $[\bar{1}14]$ zone axis	112
4.12	High Temperature XRD patterns from (a) SS and (b) TiTa Nb sides of clad respectively	114
4.13	Change in the volume fraction of (a) α' martensite in SS and (b) fcc Ti in TiTa Nb with thermal exposure	116
4.14	SE images of SS heat treated for 2 h at temperatures of (a) 400 °C, (b) 500 °C, (c) 600 °C and (d) 700 °C and quenched respectively; microhardness value is superimposed	117
4.15	EBSD crystal orientation maps from SS heat treated at two different temperatures for 2h and quenched (a) 500 °C - fcc, (b) 500 °C - bcc, (c) 700 °C – fcc and (d) 700 °C - bcc phases of Fe; inset in each panel represents the legend	118
4.16	EBSD pole figures for (a) fcc and (b) bcc phases along $\{111\}$ and $\{110\}$ plane normal respectively	119
4.17	TEM-BF images showing (a) fine martensite laths, (b) coexistence of coarse and fine laths and (c) equiaxed grains of SS heat treated at temperatures of 500, 600 and 700 °C for 2 h and quenched	120
4.18	TEM-BF image of the steel heat treated at 500 °C for 2 h showing (a) fine martensite laths, (b) enlarged view of a typical martensite lath, (c) overlapping reflections revealed coexistence of γ and α' phases along $[\bar{1}12]$ and $[\bar{1}11]$ zone axis respectively and (d) DF image for the $[011]_{\alpha}$ reflection (marked in (c)) provided evidence for nucleation of γ within the martensite lath	121
4.19	TEM-BF image showing lath morphology of the steel heat treated at 600 °C for 2 h, (b) corresponding SAD pattern showed coexistence of γ and α' phases along $[\bar{1}22]$ and $[\bar{1}11]$ zone axis and DF image for the (c) $[420]_{\gamma}$ reflection confirmed nucleation of γ within the α' lath (d) $[\bar{1}\bar{1}0]_{\alpha}$ reflection provided further confirmation	122
4.20	TEM (a) BF showing high density of dislocations of the steel heat treated at 700 °C for 2 h (b) corresponding SAD pattern showed coexistence of γ and α' phases along $[\bar{1}12]$ and $[\bar{1}11]$ zone axis and (c) DF image for the $[011]_{\alpha}$ reflection confirmed that the reversion was not complete at this temperature	123

4.21	TEM (a) BF showing fine laths and dislocations within a wedge shaped region of the steel heat treated at 700 °C for 2 h, (b) high magnification BF image showing fine grains obtained from the region circled in (a) and (c) corresponding SAD pattern showed γ phase along $[013]$ zone axis	125
4.22	SE images of TiTaNb alloy heat treated at temperatures of (a) 100, (b) 400, (c) 600, and (d) 900 °C for 2 h and quenched respectively; microhardness value is superimposed	127
4.23	(a) TEM-BF image of the alloy heat treated at 100 °C showing elongated grains and fine lamellae, (b) SAD pattern obtained from the circled region in (a) confirmed overlapping reflections of α and fcc phases along $[0001]$ and $[112]$ zone axis respectively (c) DF image for $[0110]$ reflection confirmed the fine lamellae as α phase of Ti	128
4.24	TEM (a) BF image obtained from a wedge shaped grain at 100 °C, (b) corresponding SAD pattern showed metastable fcc phase and α phase along $[112]$ and $[0001]$ zone axis and (c) DF image for fcc phase and inset in (c) is the DF image for the α phase respectively provided confirmation for the nucleation of α phase within the fcc phase	129
4.25	Overlapping standard $[112]$ and $[0001]$ stereographic projection of fcc and α phases of Ti respectively	130
4.26	TEM (a) BF image of TiTaNb heat treated at 400 °C showing a lamellae shaped grain, (b) SAD pattern revealed presence of fcc and α phases along $[011]$ and $[0110]$ zone axis and (c) DF image for the $[0002]$ reflection of α respectively	132
4.27	TEM (a) BF image showing equiaxed grains at 600 °C, (b) corresponding SAD pattern from circled region A shows α phase along the zone axis $[2110]$, (c) BF image showing enlarged view of the triple point intersection of equiaxed grains revealed screw dislocations and stacking faults and (d) corresponding SAD pattern showed α phase and retained fcc phase along the $[112]$ and $[0001]$ zone axis respectively; DF in inset confirmed $[020]$ fcc reflection	133
4.28	TEM (a) BF image showing martensite laths of α phase at 900 °C, (b) corresponding SAD pattern confirmed α phase of Ti along the zone axis $[0001]$	135
4.29	Plot of volume fraction of metastable fcc phase as a function of temperature	136
4.30	BSE images obtained from the cross-section of the clad heat treated at temperatures of (a) 550, (b) 600, (c) 700, (d) 800 °C for 20 h respectively; hardness profiles are superimposed on the micrographs	137

	and inset in (d) is high magnification micrograph revealing the presence of submicron sized zones at the interface	
4.31	Concentration profiles obtained across cross-section of the SS/TiTaNb explosive clads heat treated at temperatures of (a) 550, (b) 600, (c) 700 and (d) 800 °C for duration of 20 h respectively	139
4.32	Predicted mole fraction of the phases for 20 h at (a) 550, (b) 600, and (c) 800 °C respectively as a function of distance	142
4.33	XRD patterns from cross-section specimens heat treated at temperatures of (a) 500 and (b) 600 °C (for 1 and 20 h duration) respectively	145
4.34	XRD pattern obtained at 800 °C (for 1 and 20 h duration)	146
4.35	TEM (a) BF image obtained from zone 7, (b) overlapping diffraction patterns from α and β phases of Ti along $[01\bar{1}0]$ and $[\bar{1}11]$ zone axis respectively, (c) DF image corresponding to $[2\bar{1}1\bar{2}]_{\alpha}$ reflection (circled in (b)) revealed α plates and β phases of Ti (d) EDS spectrum from (matrix) phase shows the presence of Fe	147
4.36	TEM (a) BF image of specimen extracted from zone 3, (b) SAD pattern obtained from the circled region in (a) confirmed the presence of FeTi intermetallic phase along $[\bar{1}11]$ zone axis, (c) DF image from $[0\bar{1}1]$ reflection (circled spot in (b)) and (d) EDS spectrum revealed almost equal intensity for Fe and Ti in the selected region	148
4.37	TEM (a) BF image of a region close to the clad interface, (b) SAD pattern showing overlapping reflections from both FeTi and Fe ₂ Ti phases and DF images for the (c) $[0\bar{1}1\bar{2}]_{Fe_2Ti}$ and (d) $[\bar{1}01]_{FeTi}$ reflections provided further confirmation	149
4.38	TEM (a) BF image for zone 2, (b) overlapping electron diffraction patterns from σ and γ -Fe phases; DF images corresponding to (c) $[\bar{1}11]_{\gamma}$ and (d) $[425]_{\sigma}$ reflections (e)-(f) – EDS spectra obtained from γ -Fe and σ phases respectively	151
4.39	Predicted variation in UTS across the clad interface at 800 °C after 20h of heat treatment	152
5.1	BSE images showing the interface microstructure of MS/Ti friction joints diffusion annealed for 100 h at temperatures of (a) 500 °C, (b) 600 °C, (c) 700 °C and (d) 800 °C respectively	158
5.2	(a) Growth of the diffusion zone in MS/Ti friction joints as a function of time at a temperature 800 °C and (b) Arrhenius analysis of the growth constant	160

5.3	Concentration profiles obtained across MS/Ti friction welds diffusion annealed at (a) 500, (b) 600, (c) 700 and (d) 800 °C for 100 h respectively	162
5.4	Temperature dependence of effective interdiffusion coefficients in MS-Ti system	164
5.5	BSE images showing variation in the interface microstructure of MS/Ti explosive clads diffusion annealed at (a) 500, (b) 600, (c) 700 and (d) 800 °C for 1 h respectively; corresponding hardness profiles are superimposed	165
5.6	BSE images showing variation in the interface microstructure of MS/Ti explosive clads diffusion annealed at (a) 500, (b) 600, (c) 700 and (d) 800 °C for 100 h respectively; hardness profiles are superimposed	166
5.7	Growth of the diffusion zone in MS/Ti explosive joints as a function of time at temperatures 700 and 800 °C and (b) Arrhenius analysis of the growth constant	168
5.8	Concentration profiles obtained across the MS/Ti explosive clads heat treated at temperatures of (a) 500, (b) 600, (c) 700 and (d) 800 °C for 1 h respectively	169
5.9	Concentration profiles obtained across the MS/Ti explosive clads heat treated at temperatures of (a) 500, (b) 600, (c) 700 and (d) 800 °C for 100 h respectively	171
5.10	Variation in the molar volume (V_{mix}) in MS-Ti system during equilibrium and non-equilibrium diffusion as a function of atomic fraction of Fe	172
5.11	Temperature dependence of effective interdiffusion coefficients under non-equilibrium conditions in MS-Ti system	174
5.12	BSE images showing variation in the interface microstructure of SS/TiTaNb explosive joints diffusion annealed at (a) 550, (b) 600, (c) 700 and (d) 800 °C for 10 h respectively	177
5.13	BSE images showing variation in the interface microstructure of SS/TiTaNb explosive joints diffusion annealed at (a) 550, (b) 600, (c) 700 and (d) 800 °C for 20 h respectively	178
5.14	Growth of the (a) total diffusion zone, (b) FeTi+Fe ₂ Ti phase, (c) β Ti(Fe) phases in SS/TiTaNb explosive joints as a function of time at different temperatures and (d) Arrhenius analysis of the growth constant	180
5.15	Concentration profiles obtained across the SS/TiTaNb explosive clads heat treated at temperatures of (a) 550, (b) 600, (c) 700 and (d) 800 °C for 20 h respectively	182
5.16	Plot of λ and u obtained for Fe in TiTaNb rich side of the concentration profile obtained from SS/TiTaNb clad heat treated at 800 °C for 20 h	185
5.17	Variation in the molar volume (V_{mix}) plotted as a function of atomic fraction of Fe at (a) 550 and (b) 800 °C respectively	186

5.18	(a) Concentration and (b) Temperature dependence of effective interdiffusion coefficients in SS/TiTaNb system	188
5.19	Interdiffusion flux across the interface of SS/TiTaNb explosive joints diffusion annealed for 20 h at temperatures of (a) 550 and (b) 800 °C respectively	191
5.20	Smoothened concentration profiles with Matano interface fixed	193
6.1	Interatomic potential for the Fe-Ti system assuming MEAM potential formalism	202
6.2	Size of the system plotted as a function of time of simulation	203
6.3	Trajectory of Fe atom in Ti lattice at temperatures of (a) 500, (b) 600, (c) 700, (d) 800 and (e) 900 °C respectively	204
6.4	Mean square displacement (MSD) vs time of simulation for Fe-Ti system	205
6.5	Arrhenius analysis of diffusivity of Fe in HCP Ti lattice	206
6.6	Schematic representation of Ti lattice showing the locations of (a) vacancies and (b) dislocations; Fe atoms are inserted in the vicinity of the defects	207
6.7	Trajectory of Fe atom in Ti lattice consisting of (a) 0.5% vacant lattice sites and (b) edge dislocation at a temperature of 900 °C	209

LIST OF TABLES

Table No.	Table Caption	Page No.
1.1	Summary of the literature showing effect of load ratio (R) on joint interface	8
2.1	Chemical composition of the materials studied	22
2.2	Mechanical properties of the materials	22
2.3	List of process parameters varied in friction welding	24
2.4	Experimental parameters for explosive cladding of MS/Ti	25
2.5	List of heat treatment schedules adopted in the present research work	29
2.6	Details of the chemical etchants	31
2.7	List of various methods used for calculation of the D(C) values	40
3.1	Comparison of the experimental and predicted values of UTS	53
3.2	Mechanical properties of the clads with different load ratios	75
4.1	Summary of predicted phases and their microchemistry as a function of distance from the explosive clad interface after heat treatment at 800 °C for 20 h	143
5.1	Average effective interdiffusion coefficients ($\widetilde{D}_{Fe}^{eff} \times 10^{-17} \text{ m}^2/\text{s}$) and interdiffusion parameters estimated in MS/Ti friction joints	163
5.2	Average effective interdiffusion coefficients ($\widetilde{D}^{eff} \times 10^{-16} \text{ m}^2/\text{s}$) and interdiffusion parameters estimated in MS/Ti explosive joints	174
5.3	Impurity diffusion coefficients of Fe in Ti	175
5.4	Layer growth parameters for diffusion zones in SS/TiTaNb system	181
5.5	Impurity diffusion coefficients of Fe in TiTaNb	186
5.6	Interdiffusion parameters in SS-TiTaNb system	189
5.7	Effective interdiffusion coefficients and diffusion distances in SS/TiTaNb	194
6.1	MEAM potential parameters for Fe-Ti system	199
6.2	Interaction parameters for Fe-Ti system	200
6.3	Diffusivity of Fe in HCP Ti lattice	208

LIST OF SYMBOLS AND ABBREVIATIONS

α	Hcp phase of Ti
β	Bcc phase of Ti
α'	Bcc martensite phase of Fe
ε	Hcp martensite phase of Fe
γ	Austenite (fcc) phase of Fe
σ	Cr rich phase having Tetragonal crystal structure
ρ	Density
ψ	Relative concentration term in Den Broeder's method
M	Molar
r	Rotational speed
R	Explosive load ratio
Q	Activation energy
E	Impact energy
E_{Tot}	Total Potential Energy
V	Volume
T_m	Melting temperature
$D(C)$	Concentration dependent diffusion coefficient
\bar{D}^{eff}	Average effective interdiffusion coefficient
$C_{Specimen}$	Concentration of an element in the specimen
$C_{Standard}$	Concentration of an element in the standard
$I_{Specimen}$	Intensity of characteristic X-rays from specimen
$I_{Standard}$	Intensity of characteristic X-rays from standard
V_f	Flier plate velocity
V_D	Detonation velocity
X	Width of the diffusion zone
K_p	Growth constant
T	Temperature
t	Time

n	Reaction index
R	Gas constant
$c(x)$	Concentration at any arbitrary point ‘ x ’
$c^{-\infty}$	Concentrations at the extreme left hand side of the concentration profile
$c^{+\infty}$	Concentrations at the extreme right hand side of the concentration profile
V_m	Molar volume
$V(c)$	Concentration dependent molar volume
$c(x)$	Concentration at any arbitrary point ‘ x ’
\tilde{J}_i	Flux of diffusing component ‘ i ’
$U(r)$	Total potential energy function
S_{ij}	Screening parameters
\rightarrow	Electron density of an atom
ρ_i	
$F_i(\vec{\rho}_i)$	Embedding energy function
$\phi_{ij}(R_{ij})$	Pair potential function
SS	Stainless Steel
CP	Commercially Pure
MS	Mild Steel
SS	Stainless Steel
FF	frictional Force
UF	Upset Force
BM	Boltzmann - Matano
KE	Kinetic Energy
YS	Yield strength
WD	Working Distance
HV	Vicker’s Hardness number
DB	Den Broeder
MD	Molecular dynamics

BOL	Burn Off Length
SFE	Stacking Fault Energy
SIM	Strain Induced Martensite
EAM	Embedded Atom Method
2NN	Second Nearest Neighbour
UTS	Ultimate Tensile Strength
FSW	Friction stir welding
XRD	X-Ray Diffraction
SEM	Scanning Electron Microscopy
TEM	Transmission Electron Microscopy
EDS	Energy Dispersive Spectrometer
SAD	Selected Area Diffraction
FIB	Focused Ion Beam
ROI	Region Of Interest
EPMA	Electron Probe Micro Analyzer
MEAM	Modified Embedded Atom Method
ASTM	American Society of the international association for Testing and Materials
AISI	American Iron and Steel Institute
SMAW	Shielded Metal Arc Welding
GTAW	Gas Tungsten Arc Welding
PWHT	Post Weld Heat Treatment
HTXRD	High Temperature X-Ray Diffraction
ICDD	International Centre for Diffraction Data
EBSD	Electron Back Scatter Diffraction
SE/BSE	Secondary/Back Scattered Electron
BF / DF	Bright field / Dark Field
LAMMPS	Large-scale Atomic/Molecular Massively Parallel Simulator

Chapter 1

Introduction

1.1 Dissimilar joints of 304LSS/Ti-5Ta-2Nb alloy for reprocessing applications:

Reprocessing of the mixed (U, Pu)C fuel of fast breeder reactors (FBR) is a challenge due to the high concentration of Pu, various fission products and transuranium elements [1, 2]. For faster dissolution of the spent fuel with high activity of Pu, an advanced electro-oxidative dissolution process is preferred over the conventional PUREX process [1, 3]. Nitric acid at various levels of concentration (0.01 to 11.5 M) and temperature (room temperature to 150 °C) is the main process medium. To be used as structural materials in these environments, nitric acid grade (NAG) austenitic stainless steels (SS), various Ti (Ti-5%Ta, Ti-5%Ta-2%Nb) and Zr (Zircaloy-2, Zircaloy-4) based alloys have been assessed for their corrosion rates in various phases of Conc. HNO₃ [4]. While NAG steels (Uranus 65) have unacceptable corrosion rates (550 mpy) in the condensate phase of Conc. HNO₃, Ti and Zr alloys exhibit excellent corrosion resistance [2]. Based on these studies titanium and zirconium alloys are considered as structural materials for dissolver and evaporator vessels of FBR reprocessing plants [2].

An α - β Ti alloy of nominal composition Ti-5wt.%Ta-1.8wt.%Nb with remarkable corrosion resistance (corrosion rate = ~0.98 mpy) in the condensate phase of HNO₃ is a candidate structural material for the dissolver vessel handling boiling 11.5 M HNO₃ [5]. This necessitated welding of TiTaNb alloy with AISI type 304L austenitic stainless steel, the construction material for the rest of the plant [6]. Selection of appropriate methods for joining these dissimilar materials to satisfy zero failure requirement of the weld interface is critical.

Conventional fusion welding methods are generally not recommended to join Fe/Ti based systems due to the following reasons:

- ⇒ Poor mutual solubility of Fe and Ti (maximum solubility of Fe in α Ti is 0.05 at.% at 700 °C and Ti in γ -Fe is 0.8 at.% at 1150 °C) [7].
- ⇒ Tendency for chemical bond formation resulting in FeTi, Fe₂Ti type intermetallic phases at the interface.
- ⇒ Large difference in the coefficient of thermal expansion (SS: 17-18 $\mu\text{m/m K}$, Ti: 7.6 $\mu\text{m/m K}$) [8] resulting in residual stresses in the weldments [9].

Hence, solid state welding methods are being used where either the brittle phases are completely prevented from forming or isolated as dispersed phases in a matrix by (i) preventing melting of the base metals, (ii) forming bonds by severe plastic deformation or (iii) narrowing the heat affected zone [10-13]. Following section gives a brief overview of various solid state welding methods used to join Fe and Ti based alloys:

1.2 Review of the literature on solid state welding processes adopted to join various Fe/Ti based systems:

Diffusion couples of Fe and Ti fabricated by Wu et al. [14] showed formation of deleterious phases at the joint interface. However formation of these phases could be suppressed by (i) shortening the hold time at a particular temperature during heat treatment or (ii) introducing interlayers having solid solubility in both Fe and Ti. Diffusion bonding, a solid state welding technique was used to join various grades of Fe and Ti based alloys such as austenitic SS/Ti [15-17], 17-4 precipitation hardened steel/Ti [18, 19], ferritic steel/Ti [20] and microduplex steel/Ti [21, 22]. Diffusion bonding of low alloy steel (0.98Cr-0.3C-Fe) to commercially pure Ti (CPTi) resulted in

the formation of FeTi and TiC phases at the joint interface while the number and type of the phases changed with increase in the alloy content [23]. Typically the phases that are observed at the joint interface of AISI 304 SS/Ti are Cr rich σ phase, $\text{Fe}(\text{Cr})_2\text{Ti}$, FeTi, $\text{Fe}_2\text{Ti}_4\text{O}$ and βTi [24-27]. As a result even under optimized conditions of temperature, time and pressure, diffusion bonds had inadequate bond strength [25, 27]. To prevent the formation of brittle intermetallic phases several interlayers such as Al, Ni, Cu and Ag were examined [28-31]. Presence of interlayer with comparable thermal conductivity to that of base materials also reduced accumulated residual stresses in the weldment [32]. However, formation of deleterious phases could not be completely eliminated in diffusion bonds.

Another solid state welding technique used for the fabrication of dissimilar joints of SS and Ti (Ti alloys) with and without interlayer is friction welding [8, 33-36]. An intermetallic free weld interface could be successfully achieved in friction welded 304LSS and CPTi [8]. In contrast, Baek et al. [33] and Lee et al. [34] reported formation of $\text{Fe}(\text{Cr})_2\text{Ti}$, $\text{Fe}_2\text{Ti}_4\text{O}$ and $\beta\text{Ti}(\text{Fe})$ phases at the 321SS/Ti friction joint interface. A similar study by Kumar et al. [35] reported poor bonding in 304LSS/Ti-6Al-4V welds with increase in ductility upon introducing a Cu interlayer. Ni, as an interlayer also resulted in intermetallic free interface between SS and CPTi with appropriate selection of welding parameters [36]. Recently developed friction stir welding (FSW) process had advantages over friction welding process with respect to quality of the bond [12]. Fazel et al. [37] joined SS and CPTi by FSW and obtained sound welds between the two materials by proper optimization of the welding parameters such as tool rotation and advancing speeds.

Explosive cladding, is another solid state welding technique, in which the bonding takes place under the influence of high pressure ($\sim 1-15$ GPa) and large strain rate ($10^3/s$) [38]. This method was effectively demonstrated for fabrication of large components of SS and Ti. In this technique, upon detonation of an explosive, the flier plate (material with lower yield and tensile strength) collides with a base plate creating jet waves travelling with a detonation velocity in the subsonic range [13, 39-42]. Fluid like motion of the metals helped in removing surface impurities and contaminants leaving a virgin surface for bonding by severe plastic deformation [41, 42].

Explosive cladding process was employed to join 304LSS and Ti-5Ta-2Nb alloy [43] in our laboratory. Earlier investigations on these explosive clads revealed the formation of undesirable reaction zones at the interface during thermal exposure. Growth rate of these reaction zones was observed to be faster when compared to diffusion bonded joints [44]. The reason was attributed to the presence of large number density of defects which act as short circuit diffusion paths for the alloying elements. In order to obtain a fundamental understanding on the role of defects and alloying elements in accelerating/retarding the kinetics of formation of diffusion zones, a simple Fe-C/Ti system was chosen. Dissimilar joints of Fe-C/Ti system were fabricated employing both equilibrium and non-equilibrium processes and diffusion phenomena in both systems were studied as represented by the schematic in Fig. 1.

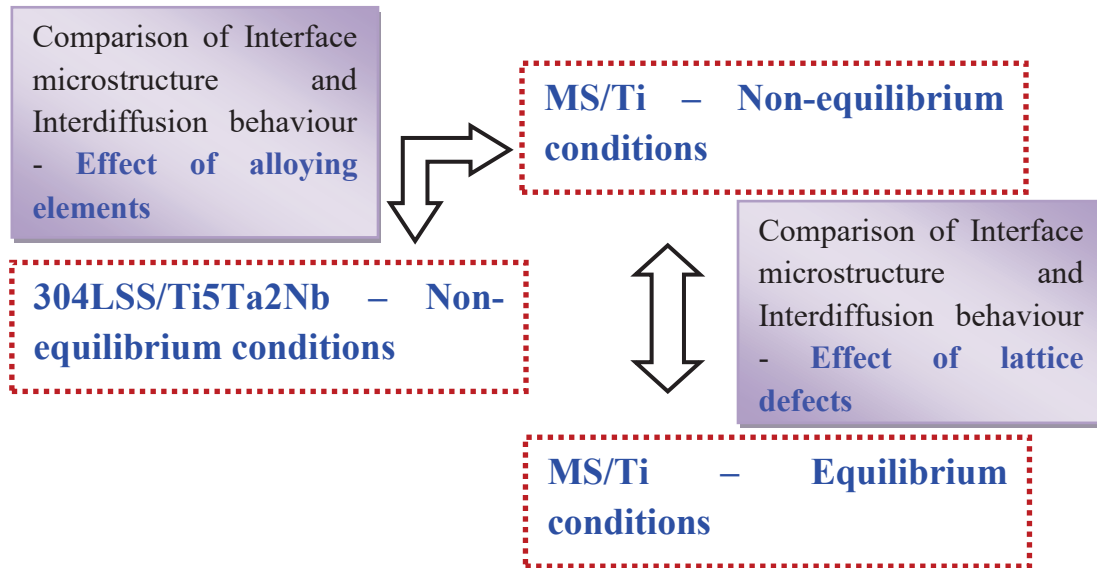


Figure 1 Schematic showing objective of the thesis

1.3 Fabrication of Fe-C/Ti joints with optimized welding parameters:

General procedure adopted to fabricate diffusion couples between systems that are difficult to join such as Fe-Ti is to initially establish a bonded interface through application of both pressure and temperature in a diffusion bonding set up followed by diffusion annealing heat treatment. However ‘as received’ diffusion bonds themselves had intermetallic phases at their interface. Hence to study diffusion under equilibrium conditions, it was decided to fabricate mild steel (Fe-0.14wt.%C)/Ti dissimilar joints by friction welding process followed by diffusion annealing. Literature reports revealed the feasibility of obtaining defect and intermetallic free joint interface using friction welding by proper selection of welding parameters namely friction force (FF), upset force (UF), burn off length (BOL) and rotational speed (ω) [8, 45]. Interfacial microstructure and associated mechanical properties for 304LSS and Ti friction welds were examined by Fuji et al. by varying friction pressure and upsetting pressure [46].

Meshram et al. [45] fabricated several dissimilar pure element combinations, such as Fe-Ti, Cu-Ti, Fe-Cu, Fe-Ni and Cu-Ni using continuous friction welding technique by varying BOL as 3 and 5 mm. With increase in the BOL (which in turn increases interaction time) weld strength decreased due to the formation of thicker intermetallic layer for Fe-Ti, Cu-Ti and Fe-Cu whereas it was increased for Fe-Ni and Cu-Ni systems due to good solid solubility. The basis for selection of 'r' in the range of 750-1500 rpm was a similar study by Fuji et al. [46] on 304LSS - Ti friction joints. The selection of FF and UF was based on yield strength and percentage elongation of mild steel (Fe-0.14C) and Ti [11].

As discussed in section 1.2, quality of the joint interface in explosive clads is highly dependent on the cladding parameters about which several reports are available in literature [38, 47-50]. Extent of bond formation is directly proportional to the dissipation of kinetic energy (KE) at the collision interface which in turn depends on the explosive load ratio (R) [51]. Akbari et al. [49] showed the importance of 'R' in obtaining a well bonded interface between 304SS and CPTi. For a flier plate (CPTi) of density 850 kg/m^3 , the load ratio was varied in the range of 0.5 to 3 in steps of 0.5 and an intermetallic free interface was obtained at $R=1$. Similar investigation by Raghukandan et al. [50] derived a relation for estimating impact velocity from load ratio during explosive cladding of thin sheets (3 mm) of 304LSS and Ti. Both these studies reported formation of vortices and secondary phases ($\text{Fe}_2\text{Ti}_4\text{O}$ and Fe_2Ti) at the interface with increasing 'R'. To circumvent this problem, interlayers were introduced to reduce the KE loss at the joint interface [52]. Kahraman et al. [47] also reported a straight interface devoid of intermetallics at a R value of 1 (flier plate density=750

kg/m³) and a wavy interface with intermetallics at $R > 1$. In general the features associated with explosive clads are as follows: (i) elongation of grains towards detonation direction, (ii) formation of non-equilibrium phases, (iii) high hardness at the collision interface, (iv) occasional presence of molten metal and (v) vortices at high explosive load ratio [39, 47-50]. Table 1.1 summarizes the reported information on variation in the nature of the explosive joint interface with load ratio and the optimized parameter chosen (marked in bold) in each study based on microstructure and phase analysis. Based on the above analysis, the load ratio for fabricating mild steel/Ti explosive clads was varied as 1, 2, and 3 keeping other parameters namely stand off distance and nature of explosive the same.

1.4 Heat treatment conditions for Fe/Ti dissimilar weld joints:

1.4.1 Selection of post weld heat treatments for Fe-C/Ti friction and explosive joints:

In general, post weld heat treatments are recommended for Fe-Ti friction joints to remove the residual stresses and to increase the ductility of the welds [46, 54]. Fuji et al. [46] reported poor bend ductility for ‘as welded’ 304LSS/CPTi friction joints and fracture occurred exactly at the interface during tensile testing. However, tensile strength and ductility considerably increased when the joints were heat treated at temperatures ≤ 600 °C with the failure occurring on the Ti side of the weld joint [46, 54]. Similarly, post weld heat treatments are essential for Fe-Ti explosive clads to obtain uniform microstructure and hardness without residual stresses [55, 56]. The recommended temperature range for stress relieving heat treatment of SS/Ti explosive clads are 538-635 °C [55].

Table 1.1 Summary of the literature showing effect of load ratio (R) on joint interface

System	Load Ratio (R)	Observations at the interface after cladding	Ref.
AISI304SS/CPTi	0.5	No welding	[49]
	1.0	Straight interface, presence of Ti₂O₃, TiO	
	1.2	Wavy interface, presence of Fe ₂ Ti ₄ O, Fe ₂ Ti, Cr ₂ Ti	
	2.0	Wavy interface with vortices, presence of Fe ₂ Ti ₄ O, Fe ₂ Ti, Cr ₂ Ti	
	2.5	Wavy interface with vortices, presence of Fe ₂ Ti ₄ O, Fe ₂ Ti, Cr ₂ Ti	
	3.0	Poor bonding	
304SS/Ti-6Al-4V	1.2	Straight interface	[47]
	1.5	Straight interface	
	2.0	Wavy interface with amplitude ~10-15 µm	
	2.5	Wavy interface with amplitude ~25-30 µm	
	3.0	Wavy interface with vortices	
304LSS/Ti	1.45	Wavy interface devoid of intermetallic phases	[50]
	2.17	Wavy interface with pockets of localized melts	
304SS/Grade 2 Ti	1.16	Smooth wavy interface	[53]
	1.4	Wavy interface with localized molten metal	
	1.94	Wavy interface with vortices	
	2.33	Wavy interface with vortices	

It was also reported that annealing at temperatures not exceeding 1000 °C was necessary for fabrication of large components from explosive clads by hot rolling [57]. Thermal exposure subsequent to cladding enhanced interdiffusion of alloying elements leading to the formation of diffusion zones consisting of FeTi, Fe₂Ti, Cr₂Ti, Fe₂Ti₄O, βTi phases at the clad interface [55, 57]. The nature and distribution of phases that form

due to interdiffusion across the interface and the width of the reaction zones influenced the shear strength and bend ductility of the joints. Based on the above analysis, the friction and explosive joints were subjected to post weld heat treatments and analysis of the microstructure along with simulated bond strength of the joint interface enabled to optimize the heat treatment conditions.

1.4.2 Reversion annealing treatments for deformation induced phases in 304LSS and Ti-5Ta-2Nb alloy:

Explosive cladding of 304LSS/Ti-5Ta-2Nb alloy resulted in the formation of strain induced α' and ϵ martensite phases in SS and metastable fcc phase in TiTaNb alloy [58]. Deformation induced phase transformations in 300 series austenitic stainless steels are well reported in literature [59-61]. 201SS with low stacking fault energy (SFE) (4.8 mJ/m^2) was reported to be more susceptible to form martensite than 304SS (18 mJ/m^2) [62]. Several other factors like alloy composition, strain rate, plastic strain, temperature and grain orientation also influenced martensitic transformation [63]. Presence of strain induced martensite (SIM) not only affected the mechanical properties [64] but also influenced the corrosion properties of 18Cr-8Ni steel (X5CrNi18-8) [65]. In the case of cold rolled 18Cr-8Ni-0.27Mo SS, the α'/γ interfaces got selectively corroded leading to overall decrease in the anodic dissolution potential of the parent material when exposed to an acid medium ($0.5\text{M HCl}+2\text{M H}_2\text{SO}_4$) [66]. SIM that formed by severe plastic deformation by cold rolling reverted to parent austenite during subsequent annealing accompanied by considerable grain refinement [67, 68]. Reversion of strain induced α' was reported to be complete at temperatures higher than

750 °C in cold worked AISI 304 stainless steel [69]. At temperatures beyond 600 °C, the mode of reverse transformation was identified as diffusion controlled [70].

Formation of metastable fcc phase has been reported in bulk Ti alloys [71, 72]. Manna et al. [72] reported the formation of metastable fcc phase during high energy mechanical milling of CPTi and rationalized the hcp to fcc phase transformation based on grain refinement, lattice expansion and plastic strain. A brittle mode of failure was reported in the case of Ti-20Zr-6.5Al-4V alloy due to the presence of fcc Ti phase [73]. Fcc phase inhibited the movement of slip at the α (hcp)- β (bcc) interface leading to decrease in the ductility of the alloy [74]. Besides, a biphasic structure consisting of metastable phases is not desirable for industrial applications. An appropriate heat treatment is therefore necessary to restore the microstructure and properties of the parent materials. The ‘interface fcc phase’ in Ti-6Al-4V alloy was reported to be stable upto a temperature of 500 °C beyond which it transforms to parent hcp (α) phase [71]. At low temperatures, and low grain sizes (\sim 5-7 nm) fcc phase was reported to be stable when compared to hcp phase, the reason for which was attributed to the temperature and grain size dependence of the Gibb’s free energy [75]. In the present research work, detailed X-ray and electron microscopy investigations were carried out to fix the temperature window within which the metastable phases were stable in SS and TiTaNb alloy and an attempt was made to identify the nucleation sites and reverse transformation mechanisms.

1.5 Growth kinetics of the diffusion zones and estimation of interdiffusion parameters:

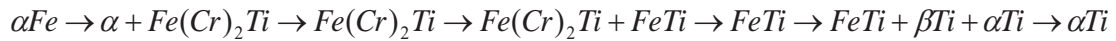
1.5.1 Growth kinetics of the diffusion zones in Fe/Ti based systems:

Several reports are available in literature where growth characteristics of the diffusion zones in Fe-Ti systems are observed to be governed by temperature and time dependent interdiffusion of the alloying elements across the interface [15, 18, 21, 76]. Formation of FeTi and Fe₂Ti type brittle intermetallics and other secondary phases could not be completely avoided in Fe-Ti system by solid state joining methods even under optimized conditions [24-30]. Ghosh et al. [15] calculated activation energy (Q) required for the growth of FeTi and Fe₂Ti intermetallics as 124.9 and 125.8 kJ/mol respectively. In contrast, Kale et al. [77] reported a low value of 73.07 kJ/mol for growth of Fe-Ti interface zones annealed in the temperature range of 852-1049 °C ignoring the formation of intermetallic phases at the interface. Additionally, there exist few reports in literature where growth kinetics of various phases have been studied as a function of temperature and time [15, 76]. Activation energy (Q) for growth of σ (Cr rich phase), Fe₂Ti and FeTi intermetallic phases at the interface of 304SS/Ti-5.5Al-2.4V diffusion bonded joints was reported as 253, 184 and 154 kJ/mol respectively [78]. In contrast, Taguchi et al. [79] reported a high value of 360 kJ/mol for the growth of β Ti (Fe) phase when annealed in the temperature range of 677-867 °C. In the present study an attempt has been made to study the growth kinetics of the diffusion zones formed in Fe/Ti systems.

1.5.2 Estimation of interdiffusion parameters:

It is well known that conventional diffusion couple technique is employed to determine the concentration dependent interdiffusion coefficients in binary and multicomponent systems. For reasons stated earlier the diffusion couples between Fe and Ti could not be prepared. Hence, the diffusion behavior under non-equilibrium was established in the present study in a Fe-C/Ti joint fabricated under severe deformation conditions. This behavior was compared with that of a joint fabricated under conditions where the extent of deformation is minimal. The two joints typically represent diffusion under equilibrium and non-equilibrium conditions for the intended purpose of this study. The estimation of diffusion coefficients in the above two cases has been carried out using the concentration profiles obtained by Electron Probe Micro Analyzer (EPMA) analysis across the diffusion annealed weld joints. Boltzmann and Matano (BM) have collectively developed an analytical solution for the Fick's second law of diffusion to evaluate the concentration dependent interdiffusion coefficients ($D(C)$) [80]. This method is used to determine the interdiffusion fluxes of individual components and interdiffusion coefficients as a function of composition using the concept of a reference plane known as Matano plane [80]. Evaluation of interdiffusion parameters from concentration profiles by BM method is rather simple in the case of binary systems with a constant molar volume. This method was successfully applied to obtain interdiffusivities in a wide variety of systems such as Zr-(Nb/Fe) [81, 82], 304SS/Ti [76], Al-Zr [83] and Zircaloy-2/(SS,Ti) [77, 84]. However, if considerable change in molar volume is involved during interdiffusion then locating the Matano plane is difficult which was overcome by Den Broeder (DB) [85] by introducing a

relative concentration variable. Although, both BM and DB methods yielded identical results in Cu-Ni and Ta-W [86] systems, the latter method was widely used due to its mathematical ease. The main drawback of this approach was ignoring the change in the molar volume of the system during the course of interdiffusion. Either intermetallic phases or secondary phases necessarily form in almost all the engineering materials due to interdiffusion. For example, the intermetallic phases that can form in Ni/Zr system, due to limited mutual solubility are: Ni₅Zr, Ni₇Zr₂, Ni₃Zr, Ni₂Zr₆, Ni₁₀Zr₇, Ni₁₁Zr₈, NiZr and NiZr₂ [87]. Among all the phases Ni₇Zr₂, NiZr and NiZr₂ are line compounds with congruent melting points at 1440 °C, 1260 °C and 1120 °C respectively. Similarly in Fe/Ti system, the phases that can form are Fe₂Ti (homogeneity range - 33 to 39 at.% of Ti), FeTi (narrow homogeneity range of 49.7 to 51.1 at.% of Ti) and FeTi+βTi (homogeneity range - 51.1 to 87.8 at.% of Ti) at 600 °C [7]. Volume fraction and type of phases increased with addition of alloying elements which was evident from the sequence of phase formation in Fe-Cr-Ti system at 600 °C [88]:



Hence, it was obvious from literature, that it is essential to consider the change in molar volume due to the formation of secondary phases during the estimation of interdiffusion coefficients. In the case of Co-Nb and Ni-Nb systems the formation of Co₂Nb, CoNb, Co₇Nb phases and NiNb, Ni₃Nb phases respectively resulted in appreciable variation in the molar volume (V_m) and hence Wagner's method was used incorporating ' V_m ' for the determination of interdiffusion coefficients in these phases [89]. A similar procedure has been adopted for estimating the interdiffusion parameters in topological close packed μ (Co₇Mo₆) phase formed in diffusion couples of Co and Mo [90].

Sangeeta and Aloke Paul in a recent publication [91] have laid emphasis on incorporating the effect of change in molar volume for accurate determination of intrinsic diffusion coefficients in V_3Ga system and have also proposed use of Wagner's method [92, 93], when substantial molar volume change is involved during interdiffusion.

1.5.3 Diffusion models available for multicomponent systems:

All the methods described in the previous section are applicable for simple binary systems and there is difficulty in extending the same to multicomponent and multiphase systems, where diffusion of one element influences the other diffusing species. For example, in a 'n' component system there are $(n-1)^2$ interdiffusion coefficients and 'n-1' diffusion couples are required for applying conventional BM method. This poses extreme difficulty in understanding the diffusion kinetics in multicomponent system. Jan et al. in the year 1991 developed a methodology for the determination of interdiffusion and intrinsic diffusion coefficients in a ternary GaAs/Ni system using a single semi infinite diffusion couple [94]. The assumption made for determining the interdiffusion coefficients of Ni and As in sufficiently wide Ni_3GaAs interface phase is that the diffusion of one element do not influence the other diffusing element i.e the cross diffusion terms $(\tilde{D}_{12}, \tilde{D}_{21})$ are ignored. Similar methodology has been adopted to estimate the interdiffusion coefficients in Ti/Inconel 600 system [95]. However, it is very essential to consider the effect of one element on the other diffusing elements for accurate determination of interdiffusion coefficients.

Further, Dayananda had proposed an alternative approach of equating the total flux of all the diffusing elements to locate the Matano plane in multicomponent systems

[96, 97]. The flux over the entire diffusion zone was considered to accurately calculate the effective interdiffusion coefficients. Using the flux calculations in Fe-Ni-Al and Fe-Ni-Cr, zero flux planes for each individual component have been identified and the average interdiffusion coefficients ($\bar{D}(c)$) were estimated in a specific compositions range [98, 99]. Ternary interdiffusion coefficients and the resultant diffusion paths in (U-Zr)/(Fe-Ni-Cr) were calculated using this approach [100]. Sangeeta and Alope Paul postulated a new pseudo binary approach to estimate the intrinsic diffusion coefficients in a ternary Cu-Sn-Ga and Cu-Sn-Si systems. This method involved fabricating infinite diffusion couples of Cu-8at.%Sn/Cu-8at.%Ga so that Cu concentration remained unaltered during the interdiffusion between Sn and Ga [101]. Following the same line of approach this procedure was further extended for determination of interdiffusivities in multicomponent systems. In the present research work, Dayananda's multicomponent approach was applied to determine the average effective interdiffusion coefficients in Fe-C-Ti and Fe-Cr-Ti systems. In the present research work, both DB and Wagner methods have been used wherever applicable.

1.6 Molecular dynamics simulations of diffusion of Fe in hcp Ti lattice:

In order to understand defect aided diffusion it was proposed to carry out Molecular dynamics (MD) simulations, ideal to predict the properties of the defects, phase transformation kinetics and resultant structural evolutions associated with the phase transformations and transport phenomena [102]. MD uses the interatomic potentials of the atoms to determine the intended properties of the materials. Interatomic potentials strongly influence the reliability and accuracy of the MD simulations [103]. Hence, selection of an appropriate interatomic potential was essential for accurate

determination of the properties of the metals. Various interatomic potentials such as pair potentials, embedded atom method (EAM), modified embedded atom method (MEAM) potentials are available in literature for Fe and Ti systems [104-108]. Among various many body potentials MEAM potentials are considered as more suitable for calculation of material properties since these potential formalism includes the directionality of interaction between the atoms also.

Second nearest neighbor modified embedded-atom method potentials (2NN MEAM) is a recently developed potential formalism [109, 110]. The 2NN MEAM is a generalized version of the MEAM [109] which is a modification of the EAM. The advantage of the 2NN MEAM is that it can describe a wide range of crystal structures (bcc, fcc, hcp, diamond and even gaseous elements) using a common formalism, and is thus applicable to multicomponent alloys where it is essential to describe individual elements using a common mathematical formalism [109]. The 2NN MEAM potential formalism has already been applied to Fe-Ti [111] and Fe-C [112]. The MEAM potentials were developed by Lee et al. [113, 114] for Fe-Hydrogen (H) system, using which atomistic phenomena such as interaction of H atoms with vacancies, dislocations and grain boundaries were successfully demonstrated. MD simulations using MEAM potentials were also found to be effective in understanding the effect of alloying elements on the number of residual point defects (vacancies and interstitials) and their clustering behavior in pure Fe [112]. Formation energies and intra, inter layer self diffusion activation energies in Fe (111) layer was studied using MEAM potentials [115]. Based on the energy minimization, single vacancy was observed to be the easiest to be formed on the surface. Recently few MD investigations on Ti were also reported

using MEAM potentials [116]. These potentials were found to be successful in reproducing certain fundamental physical properties such as enthalpy of formation, thermal expansion coefficients and elastic constants of the intermetallic compounds FeTi and Fe₂Ti, of the Fe-Ti system. Later Kim et al. [117] extended the same 2NN MEAM potential parameters to the Fe-Ti-C and Fe-Ti-N ternary systems and successfully determined the nucleation kinetics of TiC and TiN precipitates and their effect on the mechanical properties of the system. Based on the above review of literature, 2NN MEAM potentials proposed by Sa et al. [111] were used for studying the diffusion of Fe in hcp Ti lattice. Further, the simulations were extended to understand the defect aided diffusion by introducing point and line defects in the Ti lattice.

1.7 Scope of the thesis:

The present thesis entitled “**An Experimental and Computational Study on Diffusion Driven Structural Changes in Fe-Ti Based Dissimilar Joints Under Equilibrium and Non-equilibrium Conditions**” presents the results of an in depth study on Fe/Ti based systems namely (i) mild steel(MS)/Ti Grade 2 and (ii) 304LSS/Ti-5Ta-2Nb. The MS/Ti joints were fabricated by friction welding and explosive cladding methods while SS and TiTaNb alloy were joined by explosive cladding process. The main objective of the thesis was to understand the equilibrium and non-equilibrium diffusion driven structural changes in Fe/Ti based systems. The weld joints were diffusion annealed and the resultant interdiffusion across the weld joints was studied using available binary and multicomponent diffusion models. Further, atomistic based Molecular Dynamics (MD) simulations were carried out to understand the defect aided

diffusion of Fe in Ti lattice by introducing point and line defects in the lattice. This thesis consists of seven chapters which are organised as follows:

- ❖ **Chapter 1** titled as “**Introduction**”, briefly presents a review of the existing literature on various joining methods adopted to join Fe and Ti based alloy systems. Further, a brief description is provided to explain the basis for selection of a suitable joining method and associated welding parameters to join MS/Ti with an aim to avoid the formation of intermetallic and other deleterious phases at the interface. A brief review of the literature on various models available for estimation of concentration and temperature dependent interdiffusion parameters in binary and multicomponent systems is also presented. Further, the potentials available for MD simulations of Fe-Ti system is discussed in detail. This chapter also highlights the relevance and scope of the present research work.
- ❖ **Chapter 2** titled as “**Experimental and computational methods**”, describes the fabrication of Fe/Ti based dissimilar joints. The specimen preparation methods adopted for various characterization techniques namely Scanning Electron Microscopy (SEM), Electron Probe Micro Analyzer (EPMA), X-ray Diffraction (XRD), Electron Back Scatter Diffraction (EBSD) and Transmission Electron Microscopy (TEM) are elaborated. A brief description of the operating procedure of the above techniques, data acquisition and analysis is presented. In addition, to the experimental techniques a concise explanation is provided for the computational methods namely Molecular Dynamics and JMatPro[®] software.

- ❖ **Chapter 3** titled as “**Microstructure and property evaluation in Fe-C/Ti friction and explosive joints in ‘as welded’ and heat treated conditions**” presents an elaborate study on optimization of process parameters for fabrication of MS-Ti friction and explosive joints. The weld joints fabricated under optimized conditions were further characterized using various experimental techniques. Information on interface microstructure, microchemistry together with the experimentally calculated as well as JMatPro[®] computed bond strength used to assess the quality of welds, which is elaborated in this chapter. This chapter also describes the basis for optimization of post weld heat treatments (PWHT) of friction and explosive joints. Detailed transmission electron microscopy investigations were carried out for unambiguous identification of various phases formed in ‘as welds’ and heat treated weld joints.
- ❖ **Chapter 4** titled as “**Structural changes during deformation and annealing in 304LSS/Ti-5Ta-2Nb explosive clad joints**” deals with the results on deformation induced phase transformations in 304LSS and Ti-5Ta-2Nb alloy during explosive cladding. Detailed electron microscopy investigations to confirm the formation and reversion of deformation induced phases are presented. An in-depth study on mechanism responsible for the reversion process is presented with experimental evidences obtained using SEM, microhardness measurement, XRD, EBSD and TEM. Further, evolution of interface microstructure and microchemistry at the SS/TiTa Nb clad interface during diffusion annealing is discussed. This chapter also includes JMatPro[®] computations carried out to predict the presence of various phases at the clad

interface and confirmation of the predicted phases by detailed TEM investigations.

- ❖ **Chapter 5** titled as “**Interdiffusion in Fe-Ti based systems under equilibrium and non-equilibrium conditions**” provides a brief study on the structural changes in friction and explosive joints of Fe-C/Ti and SS/TiTaNb explosive clads upon long term thermal exposure at elevated temperatures. Concentration and temperature dependent interdiffusion parameters are evaluated by DB and Wagner methods from concentration profiles in SS/TiTaNb considering Fe and Ti as the diffusing species. Later, the calculations are extended to Fe-Cr-Ti system by employing Dayananda’s multicomponent approach to understand the effect of alloying elements on the interdiffusion phenomena in SS/TiTaNb system. Similarly, the multicomponent approach is used to evaluate the effective interdiffusion coefficients in the diffusion zone of Fe-C-Ti system under equilibrium and non-equilibrium conditions to understand the effect of defects on the interdiffusion phenomena.
- ❖ **Chapter 6** titled as “**Molecular Dynamics simulations of diffusion of Fe in hcp Ti lattice**” elaborates the results on MD simulation of Fe atom diffusion in hcp Ti lattice. Interatomic potentials for the simulations are validated by estimating the physical properties of Fe-Ti system. Defect aided diffusion is studied by introducing point and line defects into Ti lattice, the results of which are described in this chapter.
- ❖ **Chapter 7** presents the summary of important findings of this research work and also identifies the scope for further studies.

Chapter 2

Experimental and Computational Methods

2.1 Introduction:

The present thesis entitled “**An Experimental and Computational Study on Diffusion Driven Structural Changes in Fe – Ti Based Dissimilar Joints Under Equilibrium and Non-equilibrium Conditions**” is an elaborate study on microstructural, microchemical and phase changes in Fe-Ti based dissimilar joints due to interdiffusion under equilibrium and non-equilibrium conditions. Influence of defects and alloying additions on interdiffusion has been studied using both experimental and computational methods.

This chapter is organized as follows: Section 2.2 deals with the procedure for fabrication of (i) diffusion couples of mild steel (MS) and Grade 2 Ti (Ti) and (ii) dissimilar joints of Fe-Ti based systems by friction and explosive joining methods. Mechanical property evaluation of the weld joints is described in section 2.3, while heat treatment schedules adopted are given in section 2.4. Experimental techniques used for microstructural and microchemical characterization are described in detail in section 2.5. Section 2.6 elaborates the estimation of growth parameters of the diffusion zones and determination of interdiffusion parameters using various methods. Sections 2.7 and 2.8 deal with the computational techniques namely JMatPro[®] and Molecular Dynamics simulations adopted in the present research work. The salient features of this chapter are summarized in section 2.9.

2.2 Specimen fabrication details:

Chemical composition and mechanical properties of the metals used in the present thesis are listed in Table 2.1 and Table 2.2 respectively. The MS and Ti plates of dimensions 1000x500x20 mm and 1000x500x12 mm respectively were procured commercially. The 304LSS (SS) and Ti-5Ta-2Nb (TiTaNb) were supplied

in the form of plates of dimension 2000x1000x25 mm and 1000x247x6.5 mm respectively by MIDHANI, Hyderabad in hot rolled and annealed condition.

Table 2.1 Chemical composition of the materials studied

Element (wt.%)	Mild steel	304LSS	Grade 2 Ti	Ti-5Ta-2Nb
C	0.141	0.02	0.023	0.01
Si	0.138	0.57	--	0.03
Mn	0.786	1.66	--	--
P	0.03	0.029	--	--
S	0.032	0.004	0.03	--
Cr	--	18.15	--	0.1
Ni	--	8.59	--	0.1
N	--	0.031	0.012	0.014
Al	0.028	--	0.1	--
Fe	Bal.	Bal.	0.02	0.2
H	--	--	0.001	0.043
O	--	--	0.06	0.417
Ta	--	--	--	4.26
Nb	--	--	--	1.96
Ti	--	--	Bal.	Bal.

Table 2.2 Mechanical properties of the materials

Material	YS (MPa)	UTS (MPa)	% Elongation
Mild steel	285	445	31
304LSS	280	566	62
Grade 2 Ti	260	325	35
Ti-5Ta-2Nb	256	418	37

2.2.1 Fabrication of diffusion couples of MS/Ti:

MS and Ti specimens of dimension 8x8x6 and 8x8x6 mm were used for the fabrication of diffusion couples. Well polished surface was ensured prior to loading of the specimens in to a ‘diffusion die’ where the two materials were kept in contact and tightened. This whole assembly was vacuum sealed in quartz tube and subjected to heat treatment at a temperature of 800 °C for duration of 20 h. Cross-section of the coupled metal joint was polished for further characterization.

2.2.2 Fabrication of MS/Ti friction welds:

Friction welding process was used to join MS and Ti to avoid the formation of intermetallic and other secondary phases such as oxides. Schematic of the friction welding process is shown in Fig. 2.1(a). MS and Ti rods of 10 mm diameter and 100 mm length were machined from the plates and the contact surfaces were well polished up to a mirror finish to eliminate any surface roughness for the friction welding process. During friction welding, the MS rod was kept in the static mode and the Ti rod was rotated and moved towards MS to minimize the extent of flash (expulsion of material at the interface) due to high deformation of Ti. Through a combination of compressive force and high temperature (~1425 °C generated during the process - for 304SS/MS) [118] the metals were joined together by plastic deformation.

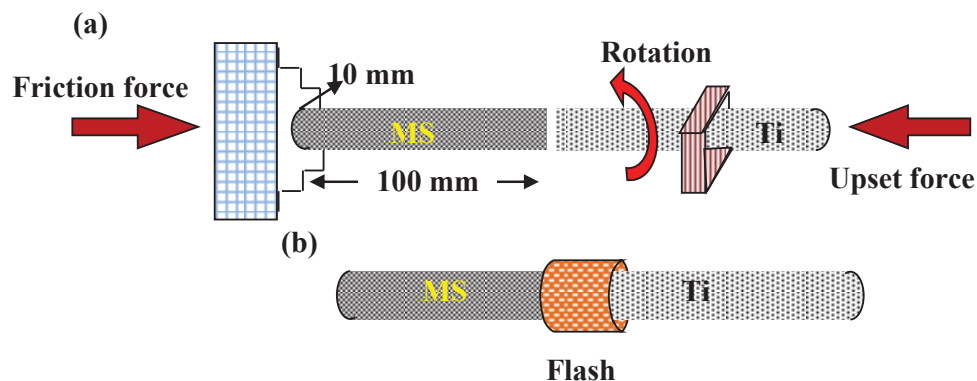


Figure 2.1 Schematic of (a) friction welding process and (b) friction joint after machining

Table 2.3 List of process parameters varied in friction welding

Trial No.	Friction Force (FF) tonnes	Upset Force (UF) tonnes	Burn Off Length (BOL) mm	Rotational Speed (r) rpm
1	0.8	1.6	3	750
2	0.8	1.6	3	1000
3	0.8	1.6	3	1500
4	0.8	1.6	2	1000
5	1	2	3	750
6	1	2	3	1000
7	1	2	3	1500
8	1	2	2	1000

For the present study, several trial welds were fabricated by varying the process parameters such as friction force (FF), upset force (UF), burn off length (BOL) and the rotational speed (r) as shown in Table 2.3, based on information available in literature [8, 45]. After welding, the flash was removed by machining (Fig. 2.1(b)). Specimens of 10x10 mm dimension were extracted from the cross-section of the bonded surfaces for further analysis.

2.2.3 Fabrication of MS/Ti explosive clads:

Explosive cladding is a solid state welding process which has been successfully demonstrated for various similar and dissimilar material combinations [119]. In this process, an explosive material is spread on the flier plate which is maintained at a fixed stand off distance from the base plate. A very high velocity collision of the base and flier plates generated by detonating an explosive charge creates an atomic level bonding between the plates. High velocity jet propagating through the clad interface removes the oxides and other impurities thereby providing favorable conditions for cladding at the interface [13, 40-42]. Explosive cladding

process was carried out by M/s Explofab Metals (I) Pvt. Ltd., Hyderabad, India. Figure 2.2 shows the schematic of the explosive cladding process of MS and Ti plates of dimension 500x500x20 mm and 500x500x12 mm respectively. In the present work, three explosive clads were fabricated with different explosive load ratio (R) as 1.07, 2.01 and 3.0 keeping other parameters such as explosive agent and stand off distance constant. Table 2.4 summarises the experimental parameters fixed during explosive cladding.

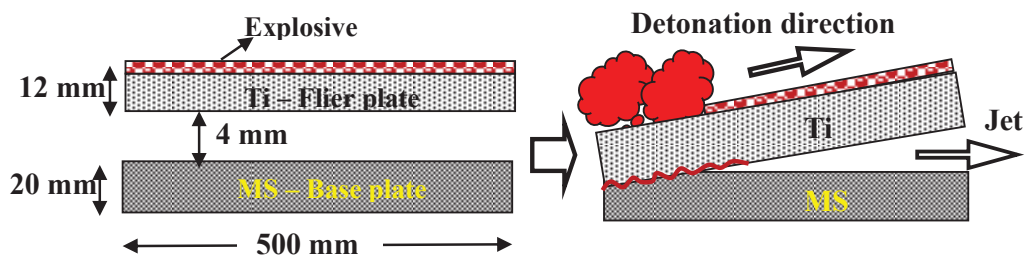


Figure 2.2 Schematic showing the (a) geometrical arrangement in explosive cladding process and (b) bonding during explosive cladding process

Table 2.4 Experimental parameters for explosive cladding of MS/Ti

Parameters fixed during the cladding process			
Type of explosive		Homogeneous mixture of TNT, Grade 1 flakes, Ammonium Nitrate, Vacuum dehydration salt (powder form)	
Type of geometry		Parallel	
Base plate		MS (IS 2062- E 250C)	
Flier plate		Ti (Grade 2)	
Acoustic velocity of flier plate		6100 m/s	
Parameter varied - Explosive load ratio (R)			
R	Detonation velocity (V_d) (m/s)	Impact velocity (V_f) (m/s)	Impact energy (E) (kJ)
1.07	2000	427	615
2.01	2100	644	2800
3.0	2200	808	4406

Figures 2.3(a) to (c) show the MS/Ti clads fabricated with load ratio of 1.07, 2.01 and 3.0 respectively. Ultrasonic examination as per SA 578 revealed de-bonding at one edge of the three clads and extent of de-bonding increased with R, which is depicted by double continuous lines in Fig. 2.3(a) to (c). Figure 2.3(d) shows the transverse view of the clad fabricated with R value of 1.07.

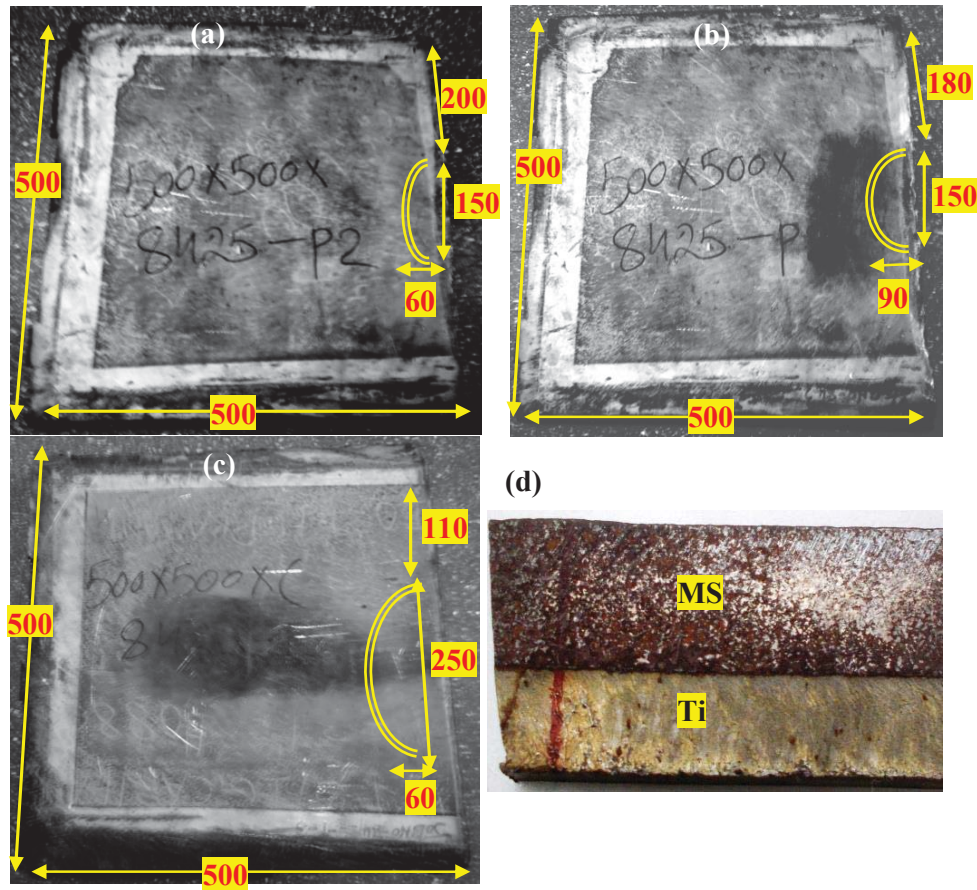


Figure 2.3 Top view (Ti side) of the MS/Ti clads fabricated with a load ratio of (a) 1.07, (b) 2.01 and (c) 3.0; de-bonding at an edge revealed by ultrasonic examination is represented by continuous double lines; (all dimensions are in mm) and (d) transverse section of the clad fabricated with R value of 1.07

The impact velocity ' V_f ' at each load ratio (R) was measured using the following equation (2.1) [50]:

$$V_f = V_D \left[\frac{0.612R}{2 + R} \right] \quad (2.1)$$

where, ' V_D ' is the detonation velocity. Further, the impact energy (E) was calculated using the expression given below [51]:

$$E = 0.5(\rho V)V_f^2 \quad (2.2)$$

where, ' ρ ' and ' V ' are detonating density (4.5 g/cm³) and volume (3000 cm³) of the flier plate respectively. The calculated impact velocity and impact energy values are also listed in Table 2.4.

2.2.4 Fabrication of 304LSS/Ti-5Ta-2Nb explosive joints:

Explosive cladding of 250x400x6 mm SS and 250x450x6 mm TiTaNb alloy plates was carried out at M/s Gulf Oil Corporation, Rourkela, India. The following parameters were optimized during the process: (i) collision velocity (2000-3000 m/s), (ii) collision angle (12-15°), (iii) flier plate velocity (500-650 m/s) and (iv) nature of explosive (a mixture of ammonium nitrate and fuel oil and an inert substance like sand). Initially a smooth surface finish was ensured for SS and TiTaNb to obtain a satisfactory interface after cladding. TiTaNb as overlay (flier plate) and SS as base plate [47] was selected based on mechanical property.

2.3 Mechanical property evaluation:

Mechanical property evaluation of MS/Ti 'as clad' explosive joints was carried out by longitudinal tensile (tensile axis parallel to clad interface) and shear testing methods as per ASTM A263 and B898. Schematic showing orientation of the specimen extracted for mechanical tests is shown in Fig. 2.4(a) and the dimensions

of tensile and shear test specimens are shown as Fig. 2.4(b) and (c) respectively [120]. In case of SS/TiTaNb explosive joints, due to the limitation with respect to thickness of the plates, it was necessary to fabricate similar welds for transverse tensile testing as per ASTM 308 standard testing method (Fig. 2.5) [121].

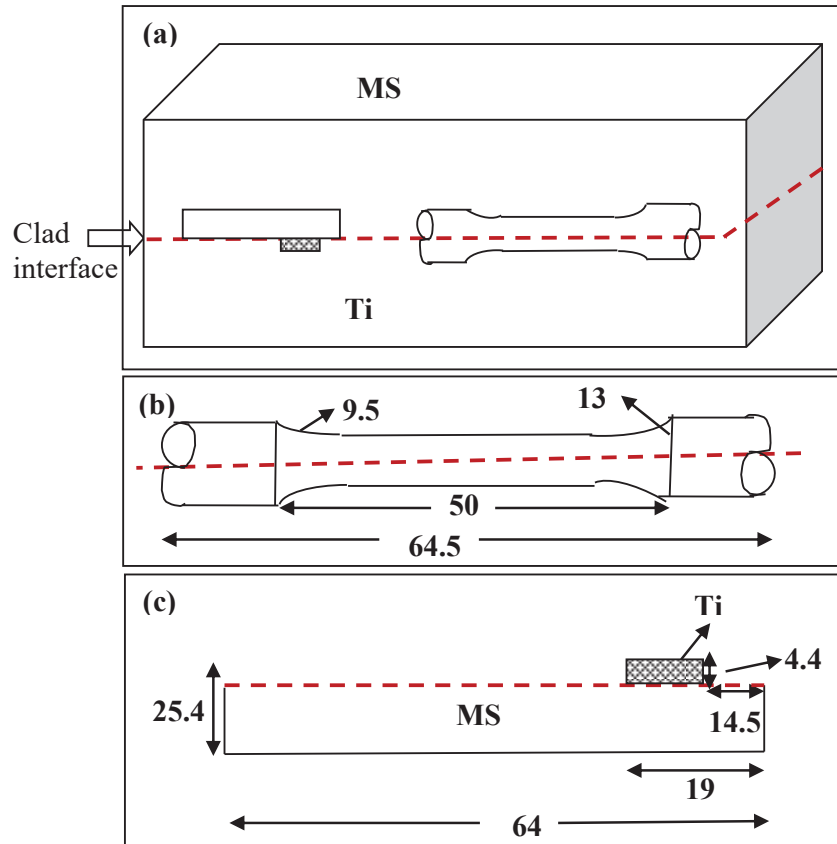


Figure 2.4 Schematic of (a) MS/Ti ‘as clad’s showing orientation of the specimens fabricated for tensile and shear tests, dimensions of (b) tensile and (c) shear test specimens (all dimensions are in mm)

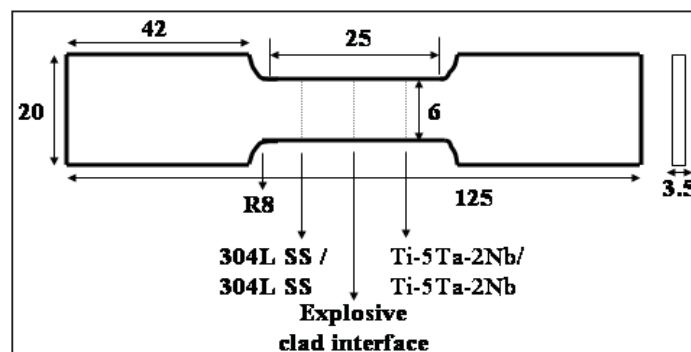


Figure 2.5 Schematic showing transverse tensile test specimen of SS/TiTaNb explosive joint (all dimensions are in mm)

2.4 Heat treatment schedules:

All the heat treatments were carried out on cut sections of the weld joints of suitable dimensions in a well calibrated resistance heating furnace with a temperature accuracy of ± 5 K monitored using Nickel-Chrome thermocouple. Table 2.5 lists the heat treatment schedules adopted in the present research work. Post weld heat treatments (PWHTs) of the MS/Ti friction and explosive joints were carried out at temperatures of 500 and 600 °C for durations in the range of 1-10 h while diffusion annealing heat treatments were carried out in the temperature range of 500-800 °C for 20 and 100 h duration. The recommended temperature range for stress relieving heat treatments of SS/Ti explosive clads is 538-635 °C [55]. Hence, SS/TiTaNb joints were subjected to PWHTs at temperatures of 550 and 600 °C for durations between 1-5 h. For interdiffusion studies, the clads were exposed to temperatures in the range of 550-800 °C for 10 and 20 h durations.

Table 2.5 List of heat treatment schedules adopted in the present research work

Post weld heat treatments		
System	Temperature; time	Condition
MS/Ti friction and explosive joints	500-600 °C; 1-10 h	Furnace cooled
SS/TiTaNb explosive joints	550-600 °C; 1-5 h	Furnace cooled
Reversion annealing treatments		
SS	400-700 °C; 2 h	Water quenched
TiTaNb alloy	100-900 °C; 2 h	Water quenched
Diffusion annealing heat treatments		
MS/Ti friction and explosive joints	500-800 °C; 20-100 h	Furnace cooled
SS/TiTaNb explosive joints	550-800 °C; 10-20 h	Furnace cooled

Further, to study the microstructural and crystal structural changes associated with the reversion of metastable phases, formed during explosive cladding process, specimens from the deformed regions of SS and TiTaNb clad were extracted separately, vacuum sealed in quartz tubes and annealed for 2 h in the temperature range of 400-700 °C and 100-900 °C for SS and TiTaNb respectively followed by quenching in ice water.

2.5 Techniques for characterization of the dissimilar joints:

2.5.1 X-ray diffraction (XRD) analysis:

Identification of phases was carried out using INEL XRG3000 model X-ray diffractometer equipped with curved position sensitive detector operated at 40 kV and 30 mA. Cu K α ($\lambda=1.5406$ Å) was used as the incident radiation to obtain patterns in the 2θ range from 10-90° with step size of 0.012°. Intensity and 2θ values were calibrated with Si standard, prior to acquisition of the spectra on the specimens. Flat specimens of dimension 10x10x2 mm were used for XRD analysis.

It is to be noted that the entire 6 mm thickness of SS and TiTaNb plates showed uniform deformation during explosive cladding process and resulted in the formation of metastable phases in both the parent metals. To study the stability of these metastable phases, High Temperature X-ray Diffraction (HTXRD) investigations were carried out on 10x10x2 mm thin specimens extracted from the deformed regions of both SS and TiTaNb alloy [122]. HTXRD patterns were acquired using the INEL XRG – 3000 diffractometer (with glancing incidence angle of 5°) using Cu K α radiation. Specimens were heated in a tantalum holder in the temperature range of 100-1100 °C at a heating rate of 20 °C/min. Measurements in the 2θ range from 20 to 90° at 2.8×10^{-6} mbar pressure were carried out using a

Buhler HDK 2.4 high temperature camera. For indexing of the hkl planes in diffraction patterns standard ©2014 International Centre for Diffraction Data (ICDD) was used.

2.5.2 Microstructural analysis and microhardness measurements:

Specimens of dimensions 10x10x10 mm were extracted from the ‘as-welded’ as well as heat treated joints for microstructural, microchemical and hardness measurements. Standard metallography procedures such as grinding using SiC sheets up to 4000 grit followed by mirror polishing using alumina suspension were adopted to obtain a perfectly polished surface for further characterization. The chemical etchants used for revealing the microstructure of the materials is listed in Table 2.6 [123].

Microstructural examination was carried out using Scanning Electron Microscopes XL 30 ESEM of M/s FEI (Netherlands) operating at a voltage of 30 kV and FEI Helios Nanolab 600i Field Emission Scanning Electron Microscope (FE-SEM) at an operating voltage and specimen current of 30 kV and 5.5 nA respectively. ESEM was operated at a working distance (WD) of 10 mm while FESEM was operated at a lower WD of 3 mm. Both secondary electron (SE) and back scattered electron (BSE) imaging modes were used to characterize the microstructure [124].

Table 2.6 Details of the chemical etchants

Material	Etchant	Composition
Mild steel	Nital	5 ml HNO ₃ in 95 ml Methanol
SS	Aqua regia	Equal amounts of Conc. HCl, HNO ₃ in distilled water
Ti and TiTaNb alloy	Kroll's reagent	4.5 ml Conc. HNO ₃ , 0.5 ml HF in 45 ml of distilled water

Microhardness measurements were carried out with an applied load of 100 g and dwell time of 15 s using Leitz microhardness tester. Vickers hardness number (HV) was calculated using the formula given below [125]:

$$HV = \frac{1854.4 * P}{d^2} \quad (2.3)$$

where, ‘ P ’ is the load applied (100 g) and ‘ d ’ is the average diagonal length of the impression made by the diamond indenter. Each reported hardness value is an average of minimum three measurements. The statistical scatter in the measured values was found to be ± 10 HV which is found to be within ± 5 %.

2.5.3 Microchemical characterization:

Qualitative identification of elements was carried out using the Energy Dispersive Spectrometer (EDS) attached to FE-SEM on fractured surface of the tensile and shear tested specimens as well as on polished surfaces. A peltier cooled SDD detector with a crystal area of 20 mm/50 mm and energy resolution 127 eV at Mn $K\alpha$ was used for the semi-quantitative analysis. Quantitative microchemical analysis was carried out using CAMECA SX50 and SX Five Electron Probe Micro Analyzer (EPMA). Elemental concentration profiles were obtained across the MS/Ti weld joints both in the ‘as welded’ condition and after thermal exposure using EPMA. The conditions used for the analysis were as follows: accelerating voltage - 20 kV, beam current - 20 nA, diffracting crystals - LLiF for Fe $K\alpha$, LPET for Ti $K\alpha$ and PC2 for C $K\alpha$. For the analysis of SS/TiTaNb joints in SX-50 the diffracting crystals used were: LiF for Fe, Cr, Ni and Mn $K\alpha$, PET for Ti $K\alpha$, Nb $L\alpha$ and TAP for Si $K\alpha$, Ta $M\alpha$ X-rays. X-ray generation volume was restricted to $\sim 2\text{-}3 \mu\text{m}^3$.

For quantitative analysis the $K\alpha$, $L\alpha$ or $M\alpha$ X-ray intensities of the elements obtained from the specimen were compared with that from the standards under identical experimental conditions. From the intensity ratio (k-ratio) obtained after back ground subtraction and dead time correction, the concentration of the elements was calculated using an automated computer program 'QUANTA' based on the following governing equation [126].

$$\frac{I_{specimen}}{I_{standard}} = \frac{C_{specimen}}{C_{standard}} * [ZAF] \quad (2.4)$$

where, ' $I_{specimen}$ ' and ' $I_{standard}$ ' are intensities obtained from specimen and standard respectively while ' $C_{specimen}$ ' and ' $C_{standard}$ ' are concentration of an element in the specimen and standard respectively. ZAF indicates the atomic number (Z), absorption (A) and fluorescence (F) corrections incorporated in the calculation to include the modification in the X-ray intensities due to interaction of primary electron beam with specimen atoms. Specimen conductivity was ensured during the course of the analysis. Elemental concentration profiles were cross checked in three regions before interpreting the observed compositional fluctuations. For low atomic number elements, concentration values were accurate to within $\pm 10\%$ and for all the other elements an accuracy of $\pm 1\%$ was obtained. The carbon content in the MS metal in the 'as received' condition was measured in many locations and compared with the carbon concentration in the base material region to determine overestimation in the C measurement.

2.5.4 Electron back scatter diffraction analysis:

Electron Back Scatter Diffraction (EBSD) analysis was carried out to determine the orientation relationship between bcc and fcc phases in 304LSS during

reversion annealing. The specimens were electrolytically polished for 20 s using an electrolyte of 20% $\text{C}_2\text{H}_4\text{O}_2$ (acetic acid) in 80% CH_4OH (methanol) at a temperature and voltage of -30°C and 15 V respectively. EBSD studies were performed at an operating voltage of 30 kV in a FEI Helios FE-SEM attached with an EBSD detector. The specimen was mounted on a 70° pre-tilt holder for better intensity and the working distance was maintained as 12 mm. Each scan was recorded for a time cycle of 0.1 s for better accuracy. During the EBSD scans, each pattern was matched with the available fcc and bcc crystals with various orientations. After the EBSD scans, the raw data was post-processed in detail by making use of the TEAM analysis software [127].

2.5.5 Transmission electron microscopy investigations:

For transmission electron microscopy (TEM) investigations, electron transparent 3 mm diameter thin foils were prepared by mechanical polishing followed by jet thinning using a solution of HClO_4 (10%) + CH_3OH (90%), at operating conditions of voltage 15 V, current 40 to 60 mA and temperature of -30°C . TEM studies were carried out by using a PHILIPS CM200 Analytical Transmission Electron Microscope (ATEM) at operating voltages of 160 and 200 kV. EDS analysis of the TEM specimens was carried out using a Oxford instruments make energy dispersive X-ray spectrometer. Bright Field (BF), Dark Field (DF) and Selected Area Diffraction (SAD) modes were used for obtaining images and crystallographic details. The images were acquired by a bottom mounted on axis TVIPS CCD camera with a resolution of 2048x2048 pixels. Magnification calibration was carried out by using a cross grating of 2160 lines/mm with a separation of 469 nm. Spatial resolution of 2.3 \AA was ensured by calibrating the camera length using standard nanocrystalline gold in holey carbon film. An aperture

of 10 μm size was used for obtaining the SAD patterns and DF images. Rotation of the SAD patterns with respect to magnification was calibrated using MoO_3 crystals. The SAD patterns were analyzed by ImageJ software and the patterns were matched with the standard ICDD data. For indexing the diffraction patterns the angles and d-spacings were measured with an accuracy of $<1^\circ$ and $\sim 0.2 \text{ \AA}^\circ$ respectively. TEM-EDS analysis was carried out using incident beam with a spot size of $\sim 50 \text{ nm}$ for analysis of fine features. A low background single tilt holder was used to reduce the noise due to spurious X-ray signals. In-hole spectra were collected periodically to ensure the absence of spurious X-ray sources in the microscope column.

Difficulties encountered while preparing specimens from the diffusion zone of the SS/TiTaNb explosive clads were (i) different milling rates of Fe and Ti in the dissimilar clad and (ii) brittleness of the interface. Hence, both conventional TEM and site-specific Focused Ion Beam (FIB) based sample preparation techniques were adopted. Site specific specimens were extracted from the SS/TiTaNb explosive joints annealed at 800°C for 20 h [128]. For preparing thin foils from the cross-section of the clad, specimen of dimension $10 \times 10 \times 2 \text{ mm}$ was initially polished on one side and etched to reveal the interface, then thinned from the opposite side to achieve $\sim 100 \mu\text{m}$ thickness. From this sample, 3 mm discs were extracted near the clad interface and further thinned by ion milling. For preparing TEM specimens using FIB, FE-SEM attached with Apollo X Silicon Drift Detector (SDD) was used. Various stages involved in the preparation of specimens are demonstrated in Fig. 2.6(a) to (c). To start with, a region of interest (ROI) was selected based on microstructure and microchemistry. On the ROI, a Pt metal strip of dimension $30 \times 1.5 \times 0.2 \mu\text{m}$ was deposited by electron beam deposition at a voltage and current of 5 kV and 2.7 nA, respectively. This was followed by milling of the selected

region using Ga ions to partially detach the lamella from the bulk specimen. The lamella was then spot welded to a manipulator arm and extracted from the bulk specimen. The extracted specimen was thinned by in-situ milling first at 10 kV and 9.3 nA followed by polishing at 5 kV and 41 pA to ensure electron transparency and then attached to a TEM grid for further investigation. Confirmation for various phases was obtained by SAD analysis with supporting EDS data.

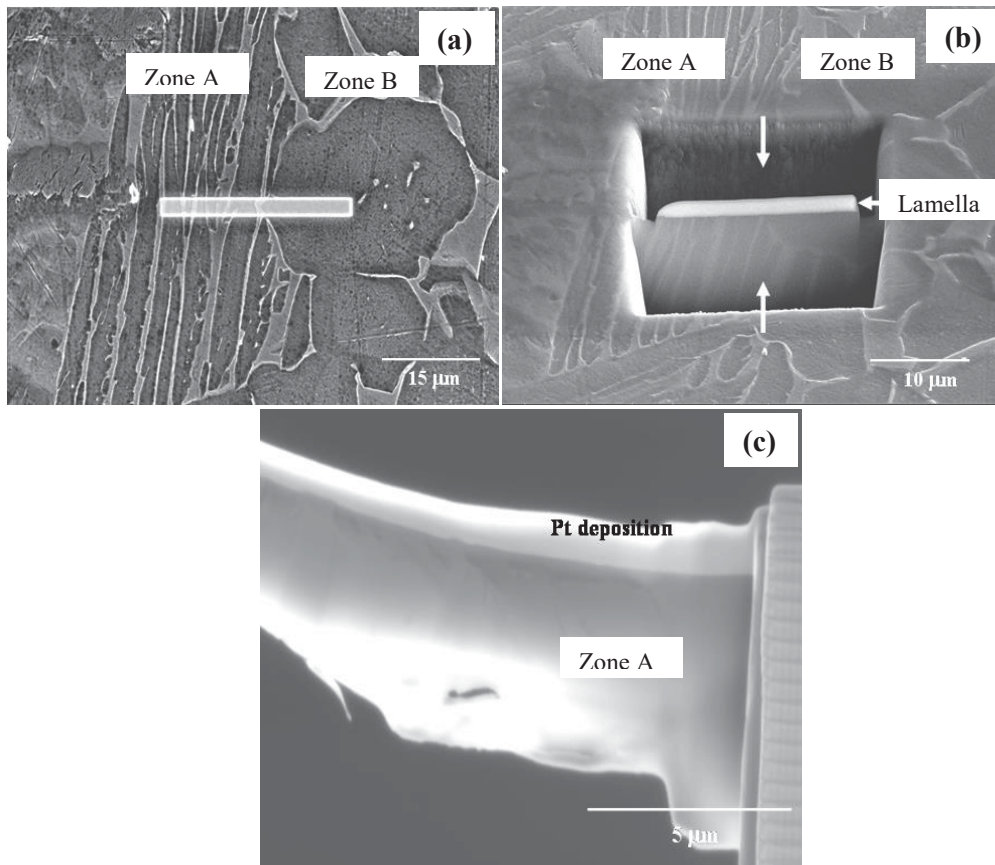


Figure 2.6 BSE images showing (a) site selection by Pt deposition for FIB-based specimen preparation, (b) trenches formed (arrow marked) due to Ga ion milling on either side of the lamella and (c) specimen lifted out using in-situ manipulator, to be further thinned for TEM analysis

2.6 Evaluation of growth kinetics of the diffusion zones and interdiffusion parameters:

Diffusion controlled growth of the reaction zone as a function of annealing time can be expressed by the following equation (2.5) [90, 129]:

$$K_p = \frac{X^2}{2t} \quad (2.5)$$

where, 'X' and 'K_p' are the width of the diffusion zone (μm) and parabolic growth constant (m²/s) respectively. Diffusion annealing time is represented by 't' (s). Further, the temperature dependence of the growth constant follows Arrhenius relation which can be expressed as:

$$K_p = K_0 \exp(-Q / RT) \quad (2.6)$$

where, 'T' is the annealing temperature (K), 'R' is the ideal gas constant (8.314 J/mol K) and 'K₀' and 'Q' represents the pre-exponential factor (m²/s) and activation energy (kJ/mol) for growth of the diffusion zone.

2.6.1 Estimation of interdiffusion parameters:

Elemental concentration profiles obtained by EPMA were initially smoothened for the determination of concentration dependent interdiffusion coefficients ($D(C)$). Figure 2.7 is a flow chart showing the procedure adopted for the determination of $D(C)$ values in the present research work. The $C_i^{-\infty}$ and $C_i^{+\infty}$ values for Fe, Ti and C are the average values of the end member composition. As described in the Section 1.5.3, for estimating the average effective interdiffusion coefficients in Fe-C-Ti system over a defined composition range the following equation given by Dayanada was used [130].

$$\tilde{D}_{i,\Delta C}^{Eff} = \frac{\int_{x_1}^{x_2} \tilde{J}_i dx}{C_i(x_1) - C_i(x_2)} \quad (2.7)$$

where, $i=1,2,\dots,n$ is the number of components and ' \tilde{J}_i ' is the flux of diffusing component 'i'. ' x_1 ' and ' x_2 ' are defined as the position coordinates over the composition ranges of interest.

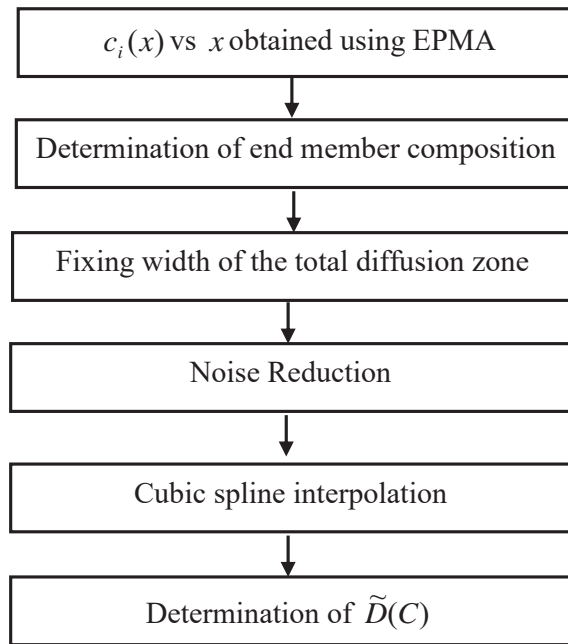


Figure 2.7 Flow chart showing the procedure adopted for determining $D(C)$ values in the present research work

For the evaluation of interdiffusion coefficients in 304LSS/TiTaNb system, it was assumed that Fe and Ti were alone the diffusing species and the interdiffusion between these two elements was not influenced by the diffusion of other alloying elements. Therefore, conventional DB [85] method was employed to evaluate the interdiffusion coefficients using error function like profiles of Fe and Ti obtained at low temperatures. The relative concentration variable (‘ ψ ’) introduced in the DB method can be expressed as:

$$\psi = \frac{c(x) - c^{-\infty}}{c^{-\infty} - c^{+\infty}} \quad (2.8)$$

where, ‘ $c(x)$ ’ is the concentration at any abscissa ‘ x ’ and ‘ t ’ is diffusion annealing time. The $D(C)$ value at any position coordinate ‘ x ’ can be determined using the following relation proposed by DB [85, 86].

$$D(C) = \frac{1}{2t} \left(\frac{dx}{dc} \right) \left\{ (1 - \psi) \int_{-\infty}^x (c(x) - c^{-\infty}) dx + \psi \int_x^{+\infty} (c^{+\infty} - c(x)) dx \right\} \quad (2.9)$$

In the present study, this method was used for determining $D(C)$ values for Fe and Ti using the concentration profiles obtained across SS/TiTaNb joints heat treated at 550 and 600 °C, where nature of the profiles resembled error function profiles. Considerable redistribution of the alloying elements at temperatures ≥ 700 °C, suggested the formation of intermetallic and secondary phases at the interface [128]. Therefore, it was expected for an appreciable variation in the molar volume during the course of interdiffusion. Hence, well known Wagner’s [92] method (equation (2.10)) was employed to estimate the molar volume dependent interdiffusivities in regions with narrow homogeneity range.

$$D(C) = \frac{N^{+\infty} - N^{-\infty}}{2t} \left(\frac{V(c)}{\partial c / \partial x} \right) \left\{ (1 - \psi) \int_{-\infty}^x \left(\frac{\psi}{V_m} \right) dx + \psi \int_x^{+\infty} \left(\frac{1 - \psi}{V_m} \right) dx \right\} \quad (2.10)$$

In the above, ‘ $V(c)$ ’ is the concentration dependent molar volume of particular phase while ‘ V_m ’ is average molar volume of the element of interest. Wagner has considered normalized atom fraction ‘ N ’ as a function of position variable ‘ x ’ where ‘ $N^{+\infty}$ ’ and ‘ $N^{-\infty}$ ’ are the atom fractions in end members.

To calculate the impurity diffusion coefficients of Fe in Ti/TiTaNb Hall’s method was employed [131] using the analytical equation given below:

$$D(c) = \frac{1}{4h^2} + \frac{k \Pi^{1/2}}{2h^2} \exp(u^2) \operatorname{erfc} u \quad (2.11)$$

where, ‘ h ’ and ‘ k ’ represent the slope and intercept of the probability plot drawn between $\lambda(xt^{-1/2})$ and $u(h\lambda + k)$. Before, employing the Hall’s method linearity of the probability curve between ‘ λ ’ and ‘ u ’ was monitored over the defined composition range. Table 2.7 summarises various methods used in the present thesis for the determination of interdiffusion coefficients.

Table 2.7 List of various methods used for calculation of the $D(C)$ values

System	Diffusing system	Nature of the concentration profiles	Method used	Reference
SS/TiTaNb	Fe-Ti	Error function	Den Broeder	[85]
		Step like	Wagner	[92]
	Fe-Cr-Ti	Error function	Dayananda	[130]
MS/Ti	Fe-C-Ti	Error function	Dayananda	[130]

2.7 Prediction of phases and computation of bond strength using JMatPro®:

A materials modeling software namely JMatPro® (version 6.2) [132] was used for the prediction of phases that would form in Fe-Ti based joints in ‘as-welded’ condition as well as on thermal exposure. Microchemical data obtained using EPMA was used as the input to predict the probability of formation of various phases. In the present research work, JMatPro® simulation was carried out to predict the phases in MS/Ti friction and explosive joints as well as in SS/TiTaNb explosive joints [120, 128, 133]. Experimental studies showed these phases have a detrimental effect on the bond strength of the joint interface [25, 27]. With the information available on type and mole fraction of phases across the diffusion zone, an attempt was made to predict the consequential variation in Ultimate Tensile Strength (UTS) of the joints. Before implementing this approach, UTS values for the parent metals namely mild steel, SS, Ti and TiTaNb alloy were estimated and compared with that of experimental data. In addition to the grain size, estimated volume fraction of phases was used to fix the simulation conditions. A reasonable agreement between computations and experimental values enabled the extension of this approach to the diffusion zones of the weldments. Due to the formation of distinct phases in the diffusion zone of Fe-Ti weld joints a direct correlation between microstructure and mechanical property was difficult. However, a methodology established to estimate the variation in mechanical property across the joint interface helped in understanding the effect of various reaction products. Although JMatPro® computations considered the influence of composition, grain size and mole fraction of various phases on mechanical property, other contributory factors like microstructure, presence of lattice defects and existence of local stresses due to

difference in thermal expansion of various phases within a multi phase region were not considered.

2.8 Diffusion of Fe in hcp Ti lattice - Molecular Dynamics Simulations:

Diffusion of a single Fe atom in hcp Ti lattice was computed in two different conditions of (i) defect free lattice and (ii) introducing point and line defects in the lattice. Simulations were performed using Molecular Dynamics (MD) on Large-scale Atomic/Molecular Massively Parallel Simulator (LAMMPS) platform. Modified Embedded Atom Method (MEAM) potentials, derived by Sa et al. [111] were used for carrying out the MD simulations.

In MD simulations the time dependent position and velocity coordinates of atoms were determined by solving Newton's classical laws of motion and the force ($F(r)$) acting between any two atoms is obtained from the interatomic potential as shown below [103]:

$$F(r) = -\left(\frac{\partial}{\partial r}\right)[U(r)] \quad (2.12)$$

where, 'U(r)' is the total potential energy function which can be further split into 1-body, 2-body and many body interaction terms. In MEAM potential formalism, the total energy (E_{tot}) of the system can be expressed by a relation shown below [109]:

$$E_{tot} = \sum_i \left[F_i(\vec{\rho}_i) + \frac{1}{2} \sum_{j(i \neq j)} S_{ij} \phi_{ij}(R_{ij}) \right] \quad (2.13)$$

where ' $\vec{\rho}_i = \sum_j \rho(r_{ij})$ ' is the electron density of an atom j at the position of atom 'i', ' $F_i(\vec{\rho}_i)$ ' is the embedding energy function which depends on the electron density distribution at site 'i' due to all other neighboring atoms, ' $\phi_{ij}(R_{ij})$ ' is the

pair potential term between the atoms separated by a distance ' R_{ij} ' and the summation is taken over all the atoms. The screening parameters ' S_{ij} ', ' $\phi_{ij}(R_{ij})$ ' were considered in such way to include the effect of interactions of second nearest neighboring atoms (2NN) also.

In the present thesis, the simulation lattice was considered as hcp Ti with lattice constants of $a=2.94 \text{ \AA}$ and $c=4.64 \text{ \AA}$. Dimension of the super cell (or the simulation matrix) was assumed as $10 \times 10 \times 10$ which corresponds to 10 hcp Ti unit cells lying in each coordinate axis. A single Fe atom with bcc as the reference structure with lattice constant of 2.88 \AA was randomly inserted in the Ti lattice. Super cell was allowed to relax for 10 ps in an NPT (volume, pressure and number of atoms assumed to be constant) ensemble. However, to eliminate the external stresses during the diffusion of substitutional Fe atom it was essential to carry out NVE (constant volume, energy and number of atoms) integration instead of NPT assuming the system to be in micro canonical ensemble. Simulations were carried out for 100 ps in the canonical ensemble in the temperature range of 500-900 °C with an interval of 100 °C. Periodic boundary conditions were applied to the super cell, in such a way that, whenever an atom leaves the super cell, the vacancy created will be filled by another atom from the preceding cell and the total number of atoms in the super cell remains constant throughout the simulation. Diffusion of the atoms was initiated by providing certain initial velocity according to Maxwell distribution. After fixing the computational parameters, the MEAM potentials were validated by estimating the cohesive energy, bulk modulus, two shear constants and melting points. For solving the force integrals, Velocity Verlet logical algorithm was used to calculate the atomic positions from the previous and current time steps. Atomic

trajectories were traced from the time of evolution of atomic positions and velocity coordinates. Using these trajectories transport properties such as diffusion coefficients and activation energies were estimated. The simulations were further extended to monitor the diffusion of Fe atom in hcp Ti lattice by introducing point and line defects. Point defects such as vacancies were created in Ti by random removal of atoms from their lattice positions while dislocations were created by deleting half plane of atoms from the centre plane of hcp lattice.

2.9 Summary:

The salient features of this chapter on “**Experimental and Computational methods**” are summarized as follows:

- Welding procedure and parameters adopted to join mild steel and Ti by friction and explosive joining methods were identified.
- Similarly, explosive cladding parameters for joining of 304LSS/Ti-5Ta-2Nb alloy were also identified.
- Operating conditions in using various characterization techniques such as SEM, XRD, EBSD and TEM were elaborated.
- Spectroscopy by EDS and WDS attached to EPMA was explained in detail.
- Distinct analytical methods adopted for estimation of interdiffusion parameters in SS/TiTaNb and MS/Ti systems was explained.
- Computational techniques namely JMatPro[®] and Molecular dynamics were described in detail.

Chapter 3

**Microstructure and property evaluation
in Fe-C/Ti friction and explosive joints in
'as welded' and heat treated conditions**

3.1 Introduction:

Fe and Ti based dissimilar joints are of industrial importance due to their application in various industries and more specifically in the spent nuclear fuel reprocessing plant of fast breeder reactors [1]. Hence, assessment of the weldability and microstructural stability of Fe and Ti joints is of paramount importance for the safe and efficient operation of the plant. Joining of metallurgically incompatible Fe and Ti by conventional fusion welding methods poses difficulties due to the formation of FeTi and Fe₂Ti type intermetallic phases and β Ti phase leading to embrittlement of the weld interface [14]. In view of this, several solid state welding techniques like diffusion bonding, friction welding, friction stir welding and explosive cladding are being employed. The conditions of pressure, temperature and stress employed during the joining process introduce changes in the microstructure, defect structure and microchemistry of the parent metals. A knowledge of these changes is essential to optimize the joining conditions as well as to assess the performance of the joints during service. In order to obtain a fundamental understanding on the role of defects and alloying elements on the interdiffusion behaviour under equilibrium and non-equilibrium conditions, a Fe-Ti based system has been taken up for study in two cases. In the first case the diffusion characteristics were studied in a joint fabricated by friction welding to just establish a bonded interface followed by diffusion annealing, and in the second case the joints were fabricated by explosive cladding process (non-equilibrium) followed by diffusion annealing and the interdiffusion characteristics were compared. Due to constraints in obtaining large plates of high pure iron required for the

fabrication, the joints were fabricated with iron containing 0.14 wt.%C (Mild steel) and Grade 2 Ti.

This chapter presents the results on the evolution of interface microstructure and microchemistry under equilibrium and non-equilibrium conditions in the MS/Ti joint. Further, post welding heat treatments were optimized with an aim to control the formation of intermetallic phases at the joint interface. The chapter is organised in the following sequence: Characterization of MS and Ti plates in 'as received' condition is described in section 3.2. Section 3.3 deals with the study on feasibility of fabricating diffusion couples of MS and Ti with defect and intermetallic free interface. Section 3.4 describes the optimization of processing parameters and fabrication of friction joints. Further, an in-depth characterization of microstructure and microchemistry in MS-Ti friction welds fabricated with optimum welding parameters is also elaborated in section 3.4. Section 3.5 describes the results of optimization of the post weld heat treatments based on the evolution of interface microstructure and bond strength of the friction welds. Section 3.6 deals with the evolution of interface microstructure during diffusion annealing treatments at elevated temperatures. Section 3.7 describes the fabrication of explosive clads and selection of optimum load ratio, in-depth characterization on structural changes in base, flier plates and interface of the clads. Sections 3.8 and 3.9 deal with the optimization of the post clad heat treatments and structural changes in the clads on long term thermal exposure at elevated temperatures. The important findings of this chapter are summarized in section 3.10.

3.2 Characterization of ‘as received’ mild steel and Grade 2 Ti plates:

Figures 3.1(a) and (b) show the secondary electron (SE) image and X-ray diffraction (XRD) pattern of the MS in the ‘as received’ condition. As expected, the structure of MS consisted of both ferrite and pearlite ($\alpha + \text{Fe}_3\text{C}$) phases and the average hardness was measured as 154 ± 5 HV. The bright phase in the SE image (Fig. 3.1(a)) corresponds to pearlite. The XRD pattern confirmed presence of α – ferrite (Fig. 3.1(b)) phase. The SE image and XRD pattern of Ti is shown in Figs. 3.2(a) and (b) respectively. Presence of equiaxed grains with an average hardness of 210 ± 7 HV corresponds to a well annealed structure of Ti (Fig. 3.2(a)).

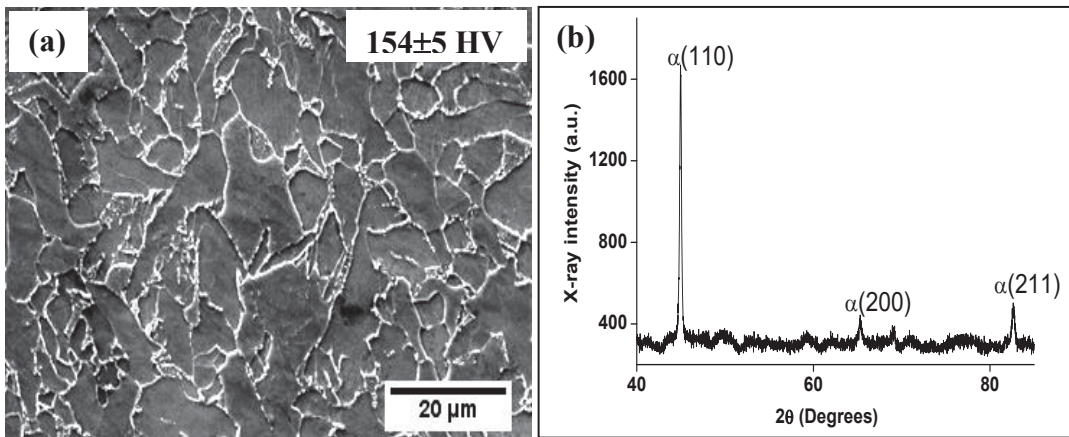


Figure 3.1 (a) Secondary electron (SE) image with superimposed hardness value and (b) XRD pattern of mild steel in ‘as received’ condition

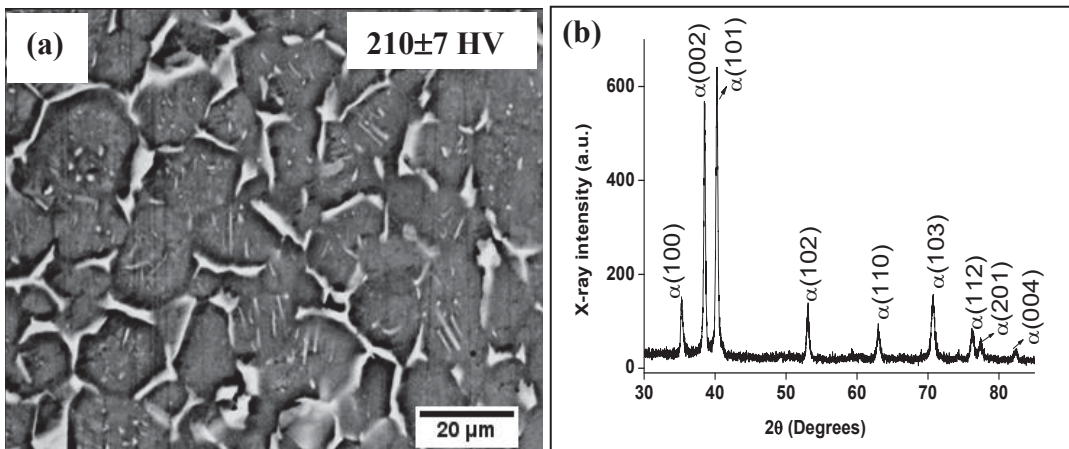


Figure 3.2 (a) SE image with superimposed hardness value and (b) XRD pattern of Ti in ‘as received’ condition

Analysis of the XRD pattern (Fig. 3.2(b)) confirmed the presence of hcp (α) phase of Ti. The chemical composition and mechanical properties of the plates are listed in Table 2.1 and Table 2.2 respectively.

3.3 Interface microstructure in diffusion couples of MS and Ti:

Fabrication of diffusion bonded MS-Ti joints is a challenge due to (i) limited mutual solubility of Fe and Ti [7], (ii) large difference in their coefficients of thermal expansion (Fe: 12 $\mu\text{m/m/K}$ and Ti: 8.6 $\mu\text{m/m/K}$) [8], (iii) tendency for formation of brittle intermetallic phases at the interface and (iv) formation of thick oxide scales. The approach adopted in literature was to initially form a bonded interface between Fe and Ti through the application of both high temperature (800-950 $^{\circ}\text{C}$) and pressure (3 MPa for 0.5 to 1.5 h) in a diffusion bonding set up followed by diffusion annealing heat treatments [26]. However, formation of a continuous layer of intermetallic phases parallel to the joint interface could not be avoided even under optimized experimental conditions [24-28].

As a part of the present research work, feasibility of joining MS and Ti by diffusion coupling technique was explored. Specimen preparation and fabrication details were explained in section 2.2.1 of Chapter 2. BSE image of the interface of MS/Ti couple is shown in Fig. 3.3(a). A modified layer with dark contrast of width $\sim 20\ \mu\text{m}$ was observed at the interface. The XRD pattern (Fig. 3.3(b)) from the cross-section showed strong Bragg reflections for FeTi, Fe₂Ti intermetallic phases and δTiO phase in addition to the parent phases. This poses problems in studying the diffusivities of elements in solid solutions which is the main objective of the investigation. It is therefore obvious that the attempt to join the two metals by conventional diffusion

couple experiments was not successful due to the formation of intermetallic phases and thick oxide layers at the interface. Therefore, friction welding process was employed to obtain a good joint between MS and Ti and change in interface microstructure was studied through diffusion annealing treatments.

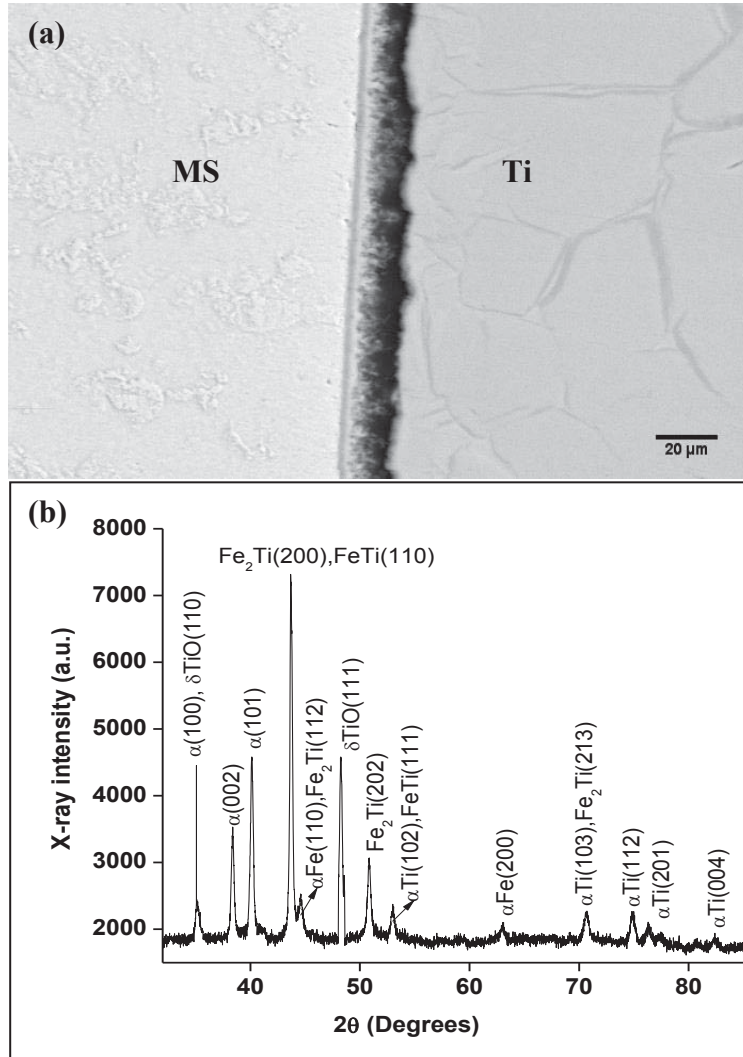


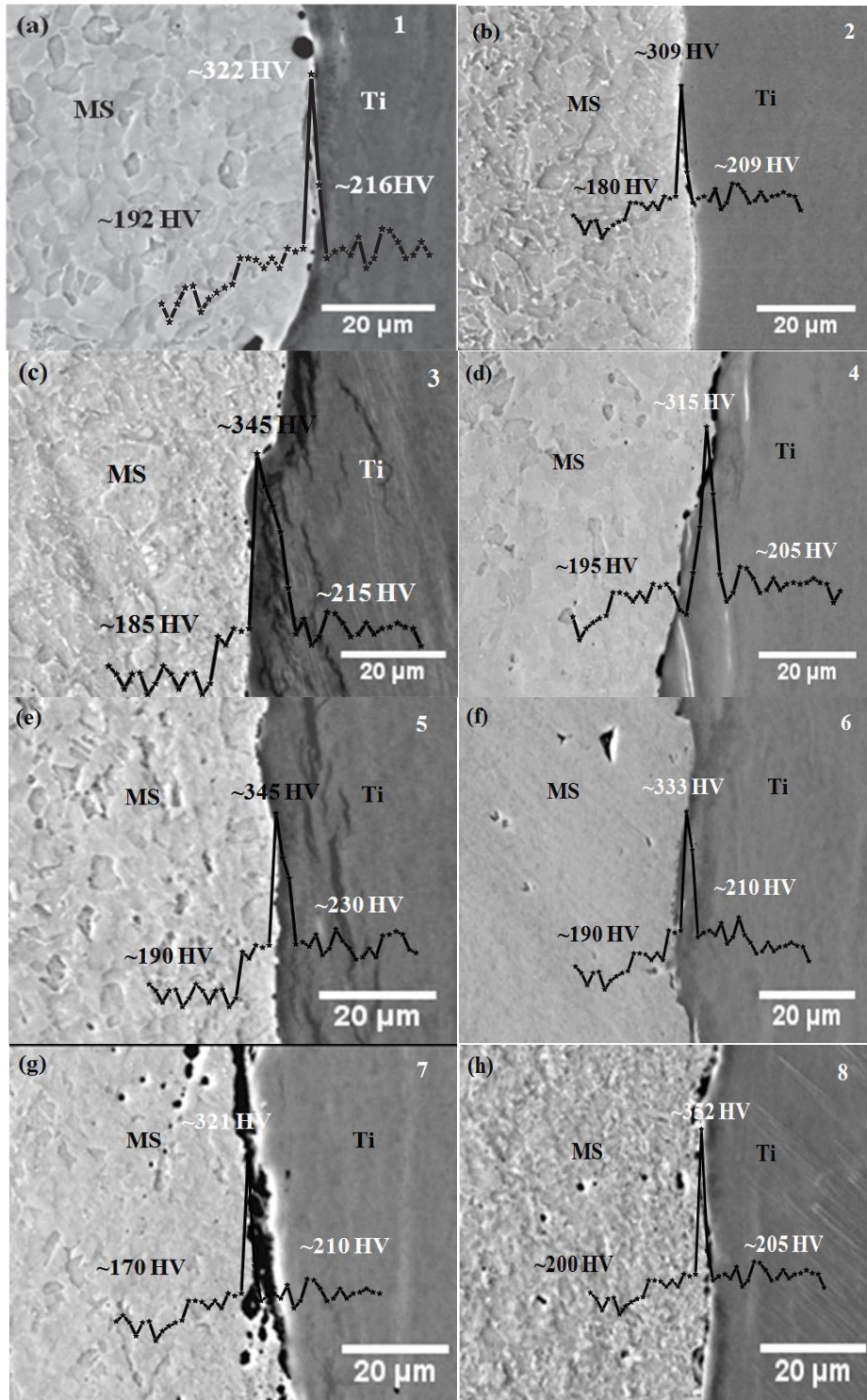
Figure 3.3 (a) Back scattered electron image of diffusion coupled MS-Ti joint and (b) XRD pattern obtained from the cross-section specimen showing evidences for the formation of secondary phases and δ TiO at the interface

3.4 Optimization of friction welding parameters and fabrication of joints:

3.4.1 Variation of welding parameters in trial welds:

The choice of friction welding to obtain a bonded interface between MS and Ti, is based on the fact that it involves no melting of the base metals unlike fusion welding techniques, and further employs low temperatures unlike diffusion bonding process [134]. Friction welding is a promising solid state welding technique where joints with adequate bond strength could be obtained by appropriate selection of process parameters [8, 45, 46]. To arrive at optimum conditions, eight trial welds were fabricated by changing friction force (FF), upset force (UF), burn off length (BOL) and rotational speed (r) as listed in Table 2.3.

BSE images obtained from these cross-sections are shown in Figs. 3.4(a) to (h) with the corresponding microhardness profiles superimposed. Optimization of the parameters was made by monitoring the change in microstructure and average hardness values of base metals in comparison to starting materials and the interface microstructure for irregularities and pores. The variation in hardness was observed to be higher for MS than Ti in all cases. Signatures of deformation were observed on the Ti side of the joint up to a distance of $\sim 50\text{ }\mu\text{m}$ from the interface. Porosities were predominant when the rotational speeds were increased beyond 1000 rpm (Fig. 3.4(c) and (g)). The average hardness at the interface was maximum ($\sim 352\text{ HV}$) for the weld fabricated using the highest FF, UF and BOL = 2 mm (Fig. 3.4(h)). The microstructure in Fig. 3.4(b) shows absence of porosities, no deformation on Ti side and relatively low increase in hardness ($\sim 309\text{ HV}$) at the interface, which is a desirable structure.



Figures 3.4 (a) to (h) BSE images from cross section of the friction welds fabricated with different welding parameters (for the number at the right corner of each image refer Table 2.3)

This weld joint corresponds to parameters of FF = 0.8 tonnes, UF = 1.6 tonnes, BOL = 3 mm and $r = 1000$ rpm [133]. Hence, these parameters were considered as optimum and have been used for fabrication of welds for detailed characterization and evaluation of mechanical properties, which are described in the subsequent sections.

3.4.2 Evolution of interface microstructure in friction joints:

Figure 3.5 shows the BSE image of the MS/Ti friction joint fabricated with optimized parameters. It is evident from the figure that the interface is free from weld defects such as pores and irregularities. Elemental concentration profile obtained across the friction joint is superimposed on the micrograph. Smoothly varying concentration profiles of Fe and Ti gave no indication for the formation of any secondary phase at the interface. At the cross over point the concentration of elements was corresponded to FeTi type intermetallic phase [135]. Diffusing distances for Fe and Ti were estimated to be $\sim 2 \mu\text{m}$ on either side of the interface. These concentration values were used as input to predict the phases that formed at the interface using JMatPro[®] software.

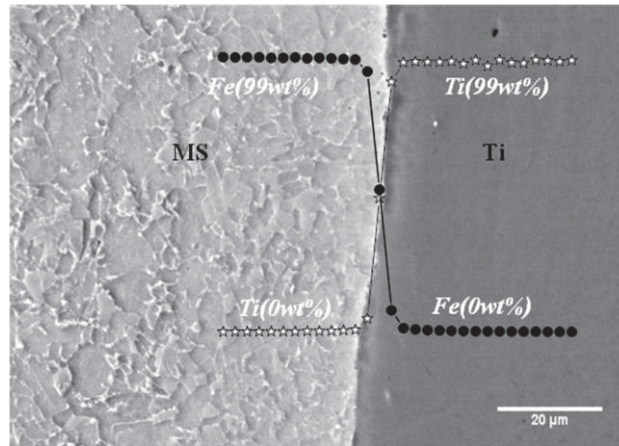


Figure 3.5 BSE image of the MS/Ti friction joint fabricated with optimized welding parameters; corresponding composition profile is superimposed

To validate the conditions for simulation, the room temperature phases and UTS values of MS and Ti base metals were initially computed. Table 3.1 lists the volume fraction of phases and the UTS obtained using JMatPro[®] for MS and Ti, which showed a close match with the experimental values. This method was extended to predict the phases and bond strength of the interface using the EPMA data input, which are also presented in Table 3.1. Simulations showed coexistence of α Fe+FeTi+TiC phases at the interface which was supported by high value of hardness (~309 HV) and UTS values (~670 MPa). XRD pattern obtained from the cross-section of MS/Ti joint (Fig. 3.6) showed strong reflections for the parent phases (bcc-Fe and hcp-Ti). In addition, Bragg reflections were observed at 2θ positions of 43.5° and 62.5° which correspond to (110) and (200) planes of FeTi phase.

Figure 3.7 shows a typical TEM bright field (BF) image obtained from the interface region of the friction weld. Isolated regions of different contrast were observed in the micrograph (dotted circles in Fig. 3.7(a)). These regions consisted of few fine sized particles ranging from 20 to 50 nm (Fig. 3.7(b)).

Table 3.1 Comparison of the experimental and predicted values of UTS

Region	Volume fraction of phases	UTS (MPa)	
		Experimental	Predicted
MS	Ferrite-0.98 α +Fe ₃ C-0.02	445	479
Interface	Ferrite-0.6 FeTi-0.3 TiC-0.1	--	670
Ti	α Ti-1	325	334

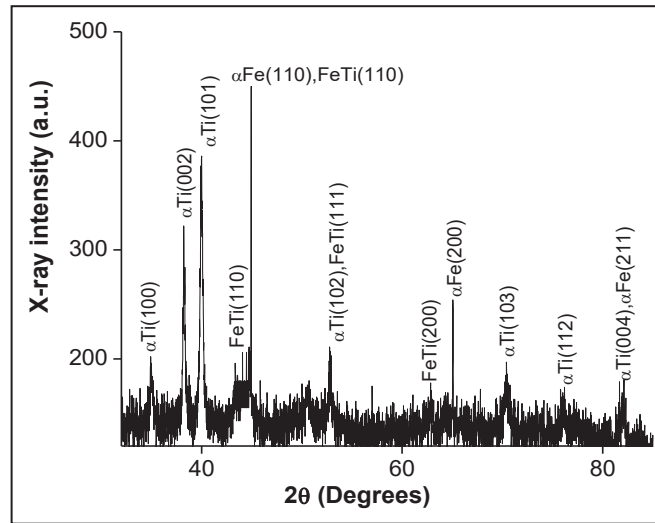


Figure 3.6 XRD pattern obtained from cross section of the MS/Ti friction joint

The SAD pattern obtained from one such region is shown in Fig. 3.7(c). Analysis of the electron diffraction pattern revealed overlapping ring and spot patterns along $[\bar{1}11]$ and $[\bar{1}12]$ zone axis for FeTi and bcc-Fe respectively which confirmed the prediction of FeTi intermetallic phase in MS/Ti joints [133]. Presence of fine intermetallic phase in isolation is in contrast to its formation as a continuous zone along the interface in diffusion bonded joints which could result in severe degradation of the bond strength [25, 27]. Although, temperature is not a variable parameter, the high strain produced at the contact surfaces during friction welding leads to increase in temperature in localized regions [118, 136] which in turn lead to interdiffusion of alloying elements, resulting in the formation of intermetallic phases. The observation of fine particles (≤ 50 nm) of intermetallic phases embedded in bcc-Fe matrix in isolated regions is attributed to the higher intrinsic diffusivity of Ti ($D_{Ti}=5.5 \times 10^{-14}$ m²/s at 900 °C) as compared to α -Fe

($D_{Fe} = 5 \times 10^{-15} \text{ m}^2/\text{s}$ at 900°C) [23]. These simulations showed coexistence of $\alpha + \text{FeTi} + \text{TiC}$ phases at the interface and the corresponding UTS value was computed as $\sim 670 \text{ MPa}$. Although, the UTS value was higher than that of the reported values [46, 137] it is very essential to monitor the bend ductility of the joints.

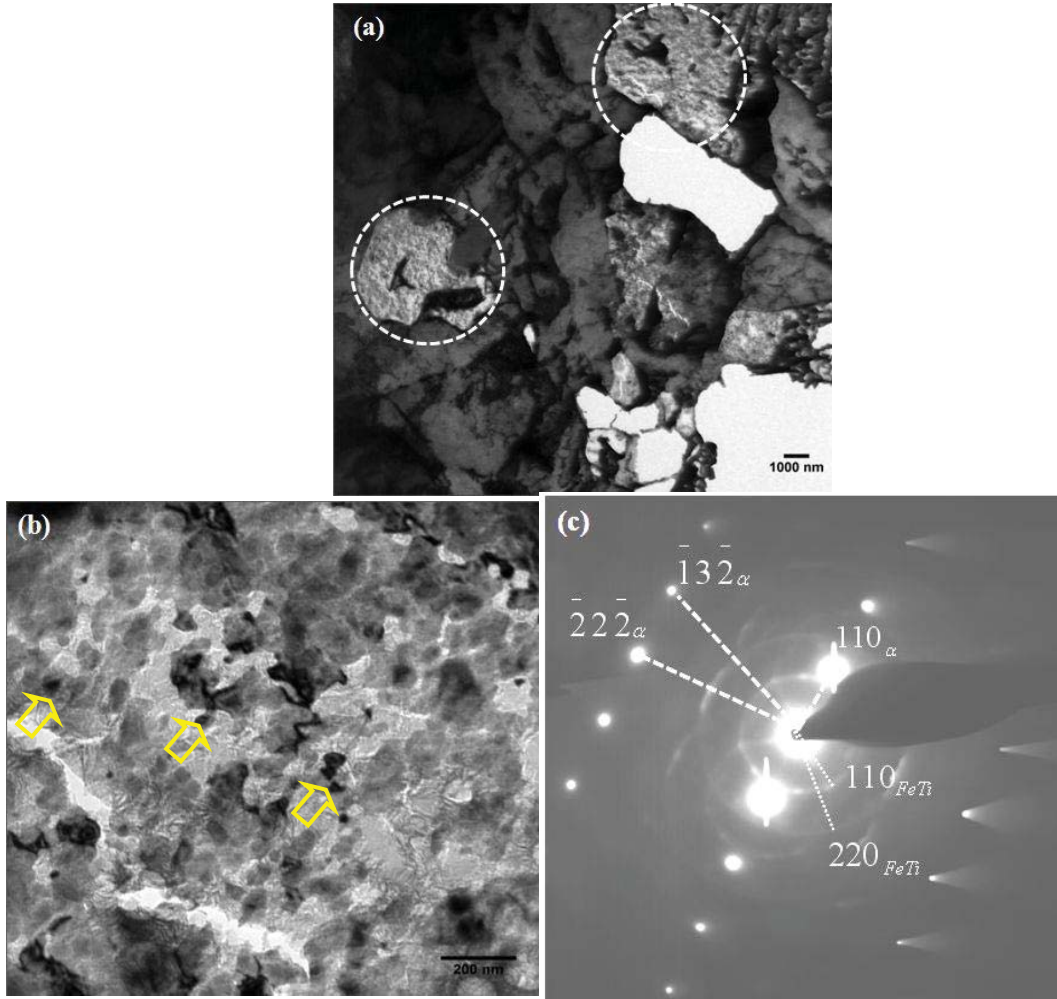


Figure 3.7 TEM bright field (BF) images obtained from the MS/Ti friction joint interface showing (a) isolated regions (shown by dotted circle) with different contrast, (b) presence of fine particles of nm size (arrow marked) in a magnified view of the isolated region circled in panel ‘a’ and (c) SAD pattern showing overlapping reflections from both bcc-Fe and FeTi phase along $[\bar{1}12]$ and $[\bar{1}11]$ zone axis respectively.

In a similar study, Dey et al. [8] reported zero bend ductility for 304LSS/Ti friction joints in spite of failure in the base metal region during tensile testing due to presence of large strain hardening and residual stresses. Residual stresses are generally present in friction joints and a maximum residual stress of the order of ~241 MPa was reported in 430 ferritic steel/austenitic steel friction joints [138]. Therefore, PHWTs are recommended for Fe-Ti friction joints to remove the residual stresses and to increase the ductility of the welds.

3.5 Optimization of post weld heat treatments for friction joints:

3.5.1 Phase evolution – simulated at different temperatures:

In the present study the friction joints were exposed to temperatures of 500 °C and 600 °C for various durations ranging from 1-20 h. The variation in microchemistry across the interface was analysed using EPMA, which was given as an input to JMatPro[®], to predict the phases that form at the interface. Figures 3.8(a) to (d) show the plot of mole fraction (X) of the phases computed across the interface at the two temperatures for durations of 1 and 20 h. At 500 °C for 1 h duration, in addition to the parent phases, intermetallic Laves (Fe₂Ti) phase with a 'X' of 0.3 was predicted exactly at the interface (Fig. 3.8(a)) whereas at a duration of 20 h, Fe₂Ti, FeTi intermetallic phases with a 'X' of 0.3 were also predicted at the interface. Very close to the interface on MS side (~1 µm), the formation of austenite phase was predicted, which can be attributed to the stabilization of fcc phase of Fe due to diffusion of carbon [135]. As the temperature was increased to 600 °C (1 h), the diffusion zone consisting of Laves phase (X_{Fe₂Ti}=0.3) extended up to a distance of ~4 µm. A high 'X' of TiC (0.5) was also predicted on Ti side (Fig. 3.8(c)). At 20 h duration, JMatPro[®] predicted the coexistence

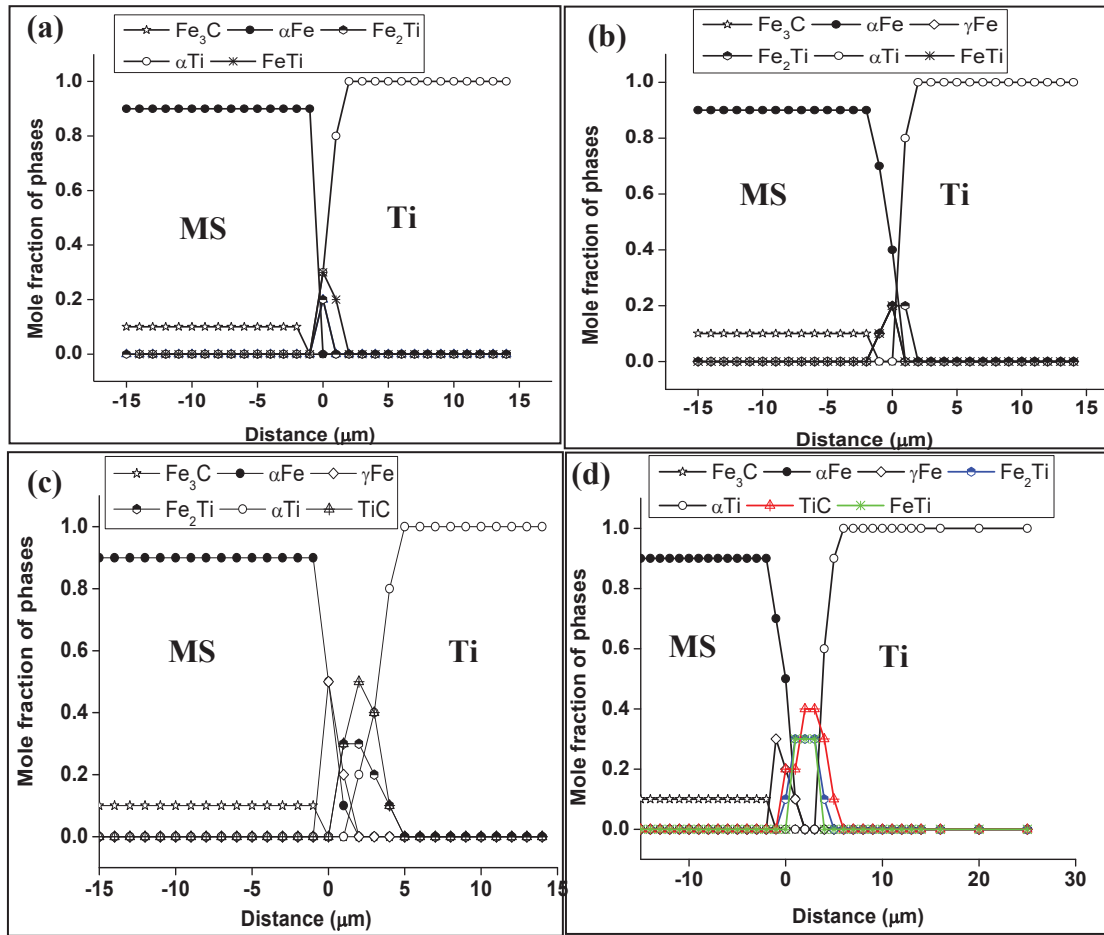


Figure 3.8 JMatPro® predicted mole fraction of the phases across MS/Ti friction joint heat treated at (a) 500 °C - 1 h, (b) 500 °C - 20 h, (c) 600 °C - 1 h and (d) 600 °C - 20 h respectively

of FeTi, Fe₂Ti and TiC phases with fractions of 0.2, 0.3 and 0.5 respectively for a distance of ~3 μm along the interface. The total width of the diffusion zone was ~6 μm.

It is evident from the above results that heat treatment at temperatures ≥600 °C led to formation of intermetallic and secondary phases such as TiC.

In order to understand the effect of secondary phases on bond strength of the interface, JMatPro® simulations were carried out at temperatures of 500 and 600 °C. Further the calculations were extended to 800 °C. Variation in the UTS was computed using the above information on phase fractions across the joint interface. Figures 3.9(a)

and (b) show the UTS values at temperatures of 500, 600 and 800 °C (for time = 1 h) plotted as a function of distance across the interface. The UTS value of the interface was obtained as 496 MPa at 500 °C which agreed well with the reported value of ~460 MPa for SS/Ti friction welds at 500 °C [54]. A similar behavior was observed for the joints heat treated at 600 °C also. However, at this temperature the UTS value showed a reduction to ~270 MPa (Fig. 3.9(a)). Further, increase in the temperature to 800 °C, the UTS value of interface reduced drastically to a value of ~110 MPa (3.9(b)), and the reason was attributed to the coexistence of intermetallic FeTi and Fe₂Ti phases.

3.5.2 Variation in the microstructure during thermal exposure:

Detailed JMatPro[®] computations indicated a decrease in the bond strength of the friction joints as a consequence of formation of intermetallic phases at temperatures ≥ 600 °C. Therefore, the joints were annealed at 500 and 600 °C for durations ranging from 1 to 20 h to optimize the post weld heat treatments for the MS/Ti friction joints.

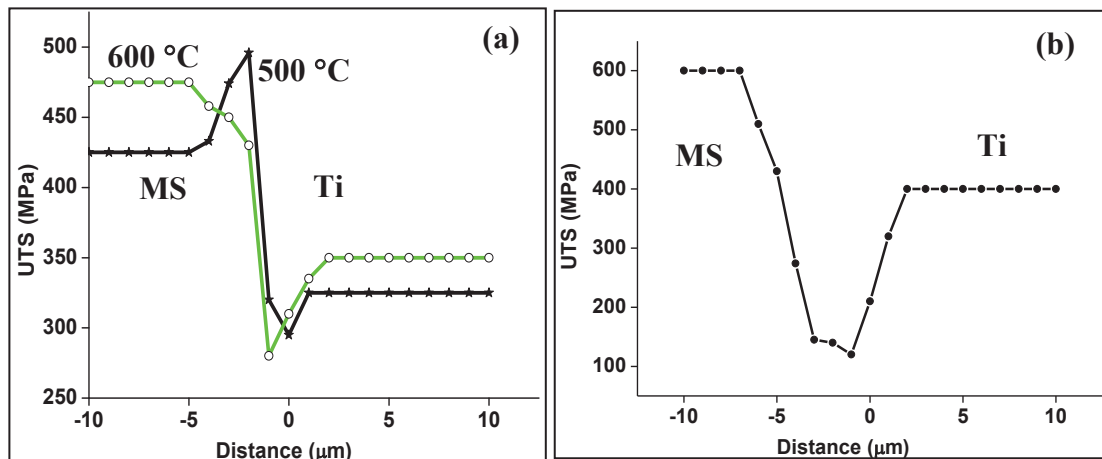


Figure 3.9 Predicted bond strength of the friction joints heat treated at (a) 500 °C, 600 °C and (b) 800 °C respectively

Figures 3.10(a) to (d) show the BSE images of the interface annealed at 500 °C for 1, 5, 10 and 20 h with superimposed hardness profiles. No significant variation in the microstructure could be seen at the interface with increasing duration of exposure. However, the interface hardness showed a small decrease with increase in duration, probably due to the relief of residual stresses. MS exhibited a high hardness of ~220 HV (as against 150 HV in ‘as received’ state), which decreased gradually with duration of exposure and reached a value of ~190 HV after 20 h (Fig. 3.10(d)).

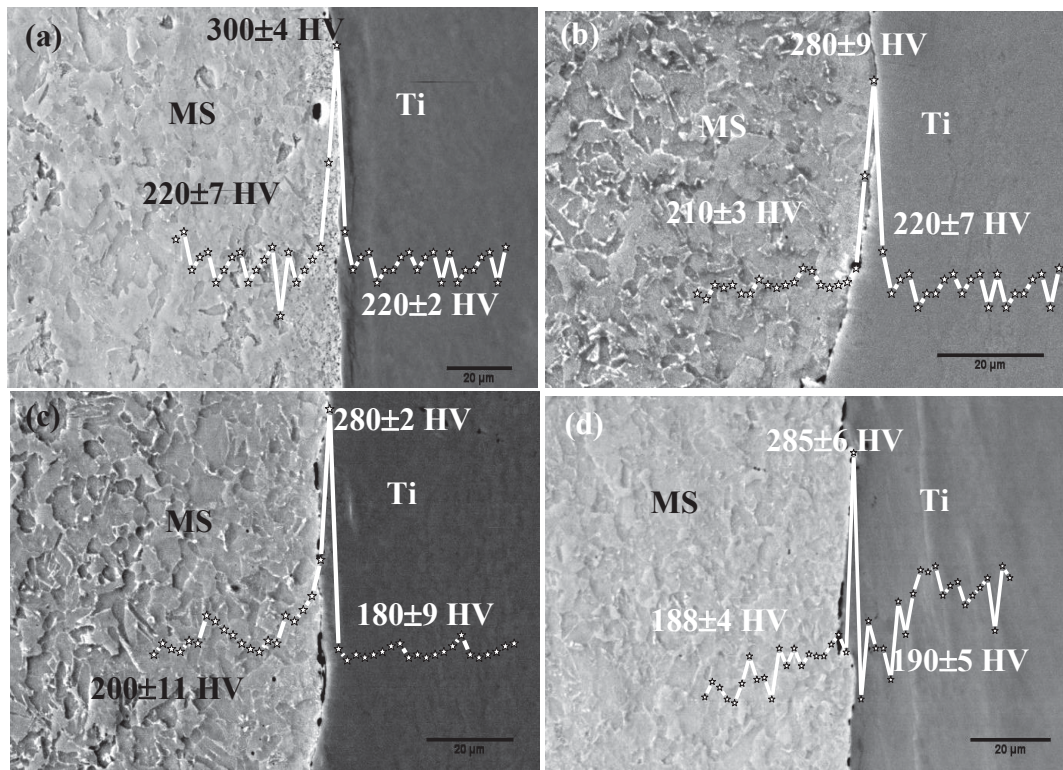


Figure 3.10 BSE images showing the interface microstructure of MS/Ti friction joints heat treated at 500 °C for duration of (a) 1, (b) 5, (c) 10 and (d) 20 h respectively; microhardness profiles are superimposed on the micrograph

The change in the interface microstructure at 600 °C for all durations is shown in Fig. 3.11. At this temperature, exposure for short durations (≤ 5 h) did not result in significant changes (Fig. 3.11(a) to (c)) in the microstructure as well as microhardness values. Beyond 10 h, formation of a ~ 0.6 μm wide dark band was observed at the interface. For all durations of exposure, the average hardness of the interface was within 280-290 HV while the difference was significant for MS and Ti. Although, the microstructure did not indicate the formation of intermetallic phases, JMatPro[®] computations did show the formation of FeTi and Fe₂Ti intermetallic phases at 600 °C even for 1 h duration, due to which the bond strength reduced noticeably. Thus, the computations validated by experiments helped to narrow down the temperature window for the post weld heat treatments as $500\text{ }^{\circ}\text{C} \leq T < 600\text{ }^{\circ}\text{C}$ for durations not exceeding 10 h.

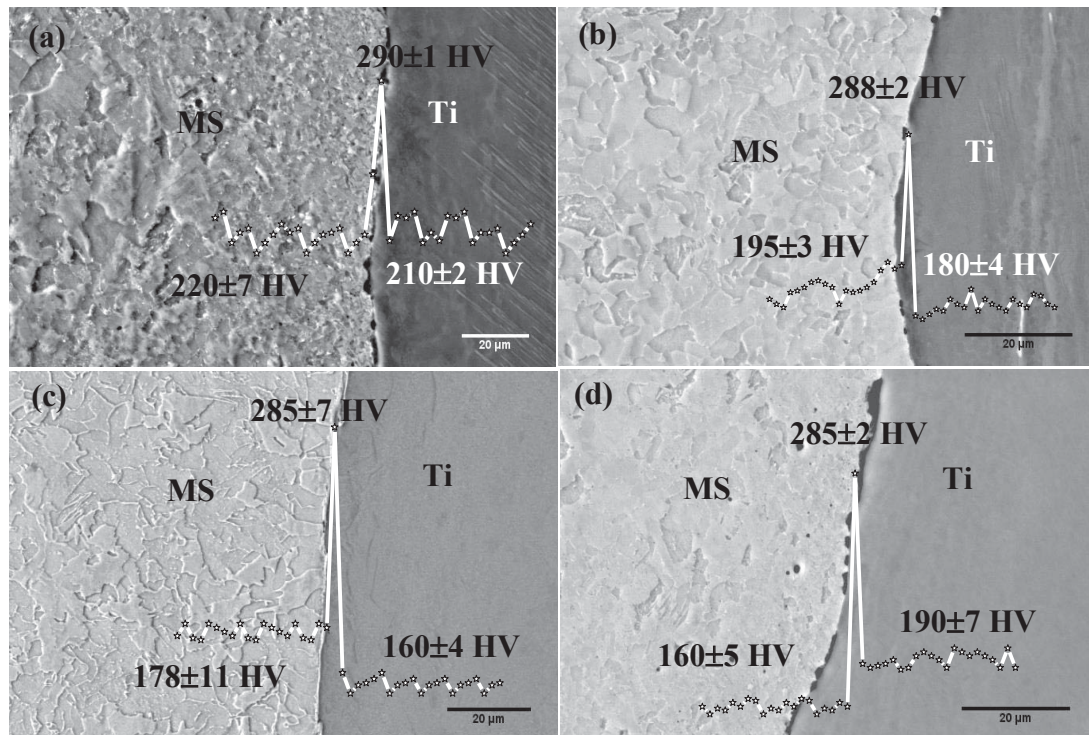


Figure 3.11 BSE images showing the interface of MS/Ti friction joints heat treated at 600 °C for duration of (a) 1, (b) 5, (c) 10 and (d) 20 h respectively; microhardness profiles are superimposed

3.6 Structural changes at the interface during diffusion annealing treatments:

3.6.1 Microstructural and microchemical changes at the interface:

In order to study the diffusion driven structural changes, the friction joints were diffusion annealed in the temperature range of 500-800 °C for long duration of 100 h (Fig. 3.12). Significant microstructural changes were observed at the interface and on the MS side with long term exposure. At the lowest temperature i.e. 500 °C, grain size in regions up to a distance of ~530 µm from the interface was low ~10-15 µm (Fig. 3.12(a)), beyond which the size increased to 50 µm (inset) resembling the parent metal.

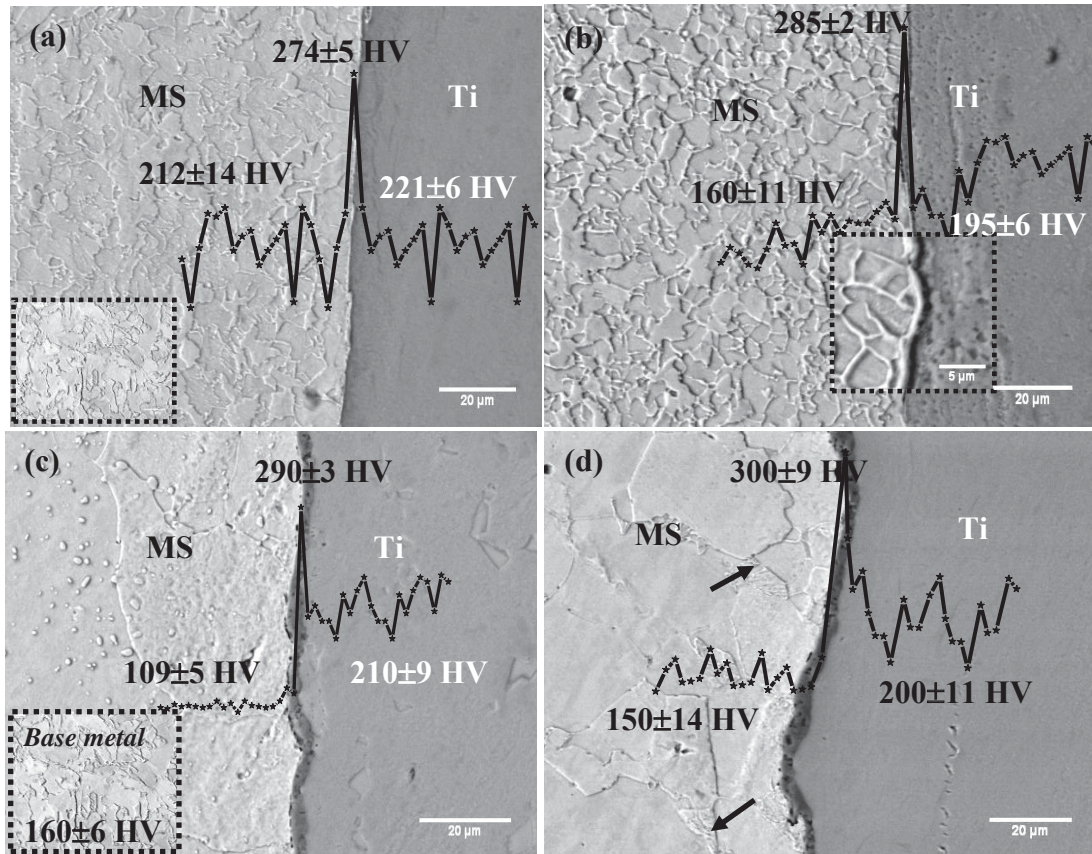


Figure 3.12 BSE images showing the interface microstructure of MS/Ti friction joints with superimposed hardness profile after heat treatment at (a) 500 °C, (b) 600 °C, (c) 700 °C and (d) 800 °C for 100 h respectively

The fine grain structure on MS side was due to the recrystallization of ferrite grains at this temperature. MS showed a hardness of 212 ± 14 HV, higher than the 'as received' material and the interface showed the highest hardness of 274 ± 5 HV. Observation of recrystallized structure indicated high strain rates, although no measurement of strain rate was carried out in the present research work. In comparison to literature on low carbon steels experiencing strain rates in the range of $10^2 - 10^1/s$ with a reported recrystallization temperature of 600°C [139], strain rates involved in the present study was expected to be $>1/s$. ABAQUS based simulations in MS/MS friction joints also showed that the strain rate experienced by the weld zone is of the order of $1/s$ [118]. Plastic strain experienced by MS/Ti friction joints decreased the recrystallisation temperature of MS due to which a fine grain structure with relatively high hardness was obtained. A decrease in the interface hardness with thermal exposure could be attributed to the recovery and recrystallisation of the deformed structure produced during the friction welding process.

Additional features were observed on the MS side at 600°C . A very narrow zone ($\sim 0.8\ \mu\text{m}$ width) (Fig. 3.12(b)) with a relatively high hardness of 285 ± 2 HV was observed at the interface, while the hardness gradually decreased from ~ 200 HV in the vicinity of the interface to $\sim 160 \pm 11$ HV at a distance of about $\sim 600\ \mu\text{m}$ from the interface. Width of this interfacial zone increased to $\sim 2.6\ \mu\text{m}$ with increase in temperature to 700°C (shown by arrow Fig. 3.12(c)). Formation of coarse grains exceeding $120\ \mu\text{m}$ was observed up to a distance of $\sim 700\ \mu\text{m}$ from the interface while the hardness reduced to very low values of 109 ± 5 HV in this region. Beyond this distance the microstructure resembled that of the base metal and is shown as an inset in

Fig. 3.12(c). At 800 °C, thickness of the interface zone increased to nearly 6 μm . Coarse grained microstructure consisting of both ferrite and pearlite (arrow marked in Fig. 3.12(d)) was observed throughout the thickness of the MS plate. Formation of uniform sized ferrite grains with randomly distributed pearlite is a consequence of heat treatment in $\alpha+\gamma$ phase field and subsequent transformation of γ to fine pearlite during cooling. This observation is in agreement with reported literature on friction welds of carbon steels [140]. The continuous formation of brittle phases along the interface was responsible for increase in hardness of the interface at elevated temperatures.

Concentration profiles obtained across the joint interface after thermal exposure are shown in Figs. 3.13(a) to (d) respectively. At 500 °C, the concentration profiles resembled the error function profiles with a maximum diffusion distance of $\sim 3 \mu\text{m}$. With increase in temperature, to 600 °C the diffusing distances for Fe and Ti in Ti side and MS side were obtained as ~ 2 and $3 \mu\text{m}$, respectively (Fig. 3.13(b)). At the interface, the average chemical composition was obtained as 45.4 wt.% of Fe, 53.1 wt.% of Ti and 1.5 wt.% of C. Considerable increase in the concentration of C was observed at the interface on Ti side at 700 °C (Fig. 3.13(c)). Composition at the cross over point was estimated as 67.3Fe-22.9Ti-9.6C (wt.%). At 800 °C, total width of the diffusion zone increased to $\sim 12 \mu\text{m}$ due to increased interdiffusion of elements with temperature. The average composition in the C enriched region was obtained as 45.9Fe-42.5Ti-11.6C (3.13(d)). It is evident that the width of the Fe-C/Ti diffusion zone was $\sim 12 \mu\text{m}$ in friction joints far lower than that reported in diffusion bonds ($\sim 25 \mu\text{m}$) [20] and explosive clads ($60 \mu\text{m}$) [128].

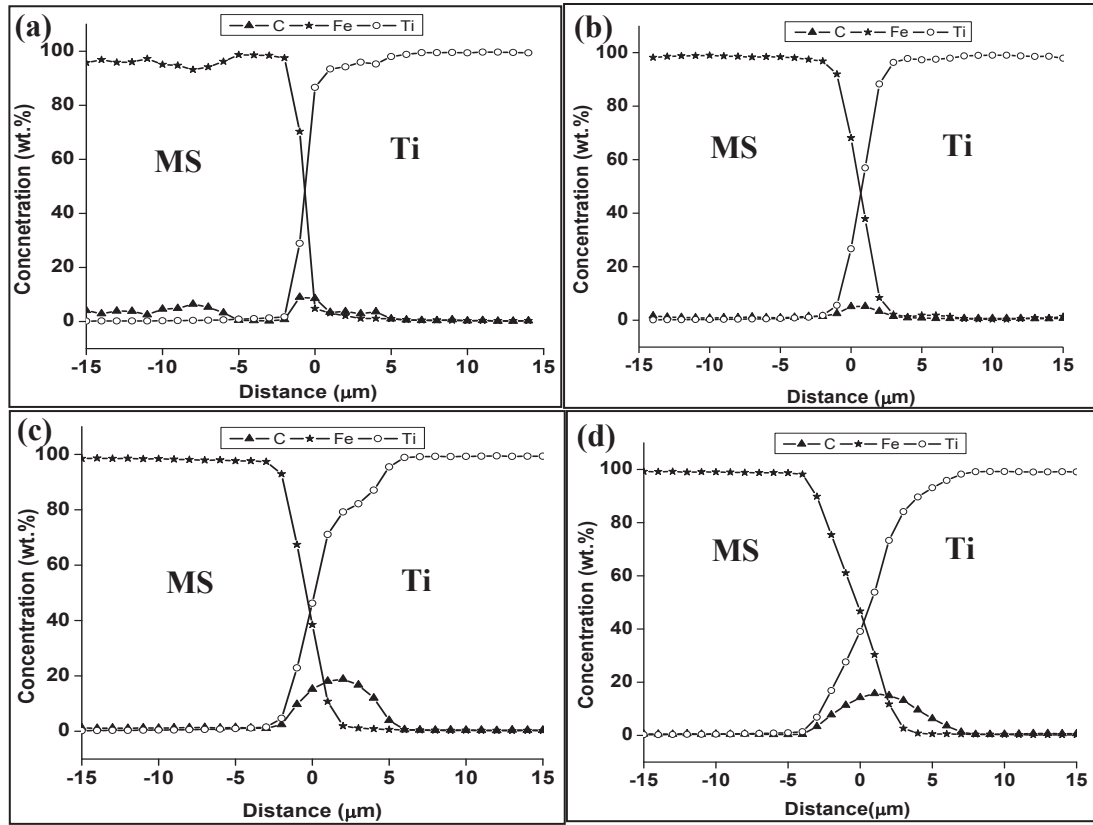


Figure 3.13 Concentration profiles obtained across the MS/Ti friction joints after heat treatment at (a) 500 °C, (b) 600 °C, (c) 700 °C and (d) 800 °C for 100 h respectively

3.6.2 Prediction of phases at the friction joint interface:

Microchemistry obtained using EPMA from the specimen annealed at 500, 700 and 800 °C for 100 h was used as the input to compute the phase fractions at the interface of the MS/Ti joints. Figures 3.14(a) to (c) show the mole fraction (X) of phases predicted by JMatPro[®] plotted as a function of distance from MS to Ti across the interface at all the three temperatures.

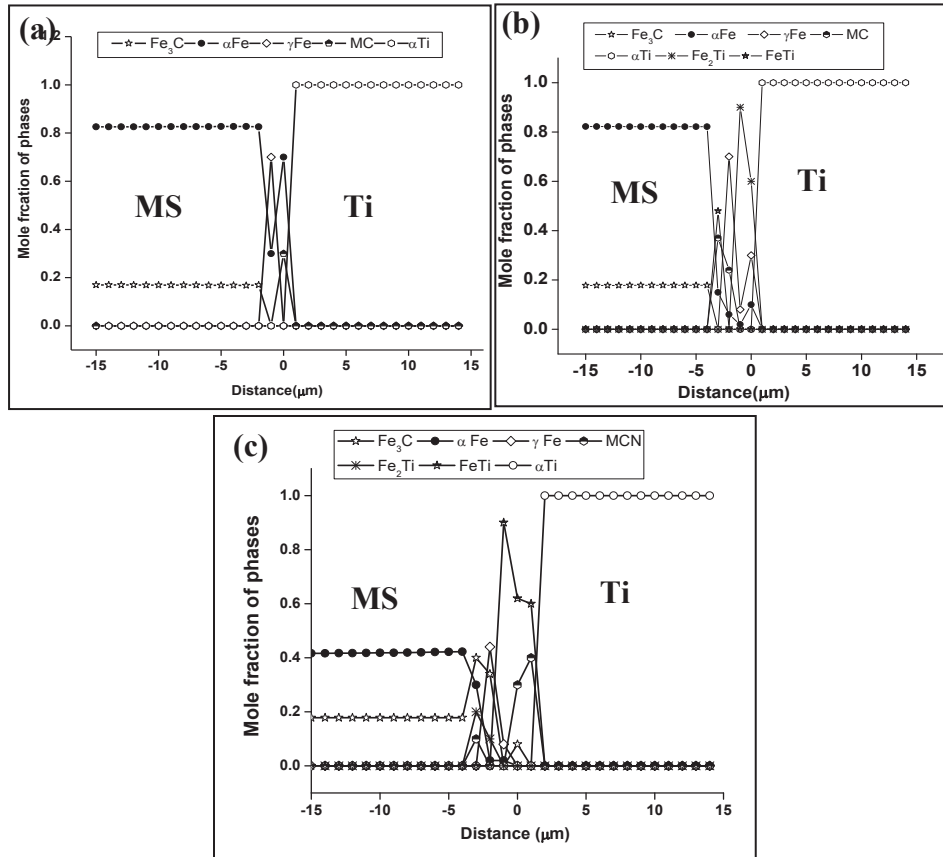


Figure 3.14 JMatPro® predicted mole fraction of phases plotted as a function of distance across MS/Ti weld interface at (a) 500 °C, (b) 700 °C and (c) 800 °C for 100 h

At 500 °C, MC type of carbides ($X_{MC}=0.4$) was observed at the interface in addition to the parent phases. High C concentration at the interface stabilized the γ phase of Fe, which was present at the interface at all temperatures [135]. With increase in temperature to 700 °C, interface consisted of intermetallic FeTi and Laves (Fe_2Ti) phases (Fig. 3.14(b)). At the highest temperature of 800 °C, near the interface on MS side, Fe_2Ti ($X=0.2$) was present in addition to parent α -Fe and Fe_3C . Very near the interface, FeTi (mole fraction - ~ 0.9) formed and as expected α (hcp) phase was stable on the Ti side. High carbon concentration at the interface stabilized the γ phase of Fe.

3.6.3. Confirmation of the phases at the interface:

The phases that formed in the weld cross-section on thermal exposure for 100 h at 500 and 800 °C were identified using the XRD patterns shown as Fig. 3.15(a) and (b) respectively. At both the temperatures Bragg peaks corresponding to parent α Fe and α Ti phases were observed distinctly while the presence of Fe_2Ti and FeTi phases could not be clearly established due to overlap with parent phases.

Further, TEM investigations were carried out on thin foil specimens extracted from the interface of the weld heat treated at 800 °C for 100 h. Figures 3.16(a) and (b) show a typical BF image and the corresponding SAD pattern obtained from the circled region in Fig. 3.16(a). Particles having an average size ~ 100 nm (circled in Fig. 3.16(a)) were observed throughout the interface. Analysis of the SAD pattern confirmed these particles to be intermetallic FeTi phase along $[\bar{1}11]$ zone axis. Further, the EDS spectrum in Fig. 3.16(c) acquired from the circled region showed that the Fe content was ~ 55.7 wt.% and Ti was ~ 44.3 wt.%.

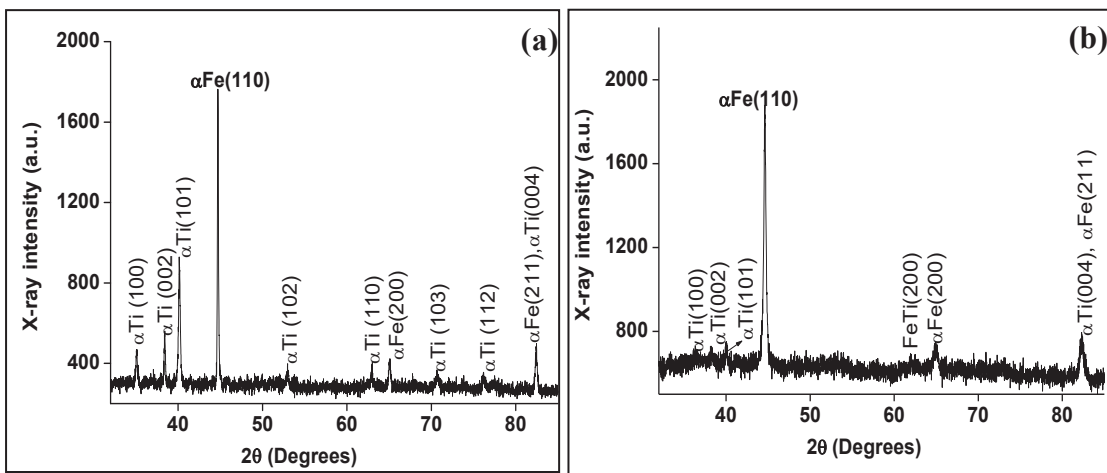


Figure 3.15 XRD patterns obtained from MS/Ti friction joint heat treated at temperatures of (a) 500 °C and (b) 800 °C for 100 h

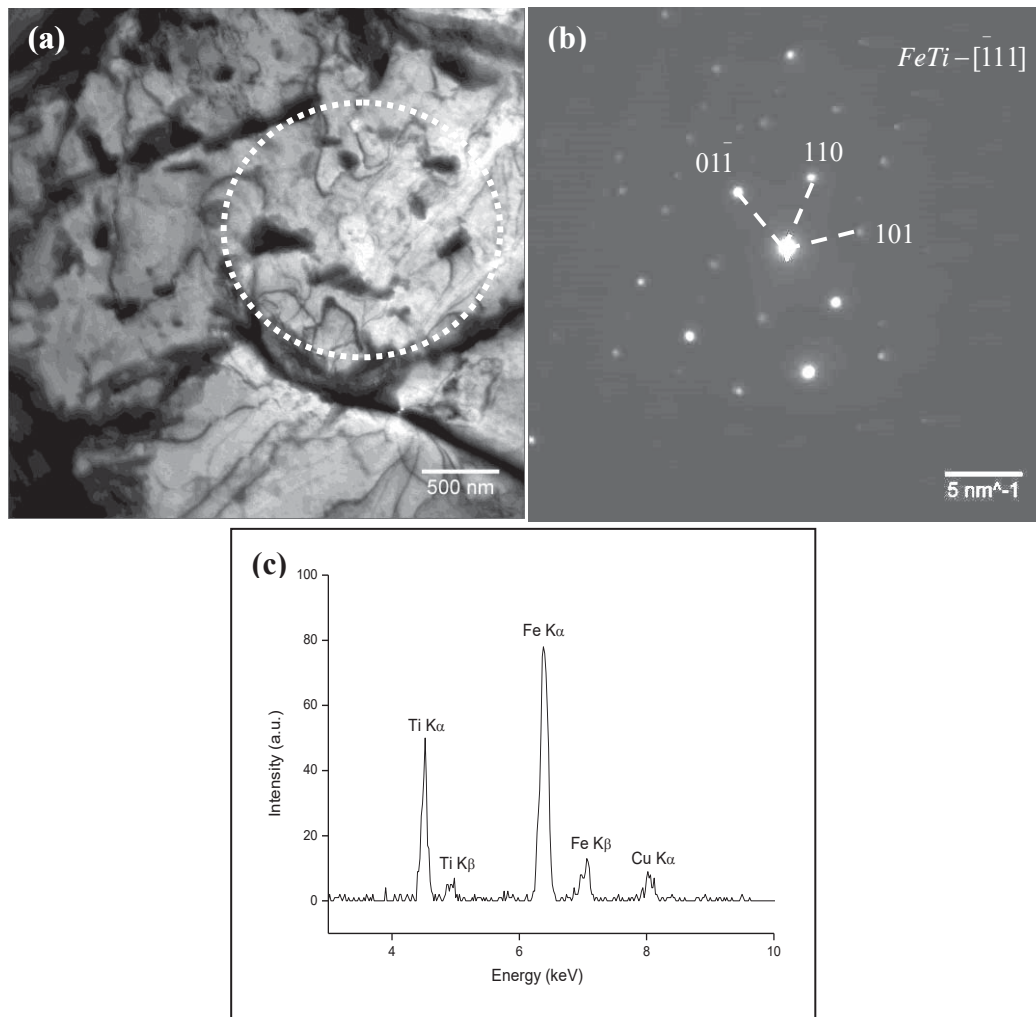


Figure 3.16 TEM (a) BF image of the friction joint heat treated at a temperature of 800 °C for 100 h showing fine secondary particles, (b) corresponding SAD pattern confirmed the presence of FeTi intermetallic phase along $[\bar{1}11]$ zone axis and (c) EDS spectrum obtained from the circled region in (a) further confirmed the Fe and Ti rich nature of the phase

This composition showed that it corresponds to the FeTi phase [7] and the overestimation of Fe was attributed to the contribution from the MS matrix. Figures 3.17(a) and (b) show the TEM-BF image and SAD pattern obtained from another region with $\sim 3 \mu\text{m}$ wide grain at the interface. Analysis of the SAD pattern identified the spot and ring pattern correspond to bcc Fe along $[\bar{1}12]$ and fcc-TiC along $[011]$ zone axis. Presence of TiC particles was further confirmed by a DF image of $[220]$ reflection (Fig. 3.16(c)). Contrary to this observation a continuous layer of TiC precipitates was reported in Fe(0.16C)/Ti explosive clads after thermal exposure at 900°C which decreased the mechanical strength of the joints [141, 142].

Comparison of the experimental results on friction welding in this study with literature information on diffusion bonded joints and explosive clads [20, 21, 58, 82, 133, 141-143], led to the following inferences: (i) Intermetallic phases are isolated as fine particles in the ferrite matrix as against a continuous zone parallel to weld interface in diffusion bonded joints, (ii) few microns of deformation at the friction weld interface is in contrast to the deformation induced metastable phases over larger distances ($\sim 6 \text{ mm}$) in explosive clads and (iii) limited diffusion zone of $\sim 10\text{-}12 \mu\text{m}$ even after heat treatment for 100 h at 800°C [133]. Thus, friction welding proved to be a promising technique for joining Fe and Ti based alloys for industrial applications provided specimens are of suitable geometry.

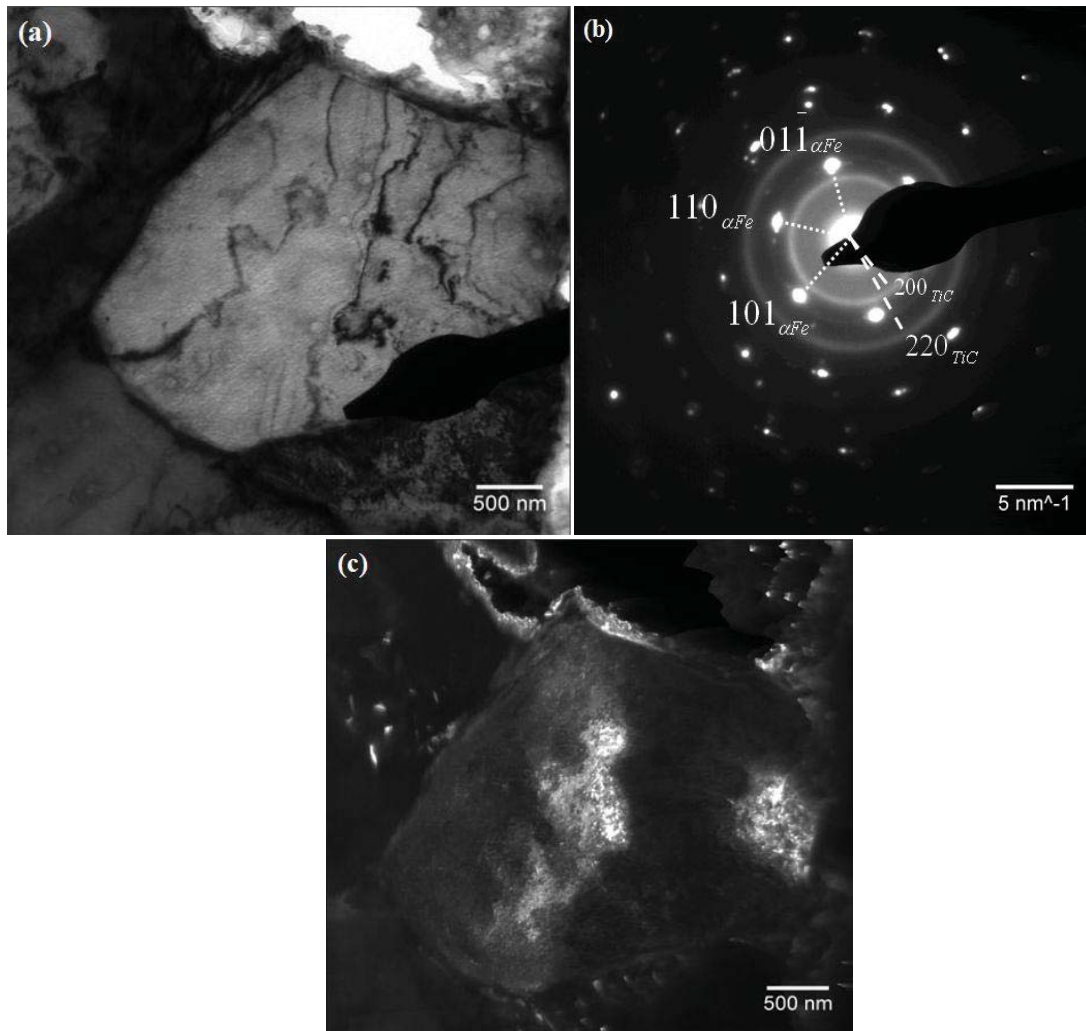


Figure 3.17 TEM (a) BF image showing a large grain at the interface, (b) corresponding SAD pattern showed with overlapping reflections from bcc-Fe and TiC phase along $[112]$ and $[011]$ zone axis respectively and (c) DF image corresponding to $[220]_{TiC}$ reflection further confirming the formation of TiC phase

The previous sections provided a comprehensive overview of welding trials to join MS and Ti by friction welding, its qualification and microstructural characterization, selection of temperature window for PWHT and the variation in interface microstructure on long term thermal exposures which degraded the bond strength of the joint. The subsequent sections would deal with a detailed study on explosive clad joints of MS and Ti.

3.7 Fabrication and assessment of explosive clads of MS-Ti:

3.7.1 Fabrication and optimization of load ratio:

In this study, three explosive clads were fabricated using different explosive load ratios (R) of 1.07, 2.01 and 3 for a fixed stand off distance and type of explosive. Details of the fabrication were explained in Chapter 2, section 2.2.3. BSE images of the MS/Ti clads with different values of R are shown in Figs. 3.18(a) to (c). Low magnification images clearly showed wavy interface for the three values of R . However, the waves became more asymmetrical with increasing R . At low R , the nature of the waves resembled a sinusoidal pattern with wavelength and amplitude measured as ~ 840 and $120\ \mu\text{m}$ respectively. A closer examination revealed entrapment of the jet at the vortex of the wavy interface which is given as inset in Fig. 3.18(a). Elongation of the grains towards detonation direction was observed on both sides up to a distance of $\sim 3\ \text{mm}$ from the interface. Localized molten zones were present in the front slope of waves and the waves were propagated towards MS side due to its high density as compared to that of Ti. With increasing R the microstructure was observed to be modified on MS side, which was attributed to its high thermal conductivity ($45\text{--}65\ \text{W/mK}$) compared to Ti ($22\ \text{W/mK}$) [144]. For R value of 2.01, the microstructural modification was observed up to a distance of $\sim 195\ \mu\text{m}$ (Fig. 3.18(b)). This modified layer consisted of a thin layer ($\sim 5\ \mu\text{m}$ width) at the interface followed by a fine grain (grain size $< 10\ \mu\text{m}$) region up to a distance of $\sim 70\ \mu\text{m}$ followed by the solidification microstructure (inset in Fig. 3.18(b)) for $\sim 120\ \mu\text{m}$. Microcracks were present throughout the thickness of this modified layer. As the load ratio was increased to 3, the width of this modified layer increased to $\sim 450\ \mu\text{m}$ (Fig. 3.18(c)), where the interfacial

zone and fine grain region were present up to ~ 10 and ~ 90 μm respectively. The solidification structure was dendritic which extended up to ~ 200 μm beyond which the microstructure resembled as that of the ‘as received’ material.

The high magnification images of the interface of MS/Ti with different R values with superimposed hardness profiles are shown in Figures 3.19. The base, flier plates and interface (~ 350 HV) showed an increase in hardness as compared to parent metals (Fig. 3.19(a)) for R value of 1.07.

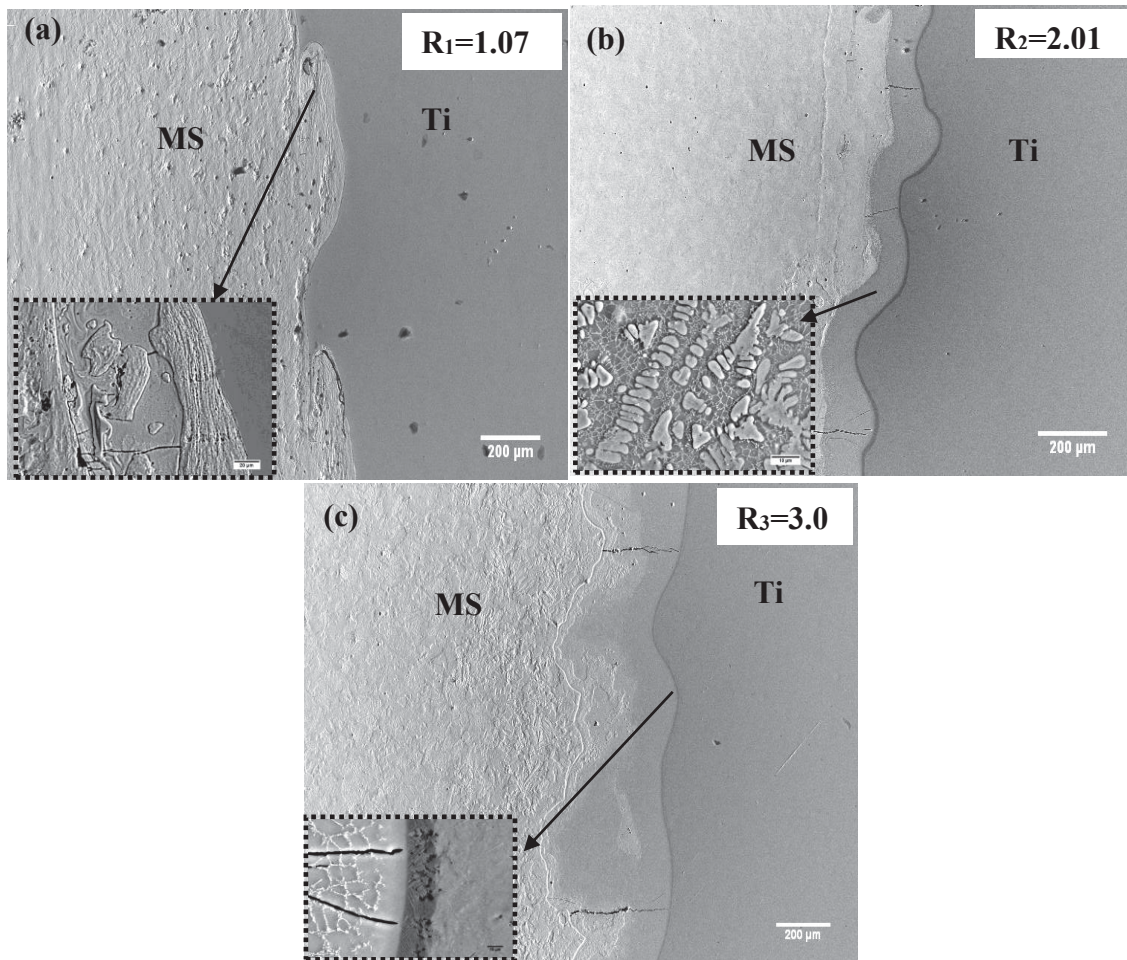


Figure 3.18 BSE images showing the interface microstructure of MS/Ti explosive clads fabricated with (a) $R=1.07$, (b) 2.01 and (c) 3.0 respectively; inset in panel (a), (b) (c) represents vortex region, dendritic structure and fine grain region along with microcracks at the interface respectively

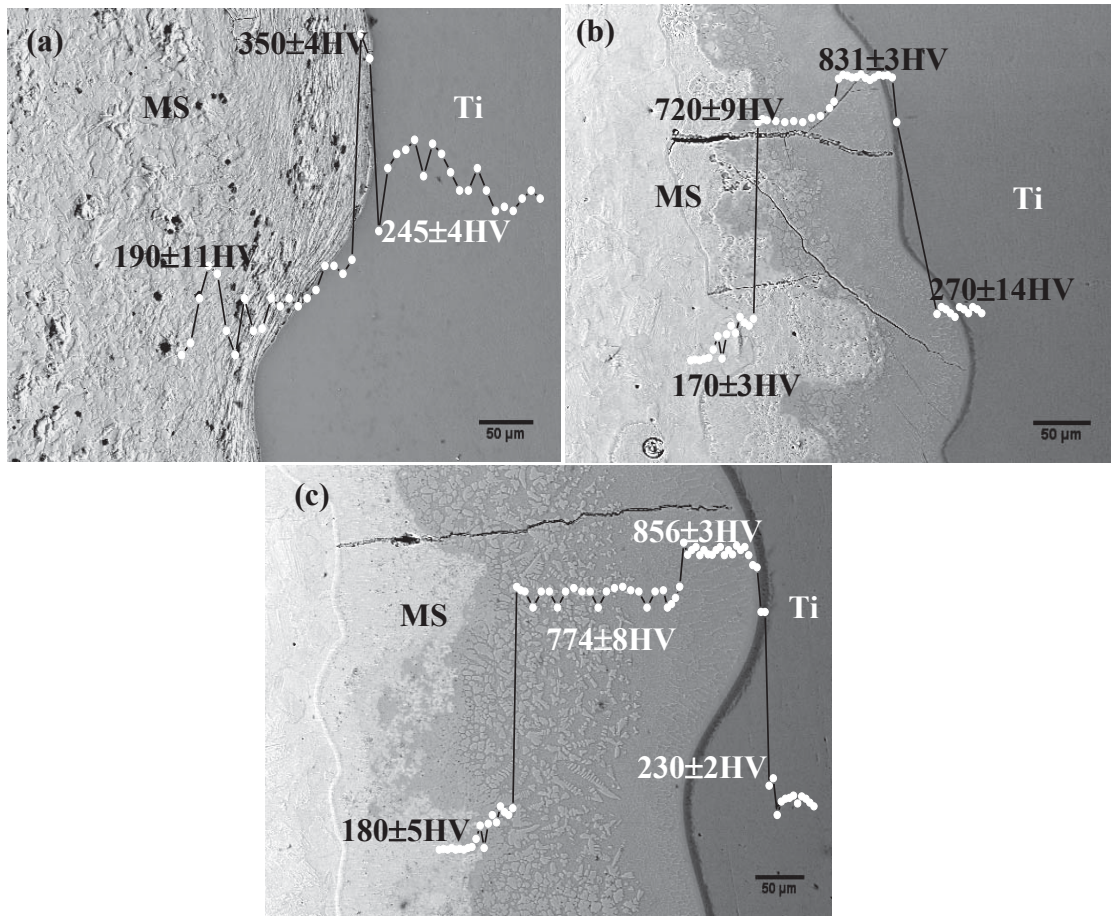


Figure 3.19 BSE images showing interface of the MS/Ti clads fabricated with (a) R=1.07, (b) 2.01 and (c) 3.0 with superimposed hardness profiles respectively

For a R value of 2.01, the fine grained region showed very high hardness of ~ 831 HV, which decreased to ~ 720 HV in the solidification microstructure (Fig. 3.19(b)). Average hardness values of ~ 856 and 774 HV were measured in fine grain structure and dendritic structure for R=3 (Fig. 3.19(c)). The average hardness of the interfacial layer was ~ 320 HV for R= 2.01 and 3. Formation of fine grain structure close to the interface followed by solidification structure typical of a cast structure (Figs. 3.19(b) and (c)) was in contrast to the expected wavy interface with increased wavelength and formation of large volume of vortices as reported by Kahraman et al. [47]. This was attributed to the

extremely large dissipation of kinetic energy at the interface due to large thickness of the flier plate (12 mm) in the present study. Saravanan et al. [145] and Manikandan et al. [52] have explained the dependence of KE loss on thickness of flier plate. In case of thin flier plates (≤ 3 mm), the dissipated heat produces large plastically deformed regions and melting of the metals. Rapid cooling of the molten metal surrounded by the cold metal leads to shrinkage cracks as observed in case of clads with $R \geq 2$.

Morphology of the interface in explosive clads is reported to be of three different types namely (i) straight, (ii) wavy and (iii) continuous solidified metal as dictated by the kinetic energy (KE) dissipation of the flier plate at the collision interface, which in turn depends on the cladding parameters such as flier plate thickness, explosive load ratio, stand off distance and flier plate velocity [47, 146]. Akbari et al. [49] have varied R in the range of 0.5-2.5 (for 4 mm thick flier plate) in 304SS Ti explosive clads and reported poor bonding in both low as well as high value of R , which was attributed to lack of jetting due to surface roughness ($R < 1$) and formation of continuous intermetallic layer ($R \geq 2$) at the interface [49]. Similar reports are available in the literature describing the significance of load ratio on deciding the nature of the clad interface in various dissimilar systems [47, 48, 50].

Longitudinal tensile and shear properties of the explosive joints were measured experimentally which are listed in Table 3.2. Fabrication of the specimens for the mechanical tests was described in section 2.3. Figure 3.20(a) shows the photographs of the tensile specimens before and after testing. Fractograph in Fig. 3.20(b) revealed brittle mode of failure of the clad. High intensity of Fe peak in the EDX spectrum (Fig. 3.20(c)) obtained from the fracture surface (arrow marked in Fig. 3.20(b)) suggested,

that the failure was on MS side of the clad, which was also supported by the microstructural observations. Additionally, microcracks were seen at the fracture surface in clads fabricated with R values of 2.01 (Fig. 3.20(d)). The clads exhibited a marginal increase in YS and UTS values whereas the elongation gradually decreased with increase in R. The interface showed a high UTS of 456 MPa ($R=1.07$) as compared to the flier plate UTS value of 325 MPa, however, this value is comparable to MS (449 MPa). Shear test was carried out as per ASTM B898 standard. Figure 3.21(a) shows the overall view of the test piece before and after testing. Explosive clad joints of 304SS and CPTi showed similar values for shear strength [147].

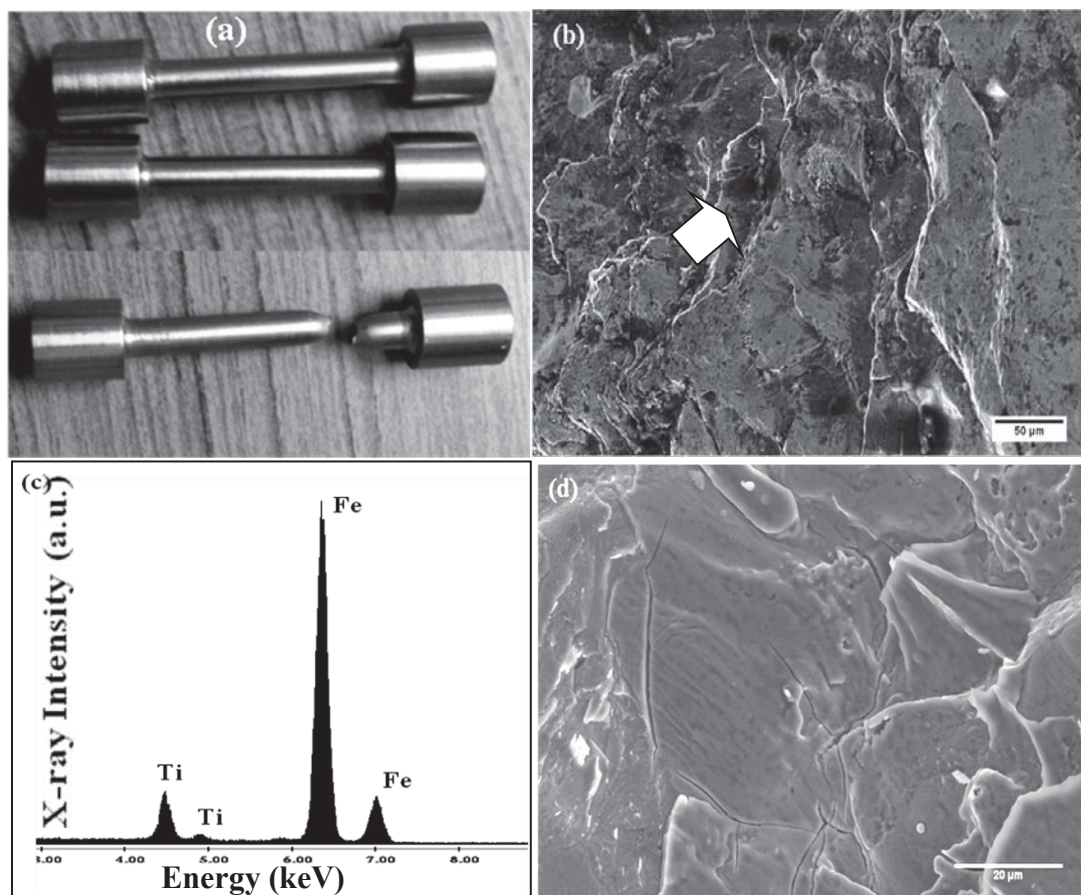


Figure 3.20(a) Tensile specimens before and after testing, **(b)** SE image of fracture surface showing typical brittle fracture, **(c)** Fe rich EDX spectrum from the fracture surface confirmed failure on MS side and **(d)** microcracks on the fracture surface of the clads fabricated with a R value of 2.01

Table 3.2 Mechanical properties of the clads with different load ratios

Property/Condition	Clad 1 ($R_1=1.07$)	Clad 2 ($R_2=2.01$)	Clad 3 ($R_3=3.0$)
Initial Gauge length (mm)	50	50	50
Final Gauge Length (mm)	62.43	60.76	59.56
% Elongation	24.86	21.52	19.12
YS (MPa)	374.7	430.4	463.9
UTS (MPa)	456.1	483.7	504.2
Shear Strength (MPa)	230 (min.) - 382.5 (max.)	217-370.7	209-357.8

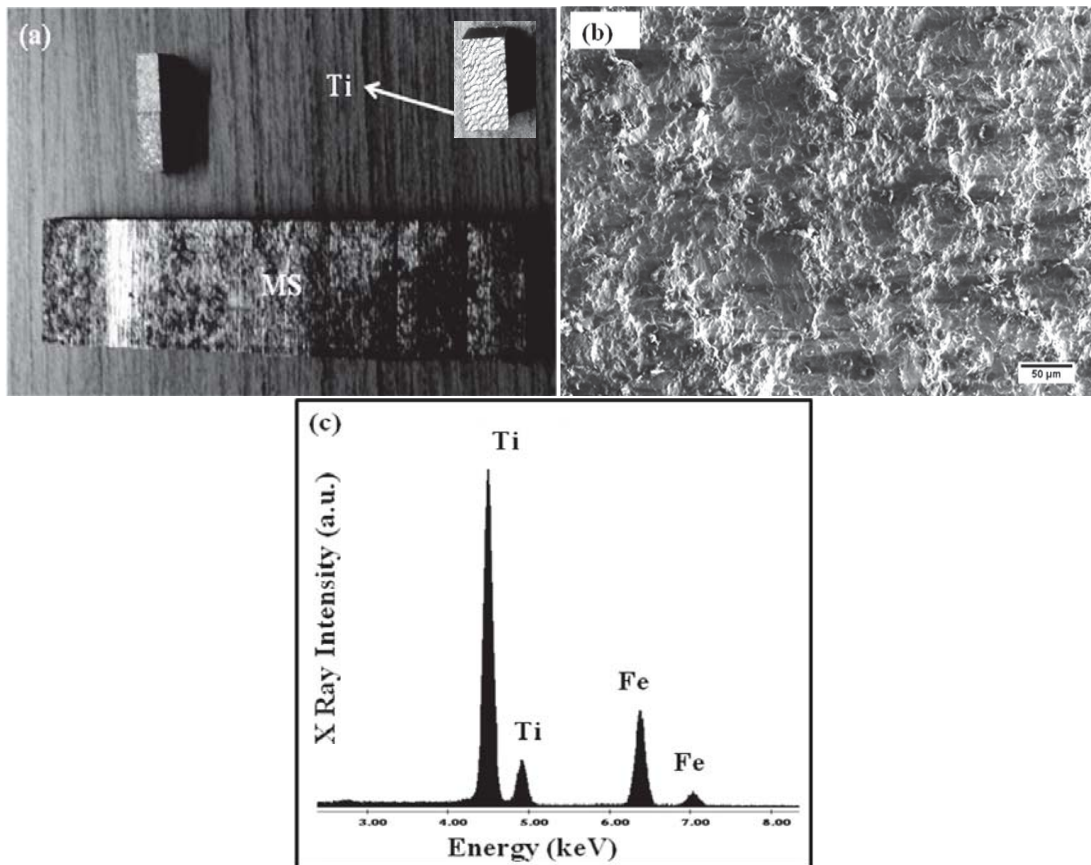


Figure 3.21(a) Shear tested specimen and the inset shows the flow pattern of the tested piece, (b) fractograph typical of a ductile + brittle mode of failure and (c) dominant Ti peaks in EDX spectrum indicated failure on Ti side

The shear tested flier plate revealed typical wavy patterns (inset in Fig. 3.21(a)), while the fracture surface showed mixed brittle and ductile failure modes (Fig. 3.21(b)). EDX spectrum in (Fig. 3.21(c)) from the fracture surface showed presence of Ti and Fe due to adherence of some amount of base metal to the clad, indicating that the fracture was on Ti side. From Table 3.2 it can be seen that the minimum and maximum values of shear strength varied between 230 and 383, for $R=1.07$. Based on the above results it is concluded that a load ratio of 1.07 imparted a uniform wavy interface microstructure and adequate mechanical properties.

The measured values of shear strength (380 MPa) in this study were lower than ~ 700 MPa, the value reported for 3 mm thick SS-Ti explosive clads [47], which can be understood in terms of the higher extent of deformation in the low thickness plate. However, the clads fabricated in the present study do possess adequate bond strength for industrial usage as the measured value was higher than the ASTM specified standard minimum bond strength of ~ 190 MPa [148] for Ti based dissimilar joints. Also, at high energetic conditions (large values of flier plate velocity or explosive load ratio) propensity for formation of intermetallic phases and molten zones is reported to be high due to large dissipation of heat at the interface [52, 53, 141]. Hence, explosive cladding with a load ratio of 1.07 was a promising method for joining MS and Ti plates of higher thickness and further studies were carried out on clads fabricated with this selected value of 'R'.

3.7.2 Evolution of microstructure in base and flier plates and interface of explosive clad joints:

Figure 3.22(a) shows a typical micrograph of the clad interface revealing the formation of vortices. Similar observation of melting and solidification of the parent metals has been reported by Kosec et al. [149] in low carbon steel-Ti system. The formation of such molten pockets at the vortices can be understood in terms of an abrupt increase in temperature to the extent of 1300-1500 °C [53, 150] followed by rapid quenching (10^5 - 10^7 °C/s) [39]. Although, explosive cladding is a solid state welding process, internal heating of the metal plates due to high pressure and adiabatic heating of the compressed gases is reported to be the cause for the large amount of heat at the contact surface leading to localized melting of the metal plates [39]. Based on the Hydrodynamics simulations, Li et al. [150] proposed the mechanism of bonding in explosive cladding as diffusion + fusion + pressure welding process. In the present study, dissipation of large KE indicated the explosive cladding process as a fusion welding process at high energy conditions ($R \geq 2$).

The X-ray maps for Fe and Ti from a vortex region in the wavy interface are shown in Fig. 3.22(b) and (c) respectively. Vigorous stirring of the molten metals during the explosive cladding process resulted in considerable redistribution of Fe and Ti. Enrichment of Ti (Fig. 3.22(c)) and some amount of unmixed Ti (arrow marked) in Fig. 3.22(c) at the vortex confirmed the entrapment of molten metal (from the flier plate) during the cladding process. EPMA concentration profiles of Fe, Ti and C obtained from a straight interfacial region is shown in Fig. 3.23(a). At the cross over point the concentration values of Fe, Ti and C were measured as ~49.5, 47.6 and 2.9

wt.% respectively. Interdiffusion of Fe and Ti resulted in a diffusion zone of $\sim 4\ \mu\text{m}$ width while C showed a diffusion distance of $\sim 3\ \mu\text{m}$. Considerable redistribution of the elements was evident from the concentration profiles obtained from the vortex regions (Fig. 3.23(b)).

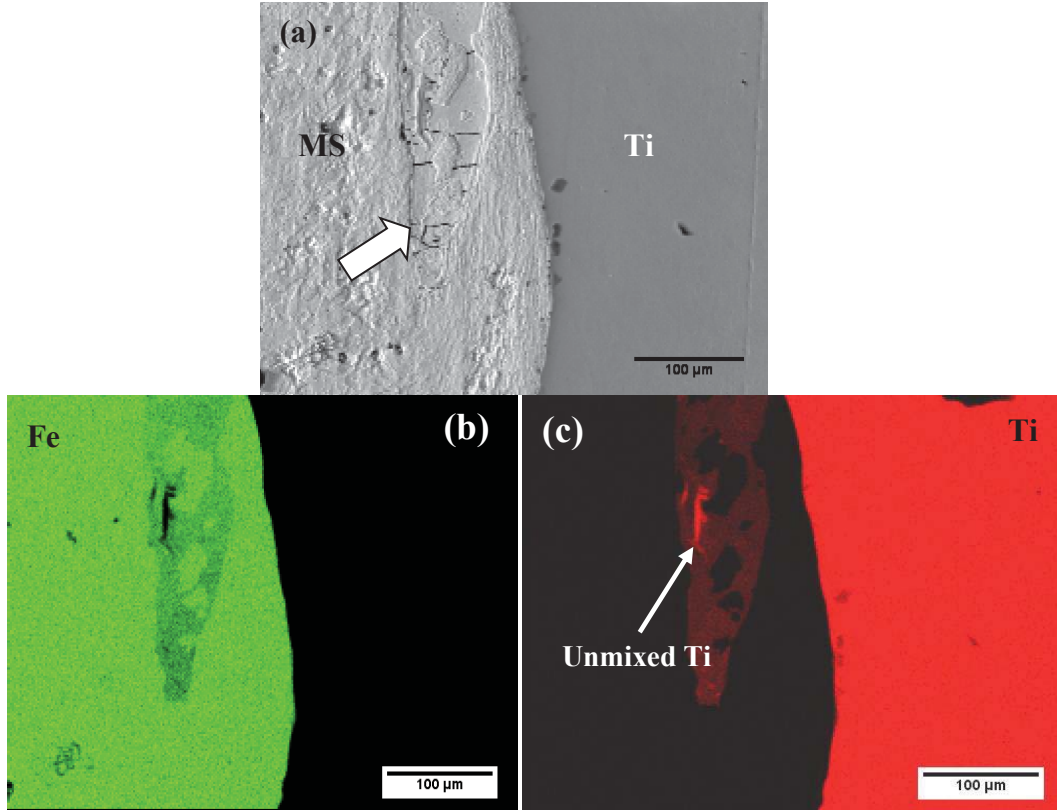


Figure 3.22 (a) Electron image of the MS/Ti ‘as clad’ interface showing a vortex region (arrow marked) and the corresponding X-ray maps for (b) Fe and (c) Ti

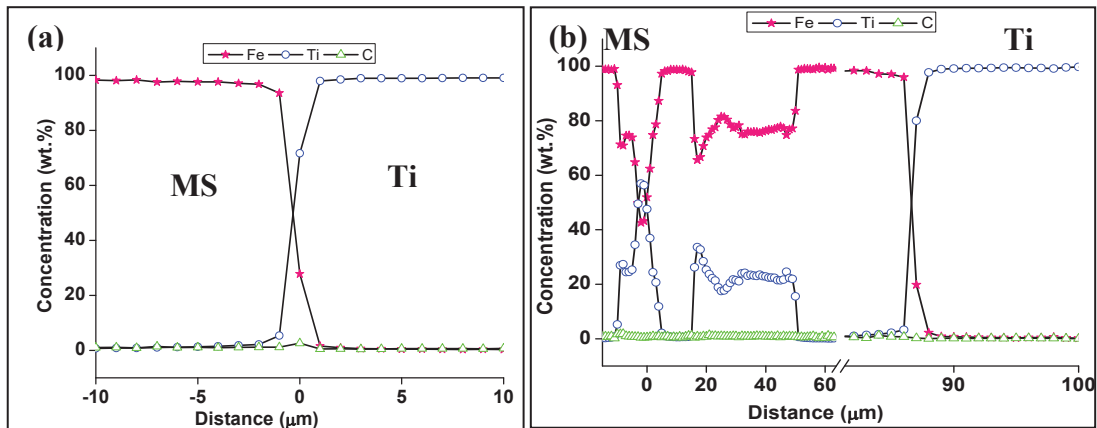


Figure 3.23 Concentration profiles obtained across the clad interface from (a) straight interface region and (b) vortex region respectively

The total width of the reaction zone was measured as $\sim 100\ \mu\text{m}$. Average composition in this zone varied between 75.2 to 77.8 wt.% of Ti and ~ 23.9 to 22.3 wt.% of Fe with C concentration changing gradually throughout the molten zone.

A similar procedure as in the case of friction joints was followed to predict the phases that form at the clad interface by JMatPro[®] using microchemical information obtained from EPMA as the input. Figures 3.24(a) and (b) show the plot of mole fraction of predicted phases at straight and vortex region of the interface as a function of distance. Formation of TiC and Fe₃C was predicted, due to increased C concentration at the straight interface. At an average composition of 24.2Fe-74.9Ti-0.9C (in wt.%) in the vortices, JMatPro[®] predicted the coexistence of Fe₂Ti and TiC phases, and this region extended up to a width of $\sim 53\ \mu\text{m}$ ($x_1=44$, $x_2=97\ \mu\text{m}$).

High pressure and strain rate of 1-15 GPa [38] and $10^6/\text{s}$ [151] respectively during explosive cladding was expected to cause significant changes in phase and microstructure of the materials. In an earlier study in this laboratory formation of metastable phases in 6 mm thick base and flier plates of explosive clads of SS/TiTaNb has been reported [43, 58].

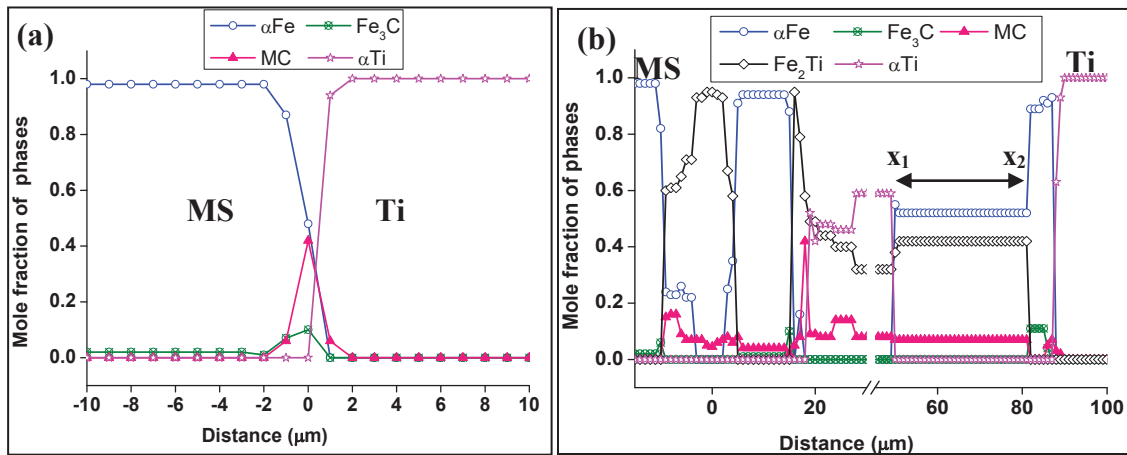


Figure 3.24 Prediction of the phases using JMatPro[®] in regions showing (a) straight interface and (b) vortex region respectively

3.7.3 Confirmation of the deformation induced phases in explosive joints:

In the present study, the use of large thickness of base (20 mm) and flier (12 mm) plate explained for the small depth of deformation region (~3 mm) on either side of the clad interface. Hence, 2 mm thick cross-section specimens from either side of interface were extracted for XRD analysis. Figure 3.25 shows the XRD patterns obtained individually from the deformed cross-section specimens corresponding to MS, Ti and interface. Analysis of the XRD patterns showed the presence of bcc phase on MS side (Fig. 3.25(a)). Additional Bragg reflection was observed at 2θ position of 44.43° on Ti side other than those belonging to parent α (hcp) phase (Fig. 3.25 (b)). This phase was uniquely identified as the metastable fcc Ti, although the other peaks of fcc Ti at 2θ positions of 38.3° and 77.4° overlapped with the (002) and (201) peak positions of hcp Ti phase. In order to eliminate any ambiguity in the experimentally observed reflections in XRD patterns, a rigorous comparison has been made against all possible reflections of various Ti phases and compounds such as oxides, carbides, nitrides and hydrides of Ti. This comparison clearly established the presence of metastable fcc and parent α phases only. XRD pattern from the interfacial region showed the reflections predominantly for two parent metals (Fig. 3.25(c)). A detailed analysis by TEM has been also carried out and discussed in the next section.

A detailed analysis by TEM was carried out to confirm the phases that were present in the MS/Ti explosive joints. Figure 3.26(a) shows a typical BF image of an equiaxed grain triple point obtained from the deformed region on MS side of the interface. Few regions showed typical lath type of structure as shown in Fig. 3.26(b) and the corresponding SAD pattern (Fig. 3.26(c)) confirmed twinning of the ferrite

grains along $[\bar{1}2\bar{3}]$ zone axis. Planar defects (arrow marked in Fig. 3.26(a)) along the grain boundary are clearly evident from the micrograph and the interior of the grains consisted of large number of dislocations [120].

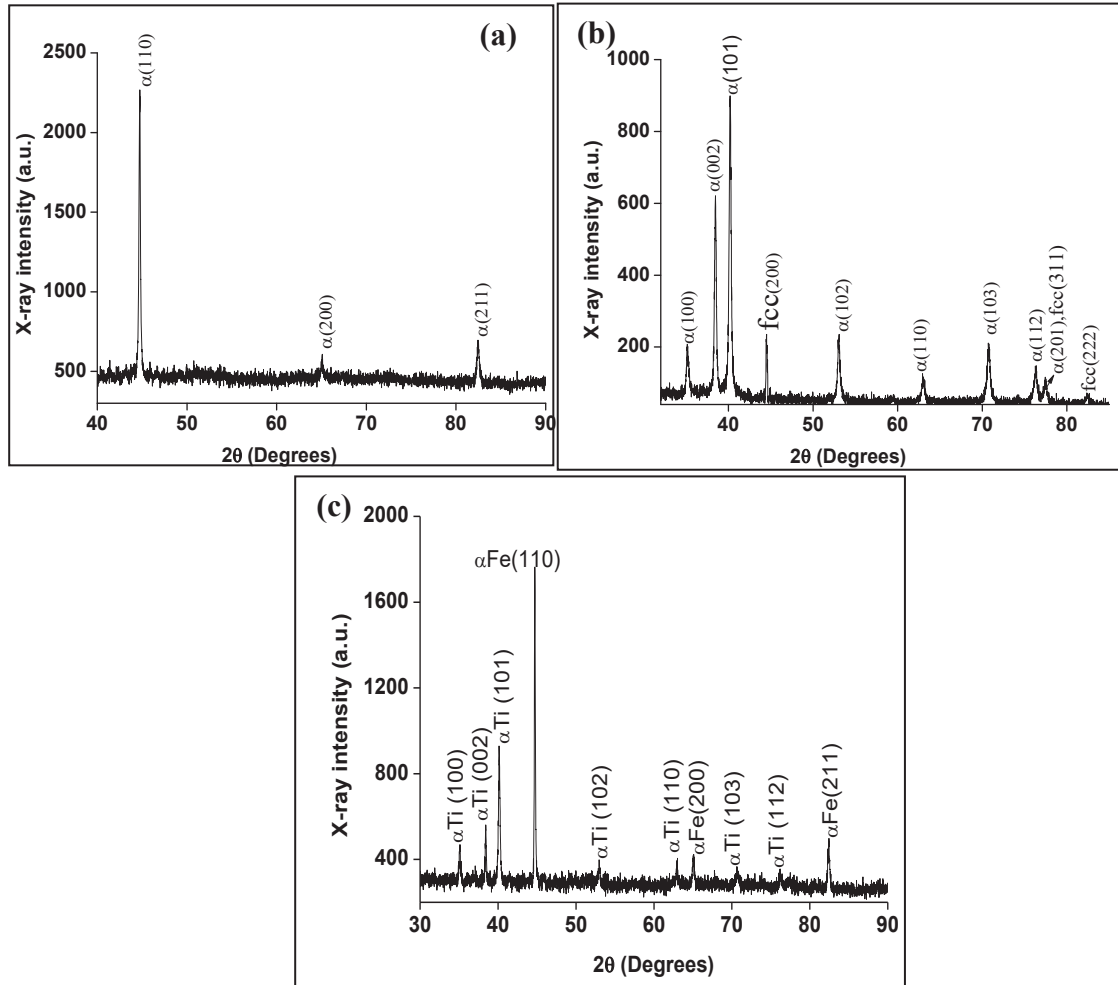


Figure 3.25 XRD patterns of (a) MS, (b) Ti and (c) interface regions of the MS/Ti explosive clad

Extensive plastic deformation of the metals resulted in the formation of deformation bands and non equilibrium phases during explosive cladding as reported in the literature [39]. It is evident from Fig. 3.26(b) that acicular lath like features formed in MS on explosive cladding. Analysis of the SAD pattern from a typical lath structure showed bcc twins along the $[\bar{1}12]$ habit plane. Oxford et al. [152] have reported a similar observation of presence of acicular martensite in explosively welded 0.1C mild steel. Based on the morphology supported by literature the lath structure observed in the present study, was attributed to the formation of acicular martensite.

The TEM-BF image from the Ti side is given in Fig. 3.27(a). Elongation of grains and regions of high dislocation density were observed. The SAD pattern (Fig. 3.27(b)) obtained from the intersection of grains (circled in figure) showed overlapping reflections corresponding to α phase along $[\bar{2}110]$ and $[0001]$ zone axis. In addition, few regions consisting of lamellae with a dark contrast was seen (Fig. 3.27(c)). The SAD pattern obtained from the lamella is shown in Fig. 3.27(d). Analysis of the SAD pattern showed the presence of metastable fcc phase of Ti along $[\bar{1}12]$ zone axis. The DF image (Fig. 3.27(e)) for the $[\bar{2}\bar{2}0]_{fcc}$ reflection further confirmed the presence of fcc Ti supporting the XRD results. Although, formation of metastable fcc Ti phase is well documented in thin films [153, 154], few reports are available in literature on formation of fcc Ti in bulk Ti alloy systems [71, 72, 155, 156]. Heerden et al. [153] reported that the change in interfacial free energy, surface free energy and strain energy are responsible for hcp to fcc phase transformation in Ti/Al multilayers. While plastic deformation and the stresses generated during the rapid cooling process are responsible

in bulk alloys [71, 155]. Based on electronic density of states, Agauayo et al. [157] report that, Ti and other Group IVA metals such as Hf and Zr possess fcc phase as locally stable structure.

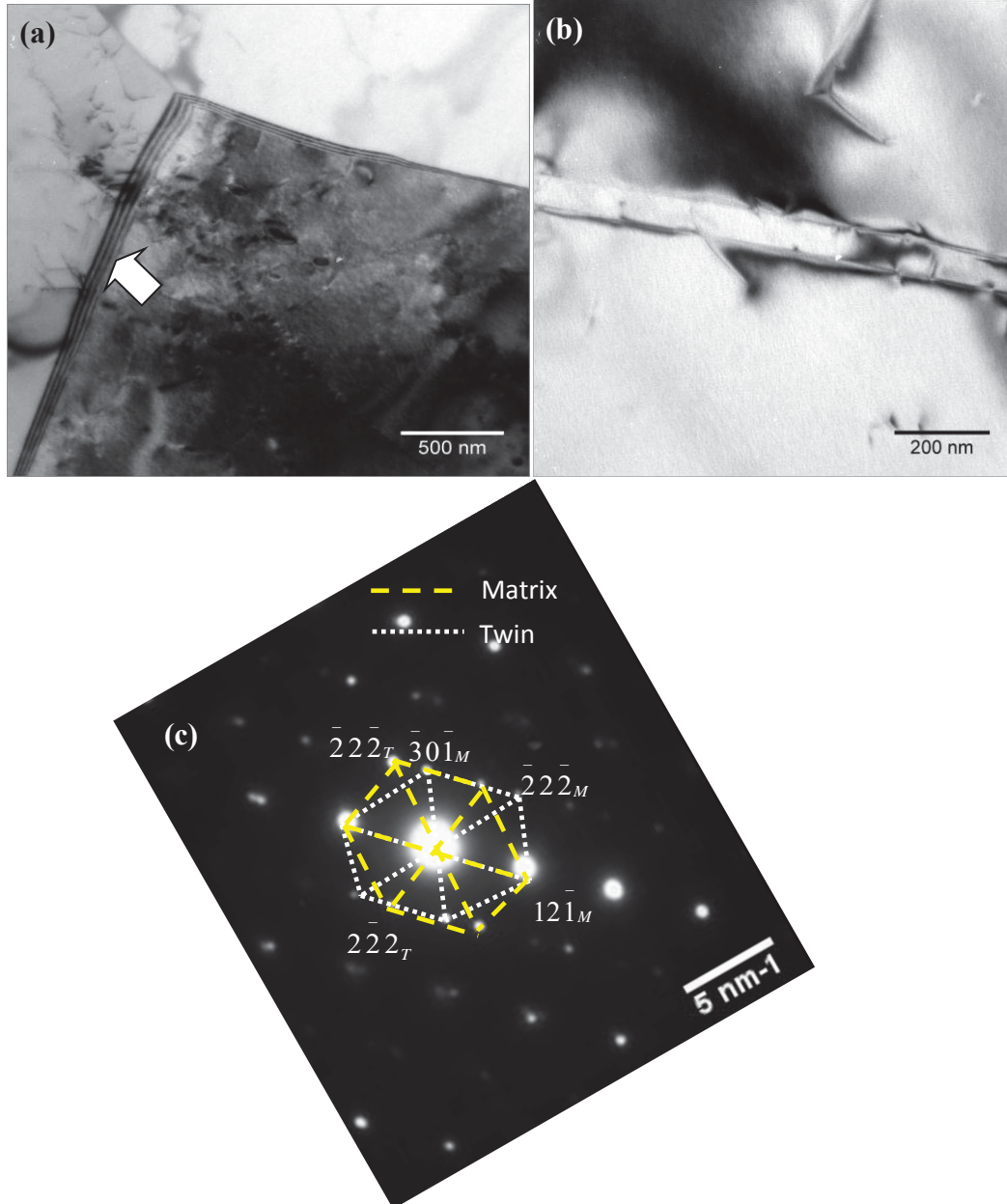


Figure 3.26 TEM-BF image obtained from deformed region on MS side showing grain triple point decorated with planar defects (arrow marked), (b) typical lath type structure and (c) corresponding SAD pattern confirmed twinning of ferrite grains along $[\bar{1}\bar{2}\bar{3}]$ zone axis

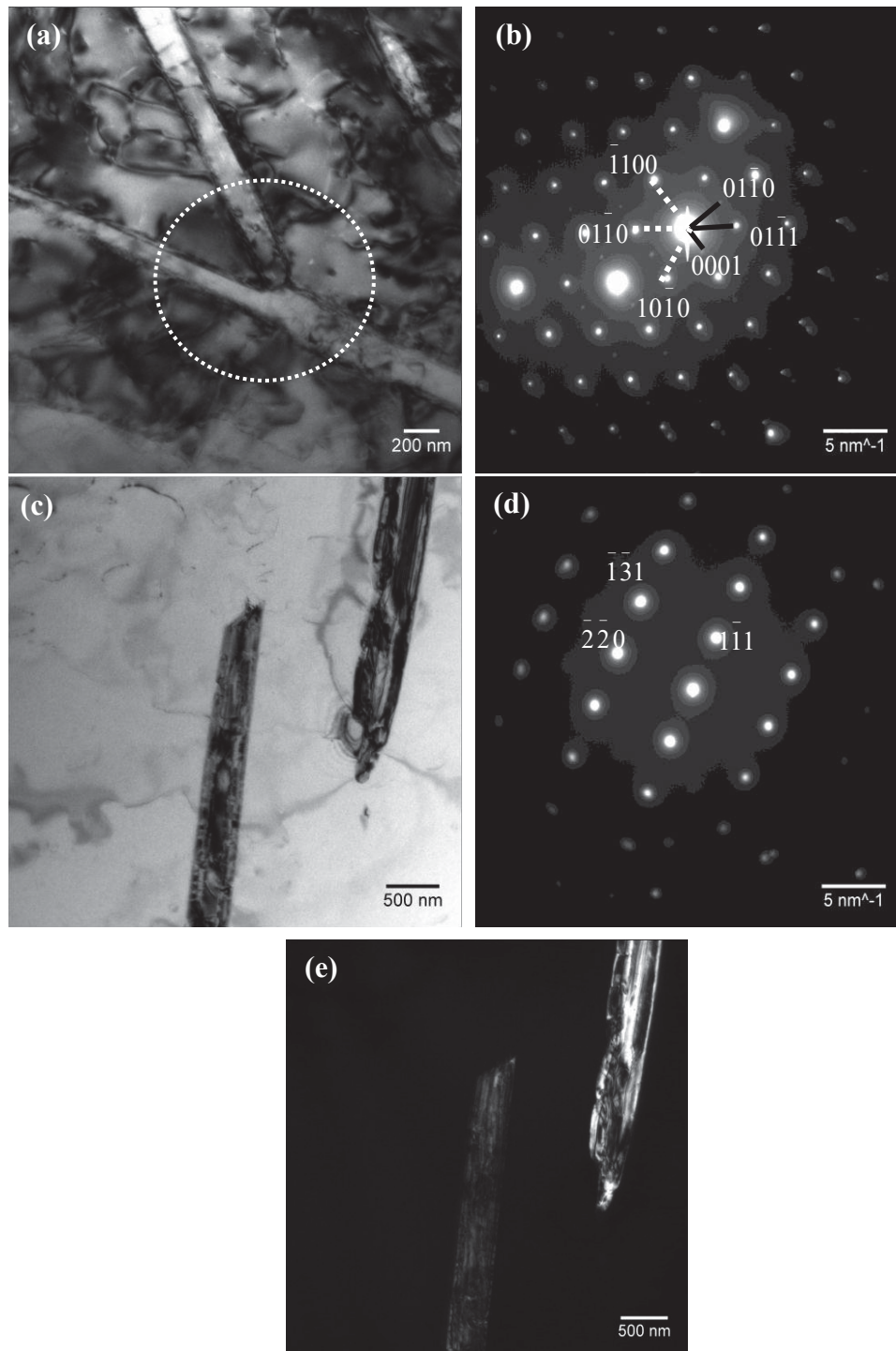


Figure 3.27(a) TEM-BF image obtained from deformed Ti side showed elongated grains, (b) overlapping reflections confirmed α phase along zone axes $[2\bar{1}\bar{1}0]$ and $[0001]$, (c) BF image showing lamellar shaped grains with different contrast, (d) corresponding SAD pattern confirmed formation of fcc phase along $[\bar{1}12]$ zone axis and (e) DF image of the $[\bar{2}\bar{2}0]$ reflection of fcc phase gave further confirmation

Analysis of the clad interface is illustrated in Figure 3.28. The TEM-BF image in Fig. 3.28(a) shows fine needle like features. Analysis of the SAD pattern from these features in Fig. 3.28(b) showed the presence of Fe_2Ti phase coexisting with parent ferrite phase along $[0001]$ and $[\bar{1}11]$ zone axis respectively. The bright contrast in DF image for the $[\bar{1}100]_{\text{Fe}_2\text{Ti}}$ reflection (Fig. 3.28(c)) provides further confirmation.

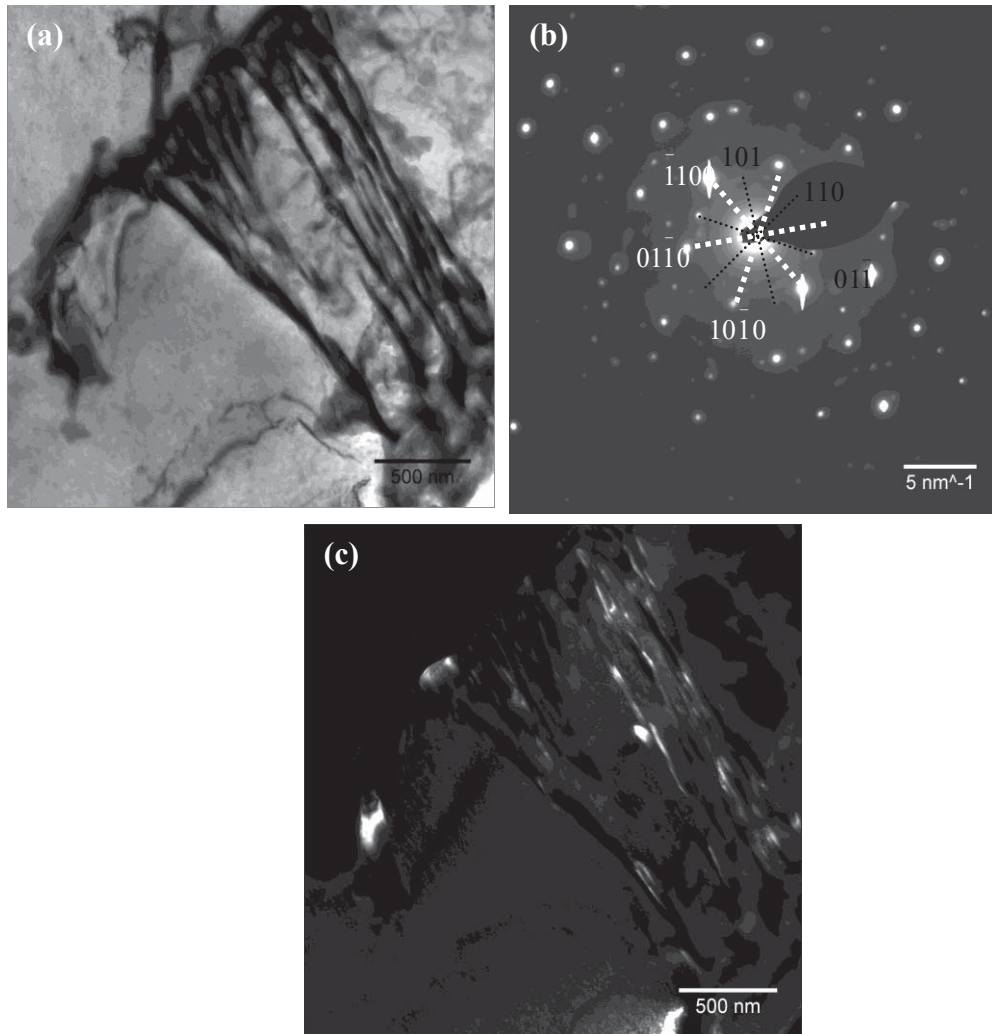


Figure 3.28(a) TEM-BF image showing fine needle like features at the clad interface **(b)** overlapping reflections confirmed coexisting of intermetallic phase Fe_2Ti and parent α Fe along the zone axis $[0001]$ and $[\bar{1}11]$ respectively and **(c)** DF image of the $[\bar{1}100]_{\text{Fe}_2\text{Ti}}$ gives further confirmation

Although, the prediction showed coexistence of Fe_2Ti and FeTi , experimental evidence for Fe_2Ti alone could be obtained. Further, in section 3.7.2 high concentration of Ti and C was reported in the vortex region of the interface. A practical limitation in preparation of thin foil exclusively from a vortex region of a wavy interface posed difficulties in identifying the TiC phase.

3.8 Optimization of post clad heat treatments:

3.8.1 Prediction of evolution of phases at the explosive clad interface:

Post cladding heat treatments are essential for the Fe-Ti and such similar systems to obtain uniform microstructure and microhardness values without residual stresses. The recommended temperature range for stress relieving heat treatments in SS/Ti explosive clads are 538-635 °C [55]. In the present study the ‘clads’ were thermally exposed to temperatures of 500 and 600°C, for various durations ranging from 1-20 h. The variation in microchemistry across the interface was analysed using EPMA, which was used as input to JMatPro® to predict the phases at the interface. Figures 3.29(a) to (d) shows the composition profile and plot of mole fraction (X) of the predicted phases as a function of distance at the two temperatures. Smoothly varying concentration profiles at both the temperatures did not give any indication for the formation of secondary phases at the clad interface. The total diffusion distance was measured as ~4 and ~6 μm at 500 and 600 °C respectively. The average chemical composition at the interface was obtained as 45.4Fe-35.1Ti-19.5C (in wt.%) at 500 °C. A considerable increase in the C concentration was observed at the interface at 500 °C and a similar trend was seen at 600 °C also. JMatPro® computations showed that at 500 °C, in addition to the parent phases Laves (Fe_2Ti) phase with a mole fraction of 0.4

could form up to a distance of 2 μm along the interface (Fig. 3.29(a)). The prediction also showed presence of γ Fe phase ($X_\gamma=0.4$) on MS side very close to the interface, which can be understood in terms of the high amount of carbon, an austenite stabilizer at the interface. Similarly, Fe_2Ti and austenite phases are predicted at temperature of 600 $^\circ\text{C}$, with an extended diffusion zone consisting of these phases up to a distance of $\sim 6 \mu\text{m}$ (Fig. 3.29(d)).

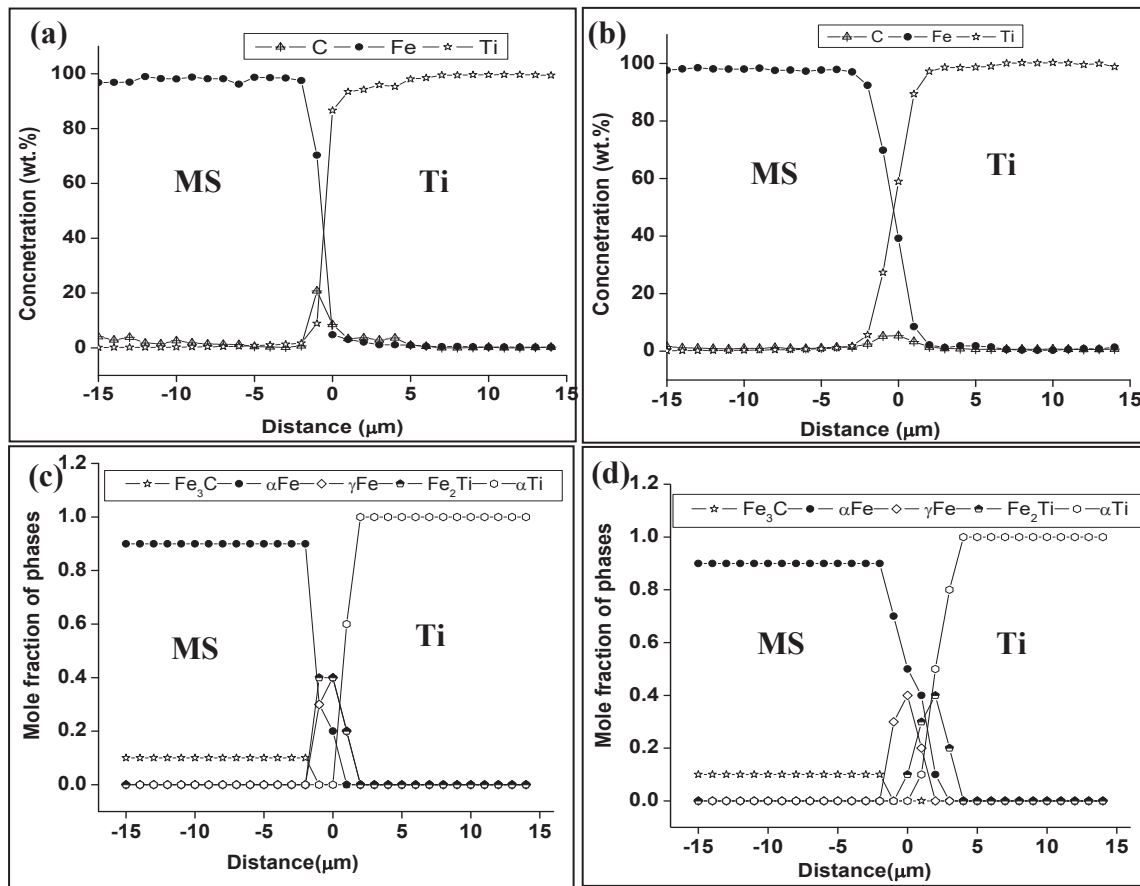


Figure 3.29 Concentration profiles across the MS/Ti explosive clad heat treated at (a) 500 $^\circ\text{C}$, (b) 600 $^\circ\text{C}$ for 1 h and corresponding mole fraction of the phases predicted using JMatPro[®] as a function of distance at (c) 500 $^\circ\text{C}$ and (d) 600 $^\circ\text{C}$ respectively

JMatPro[®] based simulations were carried out to predict the mechanical properties due to variation in composition across the two dissimilar metals at the two temperatures. The simulation was also extended to predict the UTS at 800 °C. Figures 3.30(a) shows the predicted UTS values at temperatures of 500 and 600 °C (time = 1 h) plotted as a function of distance. At 500 °C, the interface showed a high UTS value of ~580 MPa beyond which it reduced to 325 MPa, similar to that of the parent metal Ti. At 600 °C, the high UTS value of ~600 MPa very near the interface drastically reduced to ~230 MPa at the interface (within a narrow region of ~2 μm) which suggested that the interface is susceptible for failure at this temperature (Fig. 3.30(a)). The variation in UTS at 800 °C is given in Fig. 3.30(b). At the highest exposure temperature of 800 °C, JMatPro[®] predicted the coexistence of γ (Fe), Fe₂Ti and TiC phases near the interface on MS side. At the interface, Fe₂Ti, TiC and β Ti phases coexist with relative mole fractions of 0.5, 0.3 and 0.2 respectively. Adjacent to this zone on the Ti side, a 100 μm wide layer consisting of both α and β phases had formed beyond which only α -Ti is observed. The low UTS value of ~250 MPa (3.30(c)) at 800 °C is clearly due to the wide α + β phase region.

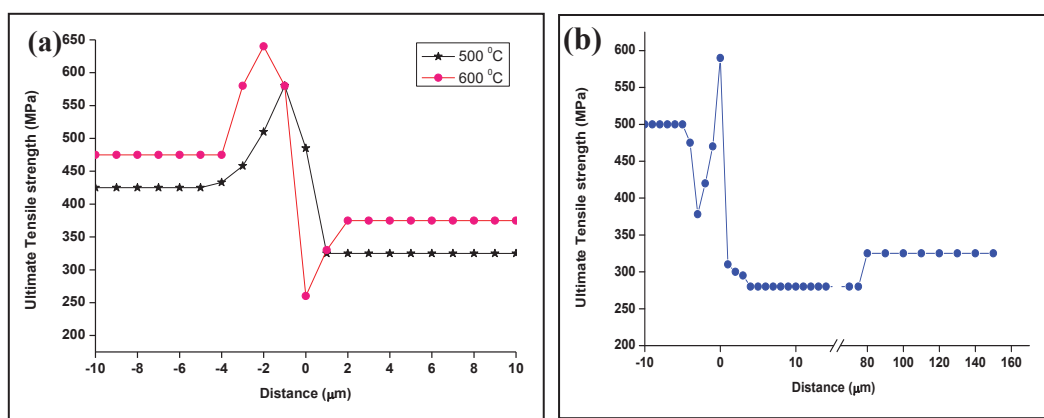


Figure 3.30 Predicted UTS value plotted as a function of distance for MS/Ti explosive clads heat treated at (a) 500 °C, 600 °C and (b) 800 °C respectively

The simulations clearly indicated that the post clad heat treatment temperature for the MS/Ti explosive clads should not exceed 600 °C to avoid the formation of brittle intermetallic phases at the interface.

3.8.2 *Evolution of microstructure during thermal exposure:*

The interface microstructure of the MS/Ti clads after thermal exposure at 500 and 600 °C for various durations has been characterized. The BSE images showing variation in the interface microstructure at 500 and 600 °C is shown in Fig. 3.31. Heat treatment at 600 °C for duration of 1 h showed formation of a narrow zone (~0.6 µm thickness) with high hardness of ~300 HV at the interface (arrow marked in Fig. 3.31(a)). Increase in the duration to 5 h showed increase in the width of the interfacial zone to ~2 µm with a concomitant increase in the hardness to 380 HV (Fig. 3.31(b)). The presence of fine equiaxed grains with no significant change in the hardness (185-190 HV) was observed on MS side. At 500 °C, after 10 h exposure presence of elongated grains was evident on MS side with average hardness of ~200 HV (Fig. 3.31(c)). Increasing the time to 20 h showed equiaxed grains but was accompanied by the formation of a diffusion zone of width ~0.8 µm with high hardness (Fig. 3.31(d)). Correlation with the microchemical data suggested that the continuous band at the interface consisted of intermetallic phases, which was also supported by the high hardness. Hence, it is concluded that the post clad heat treatments need to be carried out at temperatures below 600 °C. The above results clearly established that there are no deleterious phases forming at the interface for durations of up to 10 h at 500 °C (Fig. 3.31(c) and (d)).

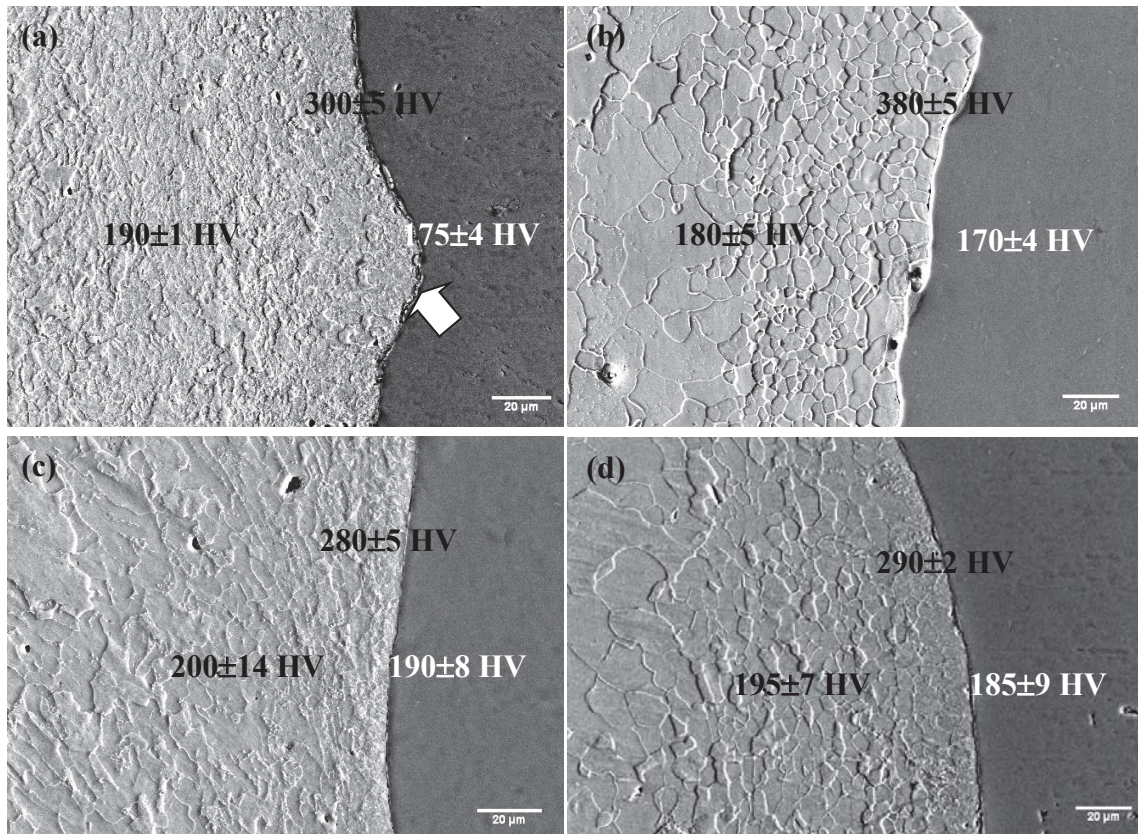


Figure 3.31 BSE images showing variation in the interface microstructure of MS/Ti explosive clads heat treated at 600 °C for (a) 1 and (b) 5 h and 500 °C for (c) 10 and (d) 20 h respectively; corresponding hardness values are superimposed

This suggests that post cladding heat treatments need to be carried out in the range of 500-550 °C for durations not exceeding 10 h to obtain a stress relieved microstructure with optimum mechanical properties.

3.9 Structural changes at the interface of MS/Ti explosive clads during diffusion annealing treatments:

3.9.1 Microstructural and microchemical changes at the interface:

Change in the interface microstructure of MS/Ti explosive clads heat treated at temperatures of 500, 600, 700 and 800 °C for duration of 100 h is shown in Fig. 3.32(a) to (d) with the superposition of the corresponding hardness profiles. At 500 °C, presence of well formed ferrite grains with a reduction in the hardness to ~180 HV was

observed. Exactly at the interface a $\sim 2\ \mu\text{m}$ wide zone with a high hardness of $\sim 370\ \text{HV}$ was observed. On Ti side Widmanstätten α - β Ti microstructure was observed up to a distance of $\sim 27\ \mu\text{m}$ from the interface, the width of which increased to $36\ \mu\text{m}$ as the temperature increased to $600\ ^\circ\text{C}$ (Fig. 3.32(b)). At $700\ ^\circ\text{C}$, growth of the ferrite grains was observed on MS side with a concomitant reduction in the hardness to $\sim 140\ \text{HV}$. Total width of the diffusion zone was obtained as $\sim 72\ \mu\text{m}$ which can be divided into $\sim 4\ \mu\text{m}$ wide interfacial zone and $\sim 64\ \mu\text{m}$ wide Widmanstätten α - β structure (Fig. 3.32(c)).

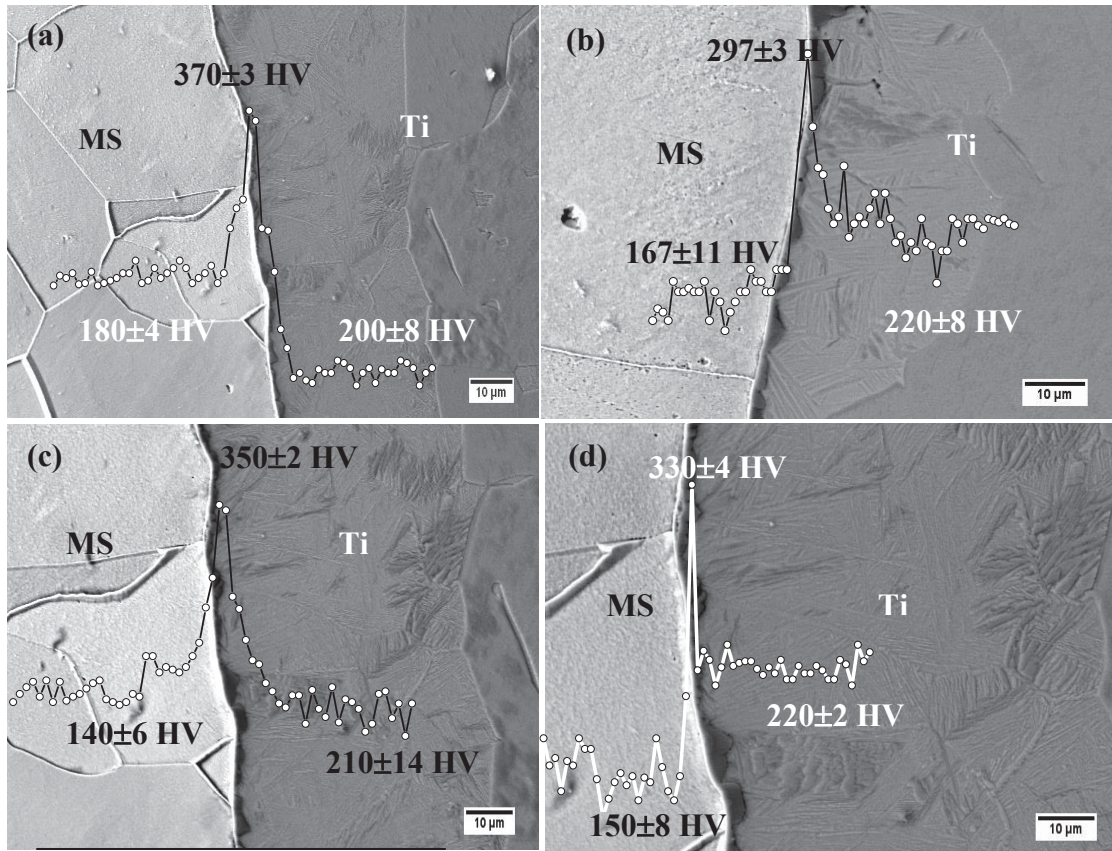


Figure 3.32 BSE images showing variation in the interface microstructure of MS/Ti explosive clads diffusion annealed at (a) 500, (b) 600, (c) 700 and (d) 800 $^\circ\text{C}$ for 100 h respectively; hardness profiles are superimposed

With increase in the temperature to 800 °C, width of the interfacial zone and Widmanstätten region increased to ~6 and ~75 µm respectively. The average hardness values were higher than that observed for duration of 1 h at all temperatures.

Concentration profiles obtained across the interface of the explosive clads heat treated in the temperature range of 500-800 °C for 100 h are shown from Fig. 3.33(a) to (d). At 500 and 600 °C, the concentration profiles resembled smoothly varying solid solution profiles and the total diffusing distances were obtained as ~11 (Fig. 3.33(a)) and 13 µm (Fig. 3.33(b)) respectively. Average composition at the transition point was measured as 44.7Fe-53.1Ti-2.2C (in wt.%). The concentration profiles at 700 and 800 °C (Fig. 3.33(c) and (d)) clearly revealed that diffusion of Fe in Ti was prominent than that of Ti in Fe. Total width of the diffusion zone increased to ~32 and ~112 µm at 700 and 800 °C respectively. At 700 °C, the composition at the interface was measured as 48.5Fe-50.5Ti-1C for ~4 µm which corresponds to the stoichiometric composition of intermetallic FeTi(C) phase [88]. Beyond the cross over point, the concentration remained constant (2.5Fe-96.2-1.2C) up to a distance of ~28 µm on Ti side. A similar trend was observed at 800 °C, where width of the intermetallic zone was ~9 µm and thereafter the concentration remained unchanged at 2.8Fe-96Ti-1.4C up to a distance of ~103 µm. These composition values were superimposed on the binary (Fe-Ti) [7] and ternary (Fe-Ti-C) [131] equilibrium phase diagrams to identify the phases. The presence of Widmanstätten α - β Ti phase (Fig. 3.33(d)) was rationalized based on the transformation of high temperature β Ti phase which was stabilized by the presence of ~2 wt.% of Fe in Ti.

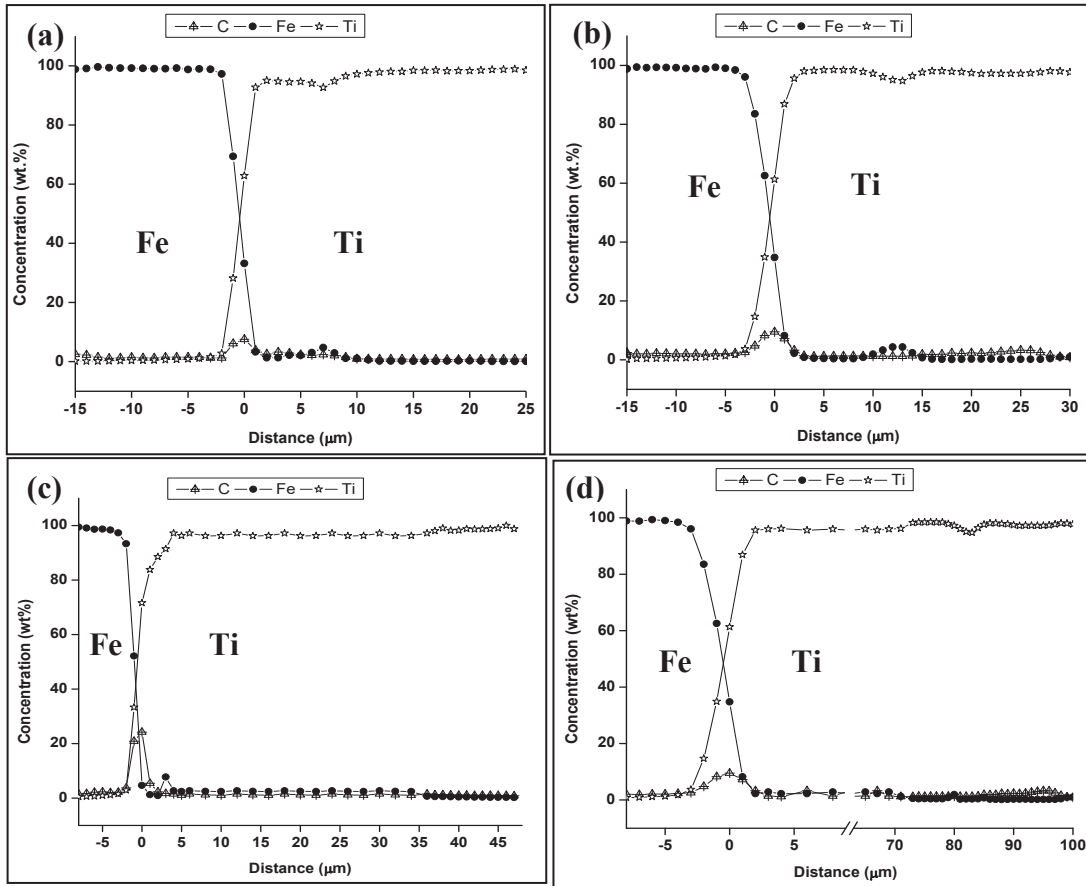


Figure 3.33 Concentration profiles obtained across the MS/Ti explosive clads heat treated at (a) 500 °C, (b) 600 °C, (c) 700 °C and (d) 800 °C for 100 h respectively

According to the Fe-Ti phase diagram, presence of more than 0.08 at.% Fe will stabilize the β Ti phase at ambient temperature. Beyond $\sim 103 \mu\text{m}$ (from the interface), the concentration of Fe decreased and the composition reached the base material composition of Ti.

3.9.2 Prediction and confirmation of the phases at the explosive clad interface:

Figure 3.34 (a) and (b) shows the JMatPro[®] computed mole fraction of the phases formed at the interface of the MS/Ti clads heat treated for 100 h at 500 and 800 °C. At 500 °C, in addition to the parent phases, Laves (Fe_2Ti) phase with a mole

fraction of 0.4 was predicted for a distance of 8 μm along the interface (Fig. 3.34(a)). The prediction showed presence of γ Fe phase ($X_\gamma=0.7$) on MS side very close to the interface, due to high concentration of carbon, an austenite stabilizer. At the highest exposure temperature of 800 $^\circ\text{C}$, it can be envisaged from the graph that α and γ phases of Fe coexist upto a distance of 2 μm followed by a three phase (γ -Fe+ Fe_2Ti +TiC) region near the interface on MS side. At the interface, Fe_2Ti , TiC and βTi phases coexist with relative mole fractions of 0.5, 0.3 and 0.2 respectively. Adjacent to this zone on the Ti side, a 100 μm wide layer consisting of both α and β phases had formed beyond which only α -Ti was observed (Fig. 3.34(b)).

XRD patterns obtained from the cross-section of specimen heat treated for 100 h at 500 and 800 $^\circ\text{C}$ is shown in Fig. 3.35. The presence of Laves phase and austenite phases at 500 $^\circ\text{C}$ were unambiguously confirmed by the XRD analysis. At 800 $^\circ\text{C}$, although unique Bragg reflections corresponding to Fe_2Ti intermetallic phase and titanium oxide were observed in addition to the parent metals, it was not possible to unambiguously identify other phases predicted by JMatPro[®].

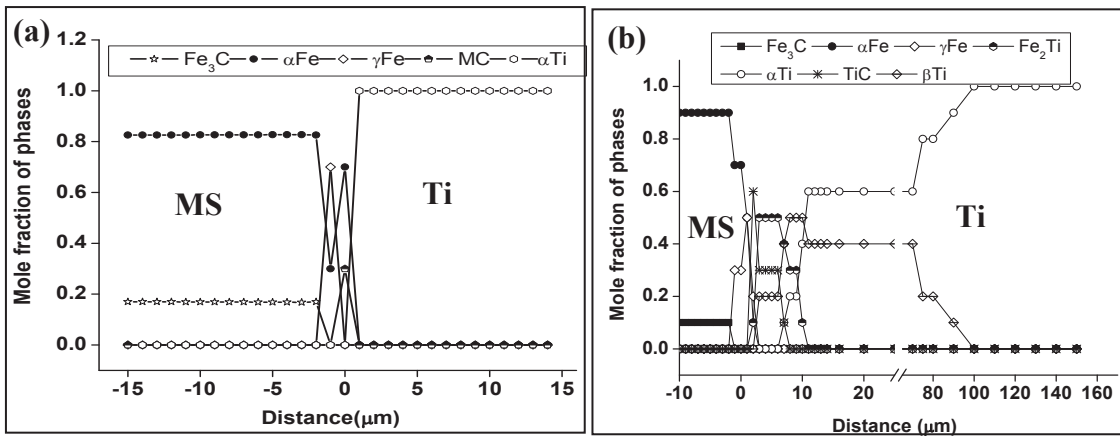


Figure 3.34 JMatPro[®] predicted mole fraction of phases across MS/Ti explosive clads heat treated at (a) 500 $^\circ\text{C}$ and (b) 800 $^\circ\text{C}$ for 100 h respectively

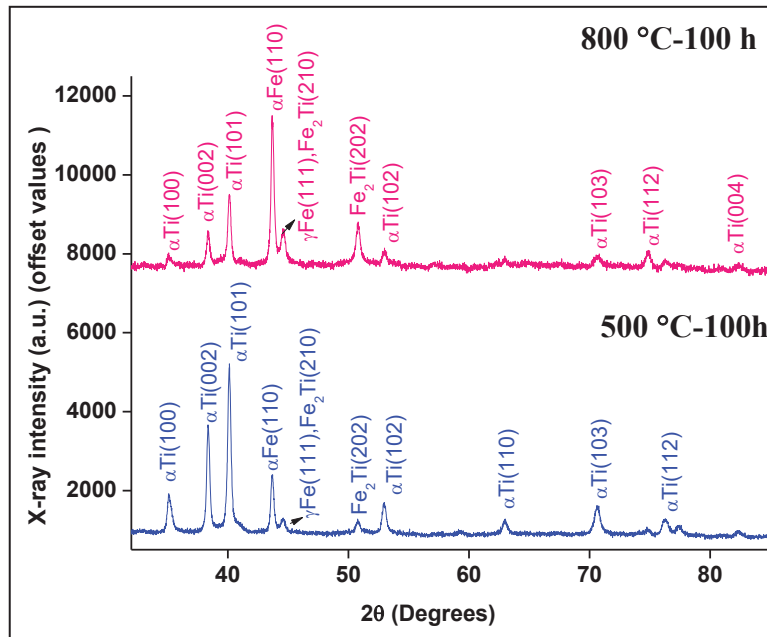


Figure 3.35 XRD patterns obtained from the cross-section specimens of the explosive clad heat treated at 500 and 800 °C (for 100 h duration)

3.10 Summary:

The important conclusions on the study of “**Microstructure and property evaluation in Fe-C/Ti friction and explosive joints in ‘as welded’ and heat treated conditions**” are as follows:

- Formation of a continuous reaction zone consisting of intermetallic phases and oxides in conventional diffusion couples of mild steel (MS) and Ti posed difficulties in joining the two dissimilar metals.
- Friction welds of MS and Ti have been successfully fabricated using optimized values of friction force, upset force, burn off length and rotational speed (0.8 tonnes, 1.6 tonnes, 3 mm and 1000 rpm respectively).

- Fine FeTi intermetallic phase was present in isolated regions at the friction weld interface, which did not affect its mechanical properties.
- A sinusoidal wavy interface was observed in MS-Ti explosive joints using the cladding parameters of flier plate velocity, detonation velocity, type of explosive and load ratio as 300 m/s, 2000 m/s, homogeneous mixture of Ammonium nitrate + TNT and 1.07 respectively.
- Fe₂Ti intermetallic phase formed at isolated regions in the vortices of the waves at the clad interface. Deformation induced phase transformations due to shock loading conditions led to formation of acicular martensite and metastable fcc phase in MS and Ti respectively.
- Based on the interface microstructure and JMatPro[®] simulations, the post cladding heat treatment for the MS/Ti explosive clads is recommended in the temperature range of 500 - 550 °C for durations not exceeding 10 h.
- The reaction zone was limited to 12 μm in friction joints while it was 120 μm in explosive clads at 800 °C for 100 h.

Chapter 4

Structural changes during deformation and annealing in 304LSS/Ti-5Ta-2Nb explosive clad joints

4.1 Introduction:

The dissolver for reprocessing of fast reactor spent fuel is made of CPTi or Ti alloys due to their excellent corrosion resistance in highly oxidizing environments of boiling 11.5 M nitric acid [1]. Among several Ti based alloys, an $\alpha+\beta$ alloy of nominal composition Ti-5Ta-2Nb exhibited remarkable corrosion resistance (corrosion rate <1 mpy) hence is a candidate structural material for dissolvers. This alloy has also been used as filler material in welds of CPTi for fabricating the dissolver. Since the rest of the plant operates at low temperatures (<100 °C) and employs dilute nitric acid austenitic stainless steel 304LSS was used. Fabrication of good quality joints of SS-Ti/Ti alloys with adequate bond strength and corrosion resistance is a challenging task [6]. Different approaches/techniques employed over the years for joining Ti and Fe alloys aimed at prevention of formation of undesirable brittle intermetallic phases if not at least disperse them as isolated phases to preserve the integrity of the joint. It was possible to avoid the formation of lamellar $\beta\text{Ti(Fe)}$ phase as well as a continuous network of intermetallic phases by shortening the holding times at high temperature or by introducing a suitable interlayer which would form continuous solid solutions with both Fe and Ti. Some of the solid state welding processes are diffusion bonding, friction welding, friction stir welding and explosive cladding. Advantage of these methods over fusion welding processes include absence of heat affected zone, no melting of base metals, high energy density of the source and formation of metallic bond by severe plastic deformation [158].

The extent of liquid zone formation at the interface of Fe-Ti diffusion couples has been studied by Wu et al. [14] in the temperature range of 1100-1400 °C for

durations ranging from 10 to 90 s. Attempts to join 300 series austenitic stainless steel with CPTi by diffusion bonding were unsuccessful due to the formation of intermetallic phases like FeTi, Fe₂Ti, Cr₂Ti, Fe₂Ti₄O, NiTi, NiTi₂ and σ , despite obtaining acceptable bond strength [25, 26]. For joining materials with wide variations in their physical, mechanical and corrosion properties such as Cu-SS, Ti-SS, Al-Cu, Mg-Al, explosive cladding was successfully demonstrated as a viable method [119]. Akbari et al. [159] proposed a welding domain (considering only impact velocity and explosive load) for welding 304SS to CPTi. There was high propensity for formation of molten zones and brittle intermetallic phases for high explosive loads (i.e. high impact energy) [49]. A thin (≤ 1 mm) interlayer between base and flier plate reduced the impact energy during explosive cladding and prevented the extensive plastic deformation of the parent metals [52, 53]. The microstructure changed as a function of distance from the clad interface in SS/Ti joints, which was systematically studied by Song et al. [160] to understand the consequence of brittle phase formation on the performance of the joints.

In this chapter, the evolution of microstructure in explosive clad joints of 304LSS (SS) and Ti-5Ta-2Nb alloy (TiTaNb) has been investigated. Further, post clad heat treatments for the explosive joints were optimized based on the evolution of interface microstructure and bond strength of the joints. This chapter is organized in the following sequence: Section 4.2 describes the characterization of SS and TiTaNb ‘as received’ plates; section 4.3 and 4.4 deal with the assessment of the joints and optimization of post clad heat treatments for the explosive joints. Section 4.5 describes the structural changes in base and flier plates due to deformation during explosive cladding process. An in-depth study on the stability of deformation induced phases

during thermal exposure is elaborated in section 4.6 including evaluation of the kinetics and mechanism of reversion. Section 4.7 deals with the evolution of interface microstructure and microchemistry at elevated temperature and the important findings are summarized in section 4.8.

4.2 Characterization of ‘as received’ SS and TiTaNb alloy:

The SE images of base (SS) and flier (TiTaNb) plates are shown in Fig. 4.1(a) and (b) respectively. Equiaxed austenite grains and equiaxed α matrix (TiTaNb) are evident in the micrograph. Average hardness values of SS and TiTaNb were measured as 230 ± 5 and 200 ± 10 HV respectively. The room temperature XRD patterns of the two parent metals are shown in Fig. 4.1(c) and (d). Analysis of the XRD patterns confirmed presence of fcc(γ) phase of Fe in SS (Fig. 4.1(c)) and α (hcp) phase in TiTaNb alloy (Fig. 4.1(d)). Due to overlap between the (110) and (211) peaks of β (Ti) at 2θ positions of 38.2° and 70.4° with (002) and (103) peaks of α (Ti) respectively, unambiguous identification of β (Ti) phase was difficult.

4.3 Assessment of SS/TiTaNb explosive clad joints:

The fabrication of explosive clad joints of SS and TiTaNb alloy was described in section 2.2.4 of Chapter 2. Although, explosive cladding is a non-fusion welding process localized melting of metals is possible due to adiabatic heating of gases compressed between plates, internal heating of component metals due to passage of shock waves and heat of detonation of the explosive [39]. In such regions the probability for formation of detrimental intermetallic phases is high. Hence, qualification of the clad with respect to defects and properties is crucial.

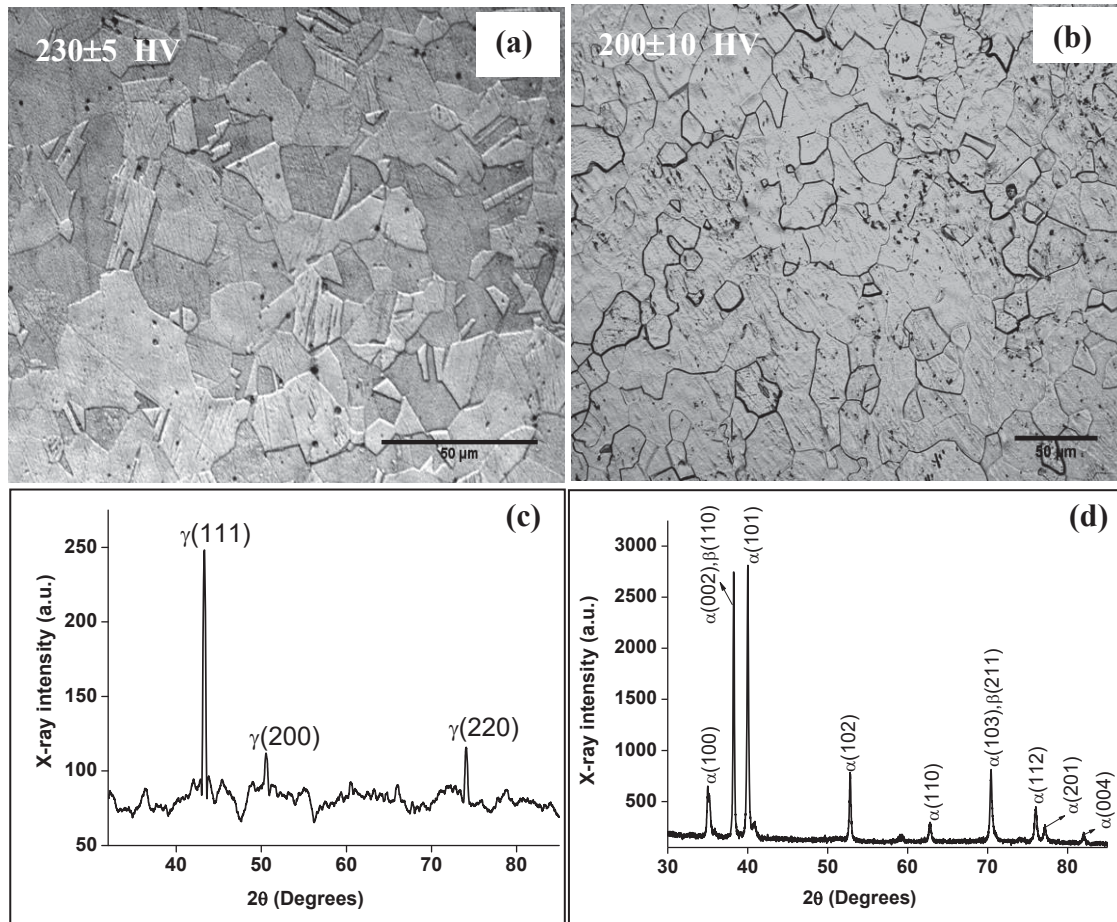


Figure 4.1 SE images of (a) SS, (b) TiTaNb alloy in ‘as received’ condition with microhardness value superimposed and corresponding XRD patterns for (c) SS and (d) TiTaNb respectively

Ultrasonic examination of the joint revealed de-bonding only at the edges (Fig. 4.2) which was avoided during specimen extraction for further studies.

Specimens were fabricated for evaluation of mechanical property as described in section 2.3 of Chapter 2 [121]. Bond strength of the interface was evaluated by tensile testing on transverse section as per ASTM E8 standard. The stress-strain curve obtained during the tensile testing is shown in Fig. 4.3(a). The values of both UTS (301 MPa) and YS (276 MPa) were lower compared to base metal. Examination of the fracture surface (Fig. 4.3(b)) showed cleavage facets (circled) typical of a brittle mode of failure.

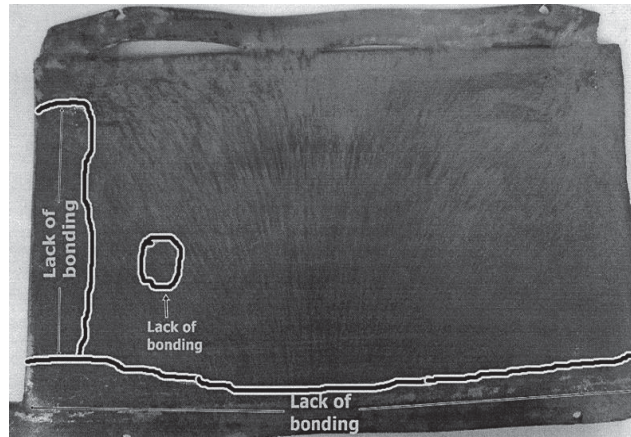


Figure 4.2 Ultrasonically tested SS/TiTaNb clad showing de-bonding at the edges

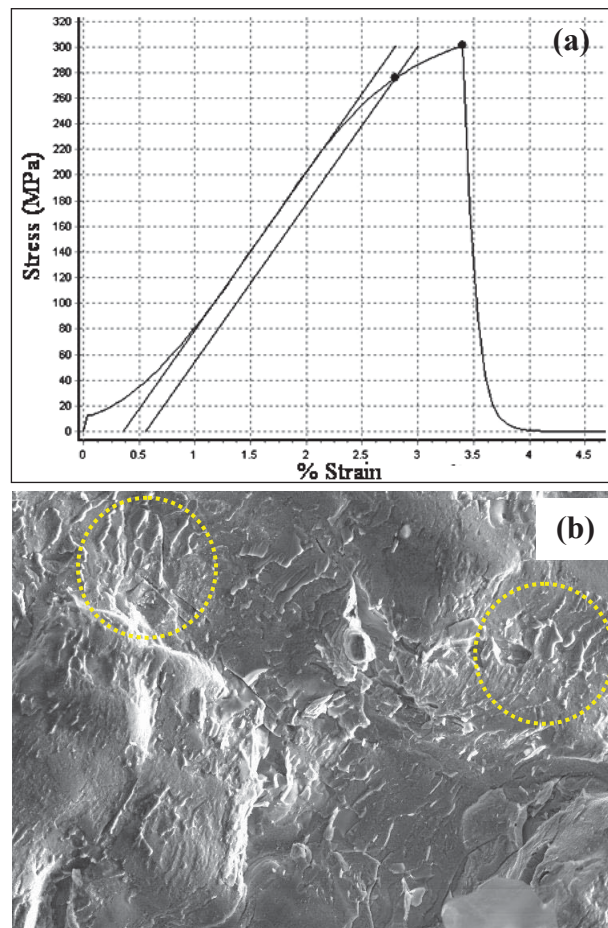


Figure 4.3(a) Stress vs strain curve for the clad and **(b)** fracture surface showed brittle mode of failure

BSE image of the SS/TiTaNb clad interface is shown in Fig. 4.4. It is evident from the micrograph that the interface is devoid of vortices indicating a good bonding between the metals. A high value of interface hardness of ~ 425 HV, higher than that of the parent metals was observed. A closer look at the two parent metals showed structures which are quite different from the annealed structures given in Fig. 4.1. A high average value of ~ 375 and ~ 210 HV on the SS and TiTaNb side indicated deformation of the parent metals during cladding which will be dealt with in detail in subsequent sections.

4.4 Optimization of post clad heat treatments:

In order to remove the residual stresses from the bond zone and to attain uniform microstructure and microhardness values, stress relieving heat treatments have been suggested for SS/Ti explosive joints [55]. It is also reported that annealing treatments at temperatures not exceeding 1000°C is necessary during fabrication of large components from explosive clads by hot rolling [57]. Thermal exposure subsequent to

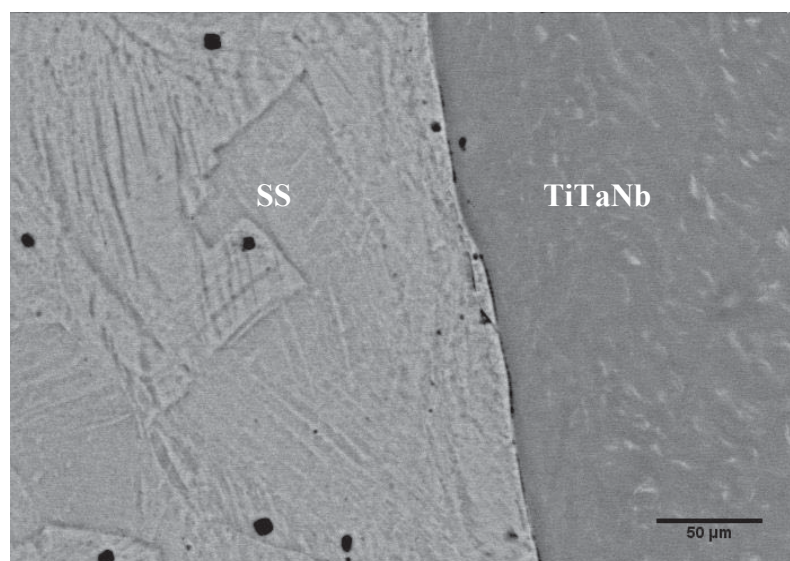


Figure 4.4 BSE image showing interface microstructure of the clad

cladding enhances interdiffusion of alloying elements leading to the formation of diffusion zones at the clad interface [55, 56, 57, 161]. The nature and distribution of phases that formed due to interdiffusion at the interface and the width of the reaction zones influenced the shear strength and bend ductility of the joints.

The post clad heat treatments for the explosive joints were optimized based on the evolution of interface microstructure with thermal exposure. It was also essential to ensure that the effect of deformation is minimized in the parent metals to obtain good corrosion properties. It was reported that post cladding heat treatment need to be carried out in the temperature range of 538-634 °C for SS-Ti explosive joints [55]. While a lower temperature may not be adequate for stress relieving, high temperatures may lead to the formation of intermetallic phases due to interdiffusion. Hence, post cladding treatment was carried out at temperatures of 550 and 600 °C for different durations.

Figures 4.5(a) to (d) show the BSE images obtained from the cross-section of the explosive clads heat treated at temperatures of 550 and 600 °C for various durations. At 550 °C, the interface is wavy and no significant microstructural change was seen at the interface, although the hardness values of the base, flier plate and interface showed a reduction due to annealing. As the temperature was increased to 600 °C, the microstructure showed no significant change except formation of porosities parallel to the clad interface on SS side (Fig. 4.5(c)) which further increased with duration of exposure (Fig. 4.5(d)). However, a high hardness of ~410 HV was observed at the clad interface suggesting formation of secondary phases.

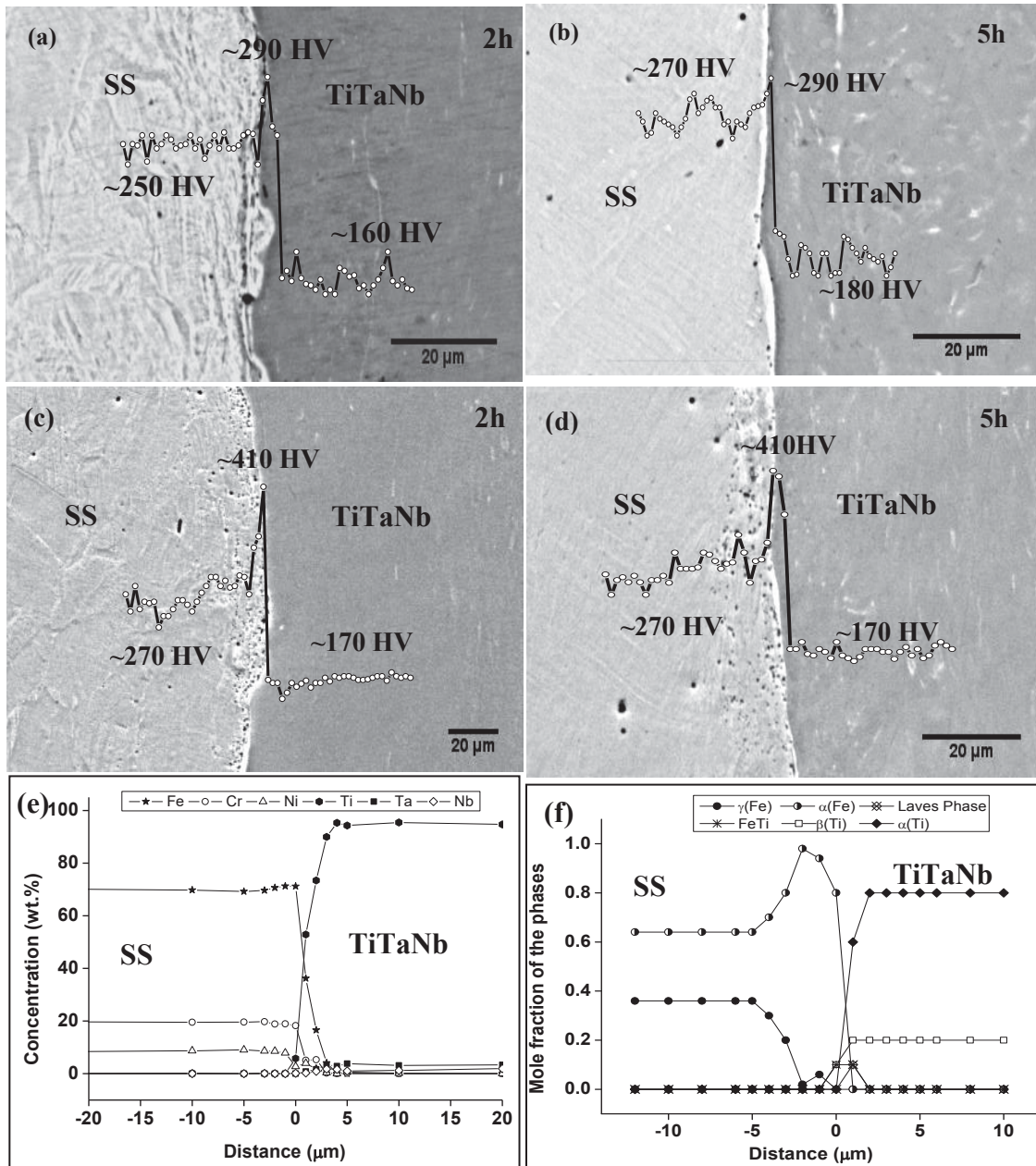


Figure 4.5 BSE images obtained from the cross-section of the clad heat treated at temperatures of 550 °C for 2 and 5 h (a and b) and 600 °C for 2 and 5 h (c and d) respectively; hardness profiles are superimposed on the micrographs, (e) Concentration profiles obtained across the clad interface at 550 °C for 5 h and (f) mole fraction of the phases predicted using JMatPro®

Formation of reaction zones containing brittle intermetallic phases and metastable microstructure was known to have detrimental effect on the bond strength of the explosive clad. Variation in microchemistry across the interface for a typical case of 5 h exposure at 550 °C is given in Fig. 4.5(e), which was used to predict (by JMatPro®) the phases that are likely to form at the interface (Fig. 4.5(f)). Smoothly varying concentration profiles showed a maximum diffusion distance of ~5 µm. The JMatPro® computations revealed presence of stabilized α -Fe and β -Ti phases (Fig. 4.5(f)). Intermetallic phases such as FeTi and Laves Fe₂Ti can form within the reaction zone due to interdiffusion of alloying elements. However, the width of the intermetallic phases was limited to ~2 µm.

Using the input on type and mole fraction of phases, the variation in UTS was computed. To validate this approach for the explosive clad, UTS values for the base and flier plates (before and after explosive cladding) were estimated which showed agreement with the experimental data [121]. Figure 4.6(a) shows the variation in UTS across the interface at 550 °C (5 h exposure). Despite an abrupt decrease in UTS at the clad interface the value (510 MPa) was comparable to the SS and TiTaNb parent metals. The simulation was extended to 600 °C using the composition profile at this temperature and duration of 5 h (Fig. 4.6(b)), which showed a similar trend but with a lower value of UTS (443 MPa). Analysis of the microstructure and microchemistry of the clads heat treated at 600 °C showed formation of Kirkendall porosities on SS side, high hardness at the interface and consequent reduction in the UTS value. Based on the above results, it was understood that the explosive clads had to be heat treated at temperatures <600 °C.

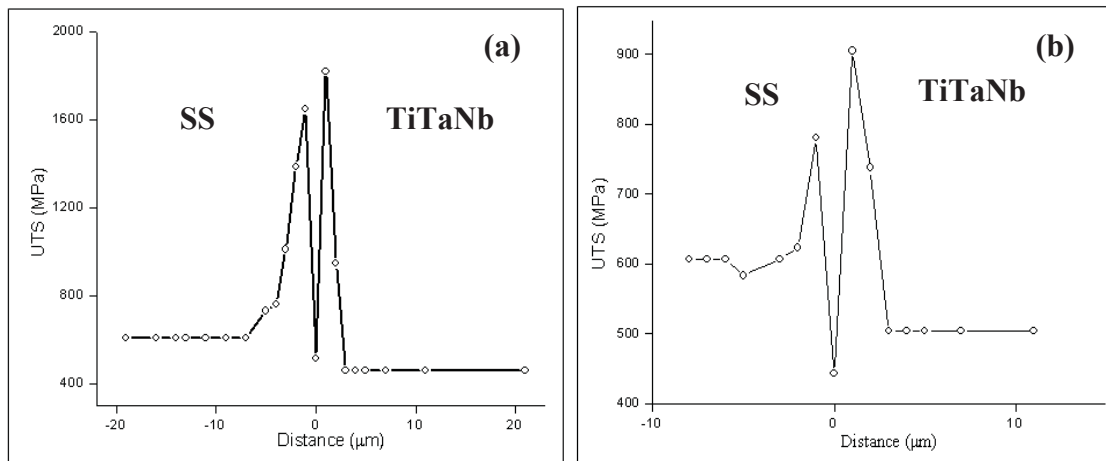


Figure 4.6 Predicted UTS across the clad interface at (a) 550 °C and (b) 600 °C respectively

However, it was essential to optimize the temperature-time window in concurrence with the knowledge on evolution of interface microstructure due to interdiffusion of alloying elements across the clad interface. Increase in the exposure time to 10 h at 550 °C showed reduction in hardness comparable to parent metals, while 20 h exposure showed formation of intermetallic zones as a continuous layer parallel to the interface, which was undesirable (described in detail in a subsequent section). Hence, a post clad heat treatment at 550 °C for duration not exceeding 10 h was found to be optimum.

4.5 Deformation induced structural changes in parent metals:

4.5.1 Microstructural changes in base and flier plates of explosive joints:

Enlarged view of the deformed parent metals SS and TiTaNb are shown in Fig. 4.7(a) and (b) respectively. Deformed austenite grains and mechanical twins in Fig. 4.7(a) possessed a high hardness of ~375 HV. Elongation of grains in the detonation direction was observed on the TiTaNb side and the measured average hardness value was 220 ± 10 HV. Additionally fine needle like features within the deformed grain were

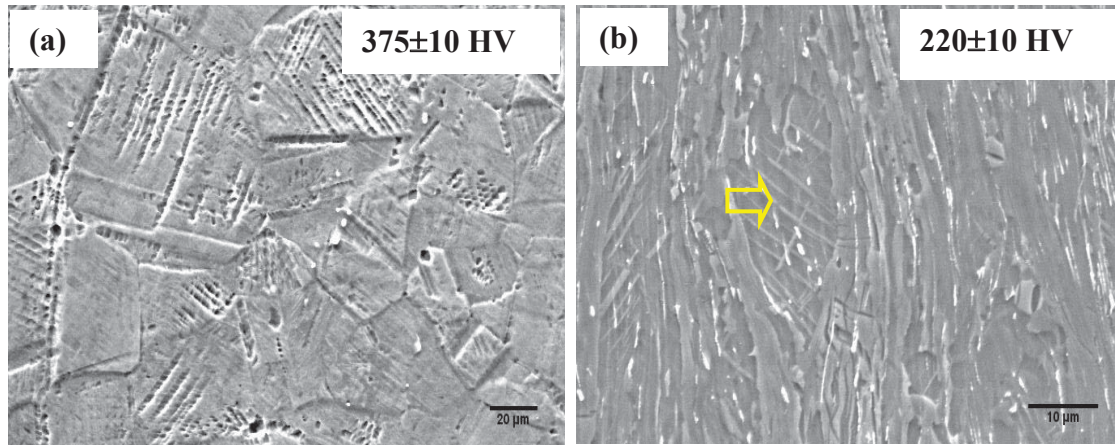


Figure 4.7 SE images showing signatures of deformation in (a) base – SS and (b) flier - TiTaNb plates respectively

observed (arrow marked) in TiTaNb alloy. Severe plastic deformation during the explosive cladding process was reported to be responsible for the elongation of grains in SS/Ti explosive joints [47], which was also supported by our study on Mild steel/Ti joints in Chapter 3.

XRD patterns obtained from the deformed SS and TiTaNb sides of the clad are shown in Fig. 4.8(a) and (b) respectively. In addition to the fcc γ phase, strong Bragg reflections for bcc α were observed in SS which provided an evidence for the presence of strain induced martensite (α') together with the parent γ phase. Analysis of the XRD pattern in Fig. 4.8(b) showed Bragg reflections at 2θ positions of 38.1° , 44.3° , 64.5° and 77.5° in addition to distinct peaks corresponding to parent α phase. The peaks at 44.3° and 64.5° have high intensity and were uniquely identified as (200) and (220) planes of fcc Ti phase. However, the peaks at 38.1° and 77.5° agree with both $(002)_\alpha / (111)_{fcc}$ and $(201)_\alpha / (311)_{fcc}$.

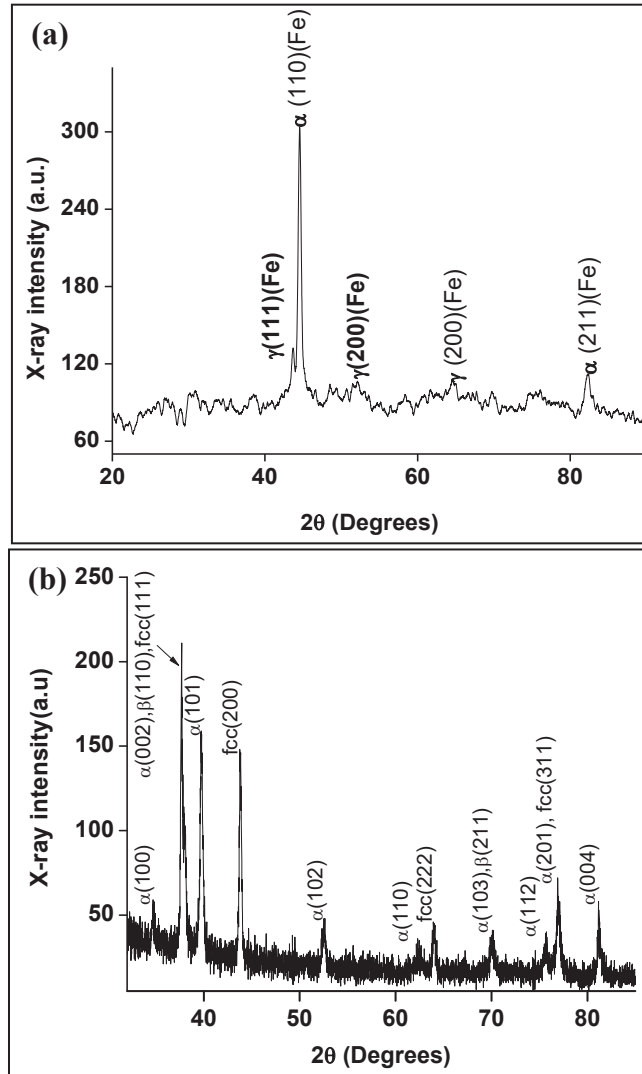


Figure 4.8 XRD patterns obtained from deformed (a) SS and (b) TiTaNb sides of the clad providing evidence for the formation of deformation induced phases during cladding

For further confirmation all the peaks in Fig. 4.8(b) were compared with all possible reflections of Ti phases and compounds which unambiguously confirmed the presence of metastable fcc Ti phase.

4.5.2 Confirmation of metastable phases by TEM investigations:

Typical TEM-BF image of the deformed SS is shown in Fig. 4.9(a). Three distinct features are clearly revealed in this micrograph namely shear bands, fine needle like inter weave and very fine twins. Analysis of the SAD pattern (Fig. 4.9(b)) obtained

from the fine features (circled in Fig. 4.9(a)) confirmed the formation of deformation (γ) twins along $[011]$ zone axis. The SAD pattern in Fig. 4.9(c) from the intersecting features (arrow marked in Fig. 4.9(a)) showed an overlap between fcc and bcc structures suggesting the existence of ferrite phase in the austenite matrix. The high hardness and fine deformation twins support the formation of strain induced α' martensite (SIM).

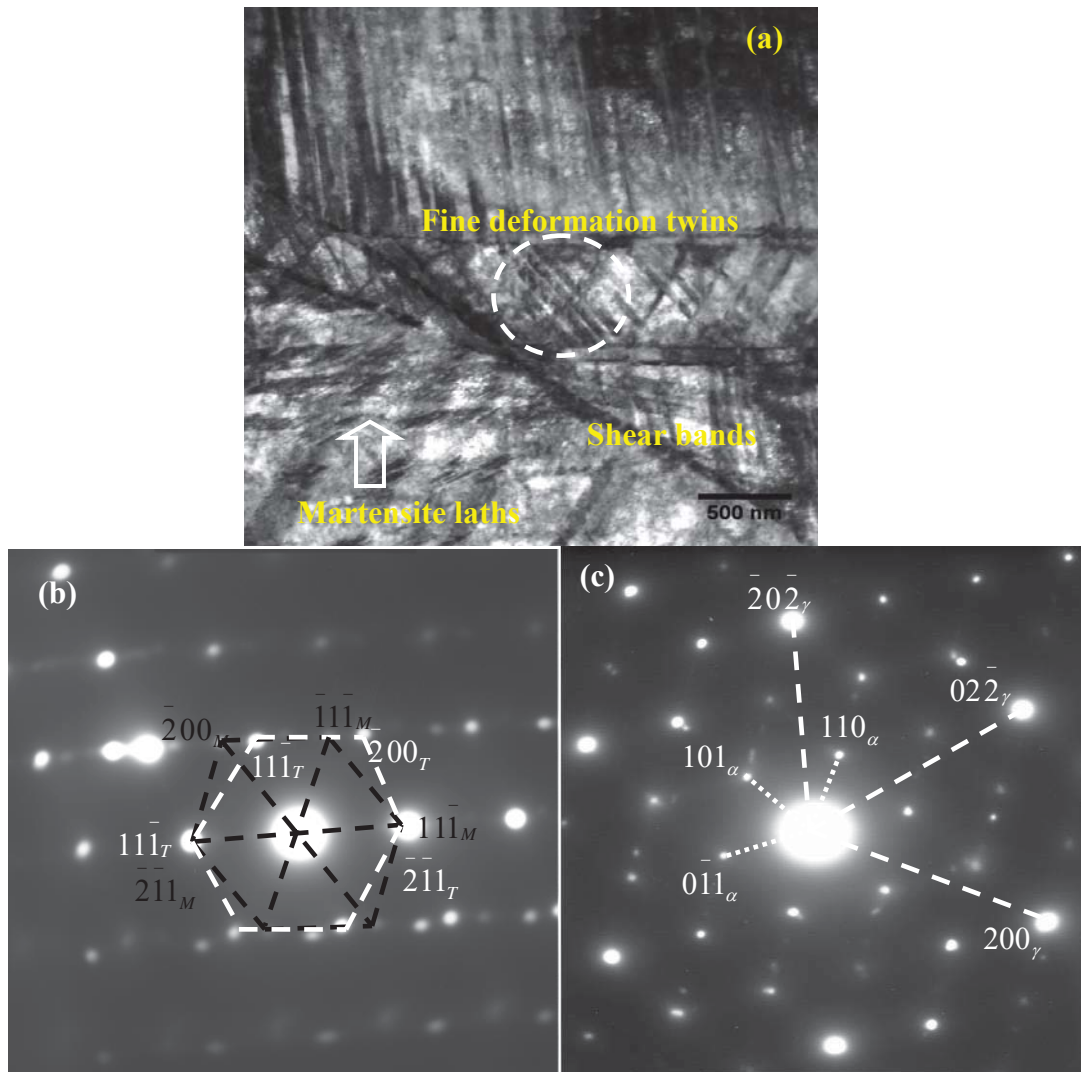


Figure 4.9 TEM (a) BF image showing deformed microstructure of SS, (b) SAD pattern obtained from circled region in Fig. 4.9(a) showing deformation twins of γ along $[011]$ zone axis and (c) overlapping reflections of arrow marked region showing coexistence of bcc and γ phases along $[\bar{1}11]$ and $[\bar{1}\bar{1}1]$ zone axis respectively

Nucleation of martensite laths on the deformation bands was evident from this result. The formation of SIM was rationalized in terms of high strain rates ($>10^6/s$) [151] in SS base plate exceeding that in shock loading conditions leading to deformation induced phase transformation during explosive cladding.

Detailed TEM analysis also helped to understand the morphology and other attributes of the fcc phase in TiTaNb alloy. A representative TEM-BF image and the corresponding electron diffraction pattern are shown in Fig. 4.10(a) and (b) respectively. Analysis of the SAD pattern obtained from the circled region in Fig. 4.10(a) confirmed elongation of α grains of Ti along $[\bar{1}2\bar{1}3]$ and $[0001]$ zone axis. Figure 4.10(c) shows globular precipitates of 150-200 nm diameter present in few regions. The SAD pattern in Figure 4.10(d) from one such globular particle corresponded to β (bcc) phase of Ti along $[012]$ zone axis. The DF image (inset in Fig. 4.10(d)) of the $[\bar{1}21]_{\beta}$ reflection (circled spot in Fig. 4.10(d)) confirmed that the β phase is globular despite the deformation.

A typical TEM-BF image obtained from TiTaNb alloy in another region is shown in Fig. 4.11(a), revealing the presence of fine needle like features (marked in figure) of average size 50 nm within the elongated grain. The diffraction pattern obtained from this circled region is shown in Fig. 4.11(b). Analysis of the diffraction pattern confirmed the presence of fcc phase along $[\bar{1}14]$ zone axis with a lattice parameter of 0.48 nm. Analysis from a large number of regions confirmed that the fine needle like features correspond to fcc Ti, the metastable phase formed during deformation. Based on our experimental results and available literature, mechanism of

$\alpha \rightarrow \text{fcc}$ transformation has been understood in terms of plastic deformation of α phase under the influence of high pressure and strain rate ($>10^6$ /s) [155] during explosive loading. High pressure shock waves traveling through the hcp matrix cause severe plastic deformation leading to generation of a large number of defects such as dislocations in the lattice.

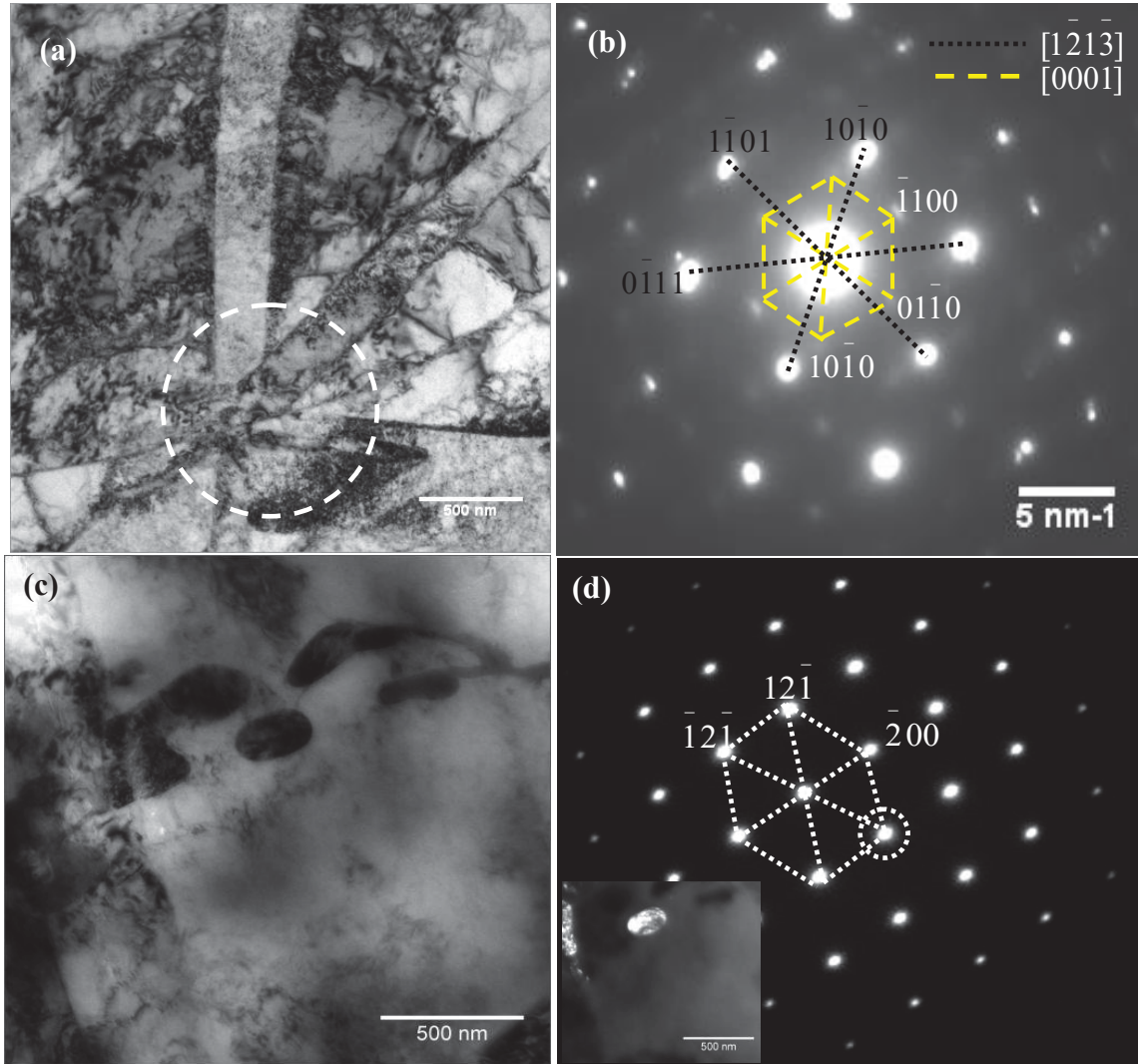


Figure 4.10 TEM (a) BF image showing elongated grains of TiTaNb clad, (b) overlapping reflections in the SAD pattern (obtained from circled region) confirmed α phase along $[1213]$ and $[0001]$ zone axes, (c) BF image of a globular particle and (d) SAD pattern confirmed presence of β phase of Ti along $[012]$ zone axis, which was further confirmed by the DF image of the $[121]_{\beta}$ reflection (inset)

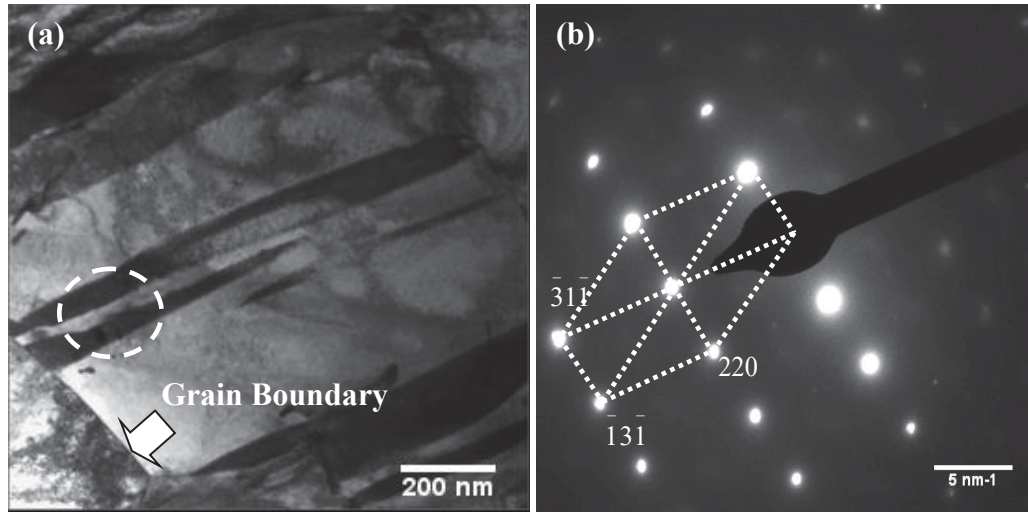


Figure 4.11 TEM (a) BF image showing elongated grains within which fine needle like features were present and (b) corresponding SAD pattern confirmed the presence of metastable fcc phase of Ti along $[114]$ zone axis

Presence of high number density of defects distorted the hcp lattice changing the stacking sequence of atomic planes from ABABAB...(hcp) to ABCABCABC... (fcc). Also, the strain field due to the large atomic radius of solute elements Ta (200 pm) and Nb (198 pm) in Ti (176 pm) matrix, offered additional driving force for the transformation apart from the compressive stresses generated during the explosive cladding process. Based on the above analysis, the structure of TiTaNb was summarized as $\alpha(\text{hcp}) + \beta(\text{bcc}) + \gamma(\text{fcc})$.

4.6 Stability of metastable phases during thermal exposure:

4.6.1 Study of reverse transformation of metastable phases by HTXRD:

Due to severe plastic deformation the explosive joints were found to be unsuitable for industrial application. It was reported that presence of SIM degrades the mechanical as well as corrosion properties of the steel [64, 65]. Kurc et al. [162] reported a drastic reduction in plasticity from 32 to 0.68% and resistance to pitting

corrosion with increase in the volume fraction of α' martensite. A similar observation of decreased corrosion resistance in 0.5M HCl+2M H₂SO₄ was reported by Alvarez et al. [66] due to presence of α'/γ interfaces. Similarly, the presence of non-equilibrium phases influenced the corrosion and mechanical properties of multiphase Ti alloys, literature on which is very scarce [73, 163]. A brittle mode of failure has been reported in case of Ti-20Zr-6.5Al-4V alloy due to the presence of fcc Ti phase [73]. Fcc phase inhibits movement of slip at the α/β interface leading to decrease in ductility of the alloy [74]. Presence of metastable Widmanstätten and acicular martensite phases influences the pitting corrosion in Ti-6Al-2Sn-4Zr-2Mo alloy [163]. Mythili et al. [164] reported that polygonal microstructure of α phase with globular β particles distributed in the matrix exhibited the best corrosion resistance in 11.5M nitric acid. Therefore appropriate heat treatments are required to restore the structure and properties of the stable parent phase.

High Temperature X-ray Diffraction (HTXRD) studies were carried out to investigate the thermal stability of the non-equilibrium phases [122]. Figures 4.12(a) and (b) show the HTXRD patterns obtained in the temperature range of 100-1100 °C from the deformed SS and TiTaNb alloy respectively. Figure 4.12(a) shows strong Bragg reflections corresponding to α' phase at 100 °C, the lowest temperature of exposure. No significant change occurred until 500 °C, beyond which the X-ray intensity of α' decreased gradually until 800 °C above which only γ phase was observed. Figure 4.12(b) shows the predominance of Bragg reflections corresponding to α and fcc phases of Ti until 800 °C, while individual reflections of β phase could not be detected due to its low volume fraction. Although the highest intensity peak for the fcc phase

overlapped with $(002)_\alpha$, its presence was unambiguously confirmed from the additional (200) peak at a 2θ position of 44.08° . Beyond 800°C , β phase was dominant due to the allotropic transformation of titanium.

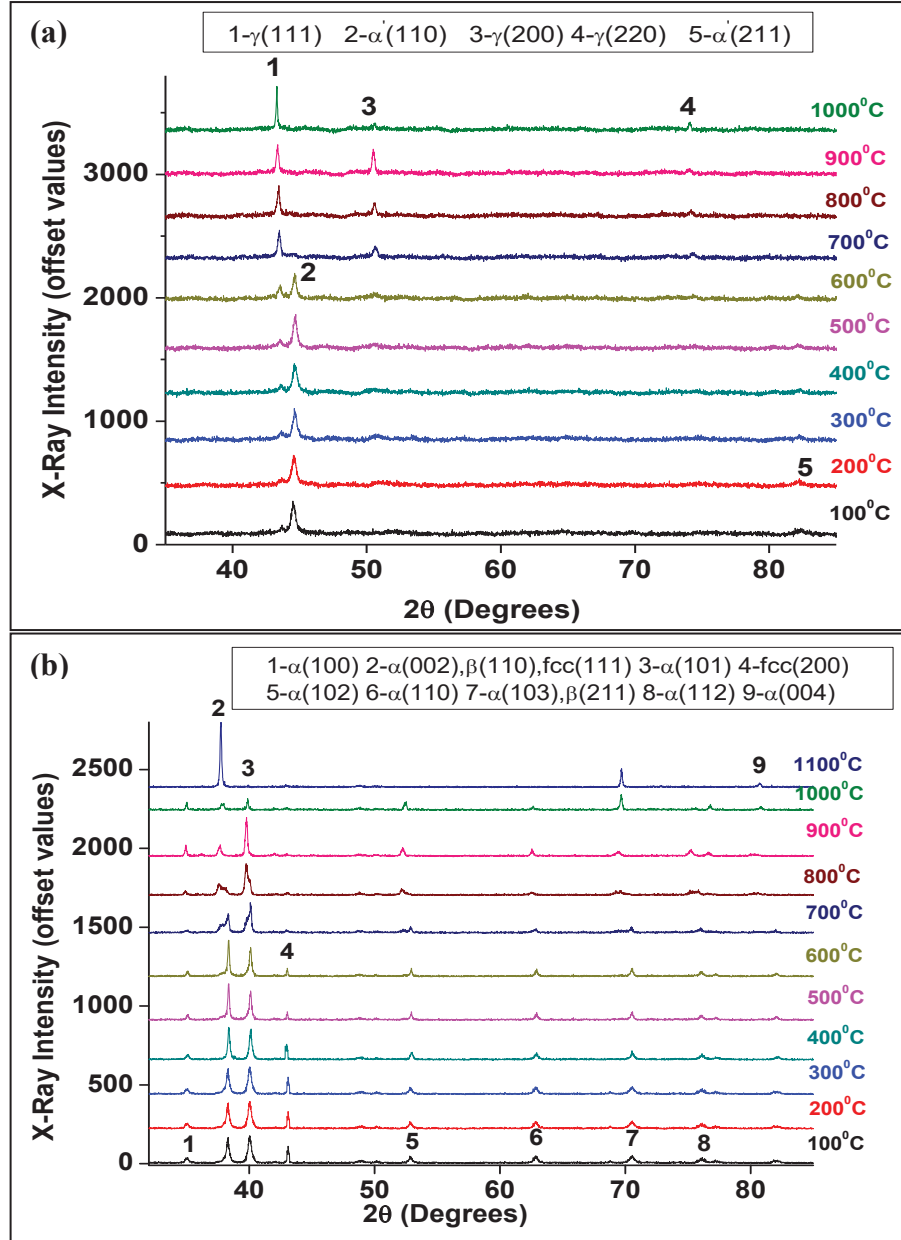


Figure 4.12 High Temperature XRD patterns from (a) SS and (b) TiTaNb sides of clad respectively

A rigorous comparison was made between the experimentally observed reflections in Fig. 4.12(b) and all possible reflections of Ti phases and compounds mainly hydrides, oxides and nitrides of Ti, Ta and Nb to ensure accuracy of the data.

Volume fraction (V_f) of metastable phases was calculated from the HTXRD pattern using the following equation [165]:

$$V_f = \frac{\frac{1}{n} \sum_{j=1}^n \frac{I_A^j}{R_A^j}}{\frac{1}{n} \sum_{j=1}^n \frac{I_B^j}{R_B^j} + \frac{1}{n} \sum_{j=1}^n \frac{I_A^j}{R_A^j}} \quad (4.1)$$

where ‘ n ’ indicates number of peaks of the phase for which volume fraction has to be estimated, ‘ I ’ is the integrated intensity and ‘ R ’ is the material scattering factor for the corresponding reflecting plane.

Figures 4.13(a) and (b) show the calculated volume fractions in SS ($V_f(\alpha')$) and TiTaNb ($V_f(\text{fcc})$) respectively plotted as a function of temperature. $V_f(\alpha')$ remained constant (~ 0.63) until 500 °C and gradually reduced to ~ 0.16 at 800 °C in SS while volume fraction of fcc Ti phase remained constant at ~ 0.48 till 600 °C beyond which gradually decreased to ~ 0.23 (Fig. 4.13(b)). Beyond 800 °C, α' peaks in SS could not be clearly distinguished. The volume fraction estimated from the intensity ratios in XRD patterns using equation (4.1) is a semi-quantitative procedure. Based on the above information, further heat treatments were carried out at temperatures in the vicinity of the transformation regimes (marked as dotted circles) to study the associated microstructural variations.

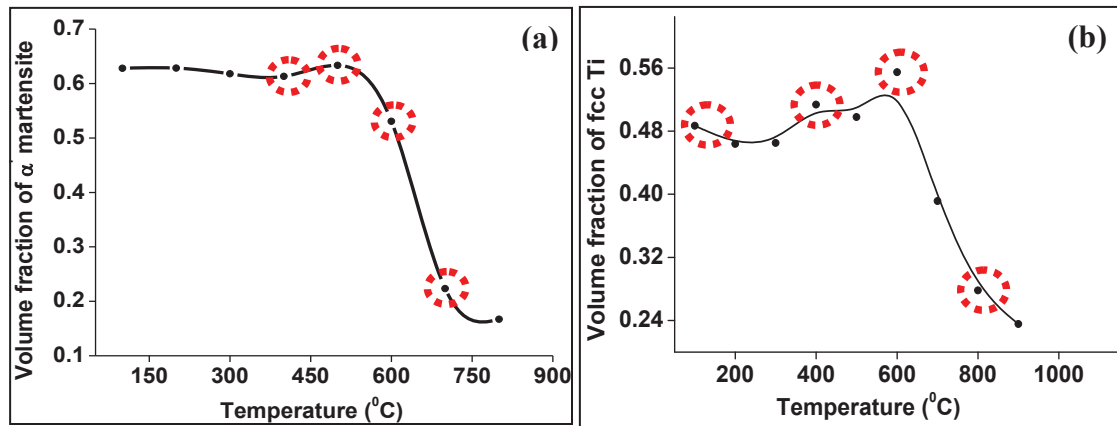


Figure 4.13 Change in the volume fraction of (a) α' martensite in SS and (b) fcc Ti in TiTaNb with thermal exposure

4.6.2 Reversion of α' martensite and associated structural changes in SS:

The SE images corresponding to the temperatures of 400, 500, 600, and 700 $^{\circ}\text{C}$ are compared in Figs. 4.14(a) to (d). The average values of hardness are also included in the figure. The fine needle like morphology (arrow marked in Fig. 4.14(a)-(c)) and high value of hardness supported the presence of SIM to different extents until 600 $^{\circ}\text{C}$, where as equiaxed austenite grains were observed at 700 $^{\circ}\text{C}$ with a commensurate reduction in the average hardness value to ~ 271 HV (Fig. 4.14(d)). It is important to note that the hardness was still higher than that of parent metal (~ 230 HV), which provides evidence for the retention of α' phase at this temperature.

A quantitative estimation of the volume fraction of bcc and fcc phases has been carried out by EBSD analysis. The percentage of indexing in all the maps was above 80%, while the confidence index, a measure of the reliability of indexing the diffraction patterns, was obtained as >0.1 .

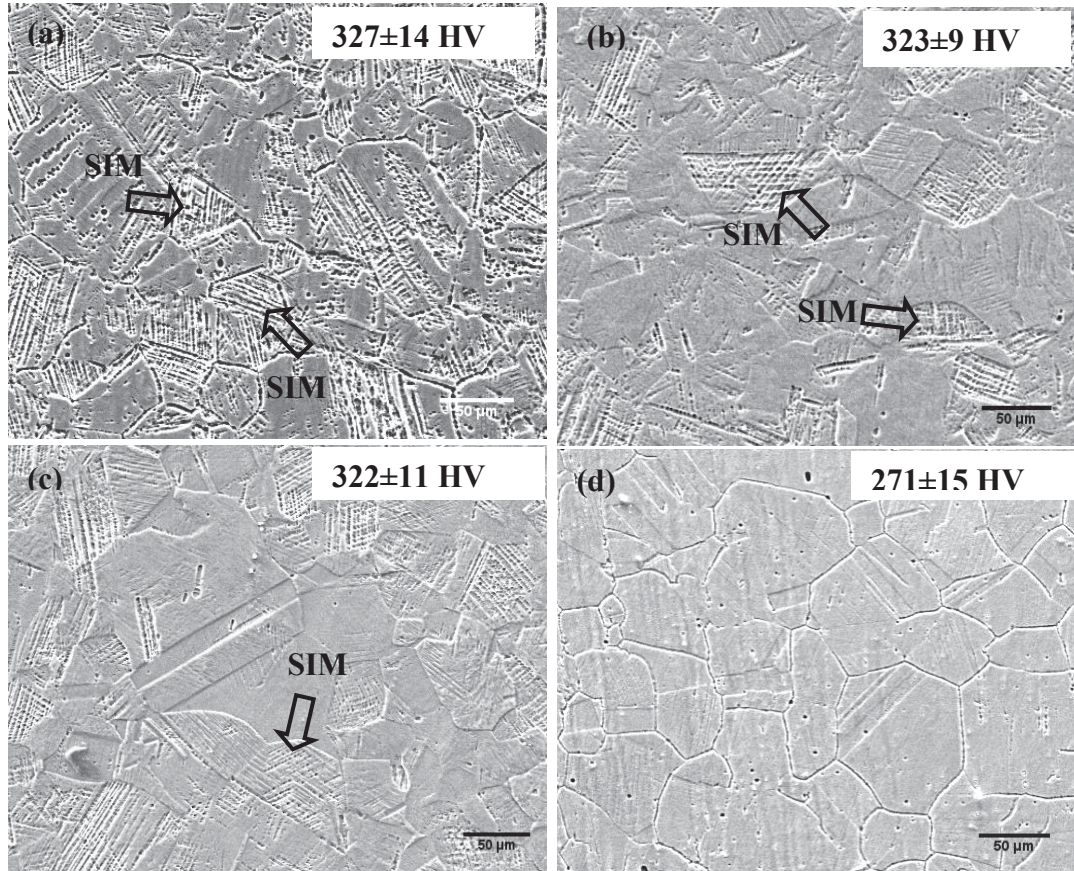


Figure 4.14 SE images of SS heat treated for 2 h at temperatures of (a) 400 °C, (b) 500 °C, (c) 600 °C and (d) 700 °C and quenched respectively; corresponding microhardness value is superimposed

Crystal orientation (or inverse pole figure) map for the product γ (fcc) and parent α' (bcc) phases obtained at 500 °C is shown in Fig. 4.15(a) and (b) and that at 700 °C in Fig. 4.15(c) and (d) respectively. The inset in each figure represents the orientation of the planes in specific direction. The inverse pole figure maps showed a random orientation of grains. Presence of considerable amount of martensite is evident from Figs. 4.15(a) and (b) while the structure became more equiaxed with annealing twins at 700 °C. The measured volume fraction of martensite amounts to ~ 0.4 in the austenite matrix ($V_F \sim 0.6$) at 500 °C from the EBSD pattern (Fig. 4.15(b)), which also explained

for the high value of hardness. The volume fraction of γ and α' phases were evaluated as ~ 0.8 and ~ 0.2 respectively at $700\text{ }^{\circ}\text{C}$ which agreed with the nearly annealed structure and low hardness (Fig. 4.15(c)) value. The volume fraction estimated from the relative peak intensity of XRD ($\alpha'=0.63$) was found to be higher as compared to that obtained by EBSD ($\alpha'=0.4$ at $500\text{ }^{\circ}\text{C}$). As the peak intensities from XRD data provided only a relative measure of volume fraction, the values obtained from EBSD was considered to be more reliable. Pole figure maps for fcc (along $\{111\}$ plane normal) and bcc phases (along $\{110\}$ plane normal) from the steel heat treated at $500\text{ }^{\circ}\text{C}$ is shown in Fig. 4.16(a) and (b) respectively.

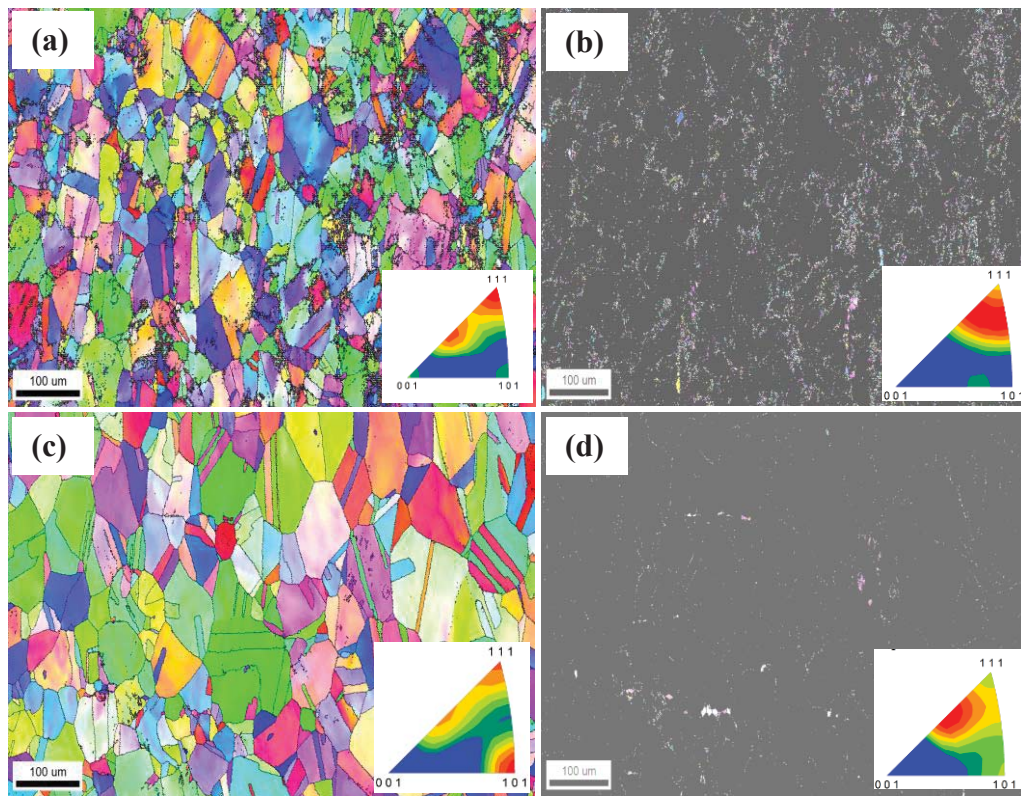


Figure 4.15 EBSD crystal orientation maps from SS heat treated at two different temperatures for 2h and quenched (a) $500\text{ }^{\circ}\text{C}$ - fcc, (b) $500\text{ }^{\circ}\text{C}$ - bcc, (c) $700\text{ }^{\circ}\text{C}$ - fcc and (d) $700\text{ }^{\circ}\text{C}$ - bcc phases of Fe; inset in each panel represents the legend

Analysis of pole figures by overlapping the corresponding pole figures of bcc and fcc phases along $\{110\}$ and $\{111\}$ plane normal obeyed the following orientation relationship (OR).

$$\begin{aligned} \{110\}_{\alpha'} // \{111\}_{\gamma} \\ \langle 111 \rangle_{\alpha'} // \langle 110 \rangle_{\gamma} \end{aligned}$$

This is nothing but the well known Kurdjumov-Sachs [166] OR established between γ and α' .

4.6.3 Mechanism of $\alpha' \rightarrow \gamma$ transformation in SS:

The TEM micrographs of the steel heat treated at 500, 600 and 700 °C are shown in Figs. 4.17(a) to (c). At 500 °C, the microstructure predominantly consisted of martensite laths of fine size (~100 nm) with high dislocation density. At 600 °C, increase in the lath width to about ~250-300 nm was observed together with very fine laths (arrow marked in Fig. 4.17(b)). Formation of equiaxed grains and annealing twins were clearly seen at 700 °C (Fig. 4.17(c)).

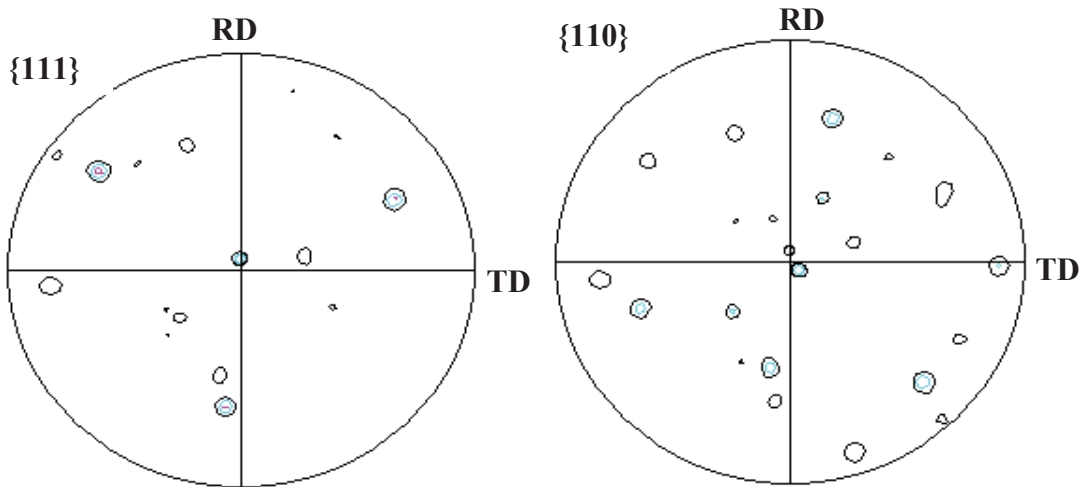


Figure 4.16 EBSD pole figures for (a) fcc and (b) bcc phases along $\{111\}$ and $\{110\}$ plane normal respectively

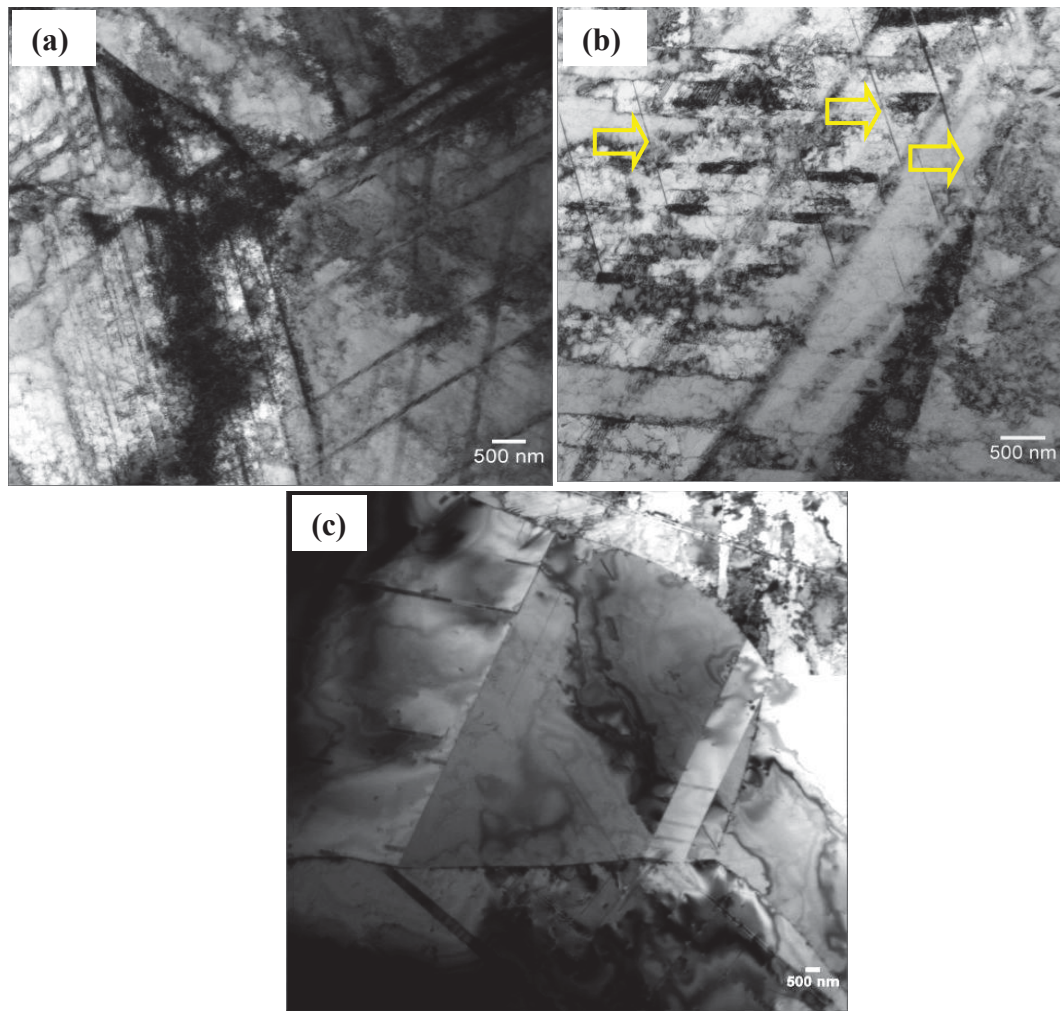


Figure 4.17 TEM-BF images showing (a) fine martensite laths, (b) coexistence of coarse and fine laths and (c) equiaxed grains of SS heat treated at temperatures of 500, 600 and 700 °C respectively for 2 h and quenched

The TEM-BF image of a typical martensite lath region at 500 °C and an enlarged view are shown in Fig. 4.18(a) and (b) respectively. SAD pattern (Fig. 4.18(c)) from the lath shows overlapping reflections for both γ and α' phases along zone axis $[\bar{1}12]_{\gamma}$ and $[\bar{1}11]_{\alpha}$ respectively. The DF image (Fig. 4.18(d)) for the $[011]$ reflection of α' (circled in

Fig. 4.18(c)) established that the γ phase was surrounded by α' phase thus providing evidence for nucleation of γ within the martensite lath.

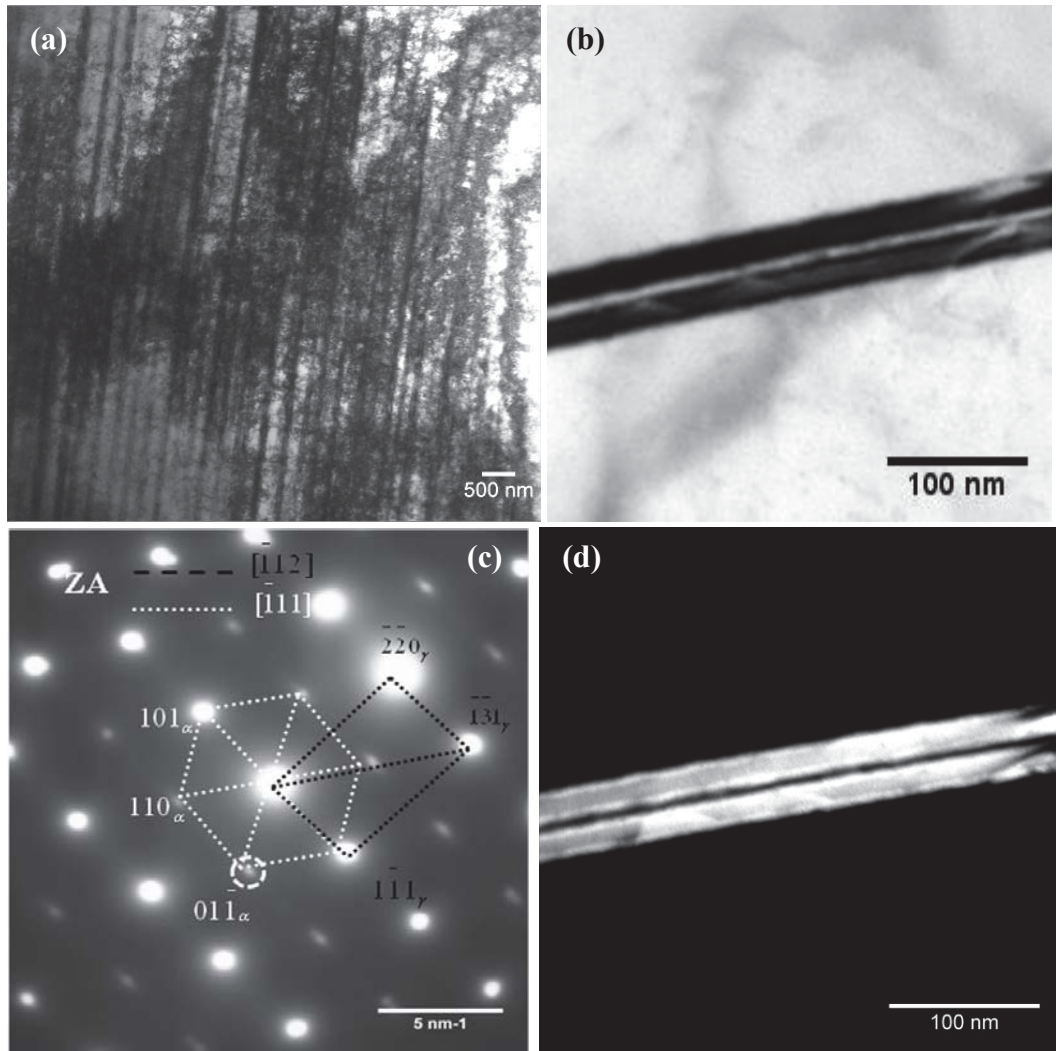


Figure 4.18 TEM-BF image of the steel heat treated at 500 °C for 2 h showing (a) fine martensite laths, (b) enlarged view of a typical martensite lath, (c) overlapping reflections revealed coexistence of γ and α' phases along $[112]$ and $[111]$ zone axis respectively and (d) DF image for the $[011]_{\alpha}$ reflection (marked in (c)) provided evidence for nucleation of γ within the martensite lath

A typical BF micrograph at 600 °C and the corresponding SAD pattern are shown in Fig. 4.19(a) and (b) respectively. Figure 4.19(a) reveals a set of intersecting laths. Analysis of the SAD pattern clearly showed overlapping reflections of γ and α' phases along $[\bar{1}22]$ and $[\bar{1}11]$ zone axis respectively.

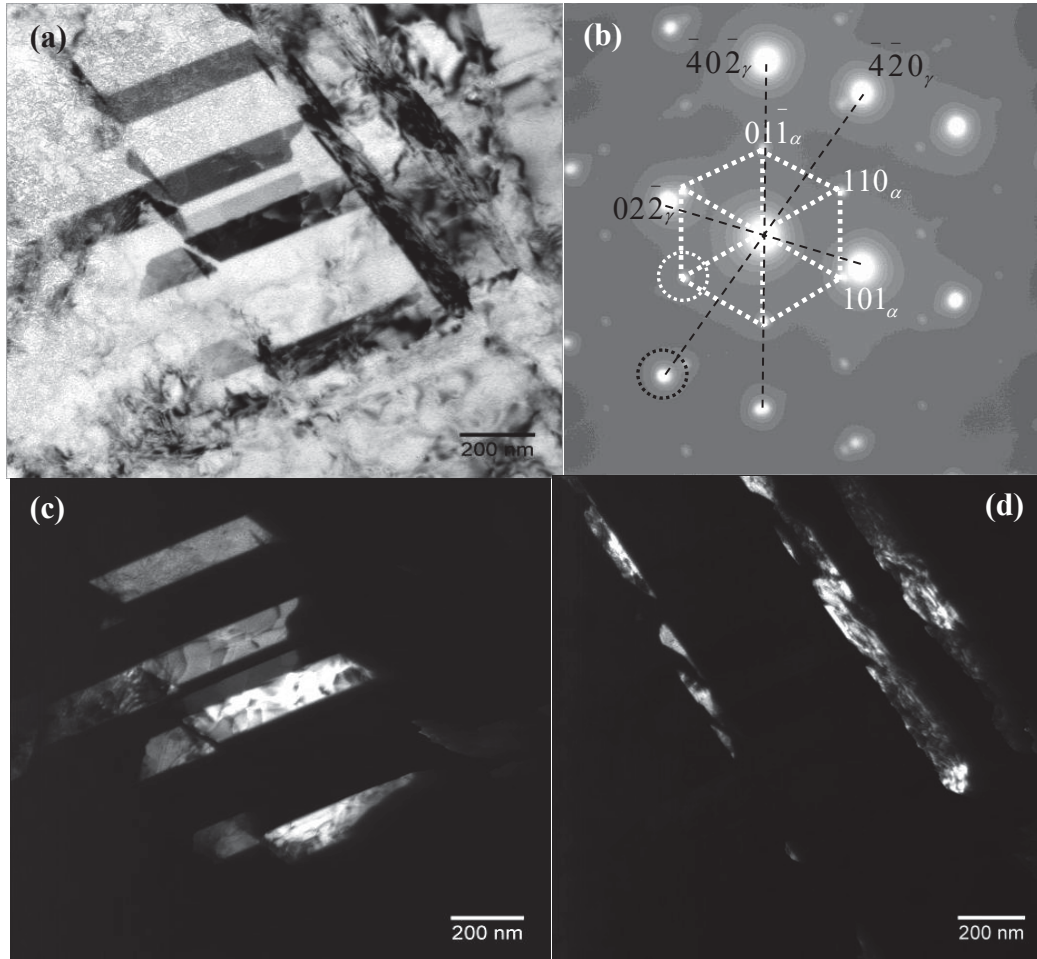


Figure 4.19 TEM-BF image showing lath morphology of the steel heat treated at 600 °C for 2 h, (b) corresponding SAD pattern showed coexistence of γ and α' phases along $[\bar{1}22]$ and $[\bar{1}11]$ zone axis and DF image for the (c) $[420]_{\gamma}$ reflection confirmed nucleation of γ within the α' lath (d) $[\bar{1}10]_{\alpha}$ reflection provided further confirmation

The DF image in Fig. 4.19(c) for the $[420]_{\gamma}$ reflection showed the growth of fcc phase within the α' lath, which supported the earlier observation. DF image for the $[\bar{1}\bar{1}0]_{\alpha}$ reflection of α' phase (Fig. 4.19(d)) confirmed its retention at 600 °C, although the emergence of γ phase at the expense of α' was evident. TEM-BF image of a typical region and SAD pattern at 700 °C are shown in Fig. 4.20(a) and (b) respectively. The micrograph revealed a high density of dislocations.

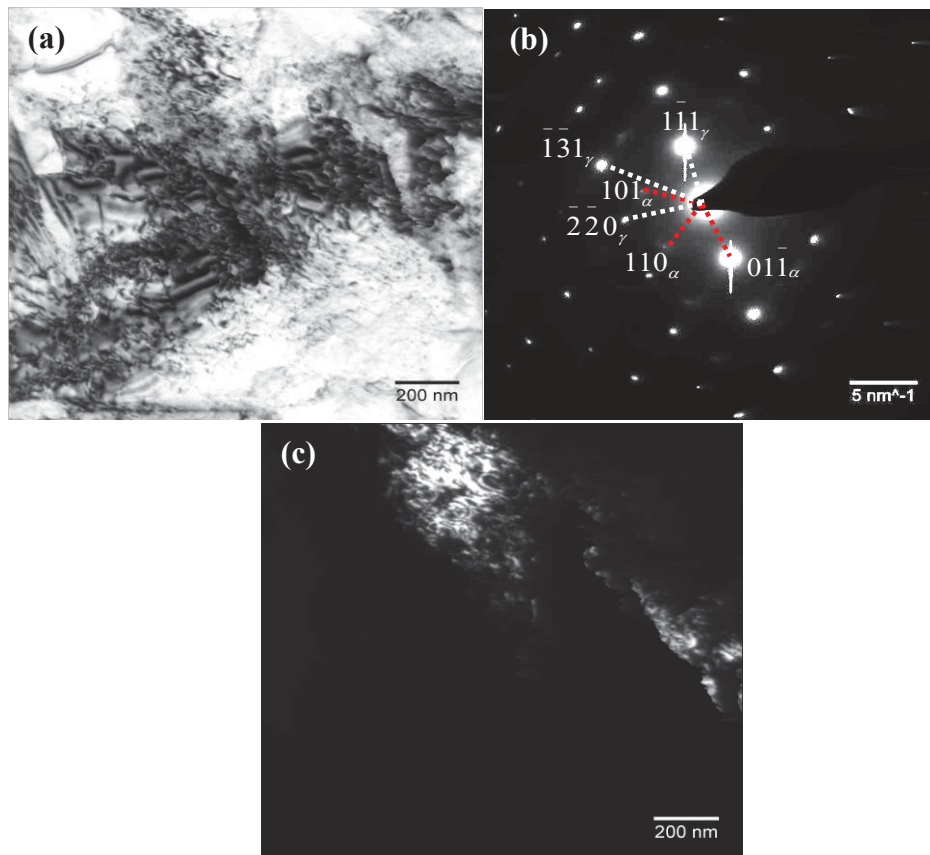


Figure 4.20 TEM (a) BF showing high density of dislocations of the steel heat treated at 700 °C for 2 h (b) corresponding SAD pattern showed coexistence of γ and α' phases along $[\bar{1}\bar{1}2]$ and $[\bar{1}\bar{1}1]$ zone axis and (c) DF image for the $[0\bar{1}1]_{\alpha}$ reflection confirmed that the reversion was not complete at this temperature

The SAD pattern showed overlapping reflections for γ and α' phases, along $[\bar{1}12]_{\gamma}$ and $[\bar{1}11]_{\alpha}$ zone axis respectively. The DF image in Fig. 4.20(c) obtained from the $[0\bar{1}1]_{\alpha}$ reflection confirmed that the reversion was not completed even at 700 °C for duration of 2 h, although the microstructure was predominantly equiaxed (Fig. 4.17(c)). A complete transformation to austenite is reported in SS304 containing ~89% of martensite at 680 °C and 8 h annealing supported the present observations [167].

The TEM-BF image from another region is shown in Fig. 4.21(a). The micrograph shows few fine laths (circled) within a wedge shaped grain. A high magnification image of the circled region (Fig. 4.21(b)) showed the presence of fine grains in the range of 30 to 40 nm. The analysis of the SAD pattern (Fig. 4.21(c)) from this region confirms the presence of austenite grains along $[013]_{\gamma}$ zone axis. This indicated the nucleation of austenite in few regions where α' lath still exists. It is expected that these γ grains would grow at the expense of the receding α' and structure would become homogeneous at higher temperatures or at longer timings.

It is well known that the $\alpha' \rightarrow \gamma$ reversion of a severely cold worked austenitic stainless steel during annealing proceeds through production of nano/submicron sized austenite grains which enhances the tensile strength significantly [67, 68, 168]. Grain size of the order of ~135 nm has been reported in severely cold worked 304LSS after thermal exposure for 20 min at 700 °C [68] in contrast to 30 to 40 nm in the present study. The higher grain size reported by these authors can be attributed to nearly 90% of martensite fraction which provides higher driving force for the reversion as witnessed from the enhanced kinetics of nucleation and growth. In the case of heavily cold worked

316L fine grain austenite was obtained at 750 °C, the higher recrystallisation temperature being due to its high SFE [167]. Arpan Das et al. [63] studied the formation of SIM in 304LNSS using strain rates in the range of 10^{-4} to 1 s^{-1} and its effect on the mechanical properties. The formation of SIM in the present study implied that the steel experienced strain rates of the order of 10^4 - 10^8 s^{-1} [169] which was associated with impact by explosive projectiles or shock waves propagation.

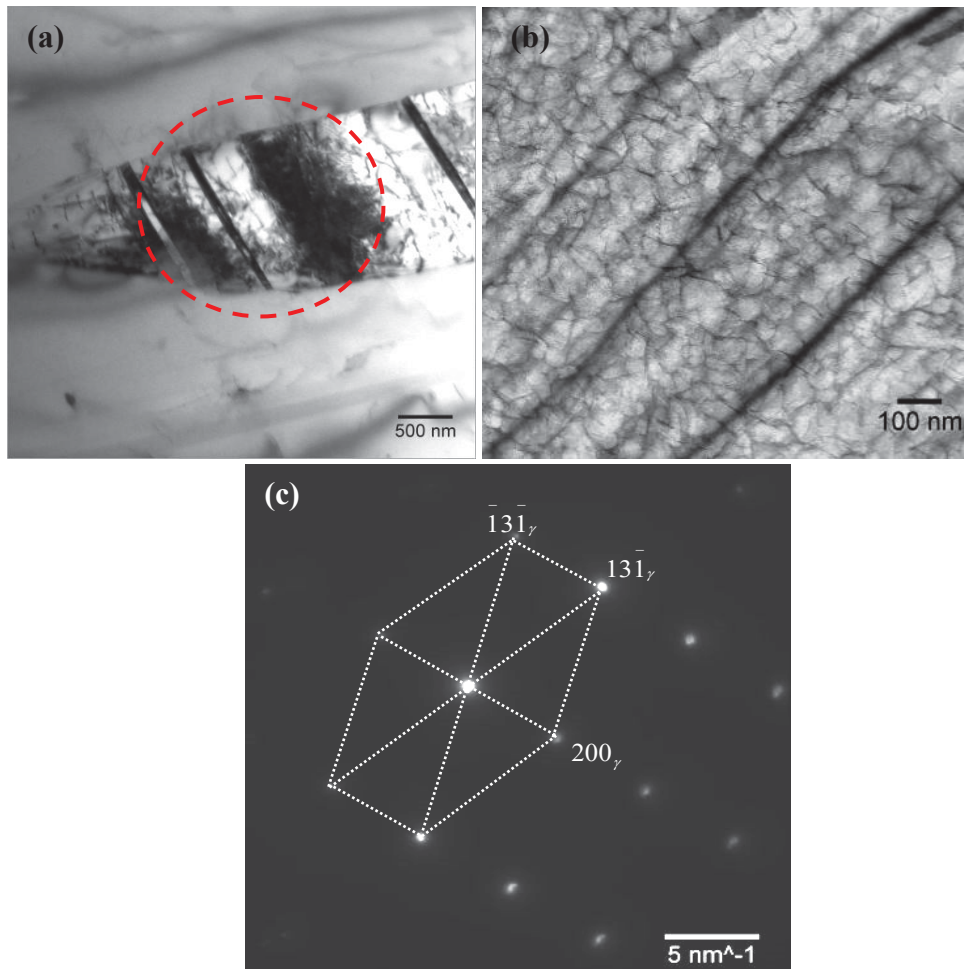


Figure 4.21 TEM (a) BF showing fine laths and dislocations within a wedge shaped region of the steel heat treated at 700 °C for 2 h, (b) high magnification BF image showing fine grains obtained from the region circled in (a) and (c) corresponding SAD pattern showed γ phase along $[013]$ zone axis

Based on literature, $\alpha' \rightarrow \gamma$ reverse transformation takes place either through athermal shear or isothermal diffusion mechanism [70, 170]. In general, the shear mode of transformation was observed at higher heating rates (>10 °C/s) and within a narrow temperature regime [171]. The characteristic features associated with shear reversed transformation were austenite with lath morphology and high number density of dislocations. However, the transformation mechanism changes from diffusionless to diffusional depending on the temperature and time of annealing. At longer annealing time periods (>20 minutes), the transformation mode changes from shear reversion mechanism to diffusional [68]. In 304SS the reverse transformation is reported to take place at 550 °C with heating rates ranging from 1-100 °C/min [172]. In the present study the presence of austenite surrounded by regions of high dislocation density at 500 °C and austenite with lamellar morphology at 600 °C suggested that the reversion followed the shear mode of transformation which changed to diffusional at 700 °C resulting in the nucleation of equiaxed grains typical of a diffusional transformation.

4.6.4 Reversion of fcc phase and associated structural changes in TiTaNb alloy:

The SE images of the TiTaNb alloy heat treated at 100, 400, 600 and 900 °C are shown in Figs. 4.22(a) to (d). The presence of highly deformed microstructure with elongated grains (Fig. 4.22(a)) showed that reversion was insignificant at 100 °C. Nucleation of equiaxed α grains in few regions was observed at 400 °C (Fig. 4.22(b)) while the formation of stress free grains (Fig. 4.22(c)) was observed at 600 °C. This suggested the onset of recrystallisation at 400 °C. The decrease in recrystallization temperature was understood in terms of the severity of deformation in explosive clad in contrast to cold rolled and stress relieved Ti-6Al-4V alloy where the recrystallization

temperature was reported as 540 °C [173]. The presence of martensite (α') structure with coarse laths was observed in the specimen heat treated at 900 °C (Fig. 4.22(d)). The microstructure at 900 °C was a manifestation of exceeding the β transus temperature and subsequent transformation of the high temperature β phase to martensite during cooling.

4.6.5 Mechanism of $fcc \rightarrow hcp(\alpha)$ transformation in TiTaNb alloy:

The ‘interface phase’ in Ti-6Al-4V alloy was reported as stable up to a temperature of 500 °C beyond which it transforms to parent hcp (α) phase [71]. At low temperatures, and low grain sizes (~ 5 -7 nm) fcc phase is reported as stable as compared to hcp phase, the reason for which is attributed to the temperature and size dependence of the Gibb’s free energy [75, 174].

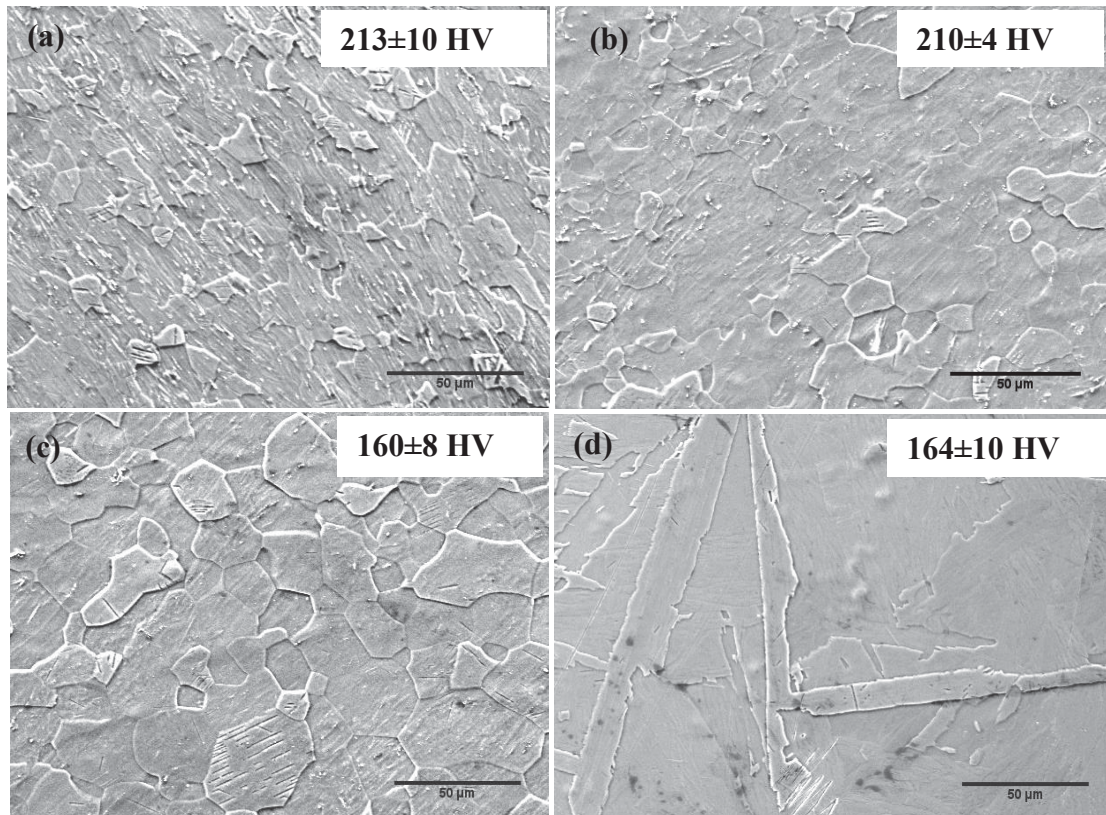


Figure 4.22 SE images of TiTaNb alloy heat treated at temperatures of (a) 100, (b) 400, (c) 600, and (d) 900 °C for 2 h and quenched respectively; corresponding microhardness values are indicated

A typical TEM-BF image of the specimen heat treated at 100 °C is shown in Fig. 4.23(a). The microstructure consisted of coarse elongated grains of width ~400 to 700 nm. Presence of fine lamellae of size ~80 to 100 nm within the elongated grains similar to that in Fig. 4.23(a) was observed. The SAD pattern from the lamella (circled in Fig. 4.23(a)) is shown in Fig. 4.23(b). Analysis of Fig. 4.23(b) showed overlapping reflections of hcp (α) and fcc phases along $[0001]$ and $[\bar{1}12]$ zone axis respectively.

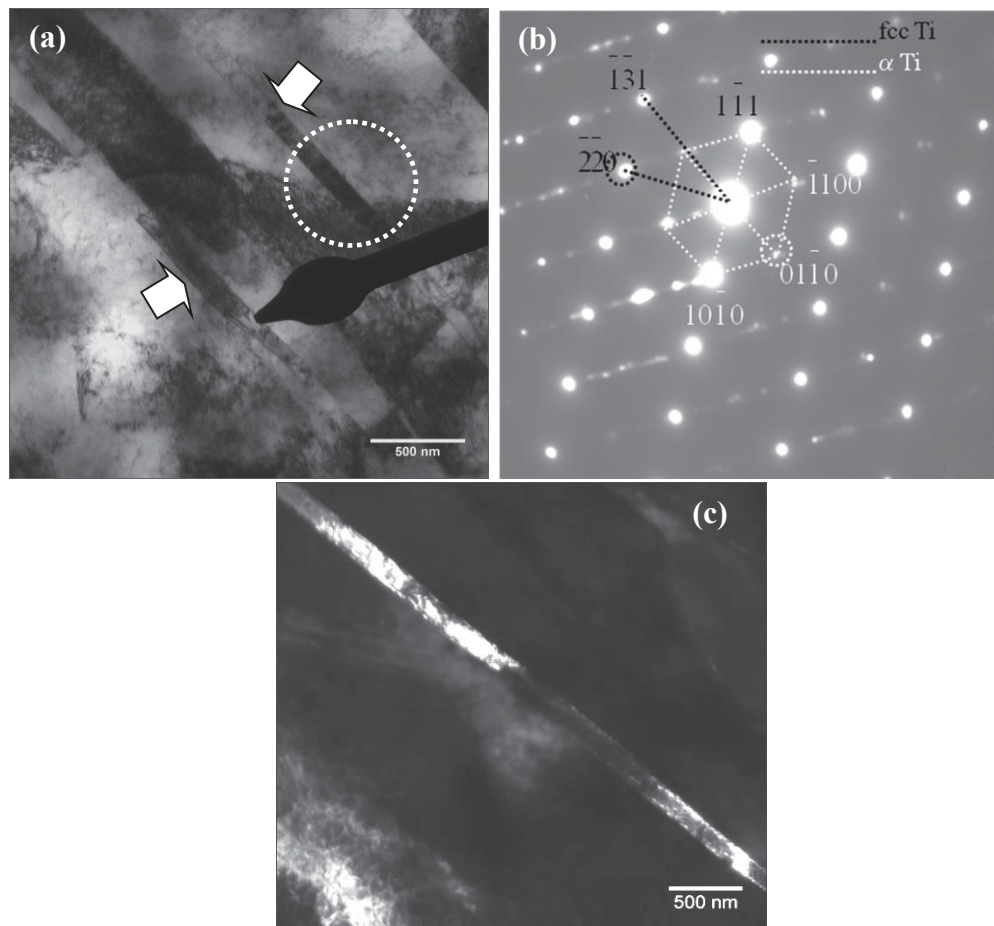


Figure 4.23(a) TEM-BF image of the alloy heat treated at 100 °C showing elongated grains and fine lamellae, **(b)** SAD pattern obtained from the circled region in (a) confirmed overlapping reflections of α and fcc phases along $[0001]$ and $[\bar{1}12]$ zone axis respectively **(c)** DF image for $[0110]$ reflection confirmed the fine lamellae as α phase of Ti

DF image (Fig. 4.23(c)) for the $[01\bar{1}0]$ reflection (circled in Fig. 4.23(b)) showed that the lamella partly consisted of α phase, which indicated the onset of reversion. Similar observation was made in several regions of the specimen. The TEM-BF image of a wedge shaped grain corresponding to metastable fcc phase is shown in Fig. 4.24(a). The presence of regions of high dislocation density surrounding the fcc phase indicated a high extent of deformation.

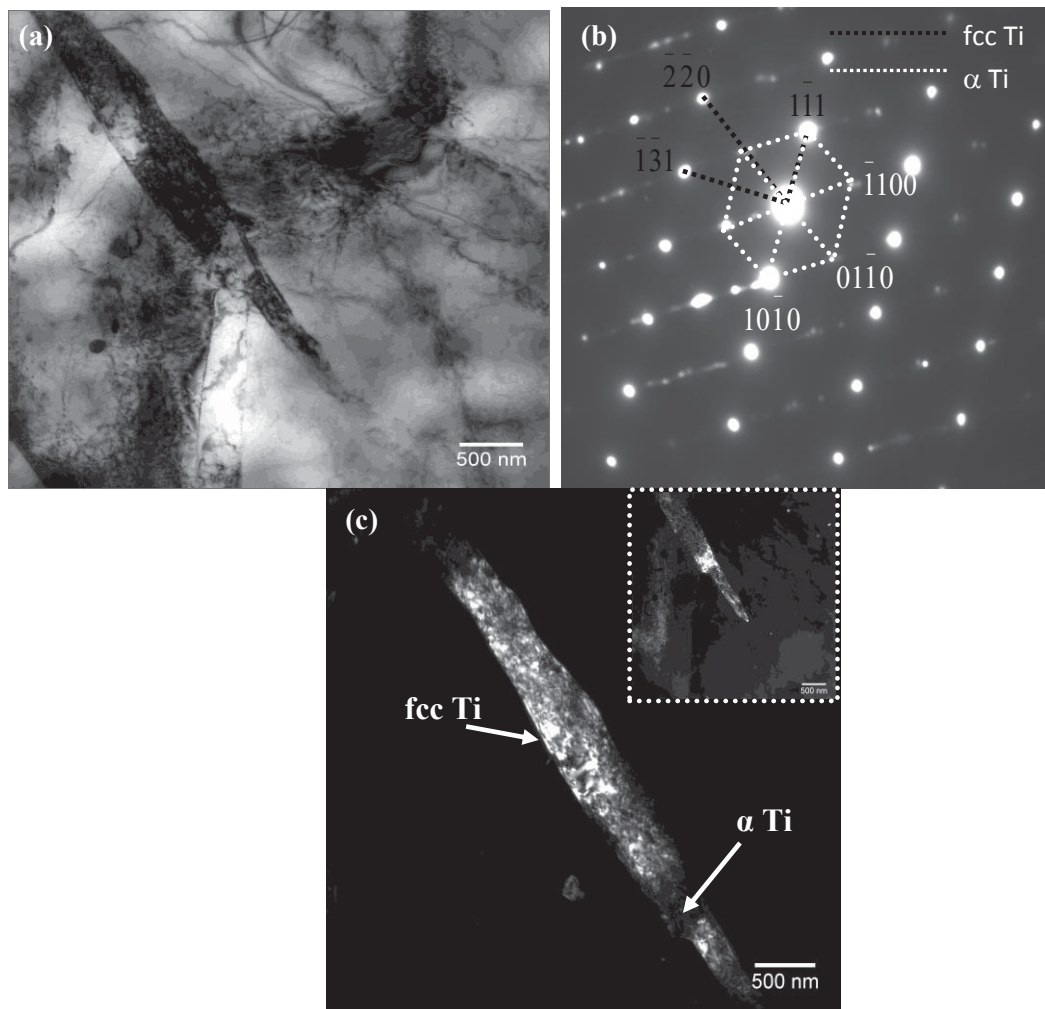


Figure 4.24 TEM (a) BF image obtained from a wedge shaped grain at 100 °C, (b) corresponding SAD pattern showed metastable fcc phase and α phase along $[\bar{1}12]$ and $[0001]$ zone axis and (c) DF image for fcc phase and inset in (c) is the DF image for the α phase respectively provided confirmation for the nucleation of α phase within the fcc phase

Electron diffraction pattern (Fig. 4.24(b)) obtained from this grain showed overlapping reflections, corresponding to α and fcc phase along $[0001]$ and $[\bar{1}12]$ zone axis respectively. The corresponding DF images for the fcc (Fig. 4.24(c)) and α (inset in Fig. 4.24(c)) phase for the $[2\bar{2}0]$ and $[01\bar{1}0]$ reflection confirmed that α has nucleated within the fcc phase. It is reported in literature that the newly formed alpha phase is associated with large number of dislocations [175] which supported our observation. From the overlapping standard $[\bar{1}12]_{fcc}$ and $[0001]_{\alpha}$ stereographic projection for fcc and hcp phase (Fig. 4.25) following orientation relationship has been derived.

$$(\bar{1}\bar{1}0)_{fcc} // (01\bar{1}0)_{\alpha}$$

$$(121)_{fcc} \sim 2^{\circ} (0\bar{1}11)_{\alpha}$$

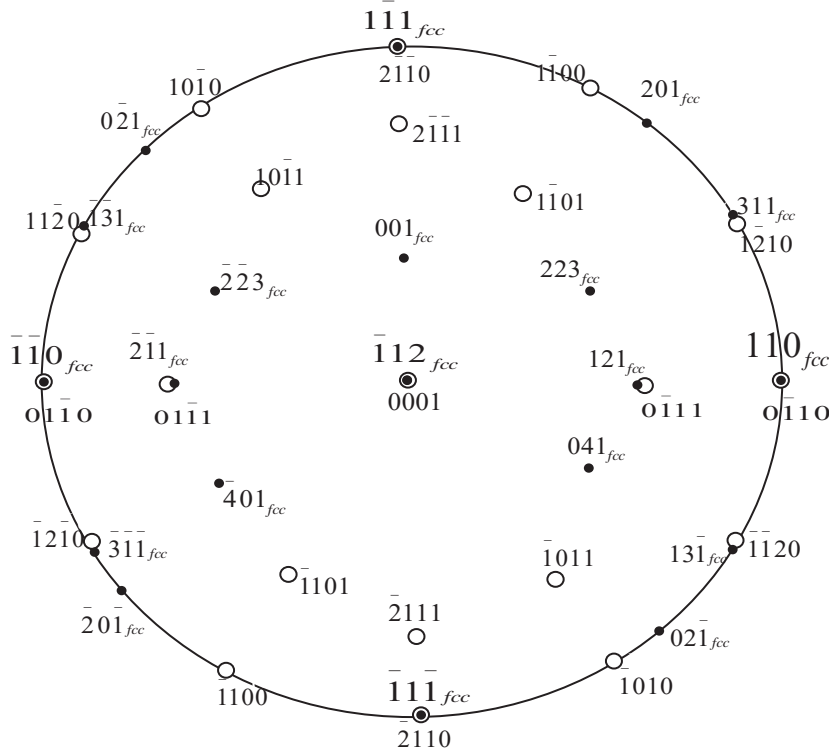


Figure 4.25 Overlapping standard $[\bar{1}12]$ and $[0001]$ stereographic projection of fcc and α phases of Ti respectively

It was evident from the above result, that the $fcc \rightarrow \alpha$ transformation takes place along the low index or the close packed planes. The lattice distortion for the fcc to hcp transformation along the close packed direction $[0001]$ was only $\sim 7.4\%$ which is far below that of high index planes (19.5%) [176]. Hence, it was quite obvious that the reverse transformation would proceed through the basal plane direction. This was in contrast with the orientation relationship $([11\bar{2}0]_{\alpha} \parallel [110]_{fcc})$ reported in α - β Ti alloys, where the fcc phase was assumed to form as an intermediate atomic arrangement between α and β during cooling [175].

As the temperature is increased to 400 °C significant microstructural changes were observed. Figure 4.26(a) and (b) shows the TEM-BF image of a lamellae (fcc) and the corresponding SAD pattern confirmed fcc and α phases along the zone axis $[011]$ and $[011\bar{0}]$ respectively. The DF image for the $[0002]$ reflection of α phase (Fig. 4.26(c)) confirmed its presence along the interface of fcc phase, which implied that the boundaries too act as sites for the nucleation of α . As the temperature was increased to 600 °C, the presence of well formed equiaxed grains together with regions of high dislocation density (regions A and B marked with dotted circles) was observed (Fig. 4.27(a)). The SAD pattern (Fig. 4.27(b)) obtained from the circled region A corresponds to α phase along $[2\bar{1}\bar{1}0]$ zone axis. On a closer examination, presence of a fine acicular phase decorating the grain boundary (Fig. 4.27(c)) was revealed. Planar defects such as screw dislocations (marked with dotted circle) and stacking faults (arrow marked) were also observed near this grain boundary which implied that the lattice was still associated with considerable amount of defects.

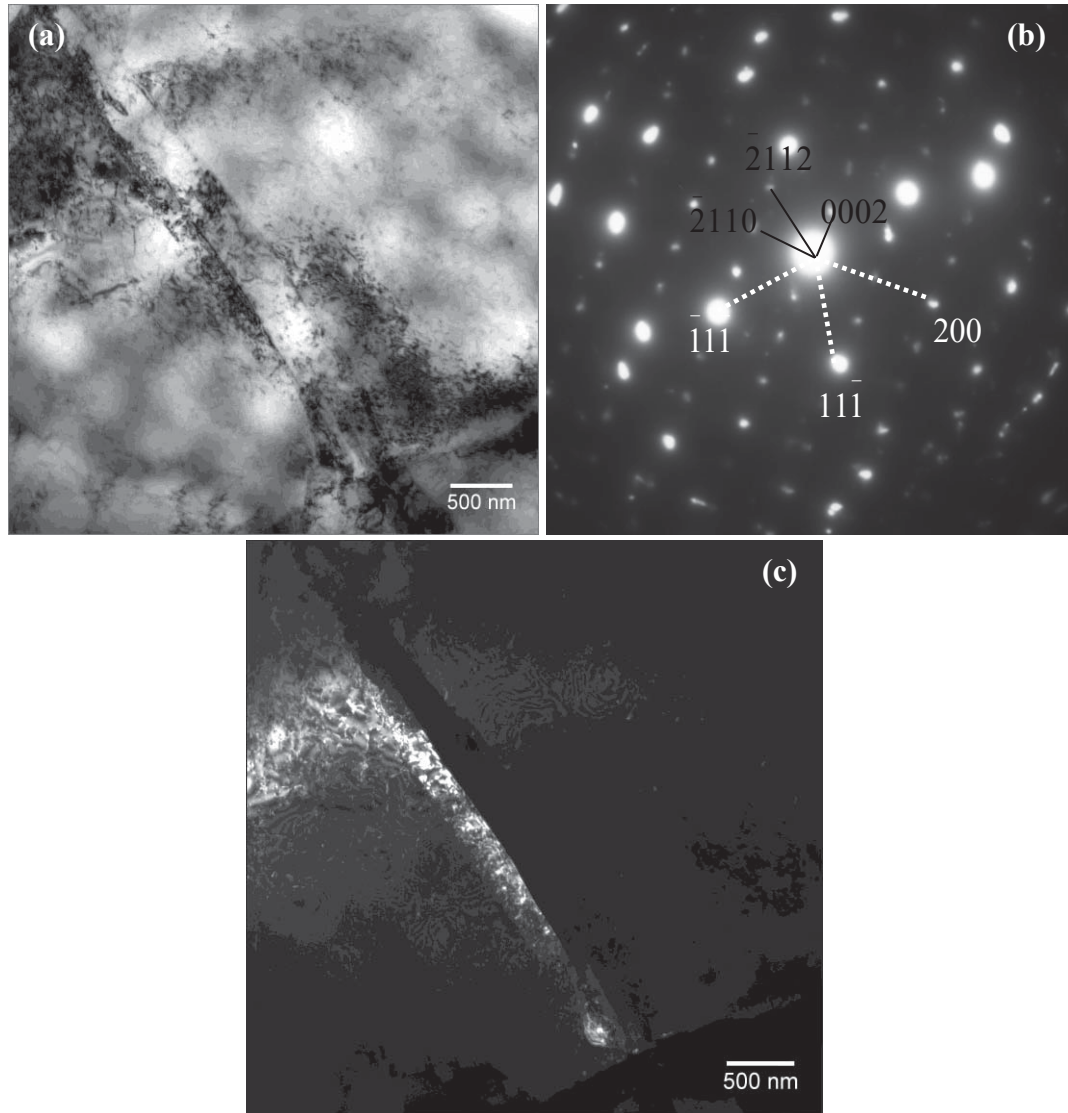


Figure 4.26 TEM (a) BF image of TiTaNb heat treated at 400 °C showing a lamellae shaped grain, (b) SAD pattern revealed presence of fcc and α phases along $[011]$ and $[0\bar{1}\bar{1}0]$ zone axis and (c) DF image for the $[0002]$ reflection of α respectively

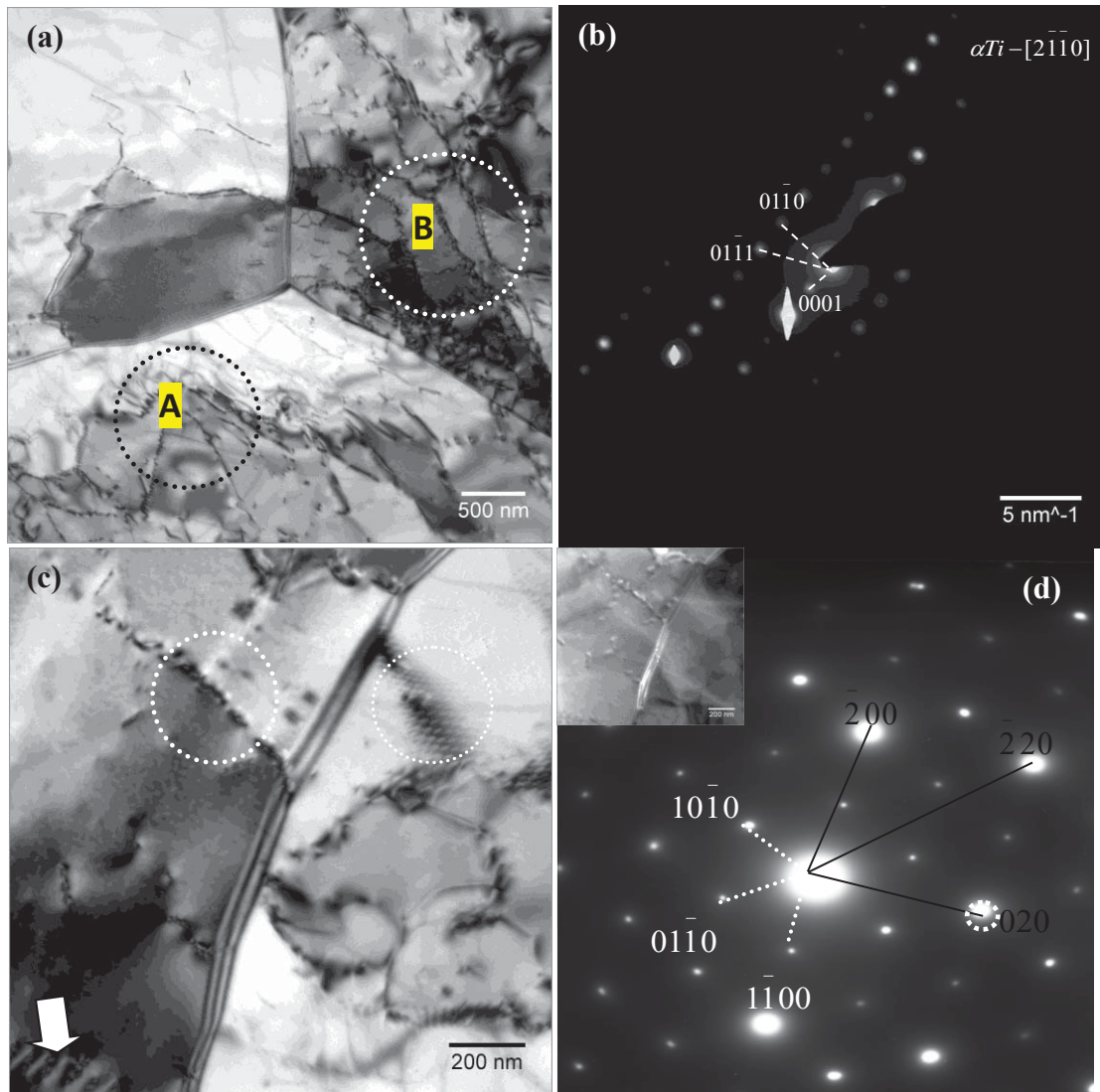


Figure 4.27 TEM (a) BF image showing equiaxed grains at 600 °C, (b) corresponding SAD pattern from circled region A confirmed α phase along the zone axis $[2\bar{1}\bar{1}0]$, (c) BF image showing enlarged view of the triple point intersection of equiaxed grains revealing screw dislocations and stacking faults and (d) corresponding SAD pattern showed α phase and retained fcc phase along the $[\bar{1}12]$ and $[0001]$ zone axis respectively; DF image in inset confirmed $[020]$ fcc reflection

The formation of large number of dislocations and planar faults as observed in Fig. 4.27(c) were understood to be manifestations of the addition of high stacking fault energy metals Ta (0.3 J/m^2) and Nb as solute elements to Ti. Also at high temperatures, stress on various slip planes becomes comparable to each other which facilitates cross slip leading to more random arrangement of dislocations [175]. The SAD pattern from this region in Fig. 4.27(d) shows overlapping reflections corresponding to fcc and α phases along $[\bar{1}12]$ and $[0001]$ zone axis respectively. The DF image in the inset confirmed that the acicular phase was nothing but the retained fcc phase although its volume fraction was low, which was also reported earlier by XRD analysis [122]. The above analysis provided evidence to the fact that the reversion of metastable fcc phase was incomplete at 600°C for a duration of 2 h.

The above results established that the nucleation of α proceed both homogeneously within fcc phase as well as along the fcc/ α interfaces. Figure 4.28 (a) and (b) show the TEM-BF image and SAD pattern of the alloy quenched from 900°C . A fully martensitic structure was observed, which was also confirmed by the SAD pattern along $[0001]_\alpha$, (Fig. 4.28(b)) which can be understood in terms of exceeding the β transus temperature for this alloy.

The reversion of fcc to hcp α can follow either a direct route or following the $\text{fcc} \rightarrow \beta \rightarrow \alpha$ transformations, since the Gibbs free energy of bcc (β) (-457.5 kJ/mol) is close to that of fcc (-460.5 kJ/mol) [174]. However, volume fraction of β phase (<0.1) showed no change until 400°C although the fcc phase fraction showed a decrease, suggesting that β did not form as an intermediate during the reversion.

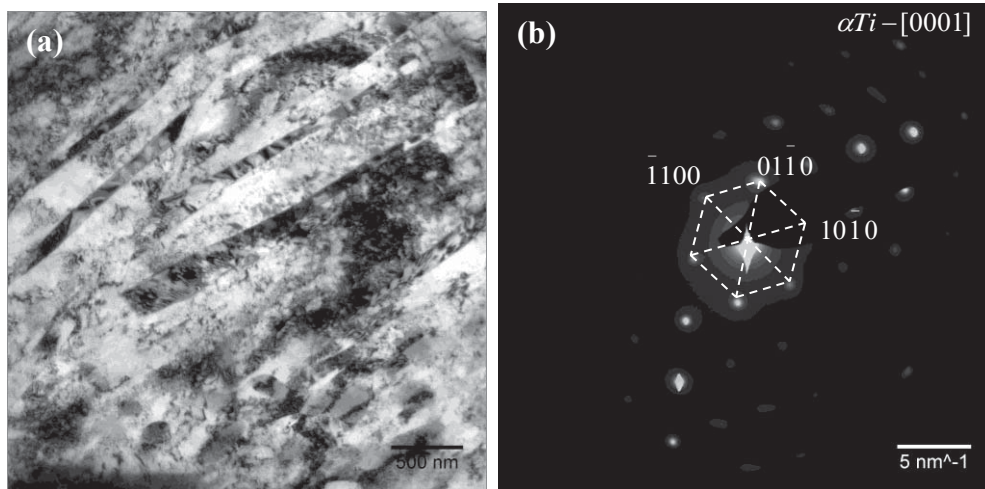


Figure 4.28 TEM (a) BF image showing martensite laths of α phase at 900 °C, (b) corresponding SAD pattern confirmed α phase of Ti along the $[0001]$ zone axis

However, the fraction of β increased above 600 °C typical of an $\alpha+\beta$ alloy. Further, no difference in chemical composition between fcc and α phase was observed at any temperature. The volume fraction of fcc phase was chosen as a kinetic parameter to monitor the reversion process. The variation of the volume fraction with temperature followed an Arrhenius behavior (Fig. 4.29) and the activation energy (Q) has been estimated as $\sim 156.7 \text{ kJ/mol}$. This was reasonably agreed with the Q value reported (149.1 kJ/mol) for the self diffusion of Ti in hcp matrix [177]. Although it was expected to obtain a lower Q in the present case due to defect aided diffusion in addition to volume diffusion the high value of Q can be understood due to the presence of the refractory solutes Ta and Nb in the Ti lattice. Hence the reversion of fcc to hcp phase follows a diffusion controlled nucleation and growth process.

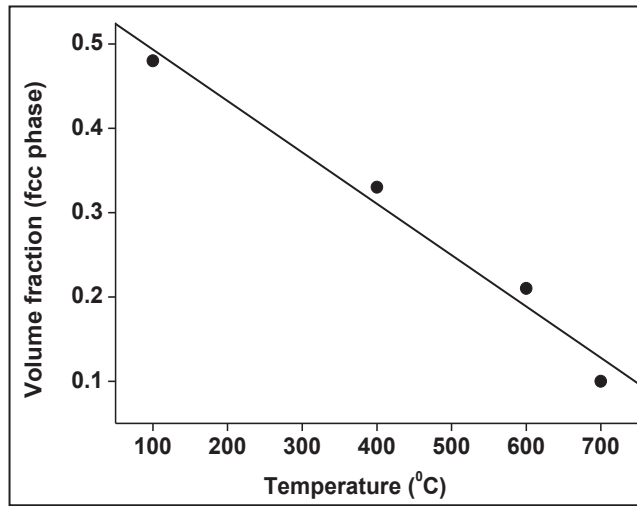


Figure 4.29 Plot of volume fraction of metastable fcc phase as a function of temperature

4.7 Structural changes due to interdiffusion on thermal exposure:

4.7.1 Microstructural and microchemical variations across the interface:

BSE images of the cross-section of clad heat treated for 20 h at 550, 600, 700 and 800 °C are shown in Fig. 4.30(a) to (d) respectively. At 550 °C other than porosities along the interface on SS side (Fig. 4.30(a)), no significant microstructural changes were observed. The average hardness values of base, flier and interface decreased to 260, 180 and 300 HV from ~375, 225 and 425 HV (as clad) respectively. At 600 °C, apart from the porosities, a continuous band of high contrast (arrow marked in Fig. 4.30(b)) was observed parallel to the interface, which also possessed a high hardness of ~350 HV in contrast to that of 270 HV of SS and 170 HV of TiTaNb. At 700 °C (Fig. 4.30(c)), the extent of porosity was considerably reduced while the width of the dark zone increased to ~6.9 μm . This dark zone of hardness ~380 HV was followed by a ~3 μm lightly etched thin zone and a ~40 μm wide unetched zone of ~288 HV on TiTaNb side, beyond which the microstructure and hardness resembled that of the flier plate.

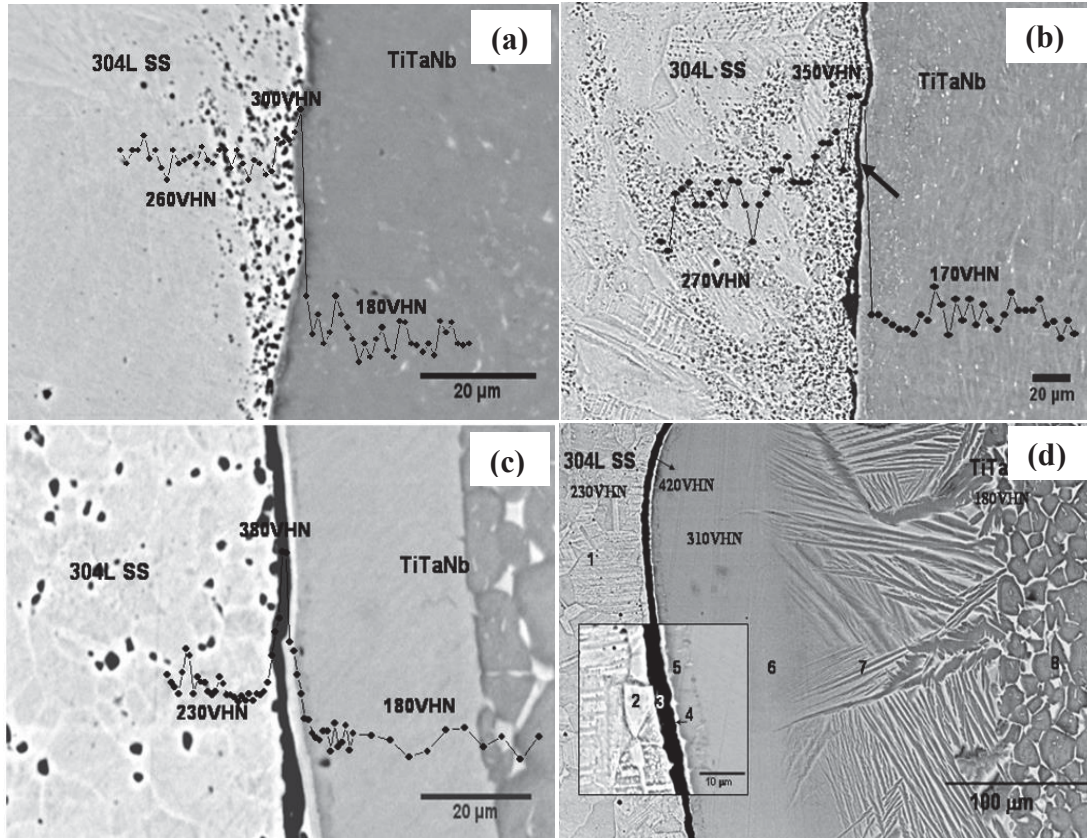


Figure 4.30 BSE images obtained from the cross-section of the clad heat treated at temperatures of (a) 550, (b) 600, (c) 700, (d) 800 °C for 20 h respectively; hardness profiles are superimposed on the micrographs and inset in (d) is high magnification micrograph revealed the presence of submicron sized zones at the interface

The observed Kirkendall porosity in SS base plate (Fig. 4.30(a)-(c)) was in contrast to reports of porosity on Ti side in diffusion bonded SS/Ti joints [23]. In the present study, interdiffusion was considered between $\alpha(\text{bcc})\text{-Fe}$ and $\alpha(\text{hcp})\text{-Ti}$ phases at 550 °C due to the presence of strain induced martensite. The higher values of diffusivity reported for diffusion of Fe in Ti ($D_{\text{Fe}}^{\text{hcp-Ti}(0.0334\%\text{Fe})} = 4.2 \times 10^{-15} \text{ m}^2/\text{s}$) [178] vis-à-vis Ti in bcc-Fe ($D_{\text{Ti}}^{\text{bcc-Fe}} = 1.58 \times 10^{-20} \text{ m}^2/\text{s}$) [179] at 550 °C clearly demonstrated the rapid diffusion of Fe in TiTaNb which supported the formation of Kirkendall porosity in SS side of the explosive clad.

Significant microstructural changes were observed as the temperature was increased to 800 °C (Fig. 4.30(d)). Closer examination of the microstructure (inset in Fig. 4.30(d)) revealed the formation of additional sub micrometer sized zones at the clad interface. The zones were classified based on contrast differences and numbered for easy identification. Zone 1 depicted the equiaxed structure of austenite phase in SS while zone 2 is a thin zone near the interface on SS side. The dark zone of width $\sim 4\text{ }\mu\text{m}$ exactly at the interface with hardness 420 HV and a submicron zone with a bright contrast ($\sim 310\text{ HV}$) are named as zone 3 and 4 respectively. A lightly un-etched zone of $\sim 10\text{ }\mu\text{m}$ is named as zone 5 and a wide band type of structure as zone 6. The observed Widmanstätten structure in TiTaNb beyond zone 6 is named as zone 7.

Concentration profiles acquired across the cross section of the heat treated clad are shown in Fig. 4.31(a) to (d). The diffusing distance of Fe in TiTaNb was observed to be more than that of Ti in SS at all temperatures. At 550 °C, the concentration profiles for Fe, Cr, Ni and Ti resembled conventional error function profiles with no indication for the formation of secondary phases. Diffusion distances for Fe in TiTaNb and Ti in SS were measured as ~ 5 and $4\text{ }\mu\text{m}$ respectively (Fig. 4.31(a)). Diffusion distances for Ni and Fe were similar, whereas it was $4\text{ }\mu\text{m}$ for Cr. Ta and Nb did not show any diffusion into SS. At 600 °C, smoothly varying error function profiles showed diffusion distances of $\sim 14, 2, 2\text{ }\mu\text{m}$ for Fe, Cr and Ni (in TiTaNb) respectively and $4\text{ }\mu\text{m}$ for Ti in SS. At the cross over point of the concentration profile, assumed to be the initial interface, the chemical composition was obtained as 45.4Fe-35.1Ti-13.6Cr-4.9Ni (in wt.%) (Fig. 4.31(b)).

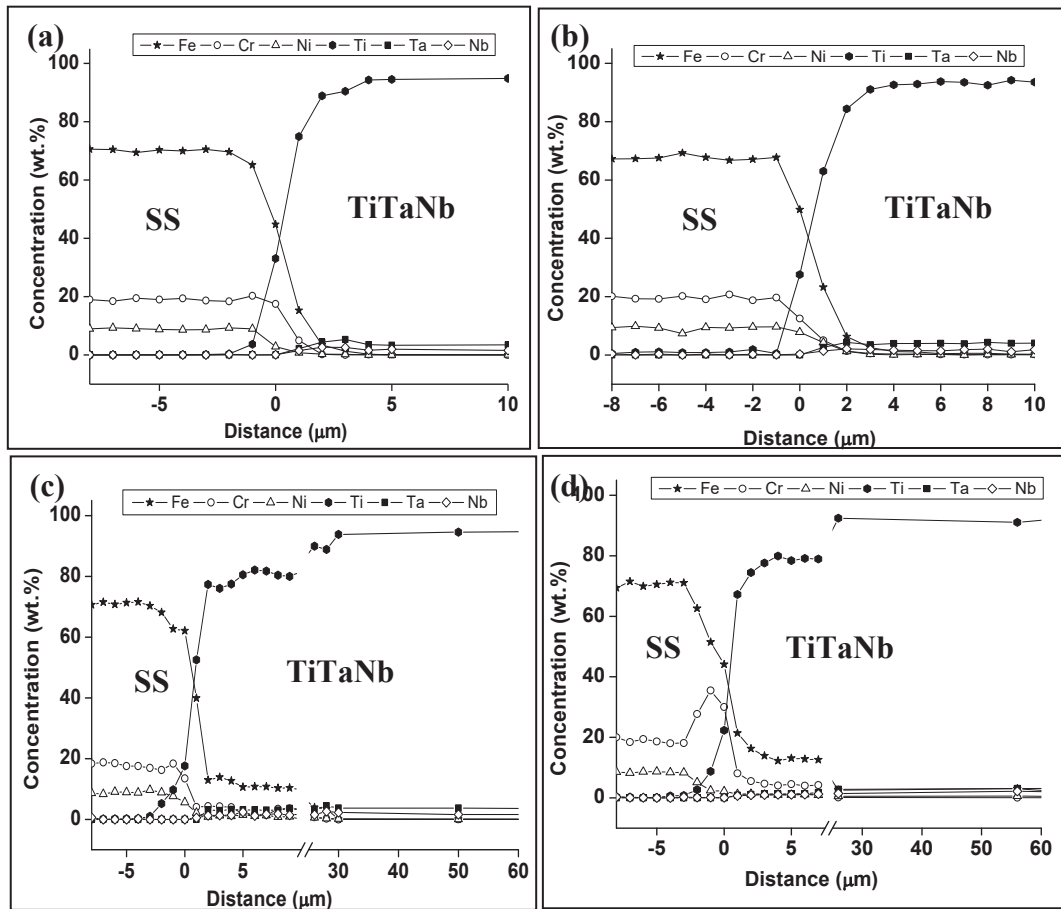


Figure 4.31 Concentration profiles obtained across cross-section of the SS/TiTaNb explosive clads heat treated at temperatures of (a) 550, (b) 600, (c) 700 and (d) 800 °C for duration of 20 h respectively

As the temperature was increased to 700 °C, step profiles were obtained for Fe, Cr, Ni and Ti (Fig. 4.31(c)) suggesting the formation of secondary phases as a consequence of interdiffusion. Average diffusion distances for Fe, Cr, Ni and Ti were measured as 32, 28, 30 and 5 μm respectively. Composition at the cross over point was obtained as 36.5Fe-51.8Ti-4.1Cr-7.2Ni (in wt.%). Beyond the cross over point, the average concentration of Fe, Cr and Ni gradually decreased from 13.8, 2.1 and 3.8 wt.% to 3.4, 0.1 and 0.6 wt.% respectively until a distance of ~28 μm in TiTaNb (corresponding to

the step in the profile). This was followed by a sharp decrease in the concentration of alloying elements to that of flier plate within 2-3 μm . At 800 °C, Fe, Cr, Ni and Ti displayed step profiles while Ta showed an error function profile (Fig. 4.31(d)). In SS, Cr enrichment was observed in regions close to the interface and the corresponding average composition was 52.9Fe-42.5Cr-2.1Ni-2.5Ti (in wt.%). This suggested the possible formation of Cr rich σ phase (zone 2). This can be understood in terms of uphill diffusion as Cr activity reduced due to diffusion of Ti to SS.

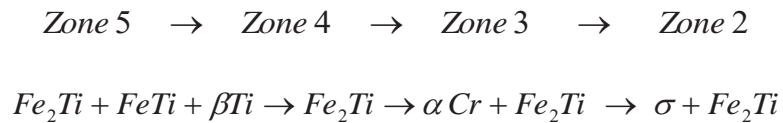
The total width of the diffusion zone was measured as $\sim 330 \mu\text{m}$ from the EPMA composition profiles. The microchemical data obtained by EPMA was correlated with the ternary isothermal section of Fe-Cr-Ti at 800 °C [88], to identify the microscopic zones at the interface. The zones corresponded to coexisting FeTi+Fe₂Ti phases (zone 3) and β Ti+Fe₂Ti phases (zone 4). Diffusion of considerable amount of beta stabilizers like Fe (10 - 14 wt.%) and Cr (1-5 wt.%) to Ti side, up to a distance of $\sim 80 \mu\text{m}$ (zone 5 and 6) stabilized the high temperature bcc (β) phase of Ti. However, beyond zone 6, gradual reduction in the concentration of β stabilizers up to $\sim 110 \mu\text{m}$ resulted in the transformation of high temperature β to Widmanstätten $\alpha+\beta$ microstructure (zone 7) which is followed by equiaxed $\alpha+\beta$ Ti structure (Fig. 4.30(d)).

4.7.2 *Prediction of phases formed due to microchemical variations:*

The phases that form across the clad interface for exposure of 20 h at 500, 600 and 800 °C were predicted using the measured change in microchemistry (Fig. 4.31) in Fig. 4.32(a) to (c). Figure 4.32(a) shows the presence of both Fe (α -Fe) and Ti (β -Ti) which can be understood in terms of their enhanced stability due to enrichment with diffusing stabilizers. The presence of intermetallic phases such as FeTi and Laves Fe₂Ti was also

predicted within the reaction zone, due to interdiffusion of alloying elements. At 600 °C the presence of bcc Fe and Ti was predicted in Fig. 4.32(b) for the same reasons stated above in addition to Fe₂Ti intermetallic phase. Presence of σ phase was also observed at this temperature. Although, the Fe-Ti binary diagram [7] predicts the formation of the two stable intermetallic compounds FeTi and Fe₂Ti, the JMatPro[®] based computations showed formation of only Fe₂Ti intermetallic phase. This is attributed to its low enthalpy of formation as compared to FeTi phase (-27.2±1.3kJ/m vis-à-vis -22.5±1.4kJ/m) [180]. The JMatPro[®] simulations at 800 °C (20 h) also predicted (Fig. 4.32(c)) the formation of Fe₂Ti and σ phase in SS, bcc Cr, intermetallic Fe₂Ti and FeTi phases at the clad interface and Ti₂Fe, β Ti and FeTi phases in TiTaNb. The plot of mole fraction of phases vs concentration of Fe (C_{Fe}) (Fig. 4.32(c)) reaffirmed the stability of β Ti phase for C_{Fe} range of 16.9 to 2 wt.%. As C_{Fe} reduces, the mole fraction of β phase reduced to yield a two phase (α - β) structure (corresponding to zone 7). Table 4.1 summarizes the type of phases expected to form across the explosive clad interface and their microchemistry at 800 °C.

The sequence of phase formation predicted using JMatPro[®] (Fig. 4.32(c)) was summarized as follows:



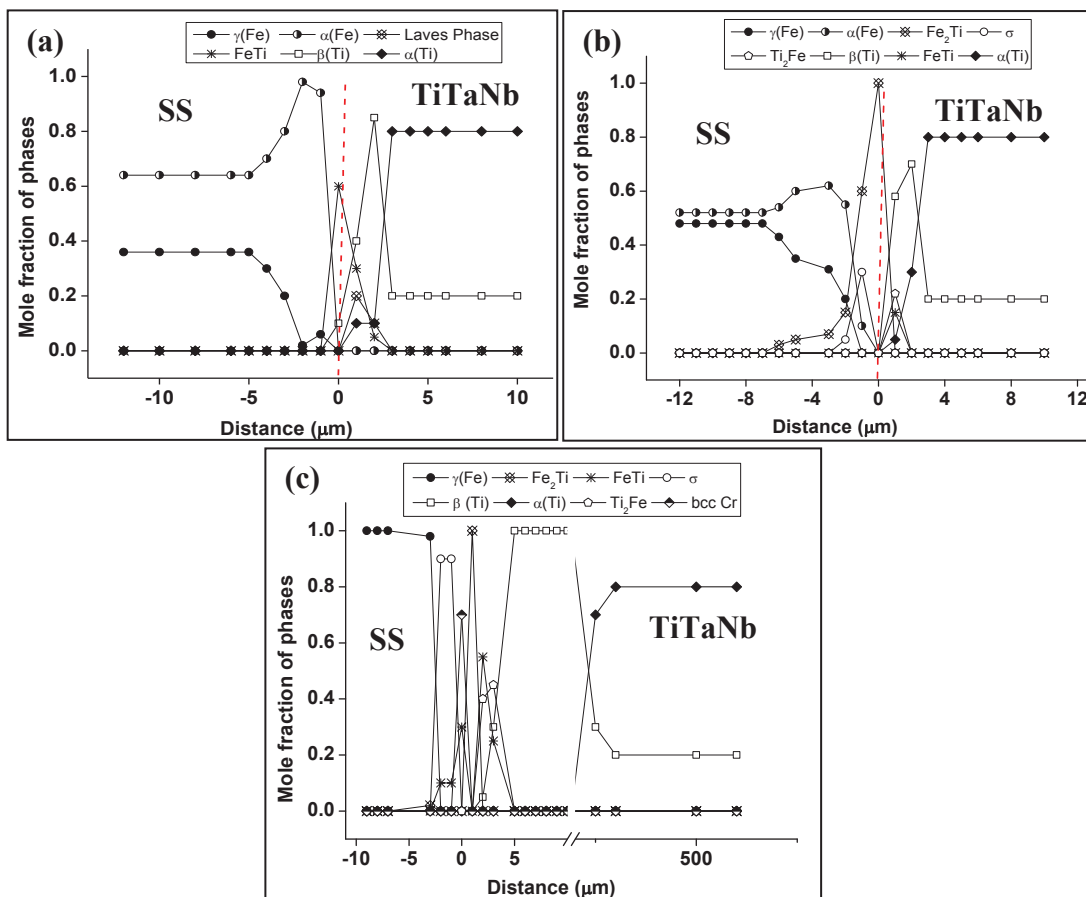


Figure 4.32 Predicted mole fractions of the phases plotted as a function of distance at (a) 550, (b) 600, and (c) 800 °C respectively

Table 4.1 Summary of predicted phases and their microchemistry as a function of distance from the explosive clad interface after heat treatment at 800 °C for 20 h

Distance -interface (μm)	Material	Predicted phases	Concentration of the elements (wt.%)					
			Fe	Cr	Ni	Ti	Ta	Nb
-15	SS	γ-Fe	72.1	19.1	8.8	0	0	0
-3		σ	50.4	47.9	1.7	0	0	0
		Fe ₂ Ti	59.2	5.0	5.6	30.0	0.20	0
-1		α-Cr	28.4	71.3	0.2	0.1	<0.01	0
		Fe ₂ Ti	59.3	5.8	3.2	31.6	0.1	0
0	Clad Interface	Fe ₂ Ti	42.6	17.9	2.6	36.7	0.2	0
1	TiTaNb	β-Ti	6.0	3.3	27	64.0	0	0
		FeTi	49.8	0	0	50.2	0	0
		Ti ₂ Fe	30	28.7	0	40.7	0.6	0
4-275		β-Ti	16.9- 2.0	4.9- 0.2	0.6- 0.3	76.2- 94.8	0.6- 1.3	0.8- 1.4
325		β-Ti	1.2	0	0.2	95.6	1.5	1.5
		α-Ti	<0.01	<0.0 1	<0. 01	99.1	0.5	0.3

4.7.3 Confirmation of secondary phases in the diffusion zone:

XRD patterns obtained from the cross-section of the clad heat treated at a temperature of 550 and 600 °C for 1 and 20 h are shown as Fig. 4.33(a) and (b) respectively. At 550 °C, both the XRD patterns showed Bragg reflections corresponding to only parent ($\gamma(\text{Fe})$, $\alpha(\text{Ti})$, $\beta(\text{Ti})$) and deformation induced phases ($\alpha'(\text{Fe})$, $\text{fcc}(\text{Ti})$). With increase in the duration of exposure, reduction in the peak intensity was observed at a 2θ position of 38.2° (Fig. 4.33(a)), corresponding to overlapping reflections from (002), (110) and (111) planes of α , β and fcc phases of Ti respectively. At 600 °C, in addition to the matrix phases (α , β - Ti and α , γ -Fe) peaks corresponding to Fe_2Ti and TiO phases (Fig. 4.33(b)) were also present. Figure 4.34 shows the XRD patterns obtained from the heat treated specimen at 800 °C for 1 and 20 h. The reflections from matrix, intermetallic phases, titanium oxide and deformation induced phases showed overlapping reflections at this temperature. Due to high temperature and long durations it was assumed that the reversion of metastable phases was complete (section 4.6) and their Bragg peaks were not labeled. Due to overlapping peaks confirmatory evidence could be obtained only for the Fe_2Ti phase.

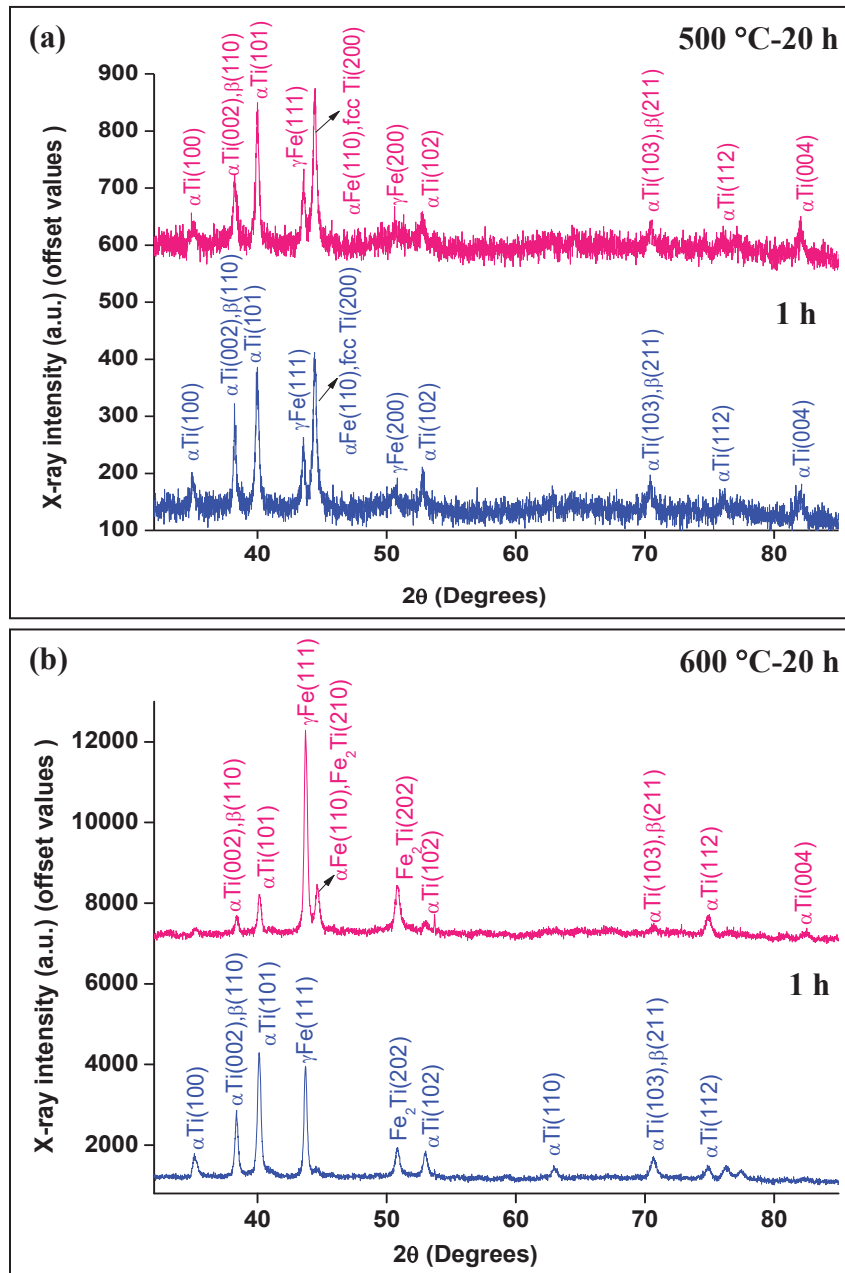


Figure 4.33 XRD patterns from cross-section specimens heat treated at temperatures of (a) 500 and (b) 600 °C (for 1 and 20 h duration) respectively

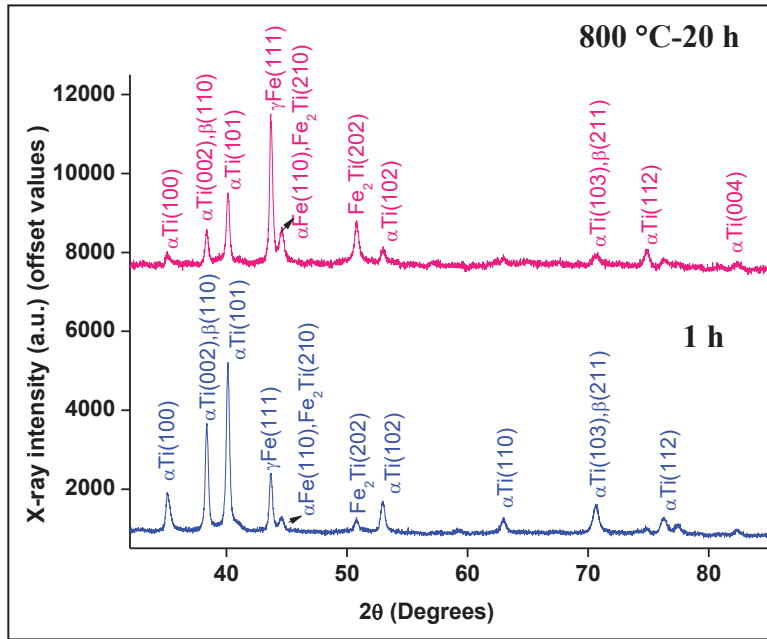


Figure 4.34 XRD pattern obtained at 800 °C (for 1 and 20 h duration)

The TEM-BF image, SAD pattern, DF image and EDS spectrum from the specimen extracted from zone 7 (Fig. 4.30(d)) is presented in Figs. 4.35(a) to (d) respectively. Figure 4.35(a) shows a high magnification BF image of the Widmanstätten Ti phase observed earlier in Fig. 4.30(d). Analysis of the SAD pattern (Fig. 4.35(b)) confirmed the existence of both α and β phases of Ti along $[01\bar{1}0]$ and $[\bar{1}11]$ zone axis respectively. DF image (Fig. 4.35(c)) corresponding to $[\bar{2}11\bar{2}]_{\alpha}$ reflection (circled spot in Fig. 4.35(b)) revealed hcp- α plates growing from the bcc- β matrix phase. The Fe peak in Fig. 4.35(d) provided evidence to the enhanced stability of β phase which is responsible for the coexistence of α and β phases in this region.

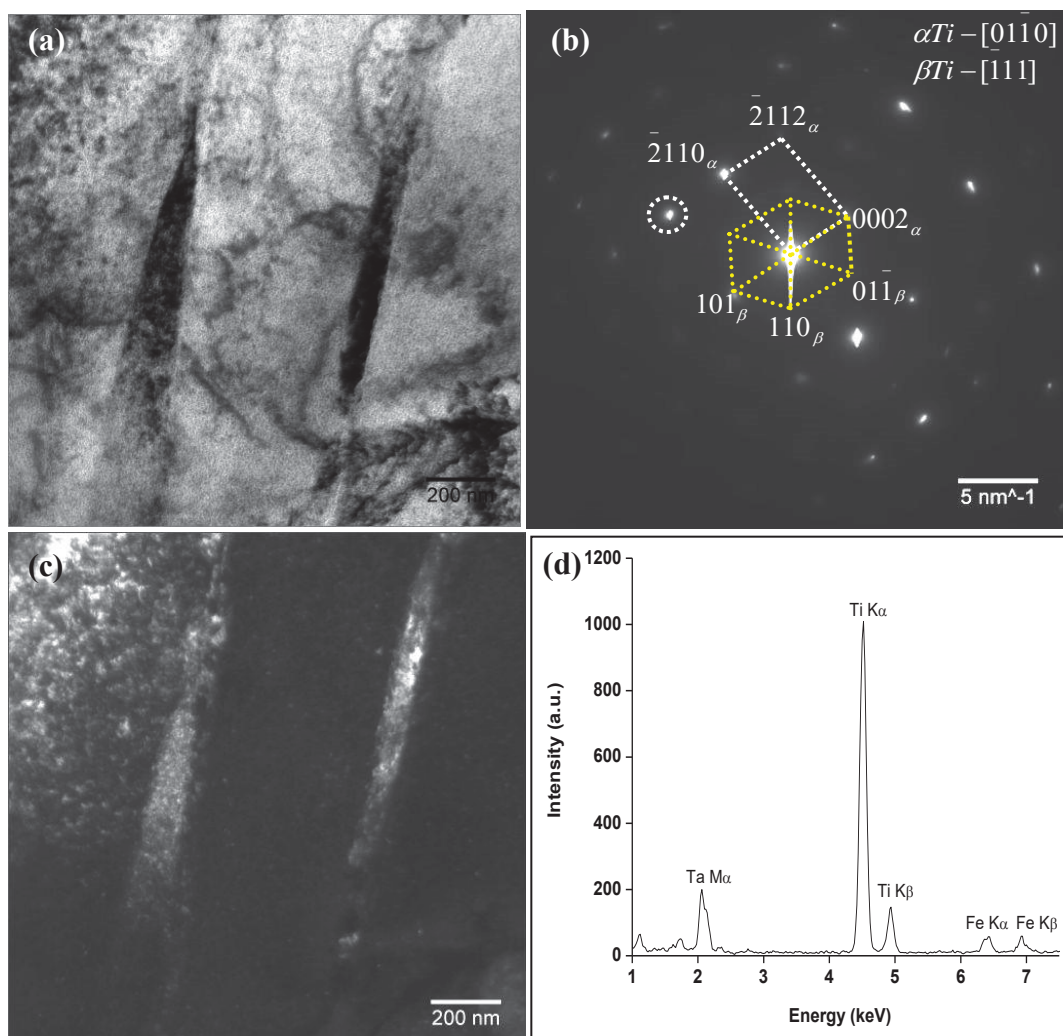


Figure 4.35 TEM (a) BF image obtained from zone 7, (b) overlapping diffraction patterns from α and β phases of Ti along $[0110]$ and $[111]$ zone axis respectively, (c) DF image corresponding to $[2112]_\alpha$ reflection (circled in (b)) revealed α plates and β phases of Ti (d) EDS spectrum from β (matrix) phase showed the presence of Fe

The TEM-BF image of the specimen extracted from zone 3 close to the interface is shown in Figure 4.36(a). Analysis of the corresponding electron diffraction pattern (Fig. 4.36(b)) confirmed the presence of FeTi intermetallic phase along $[\bar{1}11]$ zone axis.

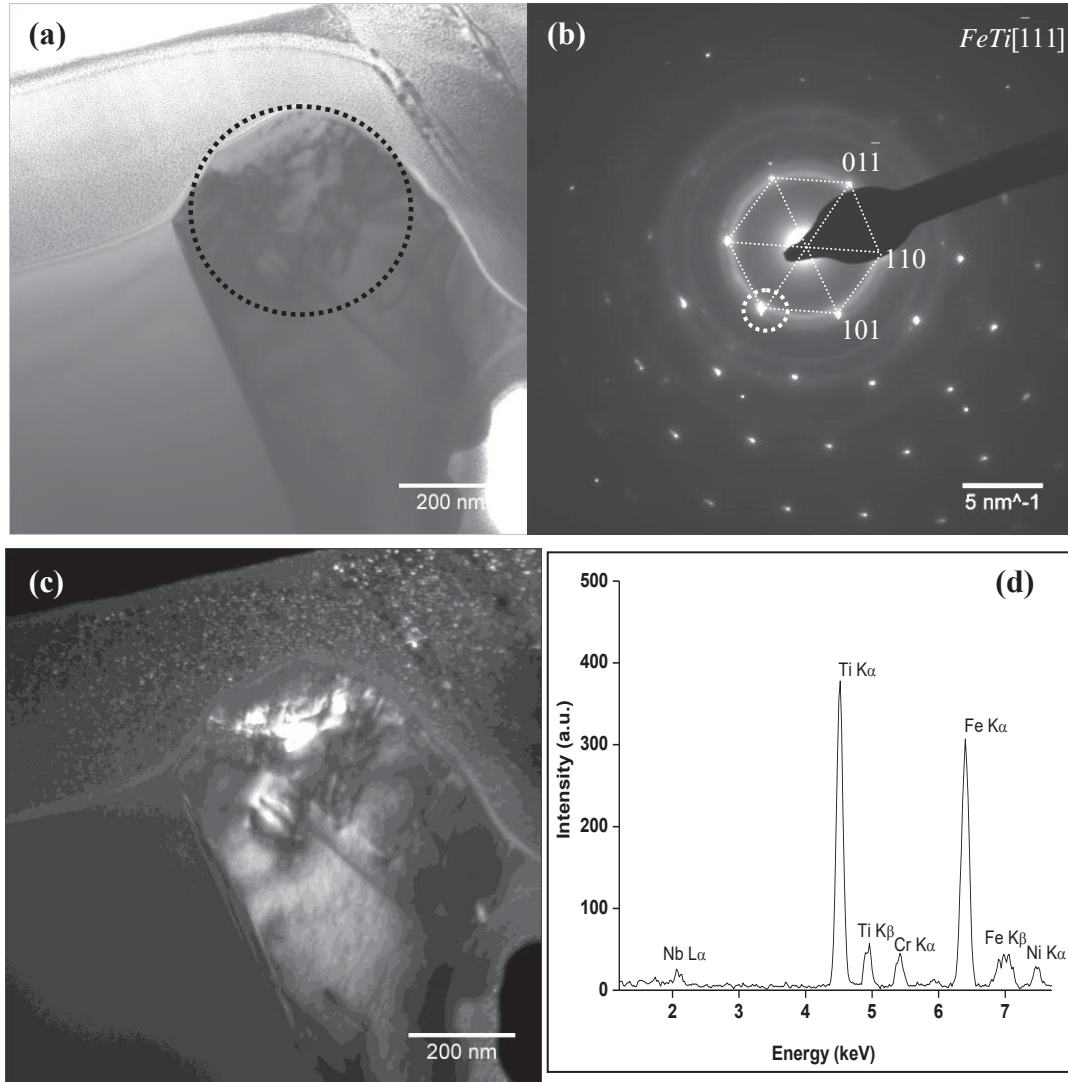


Figure 4.36 TEM (a) BF image of specimen extracted from zone 3, (b) SAD pattern obtained from the circled region in (a) confirmed the presence of FeTi intermetallic phase along $[\bar{1}11]$ zone axis, (c) DF image from $[011]$ reflection (circled spot in (b)) and (d) EDS spectrum revealed almost equal intensity for Fe and Ti in the selected region

DF image (Fig. 4.36(c)) highlights regions with FeTi phase along $[0\bar{1}1]$ orientation (circled spot in 4.36(b)). The EDS spectrum (Fig. 4.36(d)) showed presence of Fe, Cr and Ni in addition to Ti and Nb in this region. The BF image, SAD pattern and DF images from another region of zone 3 are shown in Fig. 4.37(a) to (d) respectively. SAD pattern (Fig. 4.37(b)) revealed overlapping reflections from both FeTi and Fe₂Ti phases along $[\bar{1}11]$ and $[2\bar{1}\bar{1}0]$ zone axis respectively.

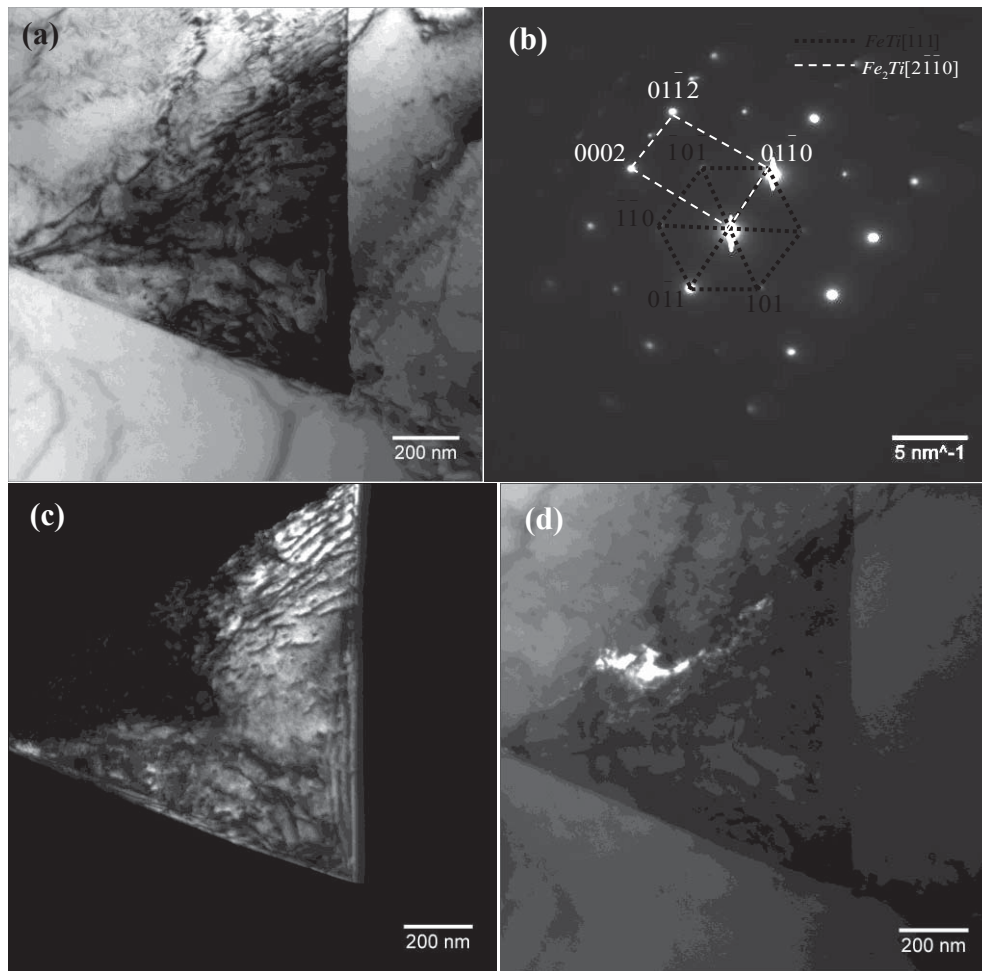
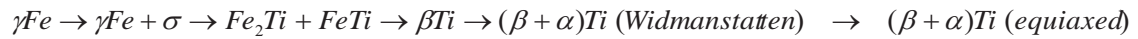


Figure 4.37 TEM (a) BF image of a region close to the clad interface, (b) SAD pattern showing overlapping reflections from both FeTi and Fe₂Ti phases and DF images for the (c) $[011\bar{2}]_{Fe_2Ti}$ and (d) $[\bar{1}0\bar{1}]_{FeTi}$ reflections provided further confirmation

The DF images (Fig. 4.37(c) and (d)) corresponding to $[01\bar{1}2]_{Fe_2Ti}$ and $[\bar{1}0\bar{1}]_{FeTi}$ diffraction spots further confirmed the coexistence of FeTi and Fe₂Ti phases.

TEM-BF image obtained from zone 2 (Fig. 4.30(d)) in SS side is shown in Fig. 4.38(a). The SAD pattern (Fig. 4.38(b)) from this region showed overlapping reflections from both γ -Fe and σ phases along $[011]$ and $[014]$ zone axis respectively. DF images (Fig. 4.38(c) and (d)) obtained from $[\bar{1}\bar{1}\bar{1}]_{\gamma}$ (continuous circle in Fig. 4.38(b)) and $[425]_{\sigma}$ (dotted circle in Fig. 4.38(b)) reflections confirmed the coexistence of (γ + σ) structure in zone 2. EDS spectrum (Fig. 4.38(e)) from the fcc region showed presence of Ti along with Fe, Cr and Ni, whereas a high intensity peak of Cr in Fig. 4.38(f) from the σ phase provided further confirmation. Based on above results the sequence of phase formation across the explosive clad after heat treatment at 800 °C for 20 h is summarized as follows:



It is necessary to mention here that the sequence of phase evolution established experimentally differed from the JMatPro[®] computations. This difference primarily comes from the fact that the JMatPro[®] simulations were carried out for equilibrium conditions, whereas the actual formation of a phase is influenced by the kinetics of interdiffusion of elements across the clad, which in turn depends on the defect structure.

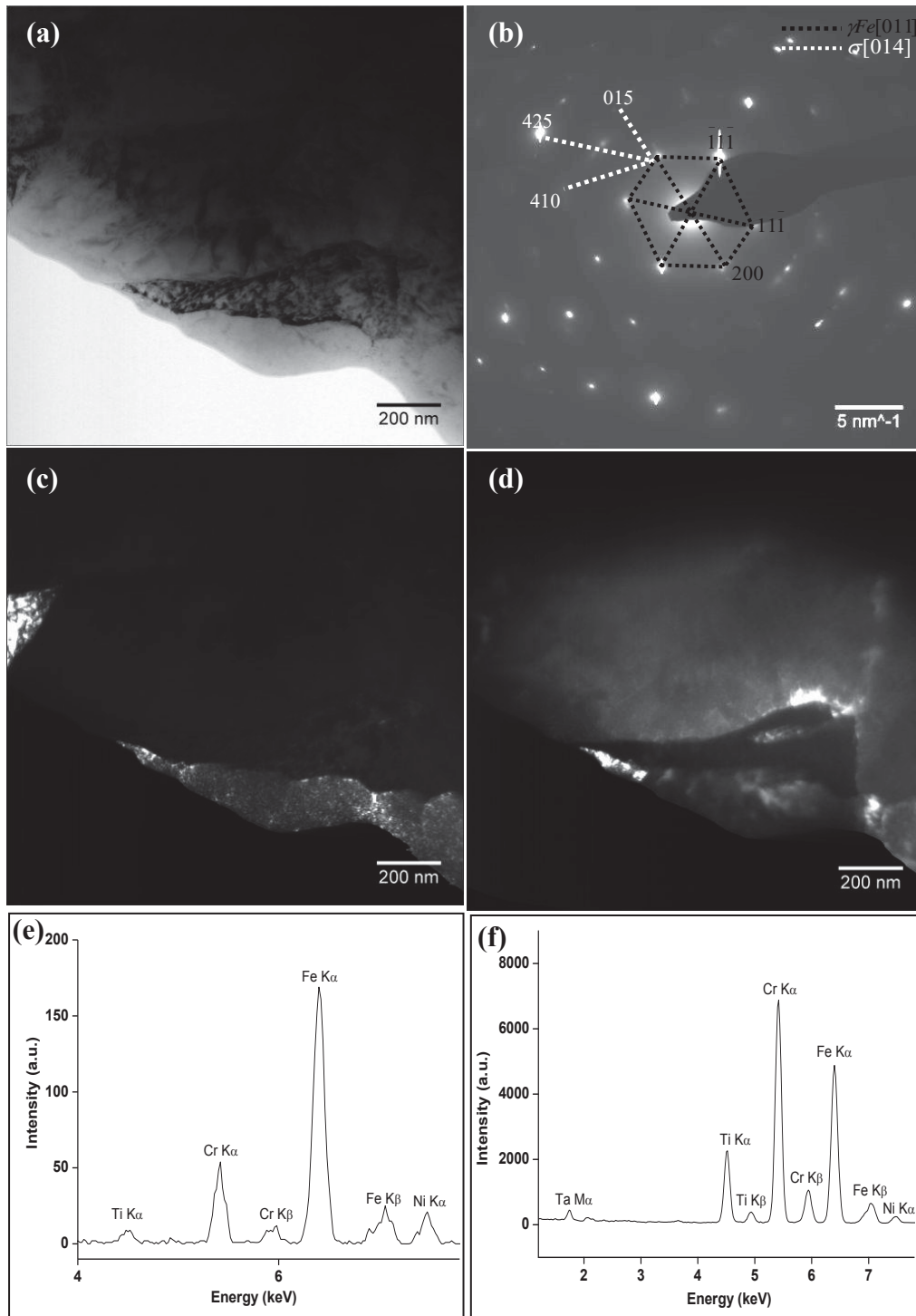


Figure 4.38 TEM (a) BF image for zone 2, (b) overlapping electron diffraction patterns from σ and γ -Fe phases; DF images corresponding to (c) $[111]_{\gamma}$ and (d) $[425]_{\sigma}$ reflections (e)-(f) – EDS spectra obtained from γ -Fe and σ phases respectively

4.7.4 Effect of secondary phases on bond strength of the explosive joints:

The effect of deleterious secondary phases on bond strength of the explosive joints has been studied by computing the UTS values using JMatPro[®], which is presented in Fig. 4.39. The value of UTS computed at the clad interface was 218 MPa which was comparable with that of the TiTaNb alloy. The values were higher in both SS and TiTaNb sides. Within the diffusion zone in TiTaNb, the UTS value exhibited a maxima followed by a gradual decrease as a function of distance from the interface and finally reaches the values corresponding to that of the flier plate well away from the interface. At this temperature the flier plate was identified to be the region more susceptible for failure.

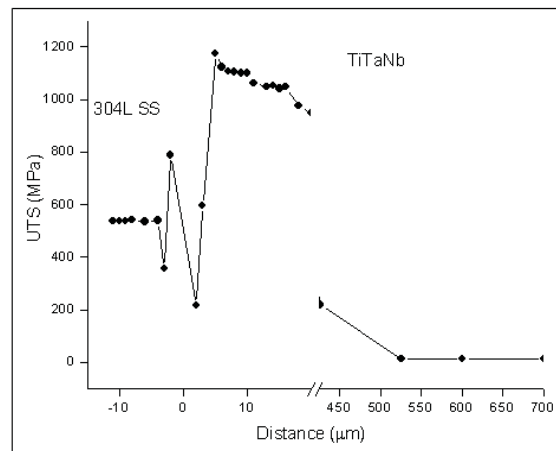


Figure 4.39 Predicted variation in UTS across the clad interface at 800 °C after 20 h of heat treatment

4.8 Summary:

The important findings of the study on “**Structural changes during deformation and annealing in 304LSS/Ti-5Ta-2Nb explosive clad joints**” are summarized as follows:

- Explosive cladding of 304LSS and Ti-5Ta-2Nb alloy resulted in the formation of deformation induced phases such as α' martensite in SS and metastable fcc phase in TiTaNb alloy.
- Systematic variation in the volume fraction of strain induced martensite and metastable fcc phase and morphological changes associated with the thermal exposure have been established in the temperature range of 100-1100 °C.
- The reversion of metastable phases followed a diffusion controlled nucleation and growth process.
- Based on the interface microstructure and JMatPro[®] simulations, the post cladding heat treatment for the explosive joints was recommended as 550 °C for durations not exceeding 10 h.
- Heat treatment at 600 °C and beyond resulted in the formation of Kirkendall porosity on SS side and intermetallic phases at the interface.
- At 800 °C poor high temperature mechanical property exhibited by TiTaNb indicated a possible shift in the region of failure to the flier plate of the explosive clad.

Chapter 5

**Interdiffusion in Fe-Ti based systems
under equilibrium and non-equilibrium
conditions**

5.1 Introduction:

Fe and Ti based dissimilar joints are encountered in the components used for reprocessing of spent nuclear fuel of fast breeder reactors and hence are of importance to the nuclear industry [1]. Over the years different joining techniques which include diffusion bonding, friction welding, friction stir welding and explosive cladding have been employed to fabricate these joints. Each of these methods have specific advantages over fusion joining methods like absence of heat affected zone, high energy density, no melting of base metals and formation of metallic bond by severe plastic deformation [10-13]. The poor mutual solubility between Fe and Ti poses challenges in the fabrication of the joints due to the formation of FeTi, Fe₂Ti type of brittle intermetallic phases at the interface [7]. This difficulty is further enhanced with alloying additions due to the formation of secondary phases and ternary compounds such as σ (Cr rich phase) and χ (Fe₂Cr₅Ti₁₇) due to interdiffusion [88]. Hence, the selection of appropriate joining method is primarily based on the ability of the technique to either prevent the formation of these brittle phases and/or disperse them as isolated phases, thereby preserving the integrity of the joint [10-13]. It is necessary to understand the time dependent evolution of the structure and chemistry of the interface especially under thermal exposure to assess the performance of the joint.

The objective of the present research work was to obtain a fundamental understanding of the interdiffusion phenomena and growth characteristics of the interface in Fe-Ti system in the presence of a high density of defects, which simulated an explosive clad joint, as the most common industrially adopted process for joining Fe and Ti based alloys. The microstructural and microchemical variations across the

interface provide the required knowledge to design appropriate heat treatments for the explosive clad joint of multicomponent 304LSS and Ti-5Ta-2Nb for fabrication of the dissolver component in the reprocessing plant [43]. The enhanced diffusion kinetics across the severely deformed interface in explosive clads as compared to diffusion bonded and friction welded joints has been presented in detail in Chapters 3 and 4 of the thesis. The present work compares the diffusion kinetics between two joints with varying extents of defects at the interface. As a typical representation of the two cases mild steel/Ti joints fabricated employing friction welding and explosive cladding have been studied. It is evident that the explosive cladding process imparts a very high defect density at the interface typical of a non-equilibrium process. In the friction welded joints the extent of deformation is far less, heat affected zone is negligible and modification of the microstructure or chemistry as compared to the parent metals is insignificant as described in Chapter 3. Due to the difficulties in joining as explained earlier, the friction welded joints were considered closest to diffusion couple and more so when annealed. Hence, the nomenclature of equilibrium and non-equilibrium has been used in this study. Apart from the role of defects the influence of alloying elements on, the diffusion kinetics has also been studied in the multicomponent 304LSS/Ti-5Ta-2Nb system.

In this chapter, the diffusion driven microstructural and microchemical changes in Fe/Ti based systems has been studied. Evaluation of interdiffusion parameters from concentration profiles is rather simple in the case of binary systems with constant molar volume by employing Boltzmann-Matano (BM) analysis [80-84]. Due to ambiguity of locating the Matano plane for multiphase and multicomponent systems with significant

variation in the molar volume den Broeder (DB) modified the governing equation for determining $D(C)$ using a concentration dependent variable [85, 86]. Sridhar et al. [86] compared the interdiffusion coefficients in Cu-Ni and Ta-W systems calculated using BM and DB methods and reported equivalent accuracy for $D(C)$ values in both the methods. However, as mentioned in section 1.5.2, the position of ' X_0 ' (Matano interface) is not required in DB method [85]. Further, from Chapter 3 and 4 it was observed that interdiffusion of the alloying elements led to the formation various intermetallic and secondary phases at the Fe/Ti based systems. Hence, it is essential to consider the variation in molar volume as a function of concentration of the diffusing species. Sangeeta et al. [91] emphasized the importance of molar volume in V_3Ga system and have proposed use of Wagner's method when considerable molar volume change was involved during interdiffusion.

Further, in multicomponent systems diffusion of one element influences the other diffusing species, hence it is necessary to consider the cross diffusion terms in addition to the direct interdiffusion coefficients. However, for an n component system ($n=i, j, k, \dots$), one should have $n-1$ independent diffusion couples ($i-j, i-k..$) with intersecting diffusion paths, determination of which becomes tedious as the number of components increases [130]. Hence, Dayananda and Sohn developed a new approach for the determination of the interdiffusion coefficients from a single diffusion couple as average values over selected composition range [181]. Ternary diffusion couples of Cu-Ni-Zn, Fe-Ni-Al and Ni-Cr-Al were long term diffusion annealed and zero flux plane as well as a reference plane ' X_0 ' were identified based on total flux of the alloying

elements in each system. The ' X_0 ' reference plane was used to estimate the average effective interdiffusion coefficients over defined compositional range [181]. A similar approach was employed in the present study to calculate average effective interdiffusion coefficients in Fe-C-Ti system. DB [85] and Wagner's methods [92] were used to determine interdiffusion coefficients in SS/TiTaNb system and Hall's method [131] was employed to estimate the impurity diffusion coefficients of Fe in Ti rich regions in both Fe-C-Ti and SS/TiTaNb systems.

This chapter is organized in the following sequence: section 5.2 and 5.3 describe the evolution of microstructure and microchemistry due to interdiffusion in MS/Ti joints under equilibrium and non-equilibrium conditions respectively. Growth characteristics of diffusion zones and estimation of interdiffusion parameters in both the cases is also explained in these sections, while section 5.4 makes a critical comparison of the diffusion behavior under the two conditions. Section 5.5 describes the role of alloying elements on the interdiffusion phenomena in SS/TiTaNb explosive joints and the important findings of the study are summarized in section 5.6.

5.2 Growth kinetics of the diffusion zones under equilibrium conditions and estimation of interdiffusion parameters in MS/Ti joints:

5.2.1 Evolution of interface microstructure:

Cross-section specimens of MS/Ti friction joints were diffusion annealed in the temperature range of 500-800 °C for duration of 100 h. Figures 5.1(a) to (d) show the BSE images of interface microstructure at the four temperatures. At 500 °C a continuous thin zone of width $\sim 0.6 \mu\text{m}$ (arrow marked in Fig. 5.1(a)) was observed at the interface followed by a fine grained region (grain size = $\sim 5 \mu\text{m}$) up to a distance of

~600 μm on MS side, beyond which the microstructure resembled that of the parent metal. With increase in temperature to 600 $^{\circ}\text{C}$, average grain size increased to 10 μm along with increase in the width of the interfacial zone to ~1 μm (Fig. 5.1(b)). Average grain size and width of the interfacial zone further increased to ~150 μm and 4 μm (Fig. 5.1(c)) as the temperature was increased to 700 $^{\circ}\text{C}$. The interfacial zone attained a width of ~8 μm and well formed equiaxed ferrite grains were observed at 800 $^{\circ}\text{C}$ (Fig. 5.1(d)).

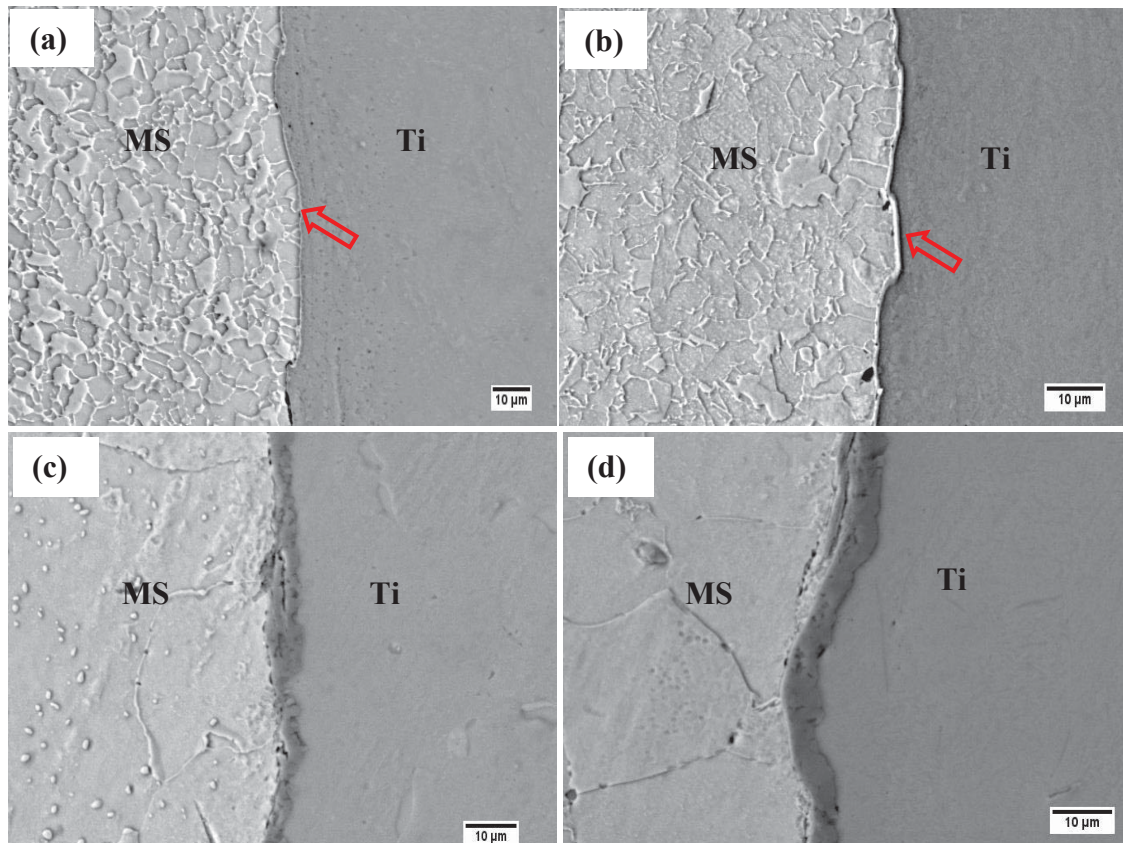


Figure 5.1 BSE images showing the interface microstructure of MS/Ti friction joints diffusion annealed for 100 h at temperatures of (a) 500 $^{\circ}\text{C}$, (b) 600 $^{\circ}\text{C}$, (c) 700 $^{\circ}\text{C}$ and (d) 800 $^{\circ}\text{C}$ respectively

Fine grains at 500 °C on MS side in Fig. 5.1(a), provided an evidence for recrystallization of the metal followed by grain growth with increase in temperature. Equiaxed ferrite grains with randomly distributed pearlite was attributed to the heat treatment in $\alpha+\gamma$ phase field and subsequent transformation of γ to fine pearlite during cooling [139, 140].

5.2.2 Growth kinetics of the diffusion zones:

As explained in section 2.6, growth kinetics of the reaction zones can be expressed as a function of annealing time and temperature (Eq. 2.5 and Eq. 2.6). At low temperatures (≤ 600 °C) width of the reaction zone could not be measured with accuracy due to its low thickness. Hence, only the data measured at high temperature (800 °C) was monitored as a function of diffusion time. A representative plot of square of the thickness of the reaction zone ' X ' vs diffusion annealing time ' t ' showed (Fig. 5.2(a)) parabolic growth of the reaction zone indicating diffusion as the rate controlling process. Using the interrelationship between X and t the growth constant (' K_p ') was determined at each temperature. From the Arrhenius analysis of ' K_p ' (Fig. 5.2(b)), the growth constant (' K_0 ') and activation energy required for the growth of the reaction zone were obtained as 1.16×10^{-3} m²/s and 137 kJ/mol respectively. AISI SS304L/Ti friction joints diffusion annealed in a similar temperature regime, showed wider reaction zones probably due to the variation in the type, number and location of the phases [46]. Typically the phases that were observed in the SS/Ti joints were FeTi, Fe₂Ti and β Ti(Fe) [46, 54] while those observed in the present at the interface of Fe-C/Ti friction joints were intermetallic FeTi and TiC phases [133]. Hence, it can be

concluded that the presence of TiC phase at the interface inhibited the growth of the diffusion zone in MS/Ti joints.

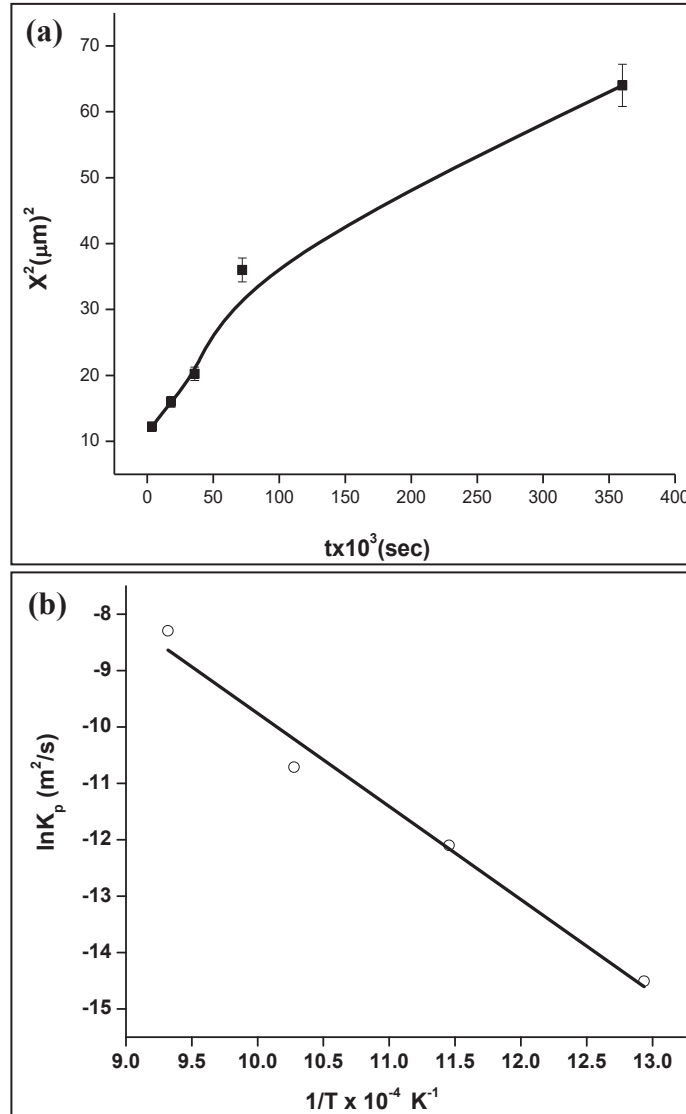


Figure 5.2(a) Growth of the diffusion zone in MS/Ti friction joints as a function of time at a temperature 800 °C and (b) Arrhenius analysis of the growth constant

5.2.3 *Diffusion driven microchemical changes at the interface:*

Typical concentration profiles obtained from the MS/Ti diffusion annealed friction joints are shown in Fig. 5.3(a) to (d) respectively. Considerable redistribution of the elements was clearly seen in the concentration profiles. Significant increase in the C concentration from ~10 to 14 wt.% was observed at the interface at all temperatures. The total diffusion distances of Fe in Ti were measured as 2, 3, 6 and 10 μm while diffusion of Ti in MS was obtained as 2, 3, 3 and 4 μm at 500, 600, 700 and 800 $^{\circ}\text{C}$ respectively. Carbon showed a gradual increase in the diffusion distance from 2 to 12 μm with increase in temperature. The concentration profiles resembled error function profiles at all the temperatures and approximate composition (in wt.%) of the elements at the cross over point at 800 $^{\circ}\text{C}$ was obtained as 45.8Fe-6C-48.1Ti. A correlation of the microchemical data (Fig. 5.3(d)) of the diffusion zone with the isothermal section of ternary Fe-C-Ti at 1000 $^{\circ}\text{C}$ [182], revealed that this interfacial zone corresponded to a three phase mixture of FeTi+Fe₂Ti+TiC. In section 3.6.3, confirmatory evidence for the formation of fcc - TiC and FeTi particles in the diffusion zone of the annealed joints has been provided based on detailed electron microscopy investigations [133].

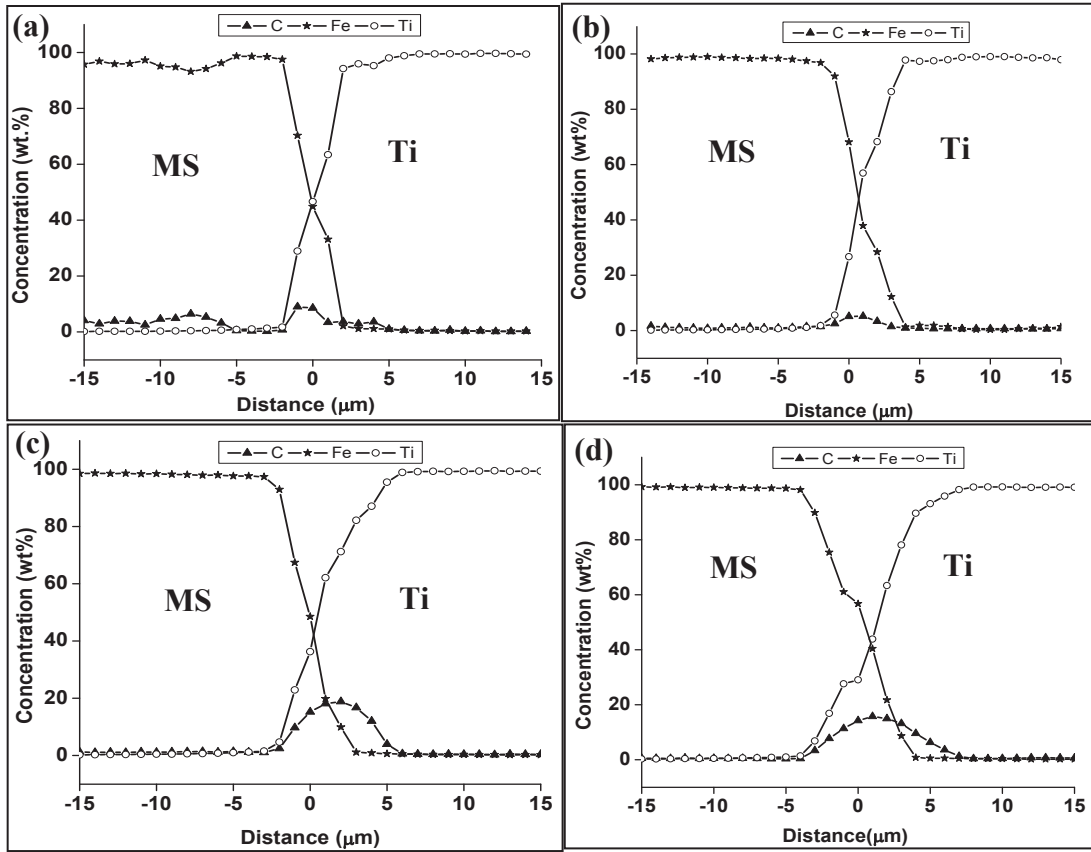


Figure 5.3 Concentration profiles obtained across the MS/Ti friction joints after heat treatment at (a) 500 °C, (b) 600 °C, (c) 700 °C and (d) 800 °C for 100 h respectively

5.2.4 Estimation of interdiffusion parameters:

As described in section 2.5, the average effective interdiffusion coefficients (\bar{D}) in a specific compositional range were calculated following the method proposed by Dayananda [131, 181]. Prior to the calculation of \bar{D} , the procedure adopted to remove the measurement errors in the experimental concentration profiles was explained in Chapter 2, page no. 37-40. Table 5.1 lists the values of \bar{D}_{Fe}^{eff} plotted as a function of concentration of Fe at different temperatures. From the tabular column it can be observed that the diffusivities increased with increase in temperature and were found to

be concentration dependent. Beyond 35-45 wt.% of Fe the increase in diffusivity values was significant at temperatures beyond 600 °C and highest values of \widetilde{D}_{Fe}^{eff} was obtained within the composition range of 60-75 wt.% of Fe at all the temperatures. The highest value of \widetilde{D}_{Fe}^{eff} was obtained as $1.71 \pm 0.3 \times 10^{-14}$ m²/s (60-75 wt.%) at 800 °C. Arrhenius analysis of the average effective interdiffusion coefficients obtained at various concentrations of Fe is shown in Fig. 5.4. A good linearity was exhibited by the diffusivity values in the range of temperatures studied. Interdiffusion parameters namely pre-exponential factor (D_0) and activation energy (Q) of MS-Ti system estimated from the above analysis are also tabulated in Table 5.1. Activation energies evaluated from the above analysis yielded high value of Q (147 kJ/mol) and D_0 value of the order of 10^{-9} m²/s in the composition range of 35 - 45 wt.% of Fe.

Table 5.1 Average effective interdiffusion coefficients ($\widetilde{D}_{Fe}^{eff} \times 10^{-17}$ m²/s) and interdiffusion parameters estimated in MS/Ti friction joints

Composition range (wt.% Fe)	Temperature (°C)				D_0 (m ² /s)	Q (kJ/mol)
	500	600	700	800		
10-18	--	0.2±0.8	1.63±0.8	2.83±0.6	$1.88 \pm 1.3 \times 10^{-13}$	113.7±9
20-30	0.34±0.12	0.4±0.8	2.07±1.3	8.27±1.7	$1.7 \pm 2.2 \times 10^{-12}$	113.9±4
35-45	0.75±0.13	0.48±0.2	3.85±1.9	20.9±4	$2.98 \pm 0.86 \times 10^{-9}$	147±6
48-58	0.22±0.7	2.14±0.8	12.7±6	540±11	$1.2 \pm 1.77 \times 10^{-10}$	100±2.1
60-75	5.10±1.5	82.6±3.3	439±21	1710±342	$7.4 \pm 2.5 \times 10^{-9}$	126.4±2.3

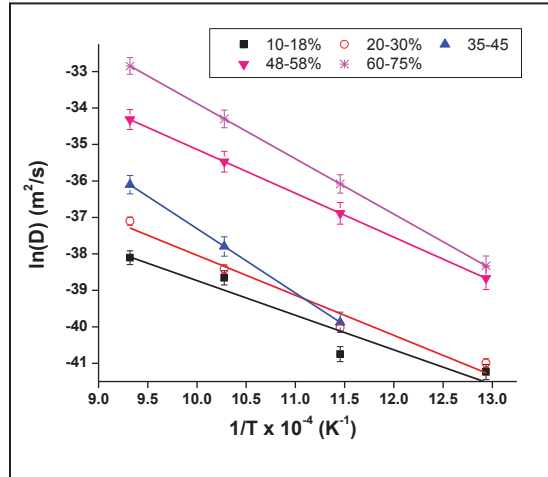


Figure 5.4 Temperature dependence of effective interdiffusion coefficients in MS-Ti system

This gave an insight into the influence of intermetallic or secondary phases on the overall diffusion kinetics of MS/Ti joints. The sluggish diffusion kinetics is a manifestation of the ordered intermetallic and stoichiometric FeTi, Fe₂Ti and TiC phases that form due to interdiffusion of elements across the interface in this composition range, which is also supported by the JMatPro[®] based predictions (section 3.5.1, Chapter 3) [133].

5.3 Growth kinetics of the diffusion zones under non-equilibrium conditions and estimation of interdiffusion parameters in MS/Ti joints:

5.3.1 Evolution of interface microstructure:

BSE images of the interface of explosive clad annealed for 1 h in the temperature range of 500-800 °C are shown in Fig. 5.5(a) to (d). Elongated grains were observed close to the interface at 500 °C with a hardness of ~210 HV resembling the microstructure and microhardness of ‘as clad’ joints. Interface showed a high hardness value (~290 HV), while the hardness of Ti was comparable to the parent metal. In

contrast a dark zone of $\sim 0.8 \mu\text{m}$ thickness was observed at the interface (arrow marked in Fig. 5.5(b)) at 600°C with a high hardness of 285 HV . Formation of equiaxed grains on MS with a concomitant decrease in the hardness to 190 HV was evident Fig. 5.5(b) which decreased further to $\sim 160 \text{ HV}$ (Fig. 5.5(c)) with increase in temperature to 700°C . However, at this temperature the interfacial zone width increased to $\sim 4 \mu\text{m}$ and hardness value to 340 HV . At 800°C , width of the interfacial zone increased as expected, but the formation of another zone of average width $\sim 30 \mu\text{m}$ and hardness of 220 HV was observed. This zone had a typical Widmanstätten microstructure.

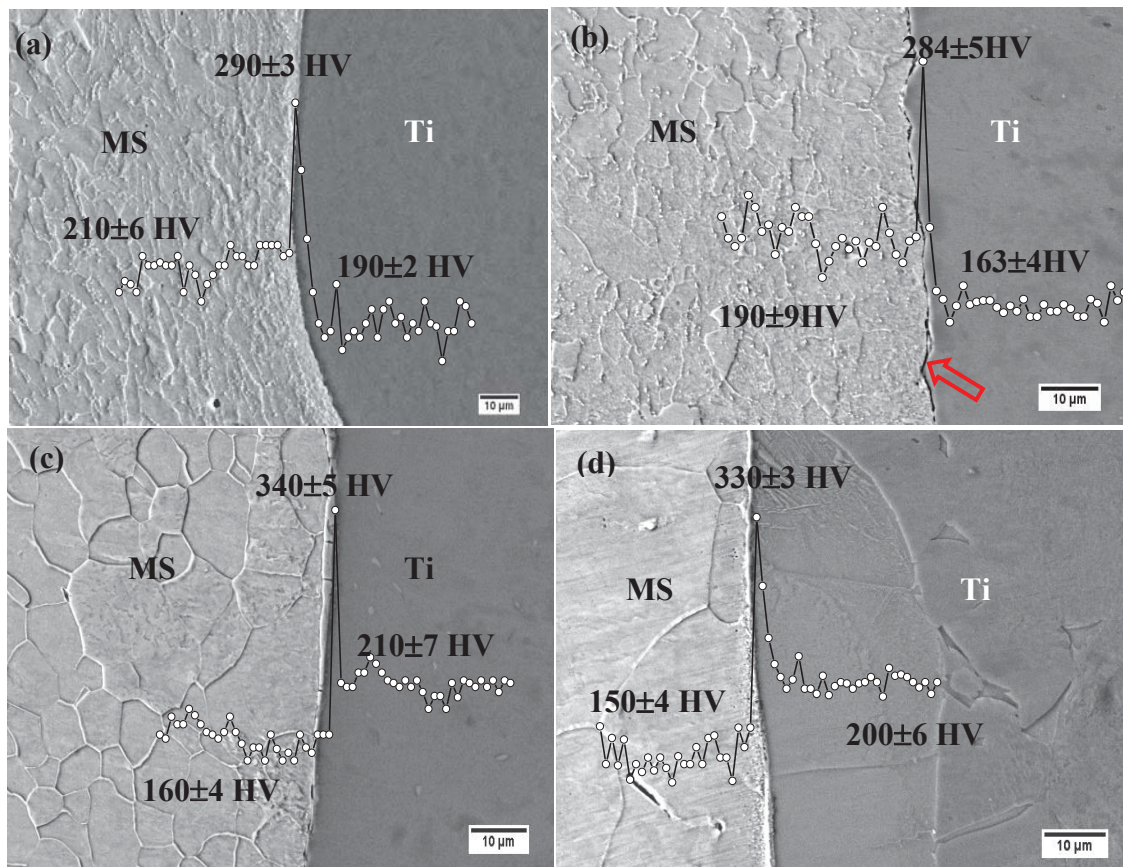


Figure 5.5 BSE images showing variation in the interface microstructure of MS/Ti explosive clads diffusion annealed at (a) 500°C , (b) 600°C , (c) 700°C and (d) 800°C for 1 h respectively; corresponding hardness profiles are superimposed

Change in the interface microstructure of MS/Ti explosive clads heat treated for duration of 100 h is shown in Fig. 5.6(a) to (d) with superimposition of the corresponding hardness profiles. At low temperature (500 °C), presence of well formed ferrite grains with a reduction in the hardness to ~ 180 HV was observed. Exactly at the interface a ~ 2 μm wide zone with a high hardness of ~ 370 HV was observed. On Ti side, Widmanstätten α - β Ti microstructure was observed up to a distance of ~ 27 μm from the interface, the width of which increased to 36 μm as the temperature increased to 600 °C (Fig. 5.6(b)).

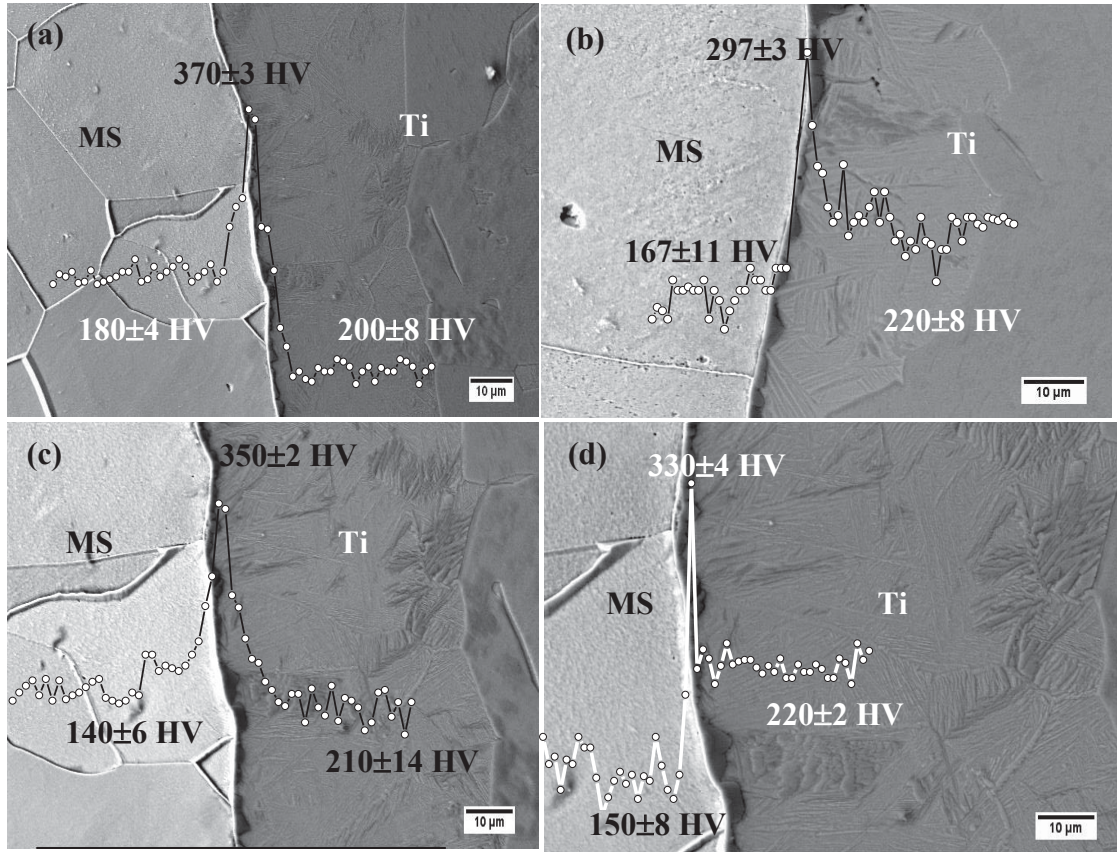


Figure 5.6 BSE images showing variation in the interface microstructure of MS/Ti explosive clads diffusion annealed at (a) 500, (b) 600, (c) 700 and (d) 800 °C for 100 h respectively; corresponding hardness profiles are superimposed

Thickness and hardness of the interfacial zone were obtained as $\sim 3 \mu\text{m}$ and $\sim 300 \text{ HV}$ respectively. At 700°C , growth of the ferrite grains was observed on MS side with a concomitant reduction in the hardness to $\sim 140 \text{ HV}$. Total width of the diffusion zone was obtained as $\sim 72 \mu\text{m}$ which can be divided into $\sim 4 \mu\text{m}$ wide interfacial zone and $\sim 64 \mu\text{m}$ wide Widmanstätten α - β structure (Fig. 5.6(c)). With increase in the temperature to 800°C , width of the interfacial zone and Widmanstätten region increased to ~ 6 and $\sim 75 \mu\text{m}$ respectively. The average hardness values were higher than that observed for duration of 1 h at all temperatures.

5.3.2 Growth kinetics of the diffusion zones:

The width of the total diffusion zone (X) in explosive joints was plotted as a function of duration of exposure in Fig. 5.7(a). At low temperatures ($\leq 600^\circ\text{C}$), growth of the diffusion zones was negligible hence, only the high temperature data was studied. From the graph it was evident that at both 700 and 800°C , reaction zone followed parabolic growth indicating diffusion as the rate controlling process. From the temperature dependence of ' K_p ' (Fig. 5.7(b)) layer growth parameters growth constant ' K_0 ', and activation energy Q were obtained as $1.32 \times 10^{-2} \text{ m}^2/\text{s}$ and 75.5 kJ/mol respectively. Similar investigations by Alemán et al. [23] reported that the activation energy required for growth of interfacial zone was 137 kJ/mol . Wide difference between the reported and the calculated values of Q and growth constants was understood as follows: reported value of Q corresponds to the growth of a zone consisting of intermetallic phases ($\lambda + \text{FeTi}$) while the Q value in the present research corresponded to growth of $\text{FeTi} + \text{TiC} + \beta\text{Ti}$ phases. The lowest value of Q was

attributed to the presence of disordered β Ti (Fe) phase. It was also observed that the thickness of the total diffusion zone in 304 SS/Ti-5.5Al-2.4V diffusion bonded joints was $\sim 36.2 \mu\text{m}$ at 850°C [26], which is much lower than the value obtained ($\sim 51 \mu\text{m}$ at 800°C -1 h) in the present study. This difference can be rationalized based on the faster diffusion of alloying elements assisted by the high volume fraction of lattice defects in the explosive clads.

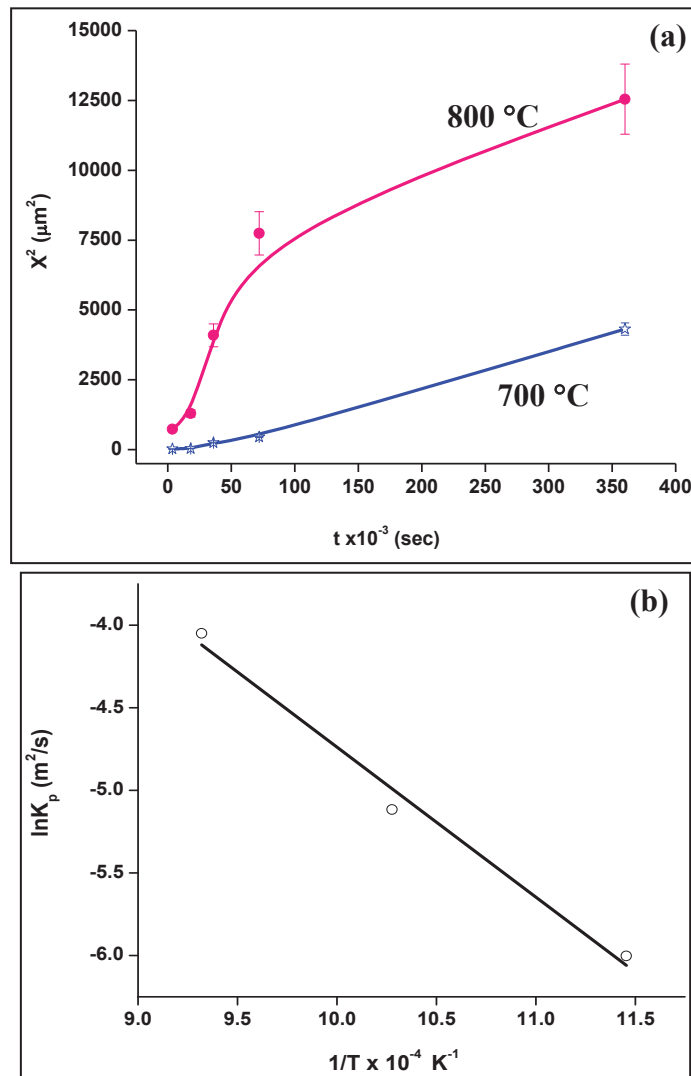


Figure 5.7(a) Growth of the diffusion zone in MS/Ti explosive joints as a function of time at temperatures 700 and 800°C and **(b)** Arrhenius analysis of the growth constant

5.3.3 Diffusion driven microchemical changes at the interface:

Elemental concentration profiles obtained across the interface of the explosive clads diffusion annealed in the temperature range of 500-800 °C for 1 h are shown in Fig. 5.8(a) to (d). At temperatures ≤ 700 °C, the profiles resembled smoothly varying error function profiles. Slight increase in the concentration of C at the interface was observed at each temperature. The total diffusion distances of Fe in Ti and Ti in MS were obtained as 5, 8, 10, 55 μm and 3, 4, 6, 8 μm at 500, 600, 700 and 800 °C respectively.

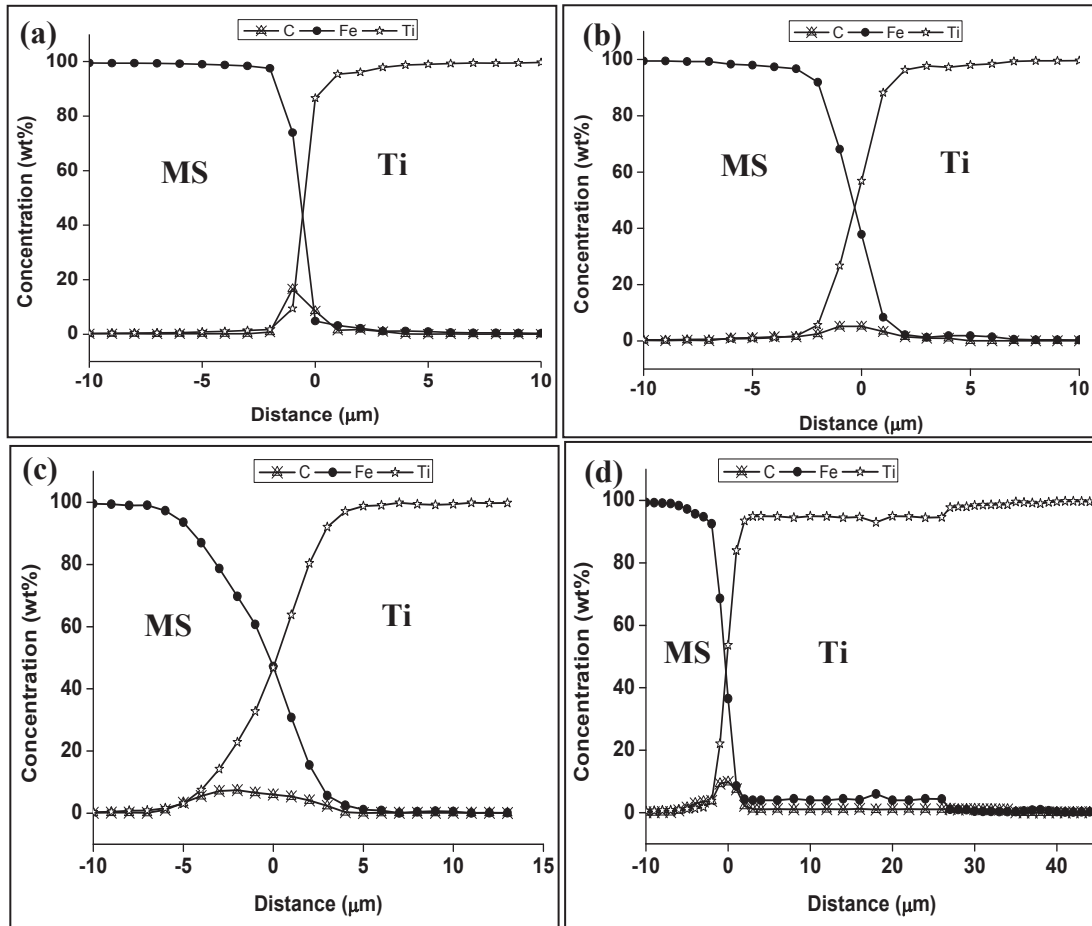


Figure 5.8 Concentration profiles obtained across the MS/Ti explosive clads heat treated at temperatures of (a) 500, (b) 600, (c) 700 and (d) 800 °C for 1 h respectively

As expected, C showed a maximum diffusion distance of $\sim 62 \mu\text{m}$ at 800°C the highest temperature of exposure (Fig. 5.8(d)). The average chemical composition at the interface was obtained as 45.4Fe-53.1Ti-1.5C at 700°C . A step like profile was seen at 800°C and the composition corresponding to this region was measured as 2.9Fe-1.2C-95.9Ti which changed gradually to Ti composition beyond $55 \mu\text{m}$. Due to increased interdiffusion of the elements; the total diffusion distance at this temperature was measured as $\sim 60 \mu\text{m}$ (Fig. 5.8(d)). Composition at the cross over point changed to 53.7Fe-36.5Ti-9.8C (in wt.%). According to the Fe-Ti phase diagram [7], presence of over 0.08 at.% Fe stabilizes the high temperature β phase of Ti at ambient temperature.

Concentration profiles obtained across the interface of the explosive clads diffusion annealed for 100 h in the temperature range of $500\text{--}800^\circ\text{C}$ are shown from Fig. 5.9(a) to (d). As expected step profiles were observed at all the temperatures. The total diffusing distances of Fe was measured as ~ 25 (Fig. 5.9(a)) and $34 \mu\text{m}$ (Fig. 5.9(b)) at 500 and 600°C respectively. The average composition (in wt.%) at the cross over point was obtained as 44.7Fe-53.1Ti-2.2C (500°C) and nearly constant composition of 2.9Fe-1.2C-95.8Ti (in wt.%) was observed in the step region of the concentration profile (Fig. 5.9(a)). As the temperature increased to 700 and 800°C , total width of the diffusion zone of Fe in Ti also increased from ~ 88 (Fig. 5.9(c)) to $\sim 112 \mu\text{m}$ (Fig. 5.9(d)) respectively. Although, the total width of the diffusion zone was obtained as $\sim 112 \mu\text{m}$ from the concentration profiles, it measured only $\sim 80 \mu\text{m}$ from the microstructure due to the diffuse interface between Widmanstätten structure and α Ti region (Fig. 5.9(d)).

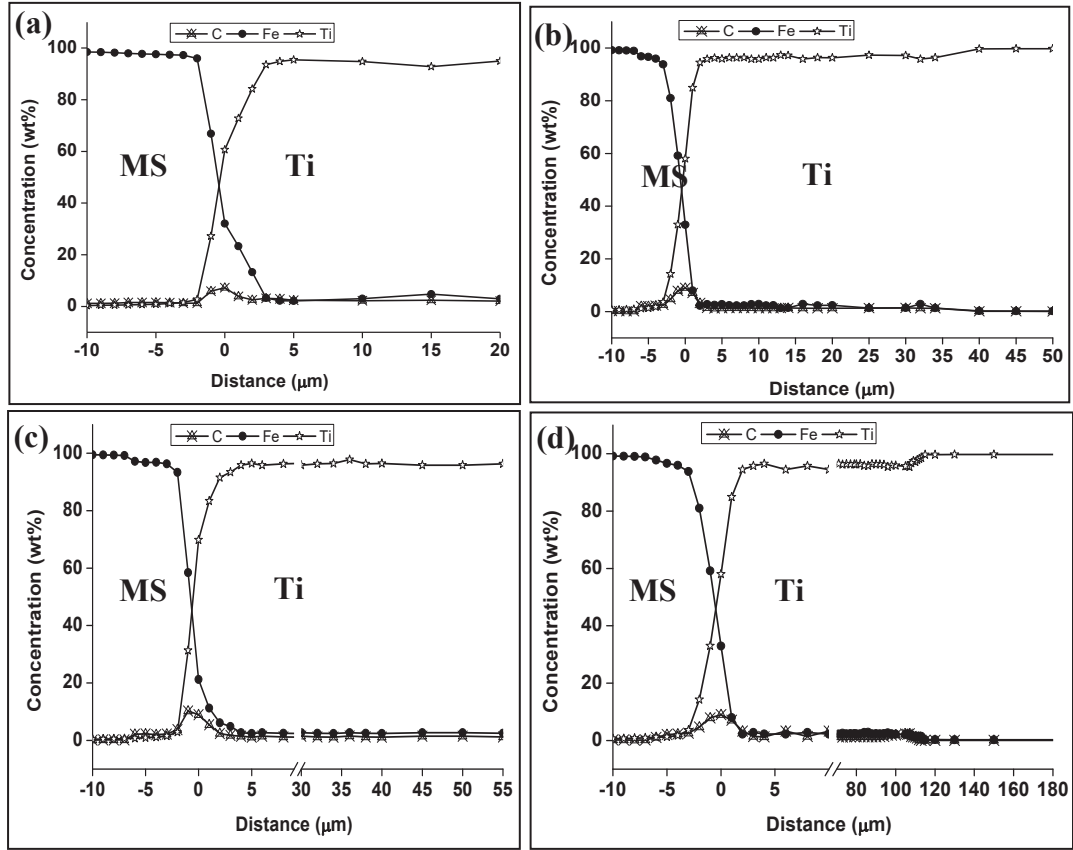


Figure 5.9 Concentration profiles obtained across the MS/Ti explosive clads heat treated at temperatures of (a) 500, (b) 600, (c) 700 and (d) 800 °C for 100 h respectively

5.3.4 Estimation of interdiffusion parameters:

The results described so far have clearly demonstrated the redistribution of Fe, C and Ti across the interface and the possible formation of intermetallic and secondary phases during thermal exposure. Prior to proceeding with the determination of average interdiffusion coefficients, molar volume has been calculated as a function of concentration using the following formula [101]:

$$V_{mix} = \sum_{i=Fe,C,Ti} N_i V_m^0(i) \quad (5.1)$$

' V_m^0 ' is the molar volume of pure element of interest; the values substituted for Fe, C, and Ti were 7.09, 5.29 and 10.64 cm³/mol [183] respectively. Figure 5.10 shows the plot of molar volume variation as a function of atomic fraction of Fe at 800 °C (for 100 h duration). The change in molar volume showed linearity following ideal Vegard's law (continuous line in Fig. 5.10) under equilibrium conditions whereas a negative deviation from ideal behavior (open circles in Fig. 5.10) was observed during diffusion under non-equilibrium conditions. Such a non linear negative deviation in the molar volume as a function of Fe concentration suggested the formation of secondary phases during the course of interdiffusion. Therefore, molar volume variation has been incorporated while calculating the effective interdiffusion coefficients in MS/Ti explosive joints in the present study. For Fe, Ti and FeTi phase the molar volume values of 7.09, 10.64 and 8.62 cm³/mol respectively were used to calculate the concentration dependent diffusion coefficients.

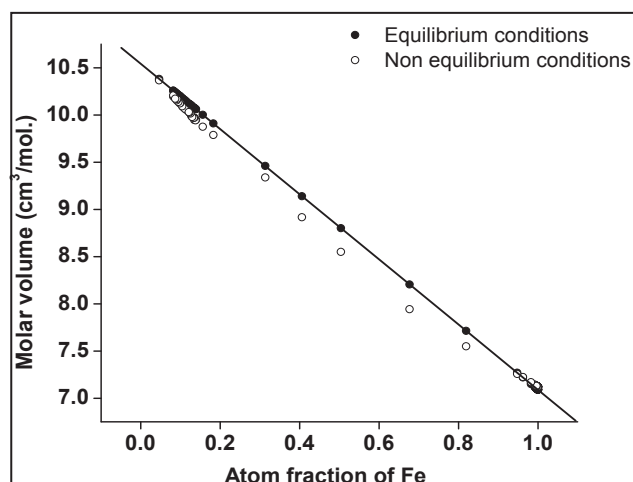


Figure 5.10 Variation in the molar volume (V_{mix}) in MS-Ti system during equilibrium and non-equilibrium diffusion as a function of atomic fraction of Fe

Table 5.2 lists the values of \widetilde{D}_{Fe}^{eff} obtained for MS-Ti explosive joints plotted in specific composition ranges of Fe at different temperatures. \widetilde{D}_{Fe}^{eff} values were found to be strongly concentration dependent and increased with increase in temperature. At 800 °C, the diffusivity values were in the order of 10^{-15} m²/s and the lowest value was observed at a composition of 49.1Fe-48.3Ti-2.6C (in wt.%). Beyond 35-45 wt.% of Fe the diffusivity values were decreased in the composition range of 48-58 wt.% of Fe beyond which the values again increased. The highest values of \widetilde{D}_{Fe}^{eff} was obtained as $1.50 \pm 0.4 \times 10^{-14}$ m²/s (75-80 wt.%) at 800 °C. Arrhenius analysis of the effective interdiffusion coefficients obtained at various concentrations of Fe is shown in Fig. 5.11. A good linearity was exhibited by the diffusivity values in the range of temperatures studied. Interdiffusion parameters namely pre-exponential factor (D_0) and activation energy (Q) of MS-Ti explosive joints estimated from the above analysis are also tabulated in Table 5.2. From the interdiffusion parameters lowest values of diffusivity was observed in the composition range of 48-58 wt.% of Fe. From the sequence of phase formation evaluated using JMatPro[®] [120], composition corresponding to the lowest \widetilde{D}_{Fe}^{eff} value at 800 °C for 100 h corresponded to a region consisting of Fe₂Ti, TiC and β Ti phases (section 3.9.2). The overall diffusion kinetics was controlled by the sluggish diffusion behavior in the diffusion zone through ordered intermetallic Fe₂Ti and TiC phases. Faster growth of Widmanstätten (α - β) Ti phase was due to increased diffusion of Fe in disordered β phase (bcc) of Ti. A similar observation

by Nakijima et al. [179] suggested that anomalous diffusion mechanism is the reason for faster diffusion of Fe in bcc phase of Ti.

Table 5.2 Average effective interdiffusion coefficients ($\bar{D}^{eff} \times 10^{-16} \text{ m}^2/\text{s}$) and interdiffusion parameters estimated in MS/Ti explosive joints

Composition range (wt.% Fe)	Temperature (°C)				D_0 (m^2/s)	Q (kJ/mol)
	500	600	700	800		
10-18	1.64±0.5	6.02±0.6	14.7±1.4	64.2±12	4.6±1.5x10 ⁻¹¹	80.6±1.7
20-30	1.81±0.5	6.3±1.6	15.8±1.6	90±1.8	9.6±2.1x10 ⁻¹¹	86±1.9
35-45	1.32±0.4	2.03±0.2	16.6±3	94.1±5.7	3.05±2.4x10 ⁻⁷	101.3±0.7
48-58	--	1.77±0.8	14.9±4	21.4±4.6	1.39±0.7x10 ⁻¹¹	99.3±7
60-70	1.38±0.4	--	21.1±8	30±2.8	2.8±0.9x10 ⁻¹⁰	117.6±1.9
75-80	1.51±0.4	2.31±2.3	22.2±11	150±47	2.06±2.8x10 ⁻⁹	104±4.3

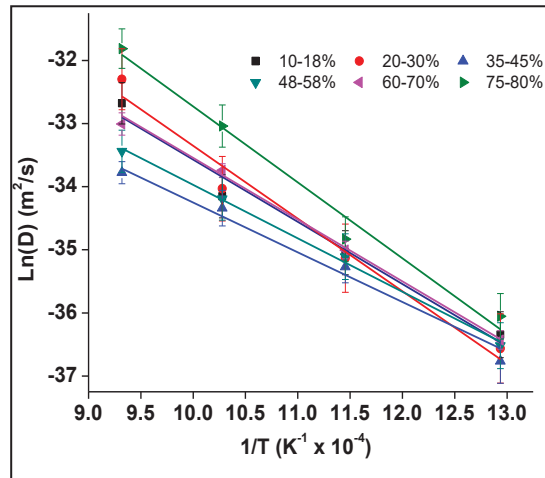


Figure 5.11 Temperature dependence of effective interdiffusion coefficients in MS-Ti system under non-equilibrium conditions

As described in section 2.6.1, the impurity diffusion coefficient of Fe in Ti was calculated using Hall's method [131] (Eq. 2.11) with the composition of <1 wt.%Fe. From Fig. 5.9 (a) to (d) it was evident that the data points were sufficiently enough to estimate the impurity diffusion coefficients of Fe in Ti whereas such an analysis could not be extended to Ti in MS due to insufficient data. Before, employing the Hall's method linearity of the probability curve between ' $\lambda(=xt^{-1/2})$ ' and ' $u(=h\lambda+k)$ ' was verified in the composition range of ~0.5 to 0.9 wt.% of Fe. Table 5.3 lists the impurity diffusion coefficients obtained at each temperature and found to be increased with increase in temperature. This value was comparable to the reported value of impurity diffusion coefficient of Fe in α -Ti (Ti-0.3 wt.%Fe) at 822 °C annealed for 672 h.

Table 5.3 Impurity diffusion coefficient
of Fe in Ti

Temperature (°C)	Diffusion coefficient x 10^{-16} (m ² /s)
500	2.45±2.2
600	22.8±1.6
700	86±1.9
800	260±4.6

5.4 Role of defects on kinetics of interdiffusion:

The variation in interface microstructure, microchemistry and nature of the phases in Fe-C/Ti system due to diffusion under equilibrium and non-equilibrium conditions can be summarized as:

- Wider diffusion distances were obtained under non-equilibrium conditions compared to that in equilibrium conditions. Typical value of width of the

diffusion zone in friction joints was $\sim 12 \mu\text{m}$ (Fig. 5.1) while it was $\sim 110 \mu\text{m}$ (Fig. 5.6) in explosive joints annealed for 100 h duration at 800°C .

- The reaction zone in friction welds consisted of only intermetallic phases and TiC whereas in explosive clads there were two distinct regions containing $\text{FeTi}+\text{Fe}_2\text{Ti}+\beta\text{Ti}$ and $\alpha+\beta$ Ti phases.
- In diffusion annealed friction joints the lowest diffusivity was obtained within the composition range of 35-45 wt.% of Fe while in explosive joints the values were lowest in the composition range of 48-58 wt.% of Fe. Overall growth of the reaction zone was controlled by diffusion through ordered intermetallic (FeTi, Fe_2Ti) and TiC phases in friction joints as against $\text{Fe}_2\text{Ti}+\text{TiC}+\beta\text{Ti}$ region in explosive clads.
- Growth kinetics of the reaction zone showed low activation energy (~ 75.5 kJ/mol – Fig. 5.7) for explosive clads than friction welded joints (~ 137 kJ/mol – Fig. 5.2) suggested faster diffusivity under non-equilibrium conditions probably due to the presence of (a) large number density of lattice defects and (ii) disordered $\beta\text{Ti}(\text{Fe})$ phase.

5.5 Effect of alloying elements on interdiffusion in SS/TiTaNb explosive joints:

5.5.1 Evolution of interface microstructure in SS/TiTaNb explosive joints:

The BSE images of the as clads annealed at temperatures of 550, 600, 700 and 800°C for 10 h are shown in Fig. 5.12(a) to (d) respectively. At 550°C , the interface was wavy and no microstructural change was observed except for the elongation of grains in TiTaNb (Fig. 5.12(a)). As the temperature was increased to 600°C , formation of significant number of pores parallel to the interface was observed on SS side (Fig.

5.12(b)). At 700 °C, in addition to the pores on SS side, a dark band of $\sim 1\text{ }\mu\text{m}$ width formed at the interface followed by an another $\sim 16\text{ }\mu\text{m}$ wide region (Fig. 5.12(c)). These zones (marked in Fig. 5.12(c)) are named as zone 1 and zone 2 for ease of discussion. Both width and number of diffusion zones increased with further increase in temperature to 800 °C. In addition to zone 1 ($\sim 1.5\text{ }\mu\text{m}$) and zone 2 ($\sim 26\text{ }\mu\text{m}$), additional reaction zones were distinctly observed on TiTaNb, which consisted of a $\sim 1\text{ }\mu\text{m}$ thick bright zone, followed by a $\sim 70\text{ }\mu\text{m}$ wide Widmanstätten ($\alpha+\beta$) Ti structure adjacent to which was the equiaxed ($\alpha+\beta$) Ti structure of the parent metal (Fig. 5.12(d)).

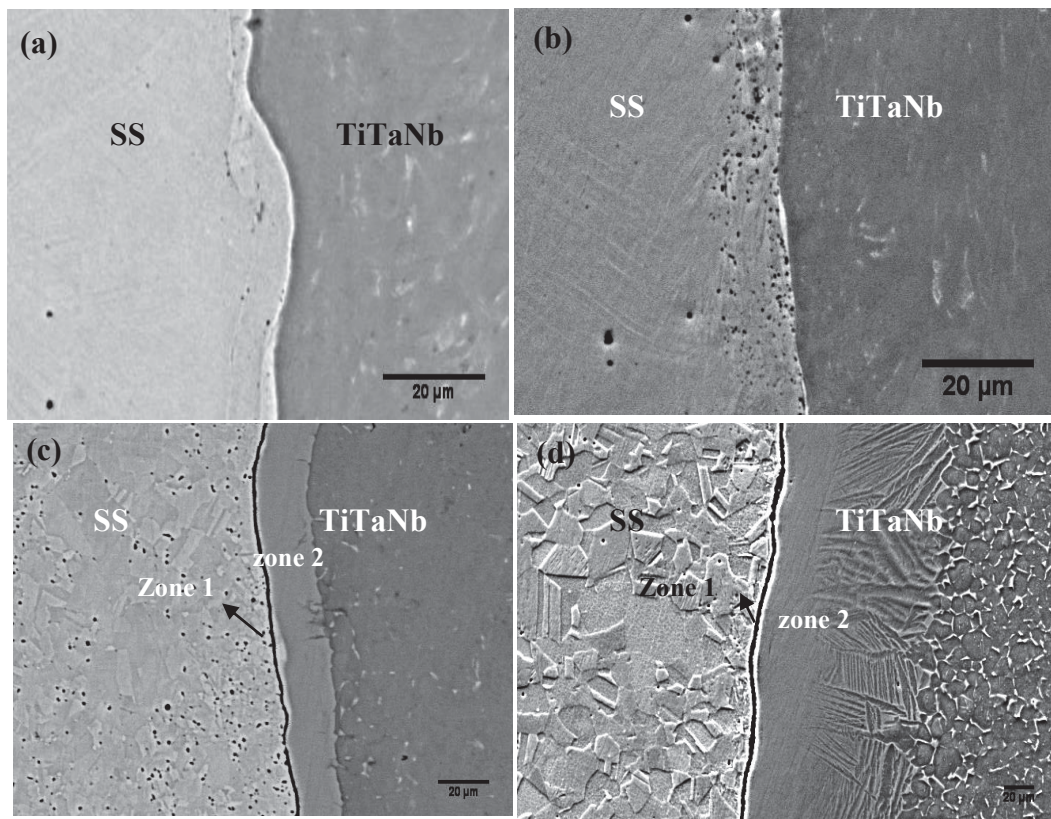


Figure 5.12 BSE images showing variation in the interface microstructure of SS/TiTaNb explosive joints diffusion annealed at (a) 550, (b) 600, (c) 700 and (d) 800 °C for 10 h respectively

BSE images of the interface annealed for 20 h at different temperatures are shown in Fig. 5.13(a) to (d). Apart from the porosity that formed parallel to the interface on SS side, no other microstructural feature was observed at 550 °C, while the width of zone 1 and zone 2 increased to ~ 1.5 and ~ 2.1 μm respectively at 600 °C (Fig. 5.13(b)). Large number density of Kirkendall pores formed on SS side parallel to the interface after 10 h of exposure. It is well known that the low melting component diffuses faster. Hence, in this system, Fe with melting point of 1534 °C diffused faster than Ti (1676 °C), which is responsible for the formation of Kirkendall porosity on SS side.

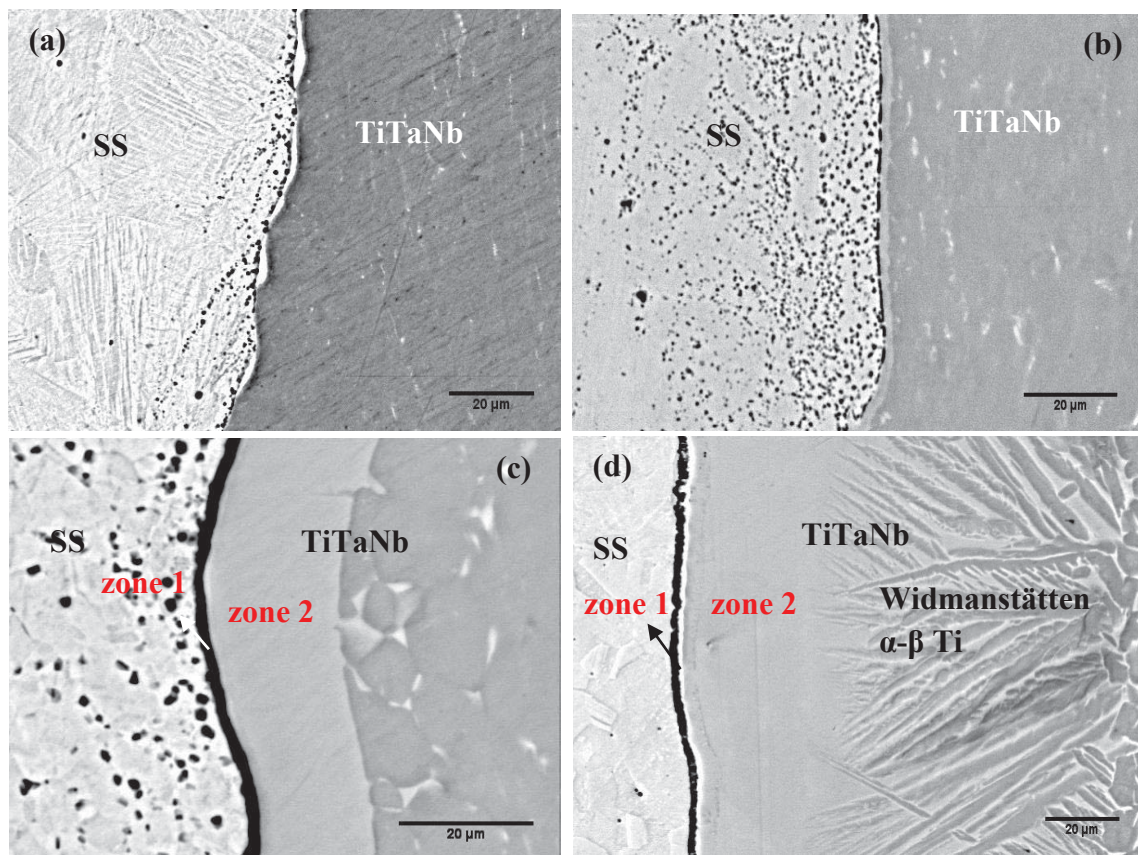


Figure 5.13 BSE images showing variation in the interface microstructure of SS/TiTaNb explosive joints diffusion annealed at (a) 550, (b) 600, (c) 700 and (d) 800 °C for 20 h respectively

Also, diffusion of Fe in hcp Ti was sluggish as compared to diffusion of Ti in fcc Fe, which also supported the formation of Kirkendall porosity on SS side. It is reported in literature that the diffusivity of Fe in hcp-Ti and Ti in Fe are of the order of 10^{-15} m²/s and 10^{-20} m²/s respectively at 550 °C [178, 179]. A relatively higher rate of growth of zone 2 was seen which resulted in wide reaction zones of ~23 and ~41 µm at 700 and 800 °C respectively (Fig. 5.13(c) and (d)). At 800 °C (Fig. 5.13(d)) formation of equiaxed strain free grains were observed on SS side, while in TiTaNb Widmanstätten microstructure extended nearly up to ~91 µm. Based on correlation of the microchemical data with the corresponding binary Fe-Ti [7] equilibrium phase diagram and ternary isothermal Section of Fe-Ti-Cr at 800 °C [88], zone 1 was identified as a two phase mixture of FeTi+Fe₂Ti and zone 2 as βTi(Fe) phase.

5.5.2 Growth kinetics of the diffusion zones:

SEM - BSE images (Figs. 5.12 and 5.13) were used to measure the width of the different diffusion zones. Each value was an average of 20 measured readings for better accuracy. Based on the above results, it was evident that the two zones which were clearly distinguishable at all the temperatures corresponded to FeTi+Fe₂Ti and βTi(Fe) phases. Square of the width of the diffusion zone (X) was plotted against the diffusion annealing time. Figure 5.14 shows X^2 of (a) total diffusion zone, (b) FeTi+Fe₂Ti phase and (c) βTi(Fe) phase plotted as a function of annealing time (t) at temperatures of 600, 700 and 800 °C respectively. Temperature dependence of the width of the diffusion zones was studied from the Arrhenius analysis of $\ln(K_p)$ for total reaction zone, FeTi+Fe₂Ti and βTi(Fe) phases (Fig. 5.14(d)). Activation energy (Q) required for the

formation of each zone was derived from the above analysis. As expected, a very high value of Q (184 kJ/mol) was obtained for the growth of intermetallic phases. Relatively faster growth of $\beta\text{Ti(Fe)}$ was observed at all temperatures (Table 5.4). The growth constant for the total diffusion zone increased linearly with temperature and reached a relatively high value of $\sim 3.4 \times 10^{-1} \text{ m}^2/\text{s}$ at 800°C .

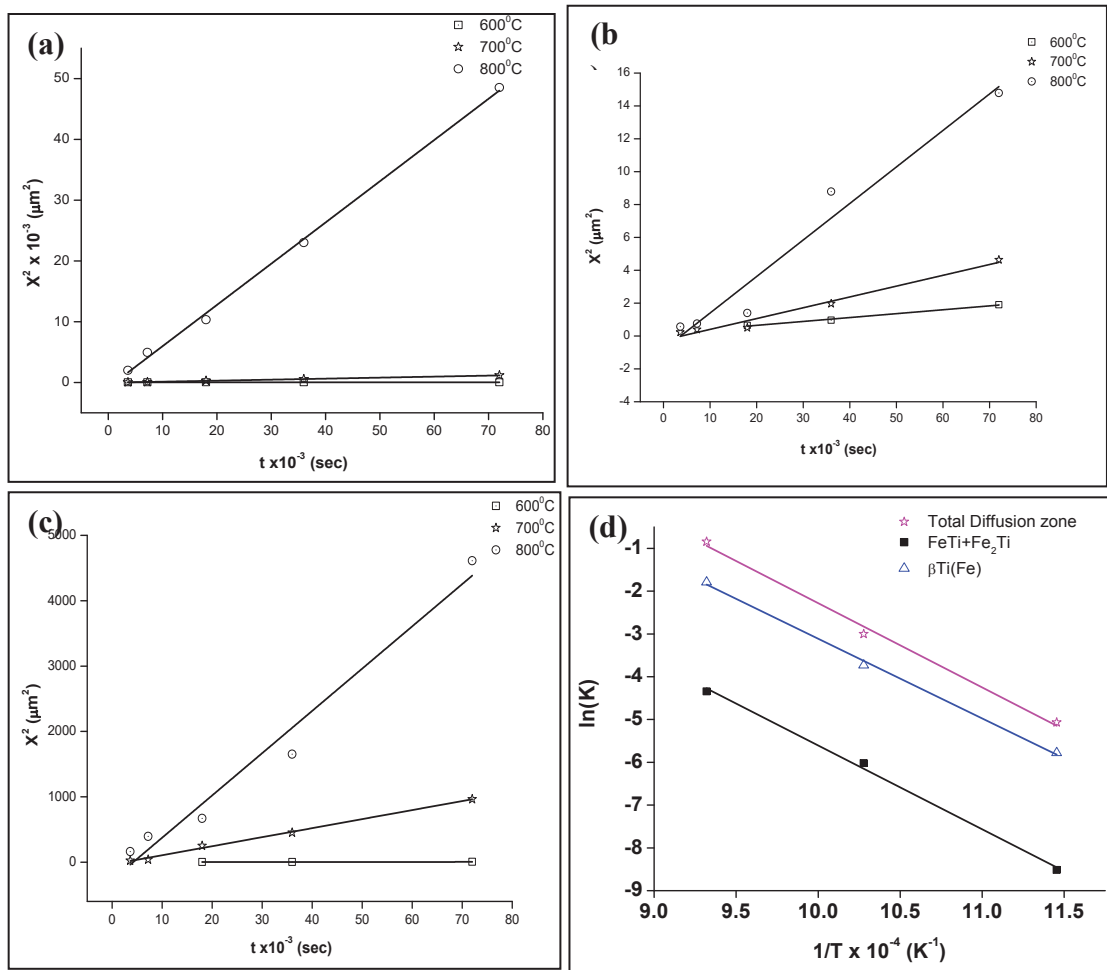


Figure 5.14 Growth of the (a) total diffusion zone, (b) FeTi+Fe₂Ti phase, (c) $\beta\text{Ti(Fe)}$ phases in SS/TiTaNb explosive joints as a function of time at different temperatures and (d) Arrhenius analysis of the growth constant

Table 5.4 Layer growth parameters for diffusion zones in SS/TiTaNb system

	k_0 (m ² /s)			Q (kJ/mol)
	600 °C	700 °C	800 °C	
Total diffusion zone	1.0x10 ⁻⁴	6.7x10 ⁻³	3.4x10 ⁻¹	163
Fe ₂ Ti+FeTi	1.32x10 ⁻⁵	3.22x10 ⁻⁵	1.3x10 ⁻⁴	184
βTi(Fe)	3.1x10 ⁻⁵	6.7x10 ⁻³	3.2x10 ⁻²	157

5.5.3 Microchemical variation due to interdiffusion:

Concentration profiles obtained across the interface of the explosive clads heat treated at temperatures of 550, 600, 700 and 800 °C for 20 h are shown in Fig. 5.15(a) to (d) respectively. At low temperatures of exposure (550 and 600 °C), the concentration profiles resembled smoothly varying solid solution profiles. At 550 °C, the diffusion distances of Fe (in TiTaNb) and Ti (in Fe) were measured as 3 and 2 μm while the values obtained were ~5 and 3 μm at 600 °C. Average composition at the cross over point (assumed to be the original clad interface) was measured as 44.7Fe-17.5Cr-2.9Ni-33.1Ti (in wt.%) at 550 °C, which changed to 49.9Fe-12.5Cr-7.9Ni-27.6Ti at 600 °C (Fig. 5.15(b)). As the temperature was increased to 700 °C, significant redistribution of the elements was observed at the interface and the diffusion distance of Fe enhanced to ~30 μm. The diffusion distances of Fe, Cr and Ni in TiTaNb at 700 °C were measured as 27, 19 μm and 11 μm (Fig. 5.15(c)) which increased to 50, 26 μm and 20 μm at 800 °C (Fig. 5.15(d)). The diffusion distance of Ti in SS was obtained as 4 μm at 700 °C and 5 μm at 800 °C while Ta and Nb did not show any diffusion within

the resolution limit of EPMA. At 700 °C, the composition at the cross over point (39.9Fe-4.1Cr-2.2Ni-52.5Ti (in wt.%)), showed a sharp transition to 12.9Fe-4Cr-0.9Ni-77.3Ti which remained nearly constant up to a distance of ~25 μm thereby resulting in a step formation in the concentration profile. Close to the end of the step profile, concentration gradually changed to 3.4Fe-0.3Cr-0.2Ni-88.9Ti-4.4Ta-2.6Nb (Fig. 5.15(c)) beyond which ‘as received’ ($\alpha+\beta$) Ti composition was observed.

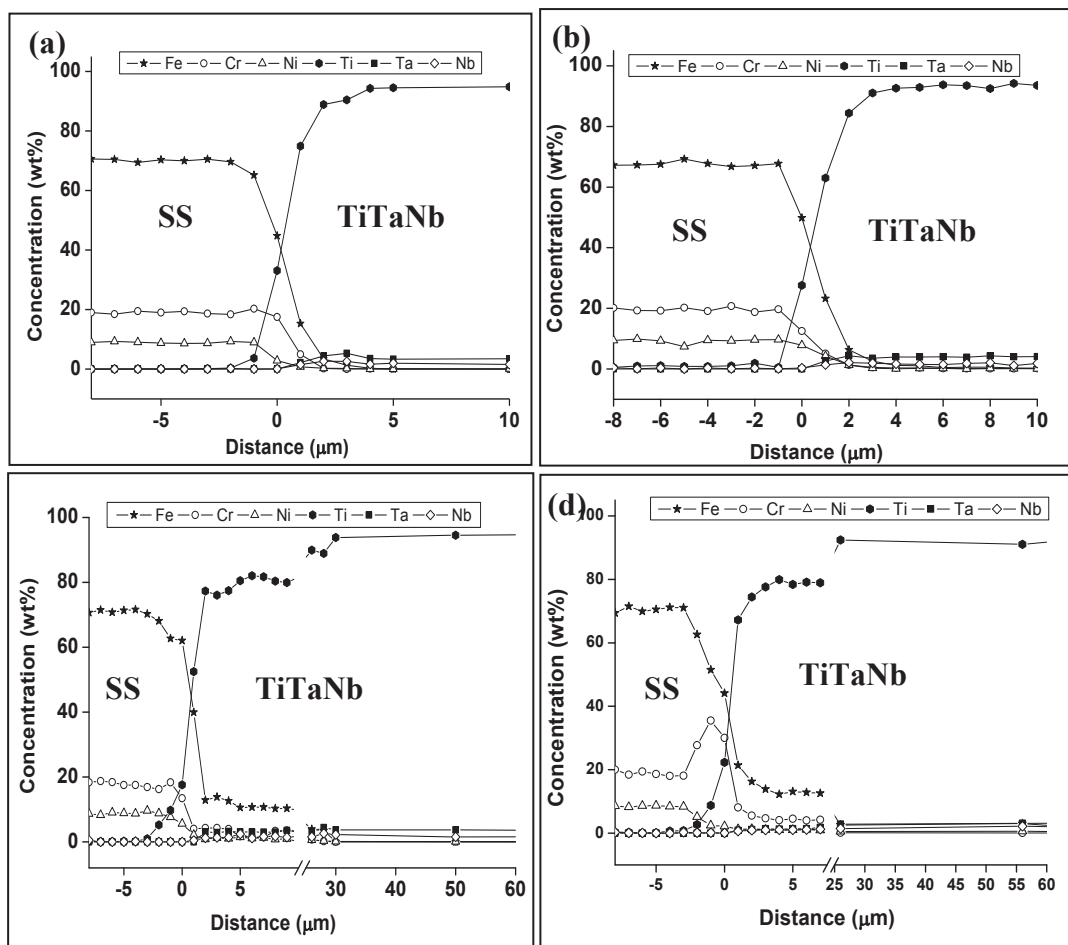
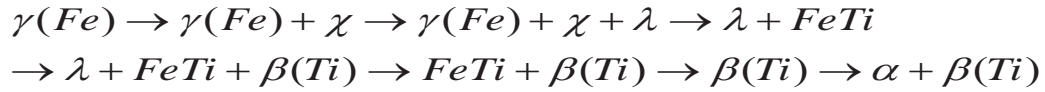


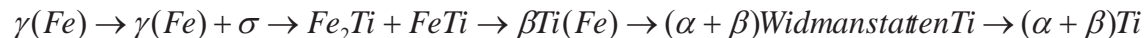
Figure 5.15 Concentration profiles obtained across the SS/TiTaNb explosive clads heat treated at temperatures of (a) 550, (b) 600, (c) 700 and (d) 800 °C for 20 h respectively

Similar observation of step formation was seen at 800 °C up to a distance of 52 µm (in TiTaNb) at a constant composition of 12.2Fe-4.1Cr-0.9Ni-79.9Ti-1.3Ta-1.1Nb while composition at the cross over point was 44.1Fe-30Cr-2.1Ni-22.3Ti. The diffusion distances of Fe, Cr and Ni in TiTaNb increased to ~56, 24 and 14 µm whereas diffusion of Ti in SS remained as 3 µm only (Fig. 5.15(d)). A steep increase in Cr concentration from 18 to 35 wt.% was observed at this temperature and this region extended up to a distance of ~3 µm on SS side. As per the isothermal ternary section of Fe, Cr and Ti at 800 °C [88], the diffusion path followed under equilibrium conditions is as follows:



where ‘ χ ’ is the ternary compound of Fe, Cr, Ti ($Ti_3Cr_7Fe_{17}$) and ‘ λ ’ is $Fe_2Ti(Cr)$ phase [23]. Apart from the Kirkendall porosity the two zones distinctly observed at all temperatures correspond to $FeTi+Fe_2Ti$ and $\beta Ti(Fe)$ phases classified as zone 1 and zone 2 in Figs. 5.12 and 5.13. Substantial increase in Cr content at the interface on SS side is due to interdiffusion of Ti towards SS, which decreased the activity of Cr leading to the phenomenon of uphill diffusion (Fig. 5.15(c)). As per the ternary isothermal section of Fe-Cr-Ti at 800 °C, the solubility of Cr in α Fe is about 35%, however, even small additions of Ti (<5%) considerably decreased the solubility of Cr [184]. Typical composition values of the alloying elements in Cr rich region on SS side was measured as 51.5Fe-35.5Cr-2.5Ni-8.7Ti (in wt.%). On cooling, this zone with high Cr concentration probably transformed to σ phase. Formation of σ phase in SS/Ti system is well reported in literature [24-27]. The present authors have also reported unambiguous

evidence for the presence of σ phase by detailed electron microscopy investigations in earlier studies [128]. Formation of $\beta\text{Ti(Fe)}$ was due to interdiffusion of beta stabilizing elements such as Fe and Cr into Ti, which stabilizes the high temperature bcc (β) phase of Ti at ambient temperatures. As the concentration of beta stabilizing elements decreases, the beta phase was not retained, but transformed to Widmanstätten $\alpha+\beta$ Ti phase, which manifested as bright β phase in the dark α Ti matrix in the microstructure (Fig. 5.12(d) and 5.13(d)). Fe traversed a higher distance in Ti ($\sim 141 \mu\text{m}$ at 800°C -10 h) as compared to Ti in Fe side ($\sim 3 \mu\text{m}$ at 800°C -10 h), which supported shifting of the interface towards SS (Fig. 5.13(d)). Based on the microstructure and microchemistry, the diffusion path followed by SS/TiTa Nb explosive clads at 800°C (20 h) can be expressed as follows:



From the above analysis it was evident that the diffusion reactions between SS and TiTa Nb did not show formation of all the compounds as depicted in the equilibrium phase diagram.

5.5.4 Determination of interdiffusion parameters:

Impurity diffusion coefficients of Fe in TiTa Nb were calculated using Hall's method are summarized in Table 5.5. The tabulated values are an average of minimum three $D(\text{C})$ values measured from regions with identical end concentration values. Typical Fe probability plot drawn between ' λ ' and ' u ' using microchemical data obtained at 800°C (20 h) from TiTa Nb rich side of the clad is shown in Fig. 5.16. As

explained earlier, the ‘ h ’ and ‘ k ’ values (equation (2.11)) were obtained from the linear fit analysis of these plots. Slight increase in the diffusivities was observed with increase in the temperature. It is evident from Table 5.5 that the impurity diffusion coefficient of Fe increases with temperature. The calculated diffusivity values exhibited a reasonable agreement with the reported impurity diffusion coefficients [185]. As discussed in preceding sections the evaluation of interdiffusion coefficients, incorporated the variation in molar volume, which was calculated as a function of concentration at different temperatures. Figure 5.17 shows the plot of variation in molar volume (equation (5.1)) as a function of atomic fraction of Fe at temperatures of 550 and 800 °C (20 h duration). The molar volume values substituted for Fe, Cr, Ni and Ti are 7.09, 7.23, 6.59 and 10.64 cm³/mol respectively [183]. At low temperatures, molar volume exhibited a linear relationship following an ideal Vegard’s law (points shown by circles), whereas a considerable non linear negative deviation was observed at high temperature (points shown by triangles) [186] (Fig. 5.17).

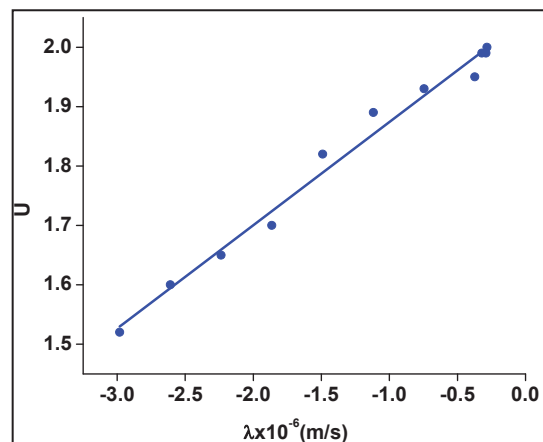


Figure 5.16 Plot of λ and u obtained for Fe in TiTaNb rich side of the concentration profile obtained from SS/TiTaNb clad heat treated at 800 °C for 20 h

Table 5.5 Impurity diffusion coefficient of Fe in TiTaNb

Temperature (°C)	Diffusion coefficient x 10^{-16} (m ² /s)
500	1.89±0.11
600	20.8±0.6
700	68±1.9
800	235±4.6

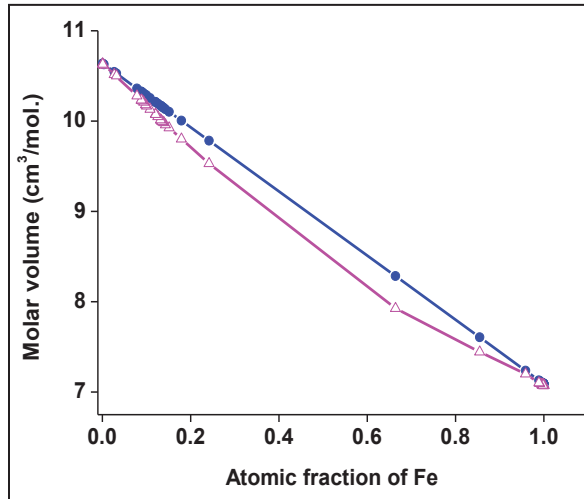


Figure 5.17 Variation in the molar volume (V_{mix}) plotted as a function of atomic fraction of Fe at (a) 550 and (b) 800 °C respectively

Maximum deviation from ideal behavior was observed in the range of 0.4 to 0.6 atomic fraction of Fe. A correlation with microchemical data from the region with considerable amount of Fe, Cr and Ni in TiTaNb showed a variation in molar volume from 9.8 to 10.3 cm³/mol (Fig. 5.17). The variation of molar volume at low temperatures (≤ 600 °C) being ideal enabled the use of DB method for estimation of the interdiffusion coefficients in Fe-Ti system, ignoring the effect of all other diffusing elements. Figure

5.18(a) shows the plot of calculated interdiffusion coefficients at different temperatures as a function of concentration of Fe (in wt.%). The $D(C)$ values were observed to be nearly independent of concentration at 550 and 600 °C and estimated values are of the order of 10^{-16} m²/s. As described in Section 2.6.1, Wagner's method was used for calculating the $D(C)$ values at temperatures of 700 and 800 °C and the values are also shown in Fig. 5.18(a). The plots clearly established the increasing trend in interdiffusivities with increasing temperature. However, significant decrease in the $D(C)$ values was seen at 700 and 800 °C within the composition range of 40-50 wt.% of Fe. As the temperature increased to 700 °C, a reduction in the interdiffusion coefficient from $1.33 \pm 0.8 \times 10^{-15}$ to $5.59 \pm 1.6 \times 10^{-16}$ m²/s was observed at a composition of ~40 wt.% of Fe. A similar trend was observed at 800 °C and the lowest value of interdiffusivity was obtained as $1.25 \pm 0.4 \times 10^{-15}$ m²/s at ~50 wt.% of Fe (Fig. 5.18(a)) while the value was highest ($6.9 \pm 0.5 \times 10^{-15}$ m²/s) at a composition of ~ 70 wt.% of Fe. A good linearity was exhibited by the $D(C)$ values in the temperature regime studied. Arrhenius analysis of the interdiffusivities at various concentrations of Fe is shown in Fig. 5.18(b). Interdiffusion parameters namely pre-exponential factor (D_0) and activation energy (Q) were determined by the above analysis and are summarized in Table 5.6. A high value of Q (114 kJ/mol) and large pre-exponential factor (D_0) of $5.3 \pm 0.5 \times 10^{-13}$ m²/s confirmed the sluggish diffusion kinetics of Fe at a concentration of 40 wt.% (Fig. 5.18(b)), while the lowest Q (83 kJ/mol) and the corresponding D_0 ($5.37 \pm 0.3 \times 10^{-12}$ m²/s) values were obtained at a concentration of 10 wt.% of Fe (Fig. 5.18(b)). Vach et al. [186] have reported that a negative deviation of molar volume enhanced diffusivities considerably.

Also, interdiffusion in metals with large difference in molar volume was reported to be faster due to availability of short circuit paths such as vacancies and dislocations formed to accommodate the local strain at the interface [95].

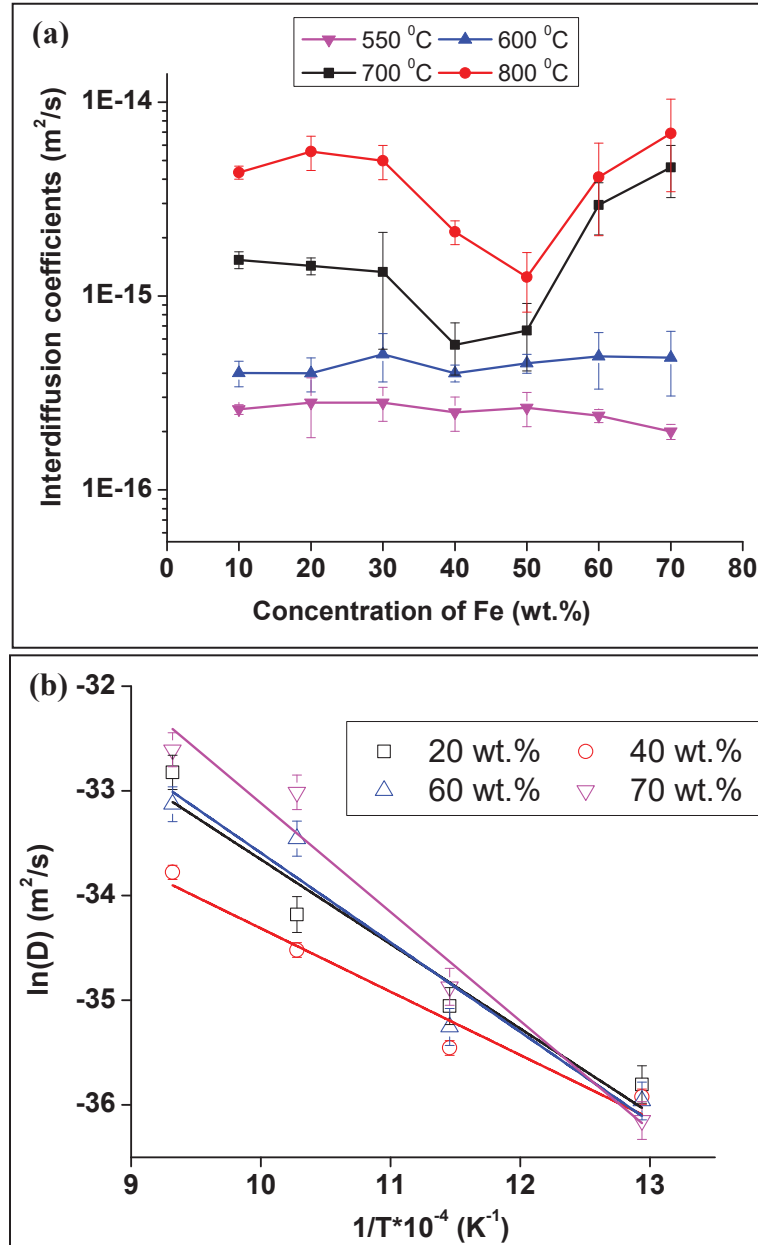


Figure 5.18 (a) Concentration and (b) Temperature dependence of interdiffusion coefficients in SS/TiTaNb system

Table 5.6 Interdiffusion parameters in SS-TiTa Nb system

Concentration of Fe (wt.%)	$D_0 \times 10^{-12}$ (m ² /s)	Q (kJ/mol)
10	5.37±0.3	83±0.17
20	8.42±1.3	98±1.3
30	5.7±0.7	100±0.12
40	0.53±0.5	114.6±11
50	0.56±1	108.8±4.3
60	10.3±1.6	89±4.1
70	172±0.2	100.6±3.1

The reported value of 8×10^{-14} m²/s at 1072 °C for interdiffusion in Ti/SS diffusion bonded joints was comparable to the value evaluated in the present study (Fig. 5.18) [26].

The lowest diffusivity of the order of 10^{-15} m²/s at 800 °C (Fig. 5.18) at a composition of 44.1Fe-30Cr-2.1Ni-22.3Ti (at the clad interface) confirmed the sluggish interdiffusion kinetics in SS/TiTa Nb system in regions where intermetallic phases were present (Table 5.6). It was also supported by the layer growth parameters (Table 5.4), where a slow rate was observed for the growth of two phase mixture containing FeTi+Fe₂Ti intermetallic phases as compared to β Ti(Fe) phase (Fig. 5.14). Faster growth of β Ti phase was due to the more open structure of β phase (bcc) as compared to α (hcp) Ti. The activation energies for the growth of FeTi+Fe₂Ti (184 kJ/mol) and β Ti (Fe) (157 kJ/mol) phases in the present study were far lower than the reported Q

values of 228 and 227 kJ/mol respectively in diffusion bonded joints of microduplex steel/CPTi [187]. This difference was attributed to the presence of large number density of lattice defects at the explosive joint interface, which aid the diffusion. Interdiffusion kinetics were found to be faster at a concentration of 10-15 wt.% of Fe (β Ti phase) with a corresponding interdiffusion coefficient of $\sim 4.1 \times 10^{-15} \text{ m}^2/\text{s}$ (Fig. 5.18(a)). Based on literature, the reason for the faster diffusion of Fe in β Ti phase has been understood as follows: Fe, due to its lower atomic radius ($r_{Fe} = 0.124 \text{ nm}$) than Ti ($r_{Ti} = 0.147 \text{ nm}$) occupied interstitial sites in Ti matrix leading to an interstitial diffusion mechanism [188]. Alemán et al. [23] reported a Q value of 137 kJ/mol for interdiffusion of Fe in β Ti phase in contrast to the Q value of $83 \pm 0.17 \text{ kJ/mol}$ obtained in the present study probably due to variation in the diffusion mechanism. Sluggish interdiffusion kinetics in a region consisting of ordered intermetallic phases (FeTi and Fe₂Ti) controlled the overall diffusional growth of the interface reaction zones in SS-TiTaNb explosive joints.

5.5.5 Estimation of effective interdiffusion coefficients:

Asymmetric diffusion profiles of alloying elements indicated non identical interdiffusion flux of atoms across the interface. Hence, the conventional BM method was modified by Dayananda [96] for multicomponent diffusion by the following expression:

$$\sum_{i=1}^k \int_{c_i^+}^{c_i^-} x dc_i = 0 \quad (5.2)$$

where, ‘ k ’ is the number of elements diffusing across the interface in one direction, consisting of ‘ n ’ number of components. In a multicomponent system, the Matano

interface may not coincide with the original clad interface due to unequal diffusion rates of alloying elements. Hence, it was appropriate to consider the mass balance over the entire diffusion zone for accurate location of the Matano plane. Hence, an attempt was made to determine the net flux of major alloying elements (Fe and Ti) across the interface at 550 and 800 °C which is shown in Fig. 5.19(a) and (b) respectively. The positive and negative flux curves in Fig. 5.19(a), represent the interdiffusion fluxes of Fe and Ti respectively. At low temperatures, both Fe and Ti exhibited an equal amount of interdiffusion flux across the interface with a flux reversal exactly at the original clad interface. At 800 °C, in addition to Fe and Ti, Cr also showed considerable enhancement in the concentration value to ~40 wt.% close to the interface on SS side (Fig. 5.15(d)). Hence, interdiffusion flux of Cr has also been calculated at this temperature. The flux of atoms across the interface is maximum at an abscissa '-1' (SS side) from the virtual clad interface (Fig. 5.19(b)).

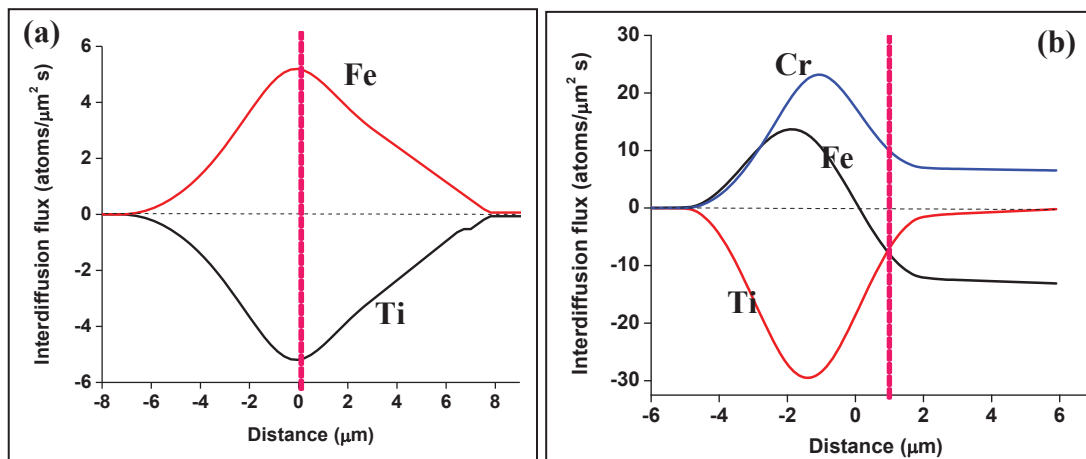


Figure 5.19 Interdiffusion flux across the interface of SS/TiTaNb explosive joints diffusion annealed for 20 h at temperatures of (a) 550 and (b) 800 °C respectively

Higher value of Cr flux as compared to that of Fe on SS side indicated diffusion of Cr against its own concentration gradient. Phase reversal at a distance of '+1 μm ' from the interface supports the positive shift of the interface.

Typical concentration profiles of SS/TiTaNb explosive joints annealed at four different temperatures for duration of 5 h are shown in Fig. 5.20(a) to (d) (with Matano interface ' X_0 ' fixed). Matano interface for the multicomponent SS-TiTaNb alloy system was located by mass balance across the clad interface (equation (5.2)). Wavelength Dispersive Spectrometer (WDS) profiles were smoothened using a polynomial function of order 2. By equating the flux of atoms across the interface, shift in the virtual clad interface was obtained as 1, 1, 7 and 22 μm at temperatures of 550, 600, 700 and 800 $^{\circ}\text{C}$ respectively. Considering the location of ' X_0 ' as the reference point, the effective interdiffusion coefficients for Fe and Cr in Ti (right side of the interface- $\tilde{D}_{i,R}$) and Ti in Fe (left side of the interface- $\tilde{D}_{i,L}$) were calculated using the following relations (equation (5.3) and equation (5.4)) given by Keiser and Dayananda [100]. Table 5.7 summarizes the effective $D(c)$ values of Fe, Cr, Ni and Ti in SS/TiTaNb system.

$$\tilde{D}_{i,L} = \frac{1}{2t} \frac{\int_{c_i^0}^{\bar{c}_i} (x - x_0)^2 dc_i}{[c_i^- - c_i^0]} \quad (5.3)$$

$$\tilde{D}_{i,R} = \frac{1}{2t} \frac{\int_{c_i^+}^{c_i^0} (x - x_0)^2 dc_i}{[c_i^0 - c_i^+]} \quad (5.4)$$

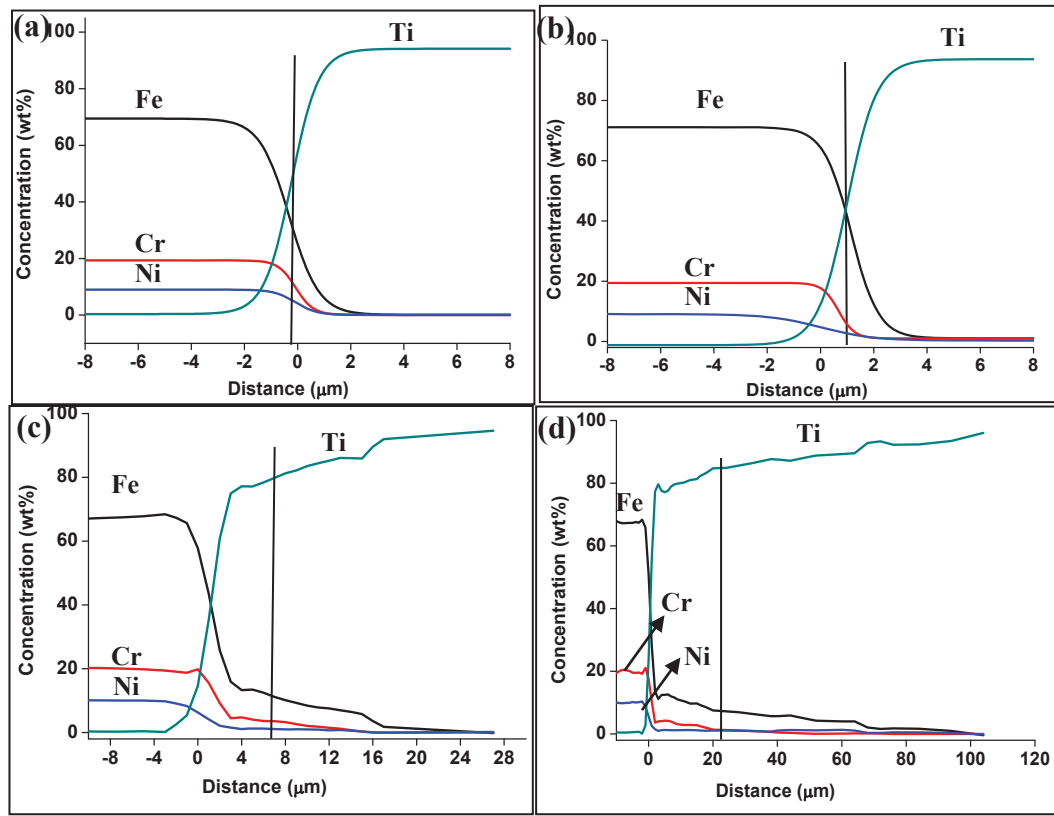


Figure 5.20 Smoothed concentration profiles with Matano interface fixed

At 600 °C, the diffusion distances calculated using the effective interdiffusion coefficients in ternary Fe-Cr-Ti system matched well with the interpretation based on z contrast in BSE images analysis while the values were far lower at temperatures of 700 and 800 °C (Table 5.7). Further, width of the total diffusion zone was obtained as ~ 101 μm at 800 °C for 5 h (Fig. 5.12(d)), which was higher than the reported value of 36 μm for 304 SS/Ti-5.5Al-2.4V diffusion bonded joints at 850 °C [78]. Thus, microstructural and microchemical changes at the interface of SS/TiTaNb joints were more pronounced in explosive clads as compared to diffusion bonded joints. This difference was

undoubtedly due to the faster diffusion of alloying elements aided by the high volume fraction of lattice defects in the explosive clads.

Table 5.7 Effective interdiffusion coefficients and diffusion distances in SS/TiTaNb

Temperature °C	Element	$\tilde{D}_{i,R}$ $10^{-16} \text{ (m}^2/\text{s)}$	$\tilde{D}_{i,L}$ $10^{-16} \text{ (m}^2/\text{s)}$	$d_{i,R}$ μm	$d_{i,L}$ μm
600	Fe	6.3±1.2	0.59±1	10	3
	Cr	0.029±0.1	0.001±0.8	0.6	0.1
	Ti	0.47±0.21	5.6±1.1	3	9
700	Fe	47±2.7	33±3.6	26	22
	Cr	0.18±1.3	0.33±0.9	2	3
	Ti	13±11	17±4.8	13	16
800	Fe	85±1.3	57±5.6	35	29
	Cr	2.3±1.3	0.88±4.7	6	4
	Ti	27±10.5	18±6.3	20	16

5.6 Summary:

The important findings of the study on “**Interdiffusion in Fe-Ti based systems under equilibrium and non-equilibrium conditions**” are summarized as follows:

- The microstructural and microchemical variations across MS/Ti dissimilar joints due to interdiffusion under equilibrium and non-equilibrium conditions as a function of temperature in the range of 550-800 °C for various durations was studied.
- Layer growth parameters revealed that the growth of the diffusion zone was faster under non-equilibrium conditions as compared to that in equilibrium conditions.
- Molar volume followed ideal Vegard’s law in equilibrium conditions while a negative deviation was observed under non-equilibrium conditions which has been incorporated in the estimation of concentration dependent diffusion coefficients in the MS/Ti system.
- Concentration and temperature dependence of effective interdiffusion coefficients for MS-Ti was established by multicomponent approach.
- Correlation of microchemical data with ternary isothermal Section of Fe-C-Ti phase diagram showed diffusion zone in MS/Ti system to consist of FeTi+Fe₂Ti+TiC phases in friction joints and FeTi+TiC+βTi phases in explosive joints.

- Variation in the interface microstructure and microchemistry in the explosive clads of 304LSS/TiTaNb heat treated in the temperature range of 550-800 °C was studied.
- Formation of Kirkendall porosity was observed beyond 10 h at 550 °C while formation of distinct reaction zones were observed at temperatures ≥ 600 °C.
- EPMA revealed that, at any particular bonding temperature, Ti traversed minimum distance in SS while Fe, Cr and Ni traversed comparatively larger distances in Ti side.
- Formation of FeTi+Fe₂Ti and β Ti(Fe) phases due to interdiffusion was established.
- Concentration and temperature dependence of interdiffusion coefficients for Fe-Ti was established using Den Broeder's and Wagner's methods.
- Effective interdiffusion coefficients were estimated in multicomponent system.

Chapter 6

Molecular dynamics simulation of diffusion of Fe in HCP Ti lattice

6.1 Introduction:

AISI type 304L austenitic stainless steel and Ti-5Ta-2Nb alloy were joined by explosive cladding with an objective of achieving a defect and intermetallic free interface [43]. Thermally activated interdiffusion of the alloying elements during subsequent annealing in the temperature range of 550-800 °C, resulted in the formation of diffusion zone consisting of various intermetallic and secondary phases [128]. The diffusion zones were wider in explosive clads than diffusion bonded joints probably due to presence of large number density of defects at the joint interface. Therefore, to understand the role of defects in enhancing interdiffusivities, an atomistic level Molecular dynamics (MD) simulation, ideal to understand structural evolutions associated with the phase transformations and transport phenomena [102] was envisaged. Further, it was also observed that at all temperatures of exposure, the diffusion distance of Fe in Ti (X_{Fe}^{Ti}) was more than that of Ti in Fe (X_{Ti}^{Fe}). For example, the values of X_{Fe}^{Ti} and X_{Ti}^{Fe} were obtained as ~330 µm and ~5 µm respectively for clads heat treated at 800 °C for 20 h [128]. Hence, the diffusion of Fe in HCP Ti lattice was simulated. Further, the calculations were extended to understand the defect aided diffusion by introducing point and line defects in the Ti lattice. Relatively, small atomic radius of Fe ($r_{Fe} = 0.124\text{nm}$) as compared to Ti ($r_{Ti} = 0.147\text{nm}$) also eliminated the computational difficulty associated with an external pressure during simulations (CLAMP method) [102].

In this chapter, the diffusion of Fe in HCP Ti lattice was studied considering modified embedded atom method interatomic potentials and the calculations were carried out on Large Scale Atomic/Molecular Massively Parallel Simulator (LAMMPS) platform. Selection of appropriate interatomic potential for a particular

system plays a vital role in MD simulations, since the governing equations of motion represent the interaction of atoms in a lattice [103]. Section 6.2 describes the validation of MEAM potentials by estimating certain physical properties of the Fe-Ti system. MD simulation of diffusion of Fe in Ti lattice is described in section 6.3 while diffusion of Fe in Ti lattice in the vicinity of point and line defects is elaborated in section 6.4. The important findings of this study are summarized in section 6.5.

6.2 Validation of modified embedded atom method potentials:

Various interatomic potentials such as pair potentials, embedded atom method (EAM), modified embedded atom method (MEAM) potentials are available in literature for Fe and Ti systems [104-108]. The MEAM potential was created by Baskes [108], by modifying the EAM potential [109] accounting for the directionality of bonding. Moreover the MEAM potential was the first interatomic potential formalism that showed the possibility of describing a wide range of crystal structures (fcc, bcc, hcp, diamond-structured and even gaseous elements) using one common formalism [108-114]. In the present thesis, the 2NN MEAM potential postulated by Sa et al. [111] was used. A 2NN MEAM formalism necessitates a total of 14 independent parameters for two elements which are classified as follows: (i) four for the universal state of equation (Cohesive energy (E_c), nearest neighbor distance (r_c) and bulk modulus (B), (ii) eight for the electron density ($\beta_i^{(0)} - \beta_i^{(3)}$ and $t_i^{(1)} - t_i^{(3)}$), embedding function (A) and (iii) two for many body screening (C_{min} , C_{max}) [111]. If an equilibrium structure of an element is selected as reference the model parameters can be directly derived from the material properties. The ‘d’ parameter was assumed to be either 0 or 0.05. Table 6.1 and 6.2 summarizes the

MEAM potential parameters and interaction parameters considered for Fe-Ti system.

Table 6.1 MEAM potential parameters for Fe-Ti system [111]

MEAM parameters	Fe	Ti
E_i^0 (eV)	4.29	4.87
R_i^0 (Å°)	2.48	2.92
A	0.56	0.66
$\beta_i^{(0)}$	4.15	2.70
$\beta_i^{(1)}$	1.0	1.0
$\beta_i^{(2)}$	1.0	3.0
$\beta_i^{(3)}$	1.0	1.0
$t_i^{(1)}$	2.60	6.8
$t_i^{(2)}$	1.80	-2
$t_i^{(3)}$	-7.20	-12.0
B(dyne/cm ²)	1.73	1.10
C_{\min}	0.36	1.00
C_{\max}	2.80	1.44
d	0.05	0.00

Simulation lattice was considered as HCP Ti with lattice constants of $a=2.94$ Å° and $c=4.64$ Å°. Dimension of the super cell (or the simulation matrix) was fixed as 10x10x10 which corresponds to 10 hcp Ti unit cells lying in each coordinate axis. A single Fe atom with BCC as the reference structure with lattice constant of 2.88 Å° was randomly inserted in the Ti lattice. Super cell was allowed to relax for 10 ps in an NPT (volume, pressure and number of atoms assumed to be constant) ensemble. Simulations were carried out for 10 ps in the canonical ensemble in the

temperature range of 500-900 °C with an interval of 100 °C. Periodic boundary conditions were applied to the super cell, in such a way that, whenever an atom leaves the super cell, the vacancy created will be filled by another atom from the preceding cell and the total number of atoms in the super cell remained constant throughout the simulation.

Table 6.2 Interaction parameters for Fe-Ti system

S. No.	2NN MEAM potential parameters	Fe-Ti
1.	Cohesive Energy (E_c)	$0.5 E_c^{Fe} + 0.5 E_c^{Ti} - 0.22$
2.	Equilibrium nearest neighbor distance (r_e)	2.58
3.	Bulk Modulus (B)	1.89
4.	d	$0.5d^{Fe} + 0.5d^{Ti}$
5.	C_{min} (M-X-M)	1.21
6.	C_{min} (X-M-X)	0.78
7.	C_{min} (M-M-X)	$0.5 [(C_{min}^{Fe})^{1/2} + C_{min}^{Ti}]^2$
8.	C_{min} (M-X-X)	$0.5 [(C_{min}^{Fe})^{1/2} + C_{min}^{Ti}]^2$
9.	C_{max} (M-X-M)	2.80
10.	C_{max} (X-M-X)	2.80
11.	C_{max} (M-M-X)	2.80
12.	C_{max} (M-X-X)	2.80
13.	ρ_0	$\rho_0^{Ti} / \rho_0^{Fe} = 1.0$

Diffusion of atoms was initiated by providing certain initial velocity according to Maxwell distribution. However, to eliminate the external stresses during the diffusion of substitutional Fe atom it was essential to carry out NVE (constant volume, energy and number of atoms) integration instead of NPT assuming the system to be a micro canonical ensemble. After fixing the computational parameters,

the MEAM potentials were validated by estimating the cohesive energy, bulk modulus, two shear constants and melting points. The lattice constant for BCC Fe lattice was varied from 2.87 to 2.89 Å in steps of 0.0001 Å for better accuracy. Variation in potential energy was monitored as a function of lattice constant for every 10 ps throughout the simulation. From the plot of potential energy (E) vs lattice constant (a) cohesive energy and bulk modulus were estimated using the procedure available in literature [189]. Following expression was involved in estimating the bulk modulus.

$$B = \frac{a_0^2}{4v} \frac{\partial^2 E}{\partial a^2} \quad (6.1)$$

where ‘ a_0 ’ and ‘a’ are lattice constants at equilibrium and after dilation respectively. ‘E’ represents the total energy of the atom and ‘v’ is the volume per atom. Cohesive energy for the Fe-Ti system was obtained as 4.36 eV at an equilibrium separation of 2.879 Å. Elastic constants were obtained by applying strain on the lattices in all the three axis of the unit cell. Relative change in length of the unit cell in comparison to equilibrium values was a measure of the elastic constants. Further the calculated bulk modulus (1.89 dyne/cm²) and sublimation energy (0.66 eV) agreed well with the values reported by Sa et al. [111].

6.3 Diffusion of Fe in HCP Ti lattice – MD simulations

6.3.1 Diffusion of Fe in defect free HCP Ti lattice:

In the hcp metals, the second nearest neighbor distance is larger than the first nearest neighbor distance by only 15% [109, 110]. Hence, the interactions between second nearest neighbors cannot be ignored which was taken into consideration in the present research work by employing 2NN MEAM formalism during computations. Default assumption in this formalism is that the ternary interaction

terms were the average of the binary terms. Figure 6.1 shows the interatomic potential function ($\phi(r)$) drawn as a function of equilibrium distance (r) for Fe-Ti system. Equilibrium separation of Fe-Ti was obtained as 2.43 Å.

In order to initiate the diffusion, a single Fe atom was introduced by replacing a Ti atom from its regular array. For simplification of the problem, a single vacancy was also created in the vicinity of the Fe atom lattice site. Total time of simulation was considered as 10 ps based on the conservation of size of the system (10x10x10 HCP matrix). A typical plot of variation in the system size plotted as a function of time of simulation is shown in Fig. 6.2. Even though a pressure CLAMP method was assumed, after each 10 ps system was again brought to the equilibrium lattice structure having a constant volume.

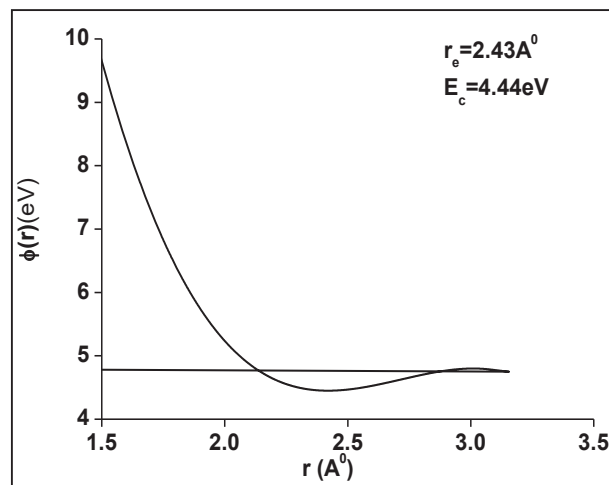


Figure 6.1 Interatomic potential for the Fe-Ti system using MEAM potential formalism

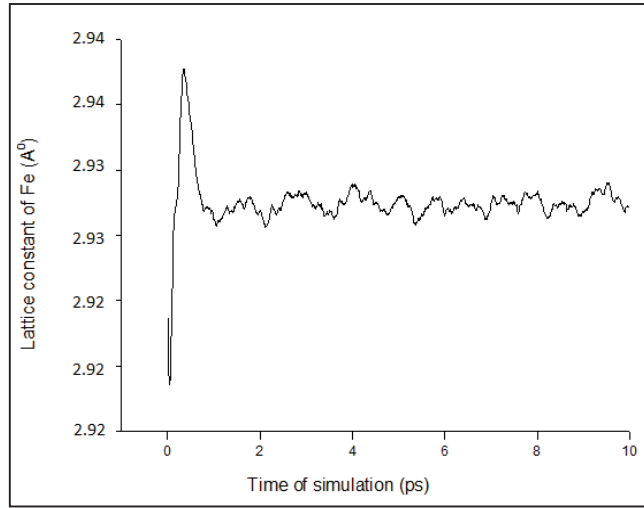


Figure 6.2 Size of the system plotted as a function of time of simulation

The trajectory of the Fe atom in HCP Ti lattice at all the temperatures in the range of 500-900 °C was traced. Figure 6.3(a) to (e) shows the 3D representation of trajectory (in XYZ coordinate axes) followed by the Fe atom in HCP Ti lattice at temperatures of 500, 600, 700, 800 and 900 °C respectively for 10 ps. From these trajectories it was observed that the number of times the Fe atom displaces from its regular lattice site increases as the temperature is increased. Total diffusing distance of Fe atom in Ti lattice at each temperature was calculated by using the equation (6.2) given below:

$$R_i = \sqrt{x_i^2 + y_i^2 + z_i^2} \quad (6.2)$$

From the total diffusing distance obtained using the above expression, mean square displacement (MSD) of diffusing species can be calculated using the following equation (6.3)

$$\langle R^2(t) \rangle = \frac{1}{N} \sum_{i=1}^N R_i^2 \quad (6.3)$$

where ' i ' is the diffusing species (Fe in this work) at any specific lattice site and ' N ' is the total number of atoms considered for simulation.

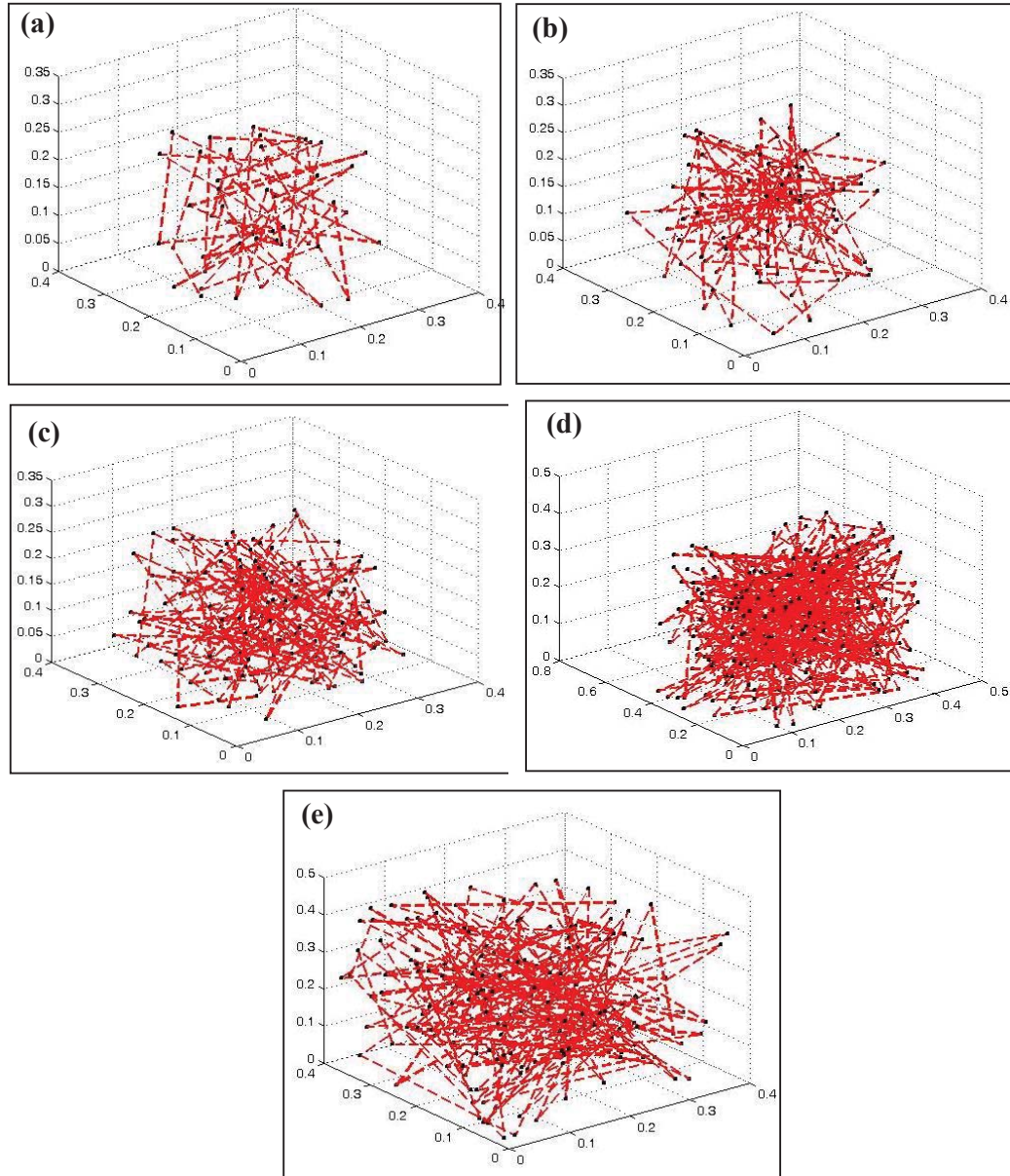


Figure 6.3 Trajectory of Fe atom in Ti lattice at temperatures of (a) 500, (b) 600, (c) 700, (d) 800 and (e) 900 °C respectively

This MSD was plotted as a function of time of simulation till 4 ps. At all the temperatures, MSD observed to be linearly dependent on the time of diffusion. Figure 6.4 shows the MSD of Fe atom plotted as a function of time of simulation at various temperatures.

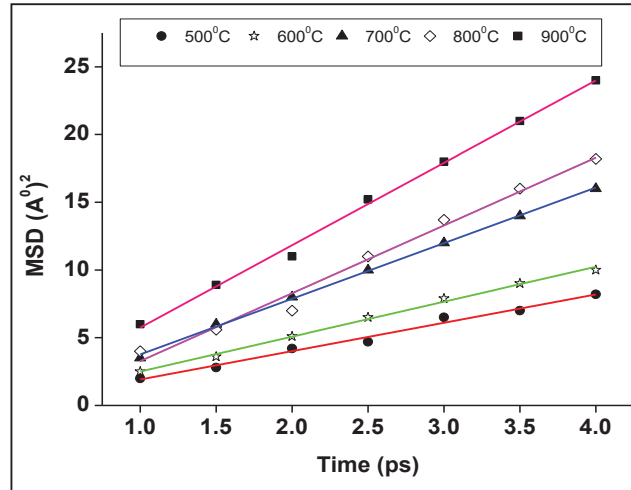


Figure 6.4 Mean square displacement (MSD) vs time of simulation for Fe-Ti system

Based on the MSD obtained at each temperature, diffusivity of Fe atom was calculated by using the following equation (6.4):

$$D_{Fe} = \frac{\langle R^2 \rangle}{6t} \quad (6.4)$$

where ' D_{Fe} ' is the diffusion coefficient of Fe in Ti lattice, ' $\langle R^2 \rangle$ ' is the MSD and 't' is the time of simulation. Using the equation (6.4) the diffusivity of Fe was obtained as $\sim 2.36 \times 10^{-16} \text{ m}^2/\text{s}$ and $\sim 7.784 \times 10^{-15} \text{ m}^2/\text{s}$ at 500 and 900 °C respectively. From the plot of $\ln D$ vs $1/T$ (Fig. 6.5), pre-exponential factor (D_0) and activation energy (Q) values were obtained as $\sim 1.257 \times 10^{-10} \text{ m}^2/\text{s}$ and 117 kJ/mol respectively.

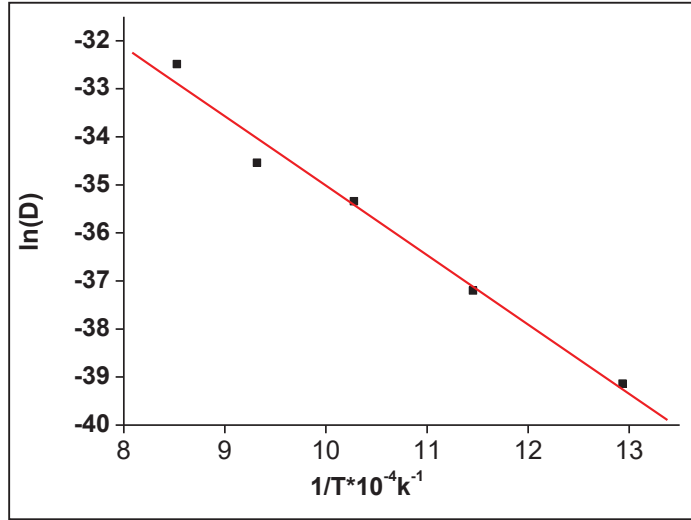


Figure 6.5 Arrhenius analysis of diffusivity of Fe in HCP Ti lattice

6.3.2 Diffusion of Fe in HCP Ti lattice-Introducing point and line defects:

The MEAM potentials developed by Lee et al. [110] for Fe-Hydrogen (H) system, successfully demonstrated atomistic phenomena such as interaction of H atoms with vacancies, dislocations and grain boundaries. MD simulations using MEAM potentials were also found to be effective in understanding the effect of alloying elements on the number of residual point defects (vacancies and interstitials) and their clustering behavior in pure Fe [191]. Formation energies and intra, inter layer self diffusion activation energies in Fe (111) layer has been studied using MEAM potentials [192]. Based on the information available from literature, it was planned to compute the diffusion of Fe atom in Ti lattice by introducing point defects like vacancies followed by line defects like dislocations.

Vacancies were created in HCP Ti lattice by removing Ti atoms randomly from their regular lattice positions. In a lattice containing 4000 Ti atoms, 0.5% of lattice sites were assigned to be vacant and 0.1% Fe atoms were allowed to diffuse. Line defects such as edge dislocations were created in a

HCP Ti lattice. A single edge dislocation was created by deleting half plane of atoms from the basal plane of hcp lattice ([0001]). Length of the dislocation was considered as $5a$, where 'a', the lattice parameter = 2.94 \AA . Figure 6.6(a) and (b) show the Ti lattices with defects created using VMD (visual molecular dynamics) software [188]. Simulations were carried out in the temperature range of 500 - 900 °C at an interval of 100 °C. Similar simulation conditions as explained in the previous section were assumed for obtaining Fe trajectories. Similar steps were followed for calculating the diffusion parameters. As, expected the total diffusion distance increased with temperature and a considerable relaxation of the Fe atom was observed in the vicinity of the line defects. Figure 6.6(a) and (b) show the schematic representation of Ti lattice with vacancies and line defects.

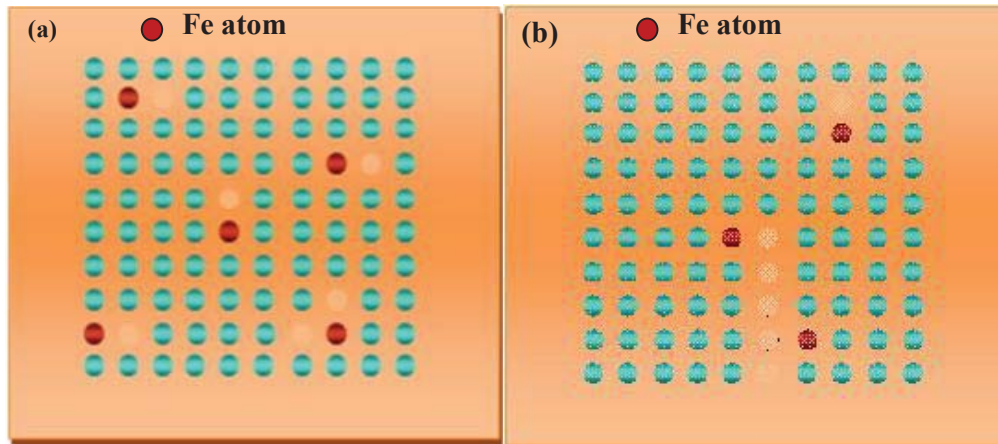


Figure 6.6 Schematic representation of Ti lattice showing the locations of (a) vacancies and (b) dislocations; Fe atoms are inserted in the vicinity of the defects

Figure 6.7 shows the 3D trajectory followed by Fe atom in HCP Ti lattice through vacancies and line defects at a temperature of 900 °C. It was evident from the diffusion trajectories, that the relaxation of Fe atom is faster in the vicinity of line defects. The diffusivity values determined using equation (6.4) are tabulated in Table 6.3. Line defects exhibited greater effect on diffusivity of Fe ($1.03 \times 10^{-13} \text{ m}^2/\text{s}$)

at 900 °C) than that of point defects ($4.23 \times 10^{-14} \text{ m}^2/\text{s}$ at 900 °C). From the Arrhenius analysis of $\ln D$ vs $1/T$, the pre exponential factor and the activation energy values were obtained as $8.64 \times 10^{-9} \text{ m}^2/\text{s}$ and 111 kJ/mol in case of point defects; $3.23 \times 10^{-8} \text{ m}^2/\text{s}$ and 98 kJ/mol for line defects. Thus MD simulations reinforced the higher diffusivity of Fe in hcp Ti lattice in the presence of lattice defects.

Table 6.3 Diffusivity of Fe in HCP Ti lattice

Temperature (°C)	D(m ² /s)-0.5% Vacancies	D(m ² /s)-Edge dislocations
500	9.90E-16	1.0E-15
600	7.43E-16	4.87E-15
700	1.15E-15	6.99E-15
800	2.02E-15	9.89E-15
900	4.23E-14	1.03E-13

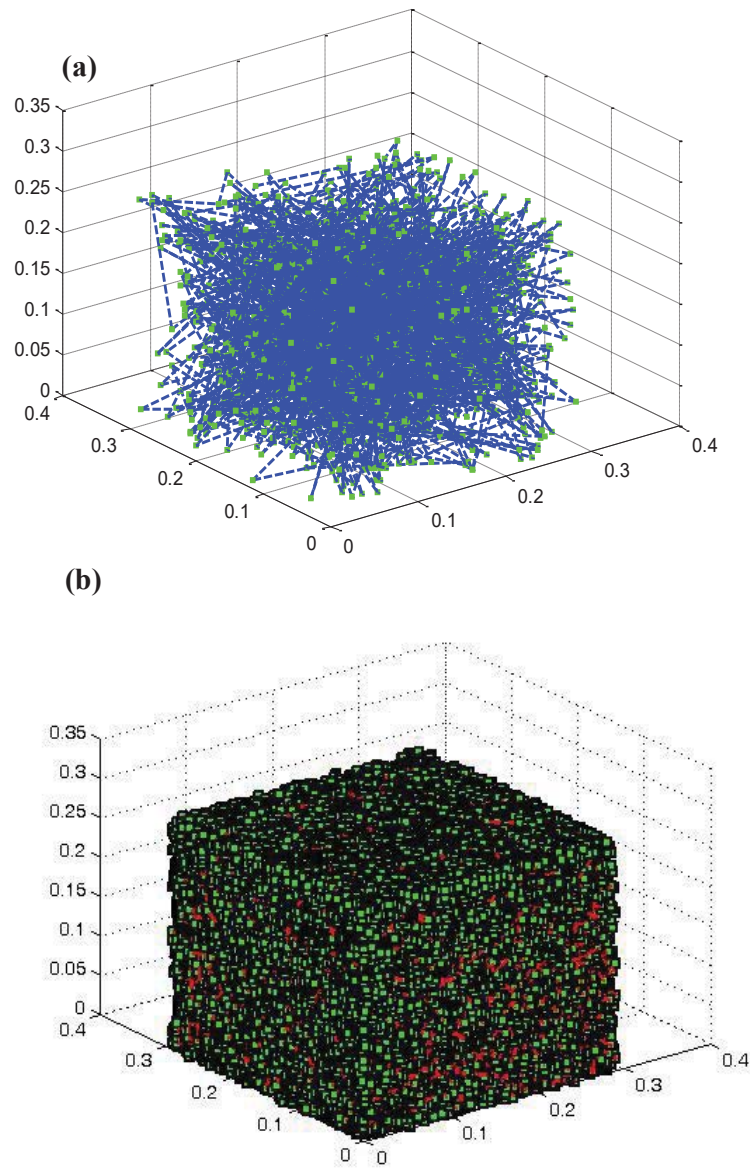


Figure 6.7 Trajectory of Fe atom in Ti lattice consisting of (a) 0.5% vacant lattice sites and (b) edge dislocations at a temperature of 900 °C

6.3.3 Estimation of jump frequency in Ti lattice consisting of point and line defects:

Above results clearly established the role of defects on the diffusivity of Fe in Ti lattice. Therefore, to understand the mechanism of defect aided diffusion an attempt has been made to estimate the jump frequency (f) associated with each vacancy jump of Fe atom using the expression $f = \frac{N}{t}$. Where 'N' is the number of events for a specific diffusion mechanism at a given temperature and 't' is the total time of simulation. Equation (6.5) was used to obtain the jump frequency values from the diffusivity of Fe in hcp Ti lattice.

$$D = \lambda f \frac{d^2}{2z} \quad (6.5)$$

where 'd' is the distance between the initial and the final states of the vacancy during a jump, 'z' is the dimensionality of the diffusion space. In the above expression we had neglected the jump correlation factor, assuming that successive jumps were uncorrelated. In the case of substitutional atoms the jump frequencies of atoms are of the order of $\sim 10^{-18}/s$ [114]. To observe diffusion of atoms with such low jumping frequencies simulations needs to be carried out for relatively longer durations by considering millions of atoms. Although, present study deal with only 4000 atoms of Ti, the simulation time was increased to 300 ps so that a single vacancy jump can be monitored. The jump frequency of Fe atom was of the order of $5 \times 10^{-18}/s$ in the presence of point defects which was lower than the value of $9.6 \times 10^{-18}/s$ in the presence of dislocations which explained for the faster diffusion of Fe in the vicinity of the defects.

6.4 Summary:

The important findings on the study of “**Molecular dynamics simulation of diffusion of Fe in HCP Ti lattice**” are as follows:

- MEAM potentials were used for carrying out MD simulations on Fe-Ti system.
- These potentials were validated by determining the physical properties of Fe-Ti system such as elastic constants, bulk modulus, cohesive energy and melting points.
- MD simulations were carried out in the temperatures range of 500 – 900 °C for 10 ps using NPT followed by NVE canonical ensemble.
- A single Fe atom trajectory in defect free and point and line defect containing HCP Ti lattice was traced and the MSD was estimated at each temperature as a function of time of simulation.
- Faster diffusion of Fe atom in the vicinity of line defects was established by MD simulations followed by jump frequency calculations.

Chapter 7

Summary and Scope for future work

7.1 Summary of the work:

This thesis entitled “**An Experimental and Computational Study on Diffusion Driven Structural Changes in Fe-Ti Based Dissimilar Joints Under Equilibrium and Non-equilibrium Conditions**” presents the results of an in-depth study on diffusion driven microstructural and microchemical changes in Fe/Ti based dissimilar joints due to interdiffusion under equilibrium and non-equilibrium conditions.

The thesis addresses the following themes:

- ⇒ Microstructure and property evaluation in Fe-C/Ti friction and explosive joints in ‘as welded’ and heat treated conditions.
- ⇒ Structural changes during deformation and annealing in 304LSS/Ti-5Ta-2Nb explosive clad joints.
- ⇒ Interdiffusion in Fe-Ti based systems under equilibrium and non-equilibrium conditions.
- ⇒ Molecular Dynamics simulations of diffusion of Fe in hcp Ti lattice.

A brief summary of the results of the above themes is as follows:

The first theme deals with the evolution of microstructure and microchemistry under equilibrium and non-equilibrium conditions in the Mild Steel (MS)/Ti joint. A detailed study has been carried out on selection of the welding parameters and fabrication of MS/Ti joints employing both equilibrium and non-equilibrium processes. Further, post cladding heat treatments were optimized based on experimental studies and JMatPro[®] based computations with an aim to control the formation of intermetallic phases at the interface of the joint. Important findings of this chapter are given below:

- ❖ Conventional diffusion couple type joining of mild steel (MS) and Ti was unsuccessful due to formation of a diffusion zone consisting of intermetallic phases and oxides at the interface.
- ❖ Friction welds of MS and Ti were successfully fabricated using optimized values of frictional force, upset force, burn-off length and rotational speed (0.8 tonnes, 1.6 tonnes, 3 mm and 1000 rpm respectively).
- ❖ Although, FeTi intermetallic phase was present at the interface of the friction joint, a high value of UTS computed by JMatPro[®], indicated a negligible effect of these on the bond strength of the joint.
- ❖ A sinusoidal wavy interface was obtained in MS-Ti explosive joints when optimized cladding parameters of flier plate velocity - 300 m/s, detonation velocity - 2000 m/s, type of explosive - homogeneous mixture of Ammonium nitrate + TNT and load ratio of 1.07 were employed.
- ❖ As the load ratio increases, formation of fine grains very close to the interface followed by dendritic solidification classified explosive cladding process as a fusion welding process, the reason for which is attributed to the increased dissipation of kinetic energy at the collision point.
- ❖ Fe₂Ti intermetallic phase formed at isolated regions in the vortices of the waves at the clad interface.
- ❖ Deformation induced phase transformations due to shock loading conditions led to formation of acicular martensite and metastable fcc phase in MS and Ti respectively.

- ❖ Based on the interface microstructure and JMatPro[®] simulations, the post cladding heat treatment for the MS/Ti explosive clads is recommended in the temperature range of 500 °C for durations not exceeding 10 h.

The second theme describes the results of an elaborate study on 304LSS/Ti-5Ta-2Nb explosive clad joints. Detailed electron microscopy investigations were carried out to establish the formation of deformation induced phases in base (304LSS) and flier (Ti-5Ta-2Nb) plates during explosive cladding process. X-ray and electron microscopy techniques were used to understand the mechanism of reversion of metastable phases. Temperature and time window was designed for post weld heat treatments of SS/TiTaNb explosive joints at which the interface was devoid of intermetallic phases and parent metal microstructure and microhardness values were restored. Important findings of this chapter are given below:

- ❖ Explosive cladding of 304LSS and Ti-5Ta-2Nb resulted in the formation of deformation induced phases such as α' martensite in SS and metastable fcc phase in TiTaNb alloy.
- ❖ Systematic variation in the volume fraction of strain induced martensite and metastable fcc phase and morphological changes associated with the thermal exposure have been established in the temperature range of 100-1100 °C.
- ❖ The reversion of metastable phases followed a diffusion controlled nucleation and growth process.
- ❖ Based on the interface microstructure and JMatPro[®] simulations, the post cladding heat treatment for the explosive joints is recommended as 550 °C for durations not exceeding 10 h.

- ❖ Heat treatment at 600 °C and beyond resulted in the formation of Kirkendall porosity on SS side and intermetallic phases at the interface for which unambiguous evidence has been obtained by electron microscopy investigations.
- ❖ The poor mechanical property exhibited by TiTaNb at high temperature of 800 °C indicated a possible shift in the region of failure to the flier plate of the explosive clad.

In the third theme diffusion driven microstructural and microchemical changes in Fe-C-Ti and multicomponent SS/TiTaNb system has been investigated. Concentration and temperature dependent interdiffusion parameters were evaluated employing both binary and multicomponent approaches. Growth of diffusion zones in these systems was measured in terms of temperature and time dependent layer growth parameters. The important findings of this chapter are given below:

- ❖ Microstructural and microchemical variations across MS/Ti dissimilar joints due to interdiffusion under equilibrium and non-equilibrium conditions as a function of temperature in the range of 550-800 °C for various durations has been evaluated.
- ❖ Layer growth parameters revealed that the growth of the diffusion zone is faster under non equilibrium conditions as compared to that under equilibrium conditions.
- ❖ Molar volume followed ideal Vegard's law under equilibrium conditions while a negative deviation is observed in non-equilibrium condition, which has been

taken into account for estimation of concentration dependent diffusion coefficients.

- ❖ Concentration and temperature dependence of effective interdiffusion coefficients for MS-Ti has been established following Dayananda's multicomponent approach.
- ❖ A superimposition of microchemical data on the ternary isothermal section of Fe-C-Ti, showed a correspondence between the diffusion zone in MS/Ti system with the presence of FeTi+Fe₂Ti+TiC (friction joints) and FeTi+TiC+βTi (explosive joints) phases.
- ❖ Variation in the microstructure and microchemistry at the interface of 304L SS/TiTaNb explosive clads heat treated in the temperature range of 550-800 °C has been studied.
- ❖ Formation of Kirkendall porosity was observed beyond 10 h at 550 °C while distinct reaction zones formed at temperatures ≥ 600 °C.
- ❖ Microchemical analysis by EPMA revealed that Ti traverses minimum distance in SS while Fe, Cr and Ni travel comparatively larger distances in Ti side, at all bonding temperatures.
- ❖ Formation of FeTi+Fe₂Ti and βTi(Fe) phases due to interdiffusion has been established.
- ❖ Concentration and temperature dependence of interdiffusion coefficients for Fe-Ti has been established using Den Broeder's and Wagner's methods.

- ❖ Effective interdiffusion coefficients have been estimated in multicomponent system.

The fourth theme elaborates the results of molecular dynamics simulation of diffusion of Fe in a defect free HCP Ti lattice as well as with introduction of point defects such as vacancies and line defects such as dislocations. The important findings of this chapter are given below:

- ❖ Modified embedded atom method potentials (MEAM) potentials given by Sa et al. have been used for carrying out MD simulations on Fe-Ti system.
- ❖ These interatomic potentials were validated by calculating the physical properties of Fe-Ti system such as elastic constants, bulk modulus, cohesive energy and melting points.
- ❖ A single Fe atom trajectory in hcp Ti lattice was traced and the MSD was estimated at each temperature as a function of time of simulation.
- ❖ Diffusion coefficient and activation energy (Q) for diffusion of Fe atom in a defect free Ti lattice were obtained as $7.784 \times 10^{-15} \text{ m}^2/\text{s}$ and 117 kJ/mol respectively.
- ❖ Point defects such as vacancies were created in Ti by random removal of atoms from their lattice position while line defects such as dislocations were created by deleting half plane of atoms from the centre plane of hcp lattice.
- ❖ The diffusivity of Fe in hcp Ti lattice, in the presence of point defects and line defects was obtained as $4.23 \times 10^{-14} \text{ m}^2/\text{s}$ and to $1.03 \times 10^{-13} \text{ m}^2/\text{s}$ respectively at

900 °C. A faster relaxation of Fe atom in the vicinity of defects has been established from the diffusion trajectories.

7.2 Scope for future work:

- ❖ In the present investigation explosive cladding process was observed to lead to metastable phase formation in the base materials, especially fcc phase in Ti/Ti-based alloys. FCC phase of Ti has not been observed under general shock loading conditions. Hence, molecular dynamic simulation of shock wave propagation in Ti will help in understanding the phase transformation kinetics under explosive cladding conditions.
- ❖ In multicomponent Fe-Ti joints interdiffusion occurs across multiphases and the diffusion coefficients calculated from the concentration profiles are only average representative values. Both experimental and computational studies can be taken up to investigate interdiffusion of alloying elements in disordered and ordered crystal structures replicating the behaviour of Fe/Cr/Ti diffusion in FeTi, Fe₂Ti and β -Ti phases. These diffusion parameters can be fed as input for Kinetic Monte Carlo (KMC) simulations for modeling the formation, growth and coalescence of Kirkendall porosities.
- ❖ Reverse transformation kinetics of deformation induced phases to parent phases can be studied for mild steel and titanium exposed to explosive cladding conditions.
- ❖ Though in the present investigation explosive clads have been fabricated with different load ratios ($R = 1.07, 2.01$ and 3.0), only clad corresponding to $R = 1.07$ has been studied in detail. Further in-depth investigations can be taken up

to understand the impact of load ratio on the change in microstructure and crystal structure of base and flier plates, a missing information in literature.

- ❖ The dissimilar material interface taken up for research in this thesis is relevant to an actual industrial application in the reprocessing plants. In that context it will be interesting to study the microstructure-corrosion-mechanical property correlation in the explosive clads and friction welded joints.

REFERENCES

- [1] Baldev Raj, U. Kamachi Mudali, *Prog. Nucl. Energy*, **2006**, vol. 48, 283-313.
- [2] Baldev Raj, U. K. Mudali, T. Jayakumar, K. V. Kasiviswanathan, R. Natarajan, *Sadhana*, **2000**, vol. 25, 519-559.
- [3] R. Natarajan, *Challenges in fast reactor fuel reprocessing*, ANCAS Bulletin, **1998**, 27-32.
- [4] U. K. Mudali, R.K. Dayal, J.B. Gnanamoorthy, *J. Mater. Engg. Perf.*, **1995**, vol. 4, 756-760.
- [5] K. Kapoor, Vivekanand Kain, T. Gopalkrishna, T. Sanyal, G.K. De, *J. Nucl. Mater.*, **2003**, vol. 322, 36-44.
- [6] U. Kamachi Mudali, B.M. Ananda Rao, K. Shanmugam, R. Natarajan, Baldev Raj, *J. Nucl. Mater.*, **2003**, vol. 321, 40-48.
- [7] H. Okamoto, *J. Phase Equilibria*, **1996**, vol. 17, 369.
- [8] H.C. Dey, M. Ashfaq, A.K. Bhaduri, K. Prasad Rao, *J. Mater. Proc. Technol.*, **2009**, vol. 209, 5862-5870.
- [9] B. Shanmugarajan, G.Padmanabham, *Optics Lasers in Engg.*, **2012**, vol. 50, 1621-1627.
- [10] A. Hill, E. R. Wallach, *Acta Metall.*, **1989**, vol. 37, 2425-2431.
- [11] M. Şahin, H. E. Akata, *J. Mater. Process. Technol.*, **2003**, vol. 142, 239-246.
- [12] R. Nandan, T. Debroy, H.K.D.H. Bhadeshia, *Prog. Mater. Sci.*, **2008**, vol. 53, 980-1023.
- [13] R.A. Patterson, *Welding, Brazing and Soldering*, ASM Handbook, ASM International, USA, **1993**, vol. 6.

- [14] M.F. Wu, C. Yu, Z.S. Yu, R.F. Li, *Mater. Sci. Technol.*, **2004**, vol. 20, 658-660.
- [15] M. Ghosh, K. Bhanumurthy, G.B. Kale, J. Krishnan, S. Chatterjee, *J. Nucl. Mater.*, **2003**, vol. 322, 235-241.
- [16] P. He, J.H. Zhang, X.Q. Li, *Mater. Sci. Technol.*, **2001**, vol. 17, 1158-1162.
- [17] X.J. Yuan, G.M. Sheng, B. Qin, W.Z. Huang, B. Zhou, *Mater. Chara.*, **2008**, vol. 59, 930-936.
- [18] S. Kundu, M. Ghosh, S. Chatterjee, *Mater. Sci. Engg. A*, **2006**, vol. 428, 18-23.
- [19] D. Poddar, *Int. J. Rec. Trend. Engg.*, **2009**, vol. 1, 93-99.
- [20] B. Kurt, N. Orhan, E. Evin, A. Çali, *Mater. Letters*, **2007**, vol. 61, 1747-1750.
- [21] S. Kundu, S. Sam, S. Chatterjee, *Mater. Des.*, **2011**, vol. 32, 2997-3003.
- [22] N. Orhan, T.I. Khan, M. Eroğlu, *Scripta Mater.*, **2011**, vol. 45, 441-446.
- [23] B. Alemán, L. Gutiérrez, J. J. Urcola, *Mater. Sci. Technol.*, **1993**, vol. 9, 633-641.
- [24] M. Ghosh, S. Chatterjee, *Mater. Chara.*, **2002**, vol. 48, 393-399.
- [25] M. Ghosh, S. Chatterjee, *Mater. Chara.*, **2005**, vol. 54, 327-337.
- [26] M. Ghosh, S. Chatterjee, *Mater. Sci. Engg. A*, **2008**, vol. 358, 152-158.
- [27] M. Ghosh, S. Das, P.S. Banarjee, S. Chatterjee, *Mater. Sci. Engg. A*, **2005**, vol. 390, 217-226.
- [28] S. Kundu, S. Chatterjee, *Mater. Sci. Engg. A*, **2010**, vol. 527, 2714-2719.
- [29] S. Kundu, S. Chatterjee, D. Olson, B. Mishra, *Metall. Mater. Trans. A*, **2007**, vol. 38, 2053-2060.
- [30] S. Kundu, M. Ghosh, A. Laik, K. Bhanumurthy, G.B. Kale, S. Chatterjee, *Mater. Sci. Engg. A*, **2005**, vol. 407, 154-160.

- [31] Y. Deng, G. Sheng, C. Xu, *Mater. Des.*, **2013**, vol. 46, 84-87.
- [32] A.V. Lyushinskii, *Weld. Int.*, **2001**, vol. 15, 830-832.
- [33] S. W. Baek, W. B. Lee, J. M. Koo, C. Y. Lee, S. B. Jung, *Mater. Sci. Forum*, **2008**, vol. 580-582, 423-426.
- [34] W. B. Lee, S. B. Jung, *Mater. Trans.*, **2004**, vol. 45, 2805-2811.
- [35] R. Kumar, M. Balasubramanian, *Defence Technol.*, **2015**, vol. 11, 65-75.
- [36] C.H. Muralimohan, V. Muthupandi, K. Sivaprasad, *Procedia Mater. Sci.*, **2014**, vol. 5, 1120-1129.
- [37] M. Fazel Najafabadi, S.F. Kashani Bozorg, A. Zarei Hanzaki, *Mater. Des.*, **2010**, vol. 31, 4800-4807.
- [38] S.A.A. Akbari Mousavi, S.T.S. Al-Hassani, *J. Mech. Phys. Solids*, **2005**, vol. 53, 2501-2528.
- [39] R.V. Tamhankar, J. Ramesam, *Mater. Sci Engg.*, **1974**, vol. 13, 245-254.
- [40] C. Merriman, *Weld J.*, **2006**, vol. 85, 27-29.
- [41] Å. Öberg, N. Mårtensson and J-å. Schweitz”, *Metall. Mater. Trans. A*, **1985**, vol. 16, 841-852.
- [42] G. Arthur, *Mater. Des.*, **1985**, vol. 6, 37-41.
- [43] C. Sudha, T.N. Prasanthi, S. Murugesan, S. Saroja, P. Kuppusami, M. Vijayalakshmi, *Sci. Technol. Weld Join.*, **2011**, vol. 16, 133-139.
- [44] C. Sudha, T.N. Prasanthi, S. Saroja, M. Vijayalakshmi, *Ind. Weld. J.*, **2011**, vol. 44, 53-68.
- [45] S.D. Meshram, T. Mohandas, G. Madhusudhan Reddy, *J. Mater. Process. Technol.*, **2007**, vol. 184, 330-337.

- [46] A. Fuji, T.H. North, K. Ameyama, M. Futamata, *Mater. Sci. Technol.*, **1992**, vol. 8, 219-235.
- [47] N. Kahraman, B. Gulenc, F. Findik, *J. Mater. Proc. Technol.*, **2005**, vol. 169, 127-133.
- [48] A. Durgutlu, B. Gülenc, F. Findik, *Mater. Des.*, **2005**, vol. 26, 497-507.
- [49] S.A.A. Akbari Mousavi, P. Farhadi Sartangi, *Mater. Des.*, **2009**, vol. 30, 459-468.
- [50] K. Raghukandan, P. Tamilchelvan, N. Meikandan, *Mater. Sci. Forum*, **2008**, vol. 566, 285-290.
- [51] H.R.Z. Rajani, S.A.A. Akbari Mousavi, *J. Fail. Anal. Preven.*, **2012**, vol. 12, 646-653.
- [52] P. Manikandan, K. Hokamoto, M. Fujita, K. Raghukandan, R. Tomoshige, *J. Mater. Proc. Technol.*, **2008**, vol. 195, 232-240.
- [53] P. Manikandan, K. Hokamoto, A. Deribas, K. Raghukandan, R. Tomoshige, *Mater. Trans*, **2006**, vol. 47, 2049-2055.
- [54] A. Fuji, K. Ameyama and T.H. North, *J. Mater. Sci.*, **1996**, vol. 31, 819-827.
- [55] J.G. Banker, J.P. Winsky, Proceedings of ALTA 1999 autoclave design and operation symposium, Alta Metallurgical Services, Melbourne, Australia, **1999**, **99-104**.
- [56] S.A.A. Akbari Mousavi, P. Farhadi Sartangi, *Mater. Sci. Engg. A*, **2008**, vol. 494, 329-336.
- [57] X. Changoing, J. Zhanpeng, *J Less Comm. Metals*, **1990**, vol. 162, 315-322.

- [58] C. Sudha, T. N. Prasanthi, V. Thomas Paul, S. Saroja, M. Vijayalakshmi, *Metall. Mater. Trans. A*, **2012**, vol. 43, 3596-3607.
- [59] M. Smaga, F. Walther, D. Eifler, *Mater. Sci. Engg. A*, **2008**, vol. 483-484, 394-397.
- [60] M.R.D. Rocha, C.A.S. Oliveira, *Mater. Sci. Engg A*, **2009**, vol. 517, 281-285.
- [61] J. Talonen, H. Hänninen, *Acta Mater.*, **2007**, vol. 55, 6108-6118.
- [62] S.S.M. Tavares, J.M. Pardal, M.J. Gomes da Silva, H.F.G. Abreu, M.R. da Silva, *Mater. Chara.*, **2009**, vol. 60, 907-911.
- [63] A. Das, S. Tarafder, P.C. Chakraborti, *Mater. Sci. Engg. A*, **2011**, vol. 529, 9-20.
- [64] J.Y. Choi, W. Jin, *Scripta Mater.*, **1997**, vol. 36, 99-104.
- [65] W. Ozgowicz, A. Kurc, M. Kuick, *Archives of Mater. Sci. Engg.*, **2010**, vol. 43, 42-53.
- [66] S.M. Alvarez, A. Bautista, F. Velasco, *Corr. Sci.*, **2013**, vol. 69, 130-138.
- [67] A. Rezaee, A. Najafizadeh, A. Kermanpur, M. Moallemi, *Mater. Des.*, **2011**, vol. 32, 4437-4442.
- [68] F. Forouzan, A. Hedayati, R. Surkialiabad, *Mater. Sci. Engg. A*, **2010**, vol. 527, 7334-7339.
- [69] H. Mirzadeh, A. Najafizadeh, *Mater. Des.*, **2009**, vol. 30, 570-573.
- [70] K. Tomimura, S. Takaki, Y. Tokunaga, *ISIJ Int.*, **1991**, vol. 31, 1431-1437.
- [71] C.G. Rhodes, J.C. Williams, *Metall. Trans. A*, **1975**, vol. 6, 1670-1671.
- [72] I. Manna, P.P. Chattopadhyay, P. Nandi, F. Banhart, H.J. Fecht, *J. App. Phys.*, **2003**, vol. 93, 1520-1524.
- [73] R. Jing, C.Y. Liu, M.Z. Ma, R.P. Liu, *J. Alloy Compd.*, **2013**, vol. 552, 202-207.

- [74] F. Li, J. Mo, J. Li, J. Huang, W. Fan, J. Fang, *Procedia Engg.*, **2014**, vol. 81, 754-759.
- [75] Z.P. Chen, Z. Wen, Q. Jiang, *Solid State Comm.*, **2004**, vol. 132, 747-750.
- [76] G.B. Kale, R.V. Patil, P.S. Gawade, *J. Nucl. Mater.*, **1998**, vol. 257, 44-50.
- [77] G.B. Kale, K. Bhanumurthy, K.C. Ratnakala, S.K. Khera, *J. Nucl. Mater.*, **1986**, vol. 138, 73-80.
- [78] M. Ghosh, S. Chatterjee, B. Mishra, *Mater. Sci. Engg. A*, **2003**, vol. 363, 268-274.
- [79] O. Taguchi, G.P. Tiwari, Y. Iijima, *Mater. Trans.* **2003**, vol 44, 83-88.
- [80] S. Mitra, J.P. Stark, S.R. Tatti, *J. Phys. Chem. Solids*, **1991**, vol. 52, 463-465.
- [81] R.V. Patil, G.B. Kale, S.P. Garg, *J. Nucl. Mater.*, **1995**, vol. 223, 169-173.
- [82] K. Bhanumurthy, G.B. Kale, S.K. Khera, *J. Nucl. Mater.*, **1991**, vol. 185, 208-213.
- [83] A. Laik, K. Bhanumurthy, G.B. Kale, *J. Nucl. Mater.*, **2000**, vol. 305, 124-133.
- [84] K. Bhanumurthy, G.B. Kale, S.K. Khera, Asundi, *J. Nucl. Mater.*, **1989**, vol. 16, 179-183.
- [85] F.J.A. Den Broeder, *Scripta Metall.*, **1969**, vol. 3, 321-325.
- [86] S. K. Kailasam, J.C Lacombe, M. E. Glicksman, *Metall. Mater. Trans. A*, **1999**, vol. 30, 2605-2610.
- [87] K. Bhanumurthy, G.B. Kale, S.K. Khera, M.K. Asundi, *Metall. Trans. A*, **1990**, vol. 21, 2897-2903.
- [88] V. Raghavan, *Phase Diagrams of Ternary Iron Alloys*, Part 1, ASM International, **1987**.

- [89] W. Sprengel, M. Denking, H. Meher, *Intermetallics*, **1994**, vol. 2, 137-146.
- [90] V.D. Divya, U. Ramamurthy, A. Paul, *Intermetallics*, **2010**, vol. 18, 259-266.
- [91] S. Santra, A. Paul, *Metall. Mater. Trans. A*, **2015**, vol. 46, 3887-3899.
- [92] C. Wagner, *Acta Metall.*, **1969**, vol. 17, 99-107.
- [93] H. Wei, X. Sun, Q. Zheng, G. Hou, H. Guan, Z. Hu, *J. Mater. Sci. Technol.*, **2004**, vol. 20, 196-198.
- [94] C.H. Jan, D. Swenson, X.Y. Zheng, J.C. Lin, Y.A. Chang, *Acta Metall.*, **1991**, vol. 39, 303-315.
- [95] R.V. Patil, G.B. Kale, P.S. Gawde, *J. Nucl. Mater.*, **2001**, vol. 297, 153-160.
- [96] M. A. Dayananda, *Scripta Metall.*, **1968**, vol. 2, 117-120.
- [97] M.A. Dayananda, Y.H. Sohn, *Scripta Mater.*, **1996**, vol. 35, 683-688.
- [98] M.A. Dayananda, *Mater. Sci. Engg. A*, **1989**, vol. 121, 351-359.
- [99] K.N. Kulkarni, M.A. Dayananda, *Def. Diff. Forum*, **2009**, vol. 289-292, 593-599.
- [100] D.D. Keiser, M.A. Dayananda, *J. Nucl. Mater.*, **1993**, vol. 200, 229-243.
- [101] S. Santra, A. Paul, *Scripta Mater.*, **2015**, vol. 103, 18-21.
- [102] M.P. Allen, Introduction to Molecular Dynamics Simulation, <http://www.fz-juelich.de/nic-series/volume23>, **2004**.
- [103] I.M. Torrens, *Interatomic Potentials*, Academic Press, New York, **1972**.
- [104] S.E. Imamova, P.A. Atanasov, N.N. Nedialkov, F. Dausinger, P. Berger, *Nucl. Instr. Met. Phys. Res. B*, **2005**, vol. 227, 490-498.
- [105] B. Wang, E. Sak-Saracino, N. Gunkelmann, H. M. Urbassek, *Comp. Mater. Sci.*, **2014**, vol. 82, 399-404.

- [106] M I Baskes, R. A. Johnson, *Modelling Simul. Mater. Sci. Engg.*, **1994**, vol. 2, 147-163.
- [107] S.P. Kiselev, E.V. Zhirov, *Intermetallics*, **2014**, vol. 49, 106-114.
- [108] M. I. Baskes, *Phys. Rev. B*, **1992**, vol. 46, 2727-2742.
- [109] B.J. Lee, M. I. Baskes, *Phys. Rev. B*, **2000**, vol. 62, 8564-8567.
- [110] B. J. Lee, M. I. Baskes, H. Kim, Y. K. Cho, *Phys. Rev. B*, **2001**, vol. 64, 1841021-10.
- [111] I. Sa, B.J. Lee, *Scripta Mater.*, **2008**, vol. 59, 595-598.
- [112] B. J. Lee, J. W. Lee, *Calphad*, **2005**, vol. 29, 7-16.
- [113] B. J. Lee, J. H. Shim, M. I. Baskes, *Phys. Rev. B*, **2003**, vol. 68, 144112(1-11).
- [114] B. J. Lee, J. W. Jang, *Acta Mater.*, **2007**, vol. 55, 6779-6788.
- [115] J.W. Jang, J. Kwon, B.J. Lee, *Scripta Mater.*, 2010, vol. 63, 39-42.
- [116] Y. M. Kim, B. J. Lee, M. I. Baskes, *Phys. Rev. B*, **2006**, vol. 74, 014101(1-12).
- [117] H. K. Kim, W. S. Jung, B. J. Lee, *Acta Mater.*, **2009**, vol. 57, 3140-3147.
- [118] S.A.A. Akbari Mousavi, A. R. Kelishami, *Mater. Sci. Forum*, **2008**, vol. 580-582, 335-338.
- [119] F. Findik, *Mater. Des.*, **2011**, vol. 32, 1081-1093.
- [120] T.N. Prasanthi, C. Sudha, Ravikirana, S. Saroja, *Mater. Des.*, **2016**, vol. 93, 180-193.
- [121] C. Sudha, T.N. Prasanthi, V. Thomas Paul, S. Saroja, M. Vijayalakshmi, *Procedia. Engg.*, **2014**, vol. 86, 42-50.
- [122] T.N. Prasanthi, C. Sudha, S. Murugesan, V. Thomas Paul, S. Saroja, *Metall. Mater. Trans. A*, **2015**, vol. 46, 4429-4435.

- [123] Metallography and Microstructures, *ASM Handbook*, ASM International, **2004**, vol. 9, 281-293.
- [124] E.N. Kaufmann, Electron Techniques, Introduction to Scanning Electron Microscopy, *Characterization of materials*, John Wiley and Sons, Inc., Hoboken, New Jersey, **2003**, vol. 1, 1049-1050.
- [125] G. Revankar, Introduction to hardness testing, Deere and Company, *Mechanical testing and Evaluation*, ASM Handbook, ASM International, **2004**, vol. 8, 416.
- [126] V.D. Scott, G. Love, S.J.B. Reed, *Quantitative electron probe microanalysis*, 2nd ed., Ellis Horwood Ltd, UK, **1995**.
- [127] T.N. Prasanthi, C. Sudha, P.K. Parida, Arup Dasgupta, S. Saroja, *J. Mater. Engg. Perf.*, **2016**, vol. 25, 536-544.
- [128] T.N. Prasanthi, C. Sudha, P.K. Parida, A. Dasgupta, S. Saroja, *Metall. Mater. Trans. A*, **2015**, vol. 46, 1519-1534.
- [129] S. Brennan, K. Bermudez, N.S. Kulkarni, Y.H. Sohn, *Metall. Mater. Trans. A*, **2012**, vol. 43, 4043-4052.
- [130] M.A. Dayananda, *Def. Diff. Forum*, **2010**, vol. 297-301, 1451-1460.
- [131] L.D. Hall, *The J Chem. Phys.*, **1953**, vol. 21, 87-89.
- [132] Z. Guo, N. Saunders, J.P. Schillè, A.P. Miodownik, *Mater. Sci. Engg. A*, **2009**, vol. 499, 7-13.
- [133] T.N. Prasanthi, C. Sudha, Ravikirana, S. Saroja, N. Naveen Kumar, G.D. JanakiRam, *Mater. Des.*, **2015**, vol. 88, 58-68.
- [134] J.W. Elmer, D.D. Kautz, Lawrence, *ASM Handbook*, vol. 6, ASM International, **1993**, USA.

- [135] H. Ohtani, T. Tanaka, M. Hasebe, T. Nishizawa, *Calphad*, **1988**, vol. 12, 225-246.
- [136] M. Sahin, *Mater. Des.*, **2007**, vol. 28, 2244-2250.
- [137] P. Li, J. Li, M. Salman, L. Liang, J. Xiong, F. Zhang, *Mater. Des.*, **2014**, vol. 56, 649-656.
- [138] V.V. Satyanarayana, G. Madhusudhan Reddy, T. Mohandas, *J. Mater. Process. Technol.*, **2005**, vol. 160, 128-137.
- [139] N.A. Raji, O.O. Oluwole, *J. Crystal. Process Technol.*, **2013**, vol. 3, 163-169.
- [140] H. Fujii, L. Cui, N. Tsuji, M. Maeda, K. Nakata, K. Nogi, *Mater. Sci. Engg. A*, **2006**, vol. 429, 50-57.
- [141] H. Jiang, X. Yan, J. Liu, X. Duan, *Trans. Nonferrous Met. Soc. China*, **2014**, vol. 24, 697-704.
- [142] D.S. Bae, Y.R. Chae, S.P. Lee, J.K. Lee, S.S. Park, Y.S. Lee, S.M. Lee, *Procedia Engg.*, **2011**, vol. 10, 996-1001.
- [143] Y. Morizono, M. Nishida, A. Chiba, T. Yamamuro, *Mater. Sci. Forum*, **2004**, vol. 465-466, 373-378.
- [144] http://www.engineersedge.com/properties_of_metals.htm.
- [145] S. Saravanan, K. Raghukandan, *Mater. Sci. Forum*, **2011**, vol. 673, 125-129.
- [146] S. Saravanan, K. Raghukandan, *Sci. Technol. Weld. Join*, **2012**, vol. 17, 99-103.
- [147] S.A.A. Akbari Mousavi, S.T.S. Al Hassani, A.G. Atkins, *Mater. Des.*, **2008**, vol. 29, 1334-1352.
- [148] A. Pocalyko, *Mater. Protection*, **1965**, vol. 4, 10-15.

- [149] B. Kosec, L. Kosec, G. Čevnik, P. Fajafar, M. Gojić, I. Anžel, *Metallurgija*, **2003**, vol. 43, 83-86.
- [150] X. J. Li, F. Mo, X. H. Wang, B. Wang, K. X. Liu, *Sci. Technol. Weld. Join.* **2012**, vol. 17, 36-41.
- [151] Y. Yang, Z. Xinming, L. Zhenghua, L. Qingyun, *Acta Mater.*, **1996**, vol. 44, 561-565.
- [152] C.H. Oxford, P.E.J. Flewitt, *Metall. Mater. Trans. A*, **1977**, vol. 8, 741-750.
- [153] D. Van Heerden, D. Josell, D. Shechtman, *Acta Mater.*, **1996**, vol. 44, 297-306.
- [154] T. Tepper, D. Shechtman, D. Van Heerden, D. Josell, *Mater. Letters*, **1997**, vol. 33, 181-184.
- [155] A.S. Bolokang, M.J. Pasha, D.E. Motaung, F.R. Cummings, T.F.G. Muller, C.J. Arendse, *Mater. Letters*, **2014**, vol. 132, 157-161.
- [156] M.T. Jovanović, S. Tadić, S. Zec, Z. Mišković, I. Bobić, *Mater. Des.*, 2006, vol. 27, 192-199.
- [157] A. Agauayo, G. Murrieta, R. de Coss, *Phys. Rev. B*, **2002**, vol. 65, 092106.
- [158] R. Dixon, *Welding, Brazing and Soldering*, ASM Handbook, ASM International, USA, **1993**, vol. 6.
- [159] S.A.A. Akbari Mousavi, L.M. Barrett, S.T.S. Al-Hassani, *J. Mater. Proc. Technol.*, **2008**, vol. 202, 224-239.
- [160] J. Song, A. Kostka, M. Veehmayer, D. Raabe, *Mater. Sci. Engg. A*, **2011**, vol. 528, 2641-2647.
- [161] F. Findik, R. Yilmaz, T. Somyurek: *Sci. Res. Essays*, **2011**, vol. 6(19), 4141-4151.

- [162] A. Kurc, M. Kuick, M. Basiaga, *Arch. Mater. Sci. Engg.*, **2010**, vol. 38, 154-162.
- [163] V.S. Raja, R.D. Angal, M. Suresh, *Corrosion*, **1993**, vol. 49, 1-7.
- [164] R. Mythili, S. Saroja, M. Vijayalakshmi, V.S. Raghunathan, *J. Nucl. Mater.*, **2005**, vol. 345, 167-183.
- [165] L.V. Jinlong, L. Hongyun, *Mater. Sci. Engg. C*, **2014**, vol. 34, 484-490.
- [166] S. Morito, H. Tanaka, R. Konishi, T. Furuhashi, T. Maki, *Acta Mater.*, **2003**, vol. 51, 1789-1799.
- [167] M. Eskandari, A. Najafizadeh, A. Kermanpur, *Mater. Sci. Engg. A*, **2009**, vol. 519, 46-50.
- [168] M. Karimi, A. Najafizadeh, A. Kermanpur, M. Eskandari, *Mater. Chara.*, **2009**, vol. 60, 1220-1223.
- [169] G.E. Dieter, *Mechanical Metallurgy*, 1988, USA McGraw Hill Book Co.
- [170] J. Singh, C.M. Wayman, *Mater. Sci. Engg.*, **1987**, vol. 93, 227-233.
- [171] D.S. Leem, Y.D. Lee, J.H. Jun, C.S. Choi, *Scripta Mater.*, **2001**, vol. 45, 767-772.
- [172] R. Montanari, *Mater. Letters*, **1989**, vol. 8, 297-300.
- [173] <http://www.totalmateria.com/Article97.htm>
- [174] S. Xiong, W. Qi, B. Huang, M. Wang, Y. Li, *Mater. Chem. Phys.*, **2010**, vol. 120, 446-451.
- [175] C.G. Rhodes, N.E. Paton, *Metall. Mater. Trans. A*, **1979**, vol. 10, 209-216.
- [176] D.H. Hong, T.W. Lee, S.H. Lim, W.Y. Kim, S.K. Hwang, *Scripta Mater.*, **2013**, vol. 69, 405-408.

- [177] Landolt-Börnstein New series III/26 pp. 240. Self diffusion in solid metal elements, 240.
- [178] Y. Liu, L. Zhang, Y. Du, D. Liang, *Calphad*, **2009**, vol. 33, 732-736.
- [179] H. Nakajima, K. Yusa, Y. Kondo, *Scripta Mater.*, **1996**, vol. 34, 249-253.
- [180] W. Gasior, A. Debski, *Archives of Metall. Mater.*, **2012**, vol. 57, 1095-1104.
- [181] M.A. Dayananda, Y.H. Sohn, *Metall. Mater. Trans A*, **1999**, vol. 30, 535-543.
- [182] V. Raghavan, *J. Phase Equilibria*, **2003**, vol. 24, pp. 62-66.
- [183] http://www.webelements.com/periodicity/molar_volume/.
- [184] B. Alemán, L. Gutiérrez, J.J. Urcola, *Scripta Mater.*, 1997, vol. 36, 509-515.
- [185] Landolt-Börnstein (1990) Diffusion in solid metals and alloys, Springer Berlin Heidelberg.
- [186] M. Vach, M. Svojtka, *Metall. Mater. Trans. A*, **2012**, vol. 43, 1446-1452.
- [187] S. Kundu and S. Chatterjee: *Mater. Sci. Engg. A*, 2008, vol. 48, pp. 316-322.
- [188] L. Pandelaers, B. Blanpain, P. Wollants, *Calphad*, **2011**, vol. 35, 518-522.
- [189] W. Cia, J. Li, S. Yip, Molecular Dynamics. In: Konings R.J.M (ed.), *Comprehensive Nuclear Materials*, Vol. 1, Amsterdam **2012**.
- [190] Y. N. Wen, J. M. Zhang, K. W. Xu, *App. Surf. Sci.*, **2007**, vol. 253, 8620-8625.
- [191] J. W. Jang, B.J. Lee, J. H. Hong, *J. Nucl. Mater.*, **2008**, 373, 28-38.
- [192] <http://www.ks.uiuc.edu/Research/vmd/>.